



**Aging of Natural Rubber Studied via
Fourier-Transform Rheology and Time-Domain NMR**

zur Erlangung des akademischen Grades eines
DOKTORS DER INGENIEURWISSENSCHAFTEN (Dr. -Ing.)
von der KIT-Fakultät für Chemieingenieurwesen und Verfahrenstechnik
des Karlsruher Instituts für Technologie (KIT)

genehmigte

DISSERTATION

von

Shouliang Nie

aus

Shandong, China

Tag der mündlichen Prüfung: 25.06.2020

Erstgutachter: Prof. Dr. Manfred Wilhelm

Zweitgutachter: Prof. Dr. Nobert Willenbacher

Ich versichere, dass die hier vorliegende Dissertation mit dem eingereichten und genehmigten Prüfungsexemplar der Doktorarbeit übereinstimmt.

Shouliang Nie

Karlsruhe, den 06. 07. 2020

to my grandfather Xing-gui Nie.
谨以此文献给我的祖父聂兴贵。

Zusammenfassung (Abstract)

Aufgrund seiner hervorragenden Elastizität und Langlebigkeit wird vernetzter Naturkautschuk (NR, natural rubber) in einer Vielzahl von Produkten eingesetzt, von Reifen bis hin zu Luftfedern. Während ihrer langen Lebensdauer werden die Produkte durch thermische Oxidation gealtert und durch die lang anhaltende große Verformung ermüdet. Daher wurden der Alterungsmechanismus von NR sowie die relevanten Charakterisierungsmethoden intensiv untersucht. Der Alterungseffekt auf die dynamisch-mechanischen Eigenschaften dieser viskoelastischen Materialien wird üblicherweise mittels linearer Rheologie mit den Parametern Elastizitätsmodul, G' , und dem Verlustfaktor, $\tan\delta$, bewertet. Im nichtlinearen viskoelastischen Bereich ist das sinusförmige Drehmomentssignal jedoch verzerrt (nichtlinear). Der nichtlineare Teil wurde in dieser Arbeit quantifiziert, um dessen physikalische Bedeutung besser zu verstehen. Die Fourier-Transformations-Rheologie (FT-Rheologie) als kürzlich entwickelte Technik kann die Nichtlinearität durch Fourier-Transformation des Drehmomentssignals direkt quantifizieren. Um die Netzwerkstrukturänderung nach dem Altern zu charakterisieren, wird zusätzlich die ^1H Kernspinresonanz (NMR) Relaxometrie in der Zeit Domäne eingesetzt. Im Vergleich zu herkömmlichen Methoden ist das Zeit-Domänen-NMR zügiger und liefert umfangreiche Informationen über die Dynamik der Polymerketten im Nanometerbereich.

In der vorliegenden Arbeit wurden die rheologischen Eigenschaften und die Netzwerkstrukturen von NR erfolgreich mit Wirkung von Heißluft oder mechanischer Alterung bewertet. Die rheologische Nichtlinearität wurde durch die relative Intensität der 3. Harmonischen der Anregungsfrequenz $I_{3/1}$ aus der FT-Rheologie quantifiziert. Das Füllernetzwerk und das Polymernetzwerk induzieren eine rheologische Nichtlinearität bei charakteristischen Dehnungsamplituden von $\gamma_{cF} = 2,5\%$ bzw. $\gamma_{cP} = 70\%$. Die Vernetzungsdichte und die Menge der Defekte wurden mittels ^1H -Doppelquanten-Kernspinresonanz (DQ-NMR) hinsichtlich der verbleibenden dipolaren Kopplungskonstante und der Defektintensität D_{res} bzw. I_{def} untersucht.

Bei einer aeroben Alterung bei 70°C für 28 Tage nimmt die Vernetzungsdichte zu, was zu

einer höheren Elastizität und einem verringerten $I_{3/1}$ führt. Bei einer aeroben Alterung bei 120 °C für 3 Tage nimmt die Vernetzungsdichte zu Beginn zu, führt jedoch später zu einer breiteren Maschengrößenverteilung mit mehr Defekten. Des Weiteren nimmt die rheologische Nichtlinearität des Materials im Frühstadium zunächst zu und dann ab. Im Vergleich zu den mit Heißluft gealterten Proben wurden in den mechanisch gealterten Proben ca. 100 μm lange Risse gefunden. Das Intensitätsverhältnis $I_{3/1}$ bei $\gamma_0 = 70\%$ nimmt in Abhängigkeit von der Anzahl Ermüdungszyklen und dem Streckverhältnis kontinuierlich ab, während das Polymernetzwerk nach der Ermüdung laut DQ-NMR Ergebnissen stabil ist. Der Abfall der rheologischen Nichtlinearität durch Ermüdung kann auf die Mikrorisse zurückgeführt werden, die zwischen den Rußagglomeraten (CB, carbon black) und der Kautschukmatrix erzeugt werden.

In Anbetracht der Ergebnisse aus beiden Charakterisierungsmethoden kann die Änderung des Polymernetzwerks auf molekularer Ebene während der Heißluftalterung durch DQ-NMR, jedoch nicht unter Verwendung der Mikroskopie, nachgewiesen werden. Die resultierenden Risse in mechanisch gealterten Proben können unter dem Mikroskop im Mikrometerbereich beobachtet werden, aber die DQ-NMR kann diese nicht differenzieren, da die mittlere Änderung des Polymernetzwerks im Nanometerbereich durch Risse vernachlässigbar ist. Das $I_{3/1}$ bei $\gamma_0 = 70\%$ reagiert jedoch auf beide strukturellen Änderungen im NR-Komposit. Darüber hinaus zeigt $I_{3/1}$ im Vergleich zu den linearen rheologischen Parametern G' und $\tan\delta$ eine höhere relative Empfindlichkeit gegenüber dem Alterungseffekt auf NR sowohl bei aeroben als auch bei mechanischen Ermüdungsbedingungen bei hohen Temperaturen.

Abstract in English:

Owing to its excellent elasticity and endurance, crosslinked natural rubber (NR) is used in a wide range of products from tires to air suspension springs. During their long term service life, the products are aged by thermal-oxidation and fatigued by the longstanding large deformation. Thus, the aging mechanism of NR as well as the characterization methodology have been intensively investigated. The aging effect on the dynamic mechanical properties of this viscoelastic material is commonly evaluated via linear rheology with parameters such as the elastic modulus, G' , and the loss factor, $\tan\delta$. However, in the nonlinear viscoelastic regime, the stress response signal is already distorted (nonlinear) and the nonlinear portion is also worth quantifying to further understand the physical meaning. Fourier-transform rheology (FT-rheology) as a recently developed technique can directly quantify the nonlinearity

through Fourier transformation of the signal. In addition, to reveal the network structural change after aging, ^1H nuclear magnetic resonance (NMR) in time domain can be employed. Compared to conventional methods, time domain NMR is more efficient and contains rich information about the polymer chain dynamics.

In the presented work, the rheological properties and the network structures of NR were successfully evaluated with effect of hot-air or mechanical aging. The rheological nonlinearity was quantified by the relative intensity of the 3rd harmonic, $I_{3/1}$, from FT-rheology. The filler network and polymer network induces rheological nonlinearity at characteristic strain amplitudes of $\gamma_{cF} = 2.5\%$ and $\gamma_{cP} = 70\%$, respectively. The crosslink density and the amount of defects were investigated by ^1H double quantum nuclear magnetic resonance (DQ-NMR) in terms of the residual dipolar coupling constant and the intensity of network defects, D_{res} and I_{def} , respectively.

For aerobic aging at 70 °C for 28 days, the crosslink density increases, leading to a higher elasticity G' and a reduced $I_{3/1}$. For aerobic aging at 120 °C for 3 days, the crosslink density increases at the beginning, but later turns into a broader mesh size distribution with more defects. Accordingly, the rheological nonlinearity of the material increases in the early stage and then decreases. Compared to the hot-air aged samples, there were ca. 100 μm long cracks found in the mechanically aged samples. The $I_{3/1}$ at $\gamma_0 = 70\%$ continuously decreases as a function of the fatigue cycles and the stretch ratio, whereas the polymer network is stable after fatigue, according to DQ-NMR. The drop of rheological nonlinearity after fatigue can be attributed to the micro-cracks generated between the carbon black (CB) agglomerates and the rubber matrix.

Considering the characterization methodologies, the alternation of polymer network at molecular level during hot-air aging can be revealed via DQ-NMR but not using microscopy. The resulting cracks in mechanically aged samples can be observed under microscope at micrometer scale, but the DQ-NMR is similar since the polymer network change is neglectable at nanometer scale. However, the $I_{3/1}$ at $\gamma_0 = 70\%$ response to both structural changes in the NR composite. Furthermore, compared to the linear rheological parameters, G' and $\tan\delta$, $I_{3/1}$ exhibits higher relative sensitivity to the aging effect on NR at both high temperature aerobic and mechanical fatigue conditions.

Contents

Zusammenfassung (Abstract)	iii
Nomenclature	ix
1. Introduction	1
1.1. Aging of Natural Rubber (NR)	1
1.1.1. NR and the vulcanization	1
1.1.2. Chemical aging of NR	7
1.1.3. Physical aging of NR	10
1.2. Fourier-transform rheology (FT-rheology)	12
1.2.1. Basics of rheology	12
1.2.2. FT-rheology and the rheological nonlinearity	18
1.3. Time Domain NMR (TD-NMR)	27
1.3.1. Fundamentals of NMR	27
1.3.2. NMR relaxometry	32
1.3.3. Double quantum NMR (DQ-NMR)	39
2. Experimental	44
2.1. Sample preparation	45
2.2. Vulcanization of NR on rheology–NMR combination	47
2.3. Aging of NR vulcanizates	50
2.3.1. Hot-air aging	50
2.3.2. Mechanical aging	50
2.4. Characterization of NR vulcanizates	51
2.4.1. Rheology	52
2.4.2. DQ-NMR	53
2.4.3. Microscopy	54
3. Vulcanization Kinetics	55
3.1. Rheology curve with in-situ NMR relaxometry	55

3.2. Analysis of the transversal relaxation time	59
3.2.1. Fitting procedures	59
3.2.2. Correlation: $1/T_{2R}$ vs G'	63
3.3. Analysis via inverse Laplace transformation	65
3.3.1. Inverse Laplace transformation	65
3.3.2. Correlation: D_{res} vs G'	66
4. Hot-Air Aging	73
4.1. Validation of the characterization protocol	73
4.1.1. FT-rheology of NR vulcanizate	73
4.1.2. $I_{3/1}(\gamma_0)$ of filled networks	79
4.1.3. DQ-NMR of NR vulcanizate	87
4.2. Hot-air aging of unfilled NR	91
4.2.1. Influence of aging temperature	91
4.2.2. Influence of vulcanization system	97
4.3. Hot-air aging of filled NR	100
4.3.1. Influence of carbon black	100
4.3.2. Influence of anti-oxidant	103
5. Mechanical Aging	107
5.1. Aged at different fatigue cycles	108
5.2. Aged at larger stretching ratio	114
5.3. Structural changes at the nano- and the micrometer scales	124
6. Conclusion and Outlook	129
Bibliography	139
Appendix	157
A. Photographs and Mechanical Drawing	158
A.1. Photographs of the sample preparation apparatus and the RheoNMR setup .	158
A.2. Mechanical drawing of the grooved ceramic plates	160
B. Supplementary Data	161
B.1. Supplementary rheological data	162
B.1.1. Strain sweep of NRCB1 with different data density	162
B.1.2. Temperature ramp of NR vulcanizates	163

B.2. RheoNMR data of all tested NRs	164
Curriculum Vitae	167
Acknowledgements	170

Nomenclature

Abbreviations

6PPD	<i>N</i> -(1,3-dimethylbutyl)- <i>N'</i> -phenyl- <i>p</i> -phenylenediamine, the anti-oxidant used in rubber
ADC	Analogue-to-Digital Converter
BPP	Bloembergen-Purcell-Pound model in NMR theory
BR	Butadiene Rubber (polybutadiene homopolymer)
CB	Carbon Black
CBS	<i>N</i> -cyclohexyl-2-benzothiazole sulfenamide, used as rubber crosslinking accelerator
CPMG	Carr-Purcell-Meiboom-Gill NMR pulse sequence
CV	Conventional Vulcanization
DSC	Differential Scanning Calorimetry
DQ	Double Quantum in NMR theory
DQ-NMR	Double Quantum Nuclear Magnetic Resonance
EDSX	Energy Dispersive Spectrometer of X-rays
EV	Efficient Vulcanization
FID	Free Induction Decay
FT	Fourier Transform
FTIR	Fourier Transform Infrared Spectroscopy
FT-rheology	Fourier Transform Rheology
I.D.	Inner Diameter
ILT	Inverse Laplace Transformation
kc	kilocycles of stretching for mechanical fatigue
LAOS	Large Amplitude Oscillatory Shear
LVE	Linear Viscoelastic regime
MAOS	Medium Amplitude Oscillatory Shear
MSE	Magic Sandwich Echo NMR pulse sequence
MWD	Molecular Weight Distribution

NMR	Nuclear Magnetic Resonance
NR	Natural Rubber (mainly <i>cis</i> -1,4-polyisoprene from natural source)
NVE	Nonlinear Viscoelastic regime
PDI	Polydispersity Index
phr	parts per hundred rubber by weight, unit used in rubber formulations
PI	Polyisoprene
PS	Polystyrene
RD	Recycle Delay time in NMR experiments
RDC	Residual Dipolar Coupling in DQ-NMR
RF	Radio Frequency electromagnetic waves in NMR experiments
RheoNMR	the setup combined Rheometer with NMR
RT	Room Temperature
SAOS	Small Amplitude Oscillatory Shear
SBR	Styrene-Butadiene Rubber (polystyrene-butadiene copolymer)
SR	Synthetic Rubber, to differentiate from NR
SEM	Scanning Electron Microscopy
SEV	Semi-Efficient Vulcanization
TQ-NMR	Time Domain Nuclear Magnetic Resonance
TTS	Time Temperature Superposition to build the master curve of the materials' properties measured at a variety of temperatures
XmCT	X-ray micro-Computed Tomography
xx4	CPMG pulse sequence with alternating phase cycling via +x and -x axis in NMR relaxometry
WLF	Williams–Landel–Ferry equation for TTS
ZnO	Zinc Oxide

Greek symbols

α	crosslinking degree
β	stretch/compress factor in an exponential function for the T_2 relaxation time analysis in NMR relaxometry
γ	shear strain in rheology; magnetogyric ratio in NMR
γ_0	shear strain amplitude
γ_c	critical shear strain amplitude for rheological nonlinearity
γ_{cF}	critical shear strain amplitude of filler network
γ_{cP}	critical shear strain amplitude of polymer network

γ_{cF-P}	critical shear strain amplitude of non-reinforcing filler filled polymer system
γ_{\min}	minimum shear strain amplitude for the onset of the scaling law
γ_{\max}	maximum shear strain amplitude to tear the network
δ	phase lag angle, the angle of the mechanical loss factor
$\delta_1, \delta_3, \delta_5 \dots$	the phase angle in the Taylor's series for a nonlinear, symmetric stress response, with the odd subscript associated with the excited and odd higher harmonics
ε_0	stretching ratio for mechanical aging
η	viscosity, [Pa·s]
η^*	complex viscosity, [Pa·s]
$ \eta^* $	absolute value of the complex viscosity, [Pa·s]
θ	instantaneous orientation angle of a freely joint Kuhn segment vector, \vec{l} , with respect to the end-to-end vector, \vec{R} , in polymer chain dynamics
ν	crosslink density of bulk rubber, i.e. the number of crosslinks per volume
ρ	mass density
σ	shear stress, [Pa]
σ'	shear stress in phase with the shear strain
σ''	shear stress in phase with the shear strain rate
σ_D	standard deviation of D_{res} distribution
τ	relaxation time in rheology; evolution time in NMR
τ_c	correlation time
τ_d	longest relaxation time of polymer melts
τ_{DQ}	double quantum build-up evolution time intervals
τ_{rec}	recovery time intervals in NMR relaxometry
$\tan\delta$	mechanical loss factor
$\tan\delta_0$	mechanical loss factor in LVE
ϕ	volume fraction of the filler in rubber compounds
ω	oscillatory deformation frequency in unit of [rad/s]
ω_0	Lamor frequency in \vec{B}_0 field in unit of [rad/s]
ω_1	the basic frequency to excite the oscillatory deformation in unit of [rad/s]
$\omega_1/2\pi$	the basic frequency to excite the oscillatory deformation in [Hz]

$\omega_c/2\pi$	crossover frequency of G' and G'' at the longest relaxation time
	τ_d
$\Delta\omega/2\pi$	the width of dipolar coupling frequency
ω_L	Lamor frequency in \vec{B}_0 field in unit of [rad/s]

Latin symbols

a_T	horizontal shifting factor for the frequencies to build-up master-curve following the TTS
\vec{B}_0	static magnetic field
\vec{B}_1	oscillating magnetic field
C_1, C_2	empirical constants in the WLF equations
$C(t)$	polymer chain orientation autocorrelation function
D	diameter of the NMR glass tube, rheometer geometry, etc.
D_e	Debroah number in rheology, dimensionless
D_{static}	static limit of dipolar coupling constant
D_{res}	residual dipolar coupling constant
$\overline{D_{res}}$	average D_{res} in the distribution curve from the regularization of double quantum build-up curve
$D_{res,n}$	number averaged D_{res} in the normalized ILT distribution of the spin-spin relaxation signals in NMR
ΔE	splitting energy of the spins
G	shear modulus, [Pa]
G'	storage/elastic modulus, [Pa]
G'_0	storage/elastic modulus in LVE, [Pa]
$G_1, G_3, G_5 \dots$	the Taylor's expansion prefactors for a nonlinear but symmetric stress response, with the odd subscript associated with the basic and odd higher harmonics
g_i	distribution amplitude after ILT of NMR transversal relaxation
G'_{max}	the maximum elastic modulus in the plateau curing period of rubber vulcanization, [Pa]
G'_{min}	the minimum elastic modulus in the induction period of rubber vulcanization, [Pa]
G''	loss/viscous modulus, [Pa]
G^*	complex modulus, [Pa]
$ G^* $	absolute value of the complex modulus, [Pa]

h	Plank's constant; distance between the moving plane to the fixed plane for shear strain calculation
I	the value of spin in quantum physics
$I_1, I_3, I_5 \dots$	the intensities of FT spectra of a nonlinear but symmetric stress response in FT-rheology, with the odd subscript associated with the excited and odd higher harmonics
$I_{3/1}$	relative intensity of the 3 rd higher harmonic
$I_{3/1}(\gamma_0=2.5\%)$	$I_{3/1}$ at oscillatory shear strain amplitude of 2.5%, representing the rheological nonlinearity of filler network of the CB filled NR in this thesis.
$I_{3/1}(\gamma_0=70\%)$	$I_{3/1}$ at oscillatory shear strain amplitude of 70%, representing the rheological nonlinearity of polymer network of the CB filled NR in this thesis.
$I_{n/1}$	relative intensity of the n th higher harmonic
I_{def}	content of network defect
I_{DQ}	double quantum build-up intensity in DQ-NMR measurement
I_{nDQ}	normalized double quantum build-up intensity in DQ-NMR measurement
I_{ref}	referential intensity in DQ-NMR measurement
I_M	intensity of the mobile chains in the normalized transversal relaxation
I_R	intensity of the rigid chains in the normalized transversal relaxation
k_B	Boltzmann's constant
k	the growth exponent of $I_{3/1}(\gamma_0)$
\vec{l}	the vector of one freely rotating chain segment in polymer
L/D	the reptation tube length to diameter ratio in Doi-Edwards model
L_{noise}	level of noise in FT-rheology
Δl	the moved distance of the moving plane for shear strain calculation
\vec{M}	vector of magnetization
M_0	magnetization at equilibrium in field of \vec{B}_0
M_c	molecular weight between two crosslinks
M_e	entanglement molecular weight
m_I	magnetic quantum number
M_n	number averaged molecular weight of polymer

M_{rec}	recovered magnetization in NMR relaxometry
$M(t)$	magnetization at evolution time t
M_{unit}	molecular weight of the repeating unit of polymer
M_w	weight averaged molecular weight of polymer
N	number of statistical chain segment (the freely jointed Kuhn segments); the total number of available spin states
n	utmost nonlinearity in the growth function of $I_{3/1}(\gamma_0)$
N_f	number of cycles for failure, i.e. the failure life
n_F	utmost nonlinearity of filler network
n_P	utmost nonlinearity of polymer network
3Q_0	intrinsic rheological nonlinearity extrapolated from the quadratic relationship of $I_{3/1}$ to a infinite small strain in FT-rheology
R	universal gas constant
\vec{R}	end-to-end vector of the chain segments between two fixed crosslinks
R_{eff}	effective radius of the branches of filler aggregates or clusters
$\langle R_G \rangle$	radius of gyration of the polymer chain
S_b	dynamic order parameter of the polymer backbone
T	temperature; also Tesla, unit of magnetic flux density, $= \frac{N}{C \cdot ms^{-1}}$, depending on the context
t	time
t_{curing}	the curing time for rubber vulcanization
T_1	longitudinal relaxation time (spin-lattice relaxation)
T_2	transversal relaxation time (spin-spin relaxation)
$1/T_2$	transversal relaxation rate
T_{2M}	transversal relaxation time of relative mobile chains
T_{2R}	transverse relaxation time of relative rigid chains
t_{90}	time length of 90° NMR pulse
t_{180}	time length of 180° NMR pulse
T_g	glass transition temperature
T_{ref}	reference temperature to build a master curve in TTS
t_{xx4}	evolution time of T_2 relaxation with xx4 pulse sequence

1. Introduction

In this chapter, the significance of the natural rubber (NR) as a widely used engineering material and its aging behavior are going to be introduced. Conventionally, the dynamic mechanical properties of NR during aging are characterized via linear rheology. However, in the nonlinear viscoelastic regime of the material, the rheological nonlinearity is also worthy to be investigated. As the state of the art, Fourier transform rheology (FT-rheology) technique is explained in both theory and application perspectives for the nonlinearity quantification of polymeric materials. The NR chain structures during aging can be revealed via time domain nuclear magnetic resonance (TD-NMR) through the polymer chain dynamics at nanometer scale. This molecular level properties later could be correlated to the rheological response on the macroscopic scale. Compared to the traditional approach for chain structure analysis of NR, such as swelling equilibrium test in solvent and differential scanning calorimetry, TD-NMR is more operationally friendly and contains a wealth information of the crosslinked chains in the vulcanizate.

1.1. Aging of Natural Rubber (NR)

1.1.1. NR and the vulcanization

In the past century, traditional materials such as metal, concrete and wood have been increasingly replaced by polymeric materials with more tunable properties and shape, such as plastics, fibers and rubbers. Due to the excellent elasticity, good durability and chemical corrosion resistance, crosslinked rubbers have become an irreplaceable material nowadays in wide range of products, ranging from bottle seals to running tires.

The term "rubber" in English originally used for the material derived from the tree *Hevea brasiliensis*, which can rub off pencil marks. Nowadays, this product is specified as the

natural rubber (NR), distinguished from the man-made rubbers, e.g. synthetic polyisoprene rubber (IR), polybutadiene rubber (BR), polystyrene butadiene rubber (SBR), etc. It was known as "cahutchu" (Kautschuk in German) to the native Latin Americans before the geographic discovery of Columbus. The milky sap from *Havea* tree was found to be waterproof, stretchable and became elastic when it was dried. The development history of NR can be found in Table 1.1. In the 1830s, people formed rubber into waterproof articles such as shoes, mailbags, etc. However, the beginning of the natural rubber industry was on the verge of collapse due to the poor properties of this material, e.g. melting in the summer and cracking in the winter.

Table 1.1: Chronology of the important development of natural rubber material [1].

Year	Usage and Development
before 1500	used by native American tribes as play balls, articles for waterproof
after 1500	native rubber articles brought to Europe, though no commercial use
1745	Charles Marie de al Condamine from France made first report about this material
1770	Priestly, an English chemist, gave the name "rubber" since this material can rub off pencil marks
1790–1830	patents and factories of rubber started in England and the United States
1839	Goodyear discovered the vulcanization of rubber, significant improvement of the properties
1846	solid rubber tires for carriage by Thomas Hancock
from 1870s	transplanting the rubber tree from South America to the Far East
1888	first pneumatic tire by John Dunlop in England
1912	rubber from Southeast Asia exceeded the output of Brazil for the first time
1920–1940	price of rubber underwent wide fluctuations during the World Wars as a strategic material for tires, boots and auto parts
1942	development of synthetic rubbers (SR)
from 1964	competition between SR and NR, forced the traditional NR process to adopt technically specified standard rubber
1979	major producing and consuming countries reached an agreement in Geneva to stabilize world NR market prices
2018	worldwide consumption of NR reached 13.9 million tonnes [2], almost the total consumption of all types of SRs

The revolution of natural rubber industry started in 1840s after Charles Goodyear (1800–1860, American) [3] coincidentally discovered the vulcanization process of NR by sulfur. The self-taught chemist was obsessed with finding a solution to stabilize the rubber, even leaving his family in debt to finance his experiments. Following many years of failure, Goodyear

accidentally combined rubber and sulfur upon a stove. Out of his expectation, the rubber did not melt but hardened with the raised heat. This is a chemical crosslinking process of rubber with sulfur by heating, specially termed as vulcanization.

Before dedicating into the chemical aging process of crosslinked NR, the chemical structures of the rubber molecules and the crosslinks are introduced. The main constituent of NR [4] is *cis*-1,4-polyisoprene, as shown in Figure 1.1, with a molecular weight between 100k to 1,000k daltons. Typically, a small percentage of other materials such as ash proteins, fatty acids, resins and salts are also found in NR. However, during manufacturing of NR, some of those components could be removed or decreased. At raised heat or pressure, the sulfur will react occasionally with the unsaturated C=C bonds in polyisoprene to build up sulfidic bridges between the NR chains. Finally, a three-dimensional network is formed. Nowadays, vulcanization is the generalized term for all kinds of crosslinking process for rubber products, including the saturated rubbers crosslinked by peroxides.

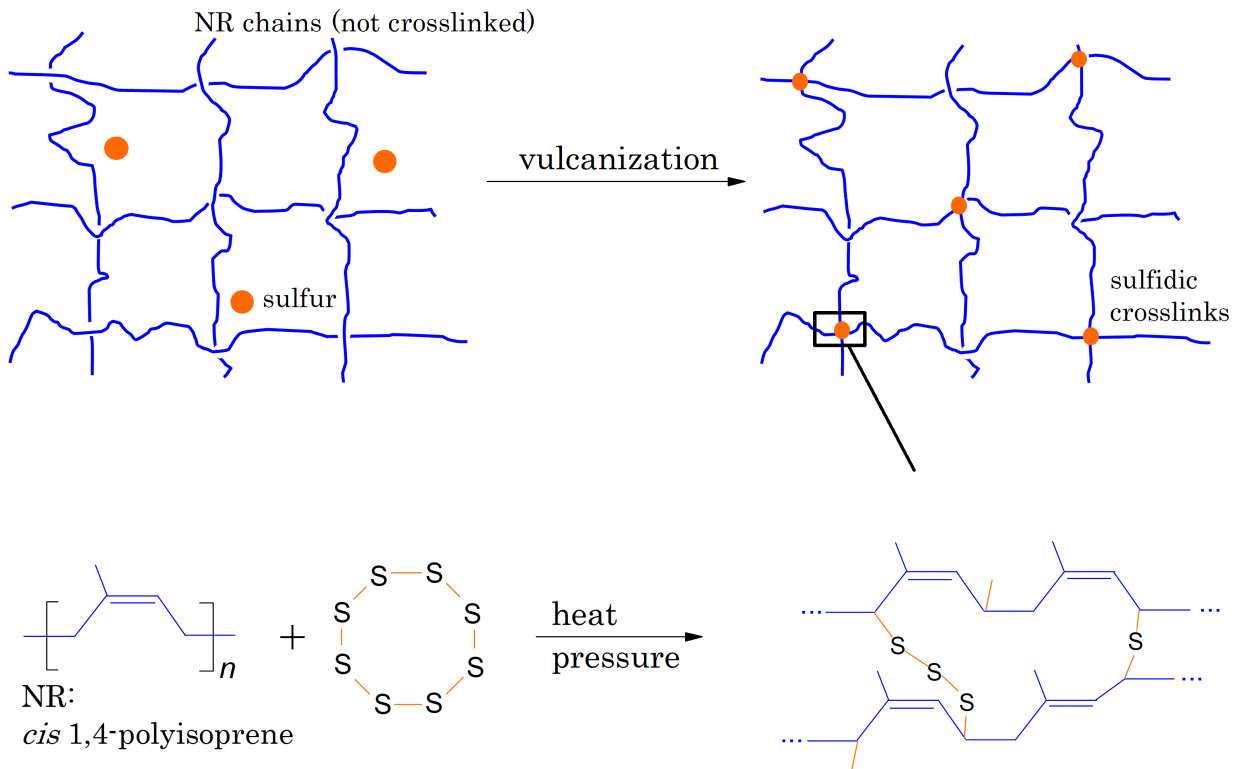


Figure 1.1: Schematic vulcanization of NR at the molecular and monomer level.

The harvest of rubber latex and manufacturing process of NR can be found in Figure 1.2.

1. Introduction

To harvest the latex from *Hevea* tree, a thin layer of the fresh bark is cut by a sharp hook shaped knife. The white sap from exposed vesicles is then tapped and collected into a tapper cup. The rubber molecules in the latex are coagulated by adding dilute acid such as formic acid. By passing through a textured rolling mill, the water from the coagulum is squeezed out. The ribbed rubber sheets are then drying upon smoke to produce ribbed-smoked natural rubber sheets (RSS). Instead of the RSS process, technically specified natural rubber (TSR) is often produced to grade the rubber more precisely by controlling the contents of impurities such as dirt, ash, protein and volatile matters. The coagulum is granulated into crumbs and some impurities get removed at the same time.

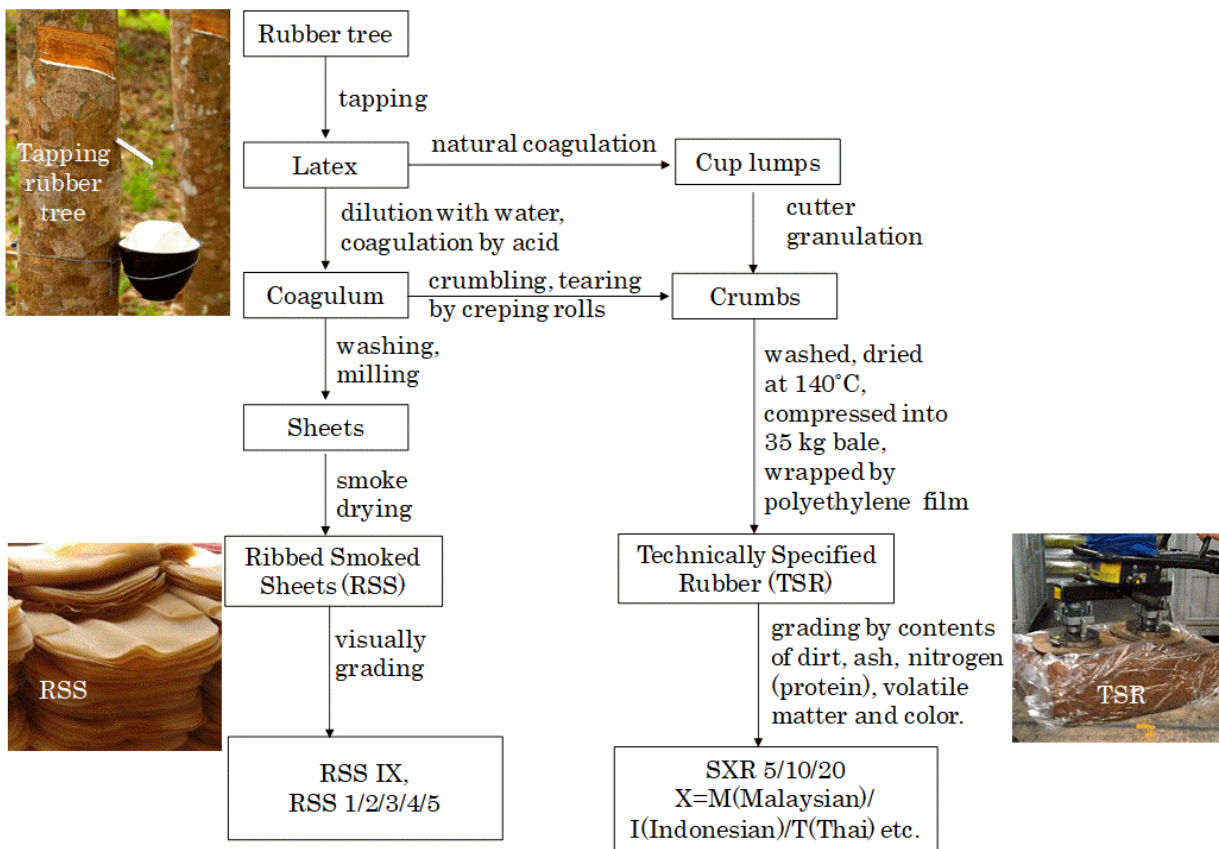


Figure 1.2: Manufacturing process of natural rubber.

During fabrication, the quality of the NR is controlled and graded [5] in a quick measure by testing the Wallace plasticity of the plasticity retention index (PRI) [6]. The unvulcanized NR is prepared into 3.4 mm thick disks with a diameter of 13 mm and aged in oven at 140 °C for 30 min. Both the original and the aged specimens are submitted to a Wallace Plastimeter and compressed at 100 N for 15 s. The Wallace plasticity is 100 times the final thickness of the test piece as expressed in unit of 0.01 mm. The PRI is calculated as $PRI = (\text{plasticity})$

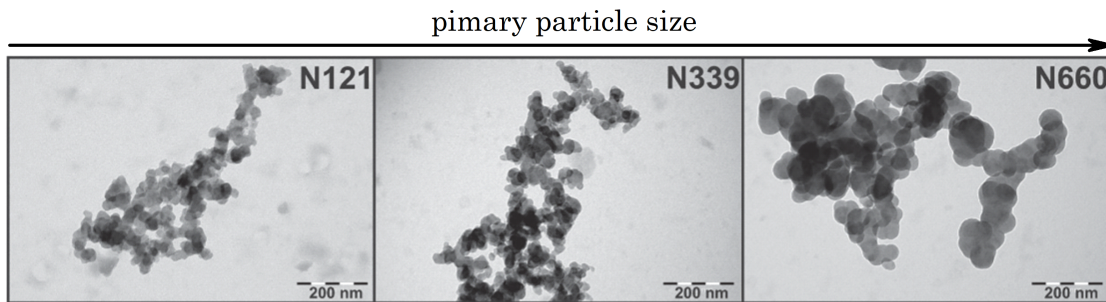
aged/plasticity original) $\times 100$. The crumbs are finally compressed into standard cubic TSR bale of typically 35 kg and wrapped by polyethylene film for easy storage and transportation. The top three NR producer countries are Thailand, Indonesia and Malaysia, which together account for about 70% of the global natural rubber production.

After mixing (compounding with crosslinking agents and other additives), shaping and vulcanization process, NR can be made into shoes, balloons, tubes, tires, etc. with good gas permeability, hyperelasticity and long life durability. In 2018, the worldwide consumption of NR reached 13.9 million tonnes [2], almost the same as the total consumption of all types of synthetic rubbers. This is due to two main reasons: 1. there are some unparalleled mechanical properties of NR comparing to SR, such as the hyperelasticity, high tear resistance; 2. the growing concern for the consumption of fossil oil and its derivatives for SR.

Besides the crosslinking agents, NR is used either pure or blended with additives such as softener, anti-aging agents, fillers to improve the process efficiency, mechanical properties or to reduce the cost of the final products. Therefore, NR vulcanizates consist of many varieties, depending on the vulcanization systems and type of fillers or other blended polymers as matrix. However, in this thesis, NR vulcanizate related to car tires are the focus since this a one of the main products in NR industry. Following the core of the topic, the aging properties of NR, the anti-aging agents are going to be introduced in detail in next sections about aging process of NR vulcanizate.

Neat NR vulcanizates only exhibit low mechanical properties that are not useful in many applications until they are blended with high surface energy solid particles, i.e. reinforcing fillers [7] like the carbon black (CB). By mixing those fillers into NR, the modulus of the products can be highly improved to meet the engineering needs. Compared to the rubber matrix, the solid particles of the fillers show several orders of magnitude higher in modulus, stiffness, hardness. Therefore, it is reasonable to expect mixing of those fillers into rubbers will result in composites with improved macroscopic mechanical properties of the unfilled. Moreover, non-reinforcing fillers such as clay, organic treated montmorillonite, aluminum trihydrate are blended into the composites to reduce the cost, improve the flame retardant properties and etc. Regarding the NR composites for tires, fillers with their reinforcing capabilities are of main interest. These fillers include CB and silanized silica. A precise definition of the term "reinforcement" [8] is difficult since it depends on the experimental conditions and the intended effects of the filler addition. However, it appears preferable to regard reinforcement broadly as the improvement of the mechanical properties of the composites by a filler.

carbon black



50 phr silica in SBR

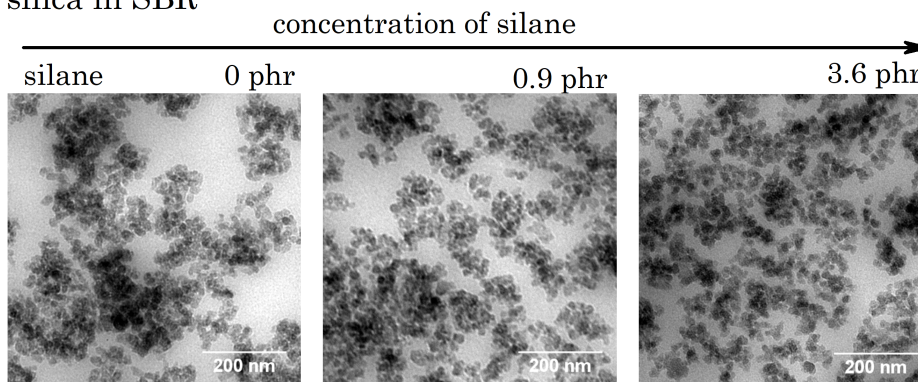


Figure 1.3: Transmission electron microscopic images of CB aggregates of different grades [9] and silica clusters in SBR rubber matrix with different silane contents [10]. In the grade number of CB reading as N---, the first digit indicates the size of the primary particle. The second and third digits stand for the structure of the CB aggregates. The silane in silica-containing compound is added as a coupling agent to bind the polar filler surface with the non-polar rubber matrix so that the compatibility can be improved.

The structure of CB and silica can be found in Figure 1.3. The primary particles of CB is between 10–90 nm and 4–20 nm that of silica. The CB are fabricated from controlled heat decomposition of hydrocarbon products (oil or gas). During the fabrication of CB, the primary particles in shape of sphere fuse together into three dimensional aggregates. Those aggregates can not be separated during mixing with rubber or deformation of the composites. The entanglement of aggregates form the agglomerates, which are finally pelletized into millimeter size granules. The aggregates can adsorb the rubber chains with high surface energy and high specific surface area, then the modulus of the composites increase with the CB network. Silica are normally prepared either by pyrogenation of silica tetrachloride or by precipitation from the solution of alkaline silicates. The polar chemical groups on silica particles can be modified by silane to improve the compatibility with hydrophobic diene

rubbers. When compared to CB filled rubber, silanzied silica filled rubber maintains lower viscous dissipation and therefore lower rolling resistance (i.e. lower gasoline consumption for the car). Therefore, the tire made from this type of rubber tread is called "green tire".

1.1.2. Chemical aging of NR

To understand the possible chemical aging process of NR vulcanizate, we need to start with the chemical structures of the whole network, including the structure of the crosslinks. For rubber vulcanization, there are mainly three choices of crosslinking systems: 1) peroxide vulcanization; 2) unaccelerated sulfur vulcanization and 3) sulfur vulcanization with accelerators. With respect to peroxide crosslinking, the network is built up through carbon-carbon crosslinks. The chemical aging process mainly occur on the unsaturated C=C bonds on the rubber backbone, where the chemical bond energy is lower than that of saturated C-C bonds. In this thesis, NR vulcanizates used in tires are selected as the only focus, which are accelerated sulfur vulcanization systems. In addition, mainly the thermal induced or thermal-oxidation induced chemical aging processes are of interest for tire related rubbers.

With respect to sulfurated NR vulcanizates, the possible crosslink features can be found in Figure 1.1 as mono-, di- and polysulfide. Those structures in sulfur-NR or synthetic polyisoprene systems and the quantities have been systemically elucidated in 1960s, e.g. by the British *Natural Rubber Producers' Research Association*. They studied the crosslinking efficiency of unaccelerated sulfur-NR system [11, 12] and the vulcanization in presence of zinc oxide [13]. Triphenylphosphine and sodium di-*n*-butyl phosphite was used to determine the type of sulfur linkages [14]. Besides, the crosslinking density can be calculated from stress-strain curves and equilibrium volume swelling measurements [15]. The types of the crosslinks were determined by the chemical structures of the accelerators, the cure time and temperatures [16–18], in comparison with the peroxide vulcanized system [19]. After cleavage of disulfide crosslinks through thiol-difulfide interchange reaction [20], the structure of accelerator residues bounded on the network [21] with radioactive ^{14}C labels was tracked during different curing conditions [22]. Those established methods were summarized by Moore, Porter, Campbell and co-workers [23].

To classify the dominate population of different type of sulfidic crosslinks in sulfur-NR systems, we need to introduce the concept of *vulcanization efficiency* of the sulfur atoms. This has been widely applied in rubber industry. This efficiency parameter E [23] is defined as the ratio between the amount of bonded sulfur and the the amount of the chemical crosslinks per

network:

$$E = \frac{\text{number of combined sulfur atoms/network}}{\text{number of chemical crosslinks/network}} \quad (1.1)$$

The vulcanization of NR by sulfur alone requires $E = 40\text{--}55$ sulfur atoms for each crosslink. The curing process is extremely slow, e.g. taking almost 6 hours to complete at 140°C , which is uneconomical by view point of production. Furthermore, the final products do not maintain adequate mechanical properties due to the poor resistance of the polysulfides to thermal-oxidative degradation. However, this drawback has been overcome through the invention of accelerators. The accelerators can increase the speed of vulcanization and permit lower curing temperature with greater sulfur efficiency with $E = 2\text{--}20$. Normally, with assistance of zinc oxide and stearic acid, the accelerator can be activated for the vulcanization reaction. The chemical classification of accelerator includes, vulcanization speed from slow to fast, aldehyde amine, guanidine, thiazole, sulfenamides, thiram, etc.

According to the vulcanization efficiency, the accelerator-sulfur-NR systems can be categorized as *Conventional Vulcanization* (CV), *Semi-Efficient Vulcanization* (SEV) and *Efficient Vulcanization* (EV). Rubber with different vulcanization systems generate varying sulfidic crosslink compositions during vulcanization and thus exhibit distinctively for heat aging resistance as listed in Table 1.2.

Table 1.2: The types of the sulfidic crosslinks in NR vulcanizates from the three accelerator-sulfur vulcanization systems and the corresponding properties [24, 25].

Vulcanization	CV	SEV	EV
<i>Curing agents composition</i>			
Sulfur [phr]	2.0–3.5	1.0–1.7	0.4–0.8
Accelerator/sulfur ratio	0.1–0.6	0.7–2.5	2.5–12
<i>Sulfidic crosslinks</i>			
Poly- & disulfidic (%)	95	50	20
Monosulfidic (%)	5	50	80
Cyclic sulfide concentration	high	medium	low
<i>Properties</i>			
Reversion (inverse reaction of crosslinking)	high	medium	low
Low temp. crystallization	high	medium	low
Heat-aging resistance	poor	medium	good

In the CV system, the accelerator/sulfur ratio is relatively low, resulting in high contents

of polysulfide crosslinks (R-S_x-R), with R as the rubber hydrocarbon chain and S_x as the crosslinks contains more than 2 sulfur atoms. To the contrary, the accelerator/sulfur ratio is relatively high in EV systems, leaving a mono- and disulfide (R-S₁-R and R-S₂-R) crosslinks dominated networks. Those different type of crosslinks together with the unsaturated C=C bonds on the network backbone do determine the heat and oxidization resistance. During vulcanization or chemical aging, the quantities of different types of bridges can be analysed by the selective cleavage with special chemicals, e.g. triphenylphosphine and sodium di-*n*-butyl phosphite in benzene [12,14]. Using high resolution solid state ¹³C nuclear magnetic resonance spectroscopy [26], the backbone structures after vulcanization or aging can be analyzed. The density of the crosslinks can be quantified via the stress-strain curve, the freezing point depression of solvent in the swollen network and volume of swelling in equilibrium techniques as mentioned before.

With respect to the chemical aging of NR, it takes place in two ways, either by the cleavage on the unsaturated backbones, e.g. via free radical triggered oxidation, or through modification of the sulfidic crosslinks. The chemical bond scission on the macromolecules cause the degradation of the polymer. The initiation of the chain scission include thermal, photochemical, radiation chemical, biological processes on the weak points of with lower bond dissociation energy. Impurities, additives and metal ions present in the material can react with the polymeric matrix at sufficient high temperature. Under photon radiation by ultraviolet or visible light, polymer chains could also degrade.

Specified for NR vulcanizates in tire products, it is mainly thermal modification and thermal-oxidation involved reactions for the chemical aging. This type of aging in lab is normally conducted in the lab via an oven with air at elevated temperatures [27] to mimic or accelerate the aging condition. The thermo-oxidative aging of NR and its effect on the network structure as well as mechanical performance has been systemically studied [28]. Under heat treatment, the -S_x- in CV vulcanizates can transfer into -S₁- or -S₂- crosslinks, producing higher density network during the initial aging period. This causes an increase in the modulus and tensile strength. On the other side, the high mole concentration of unsaturated bonds in NR molecules makes it highly susceptible to being attacked by oxygen, resulting chain degradation. It has been proven by the increased polar groups in FT-IR spectra and more sol molecule contents from acetone extraction. Therefore, for a longer period of hot air aging, the main chain scission will dominate and tensile strength decline. Compared to CV vulcanizate, efficiently vulcanized rubber with simple -S₁ or -S₂- crosslinks possess better retention during hot air aging.

1.1.3. Physical aging of NR

The physical aging process of NR is also of paramount importance for the safety of rubber products like tires. A failure of the over running tire very often causes fatal accidents of car drivers. Figure 1.4 demonstrates the broken truck tire after a running test in a lab. The separation of the tire components occurs at the edge of steel wires (belts). This is the area where the high stress is concentrated due to very different stiffness between the steel wires and rubber matrix [29].

In studies of failure during physical or mechanical aging, there are mainly two categories: brittle failure and ductile failure. For rubber or elastomers, the failure takes place at large deformation accompanied with long time fracture, which is the characteristic for a ductile failure [30].



Figure 1.4: Cross-section view of a failure truck tire after a durability test [31].

To determine the fatigue life of rubber materials, it is commonly conducted in a dynamic way where continuous cyclic force or deformation is loaded on the samples [32,33]. The load is commonly in uniaxial tension or compression mode with a fixed strain amplitude. The appearance of cracks on the sample surface or the modulus (or the loading force at specified strain) is tracked during the test. The criteria for failure is commonly based on the length of the appeared cracks on the specimen in millimeter size and the cycle number is ranging from 50 kilos to millions. To accelerate the measurement time, the specimens sometimes are notched or cut with a fixed length in the working area as an initial artificial crack. Thereafter, the crack direction can be more easily monitored. The growth rate of the crack and the

corresponding dissipated energy is calculated. Those tests are of high interest and the results normally correlate well with the practical applications.

During the physical aging process, the types of rubber and vulcanization formulations play a crucial role during the cracks nucleation and propagation [34]. As for polymers, strain induced crystallization of some rubber molecules, such as NR, polychloroprene rubber (CR), can resist the crack growth. However, the strain-crystallization is not present for other rubbers like SBR, BR and butyl rubber (IIR), which are also heavily used in tires. Therefore, blending NR into them shows strong beneficial consequences of the fatigue performance at high strain levels.

In rubber composites, the addition of reinforcing fillers can pronouncedly enhancing the anti-fatigue properties. This has been attributed into many mechanisms, including the increase of stiffness and hysteresis, crack tip branching from the non-homogeneity of the rubber-filler interface and agglomeration of the filler particles during fatigue [35]. For a specified volume of filler, a higher specific surface area is better and low structure fillers are superior to high-structure ones.

For the vulcanization perspective, crosslinks via covalent bonds improve the physical properties of the rubber. Higher number of crosslinks will generate higher stiffness to carry the loading force but reduce the hysteresis at the same time. These are two competing effects of the strengthening via increased crosslink density and the ability for energy dissipation through hysteresis. Therefore, there exists an optimum density of the vulcanization recipe to make longest fatigue life of the products. Another effect is the type of crosslinks formed through different curing systems: C-C from peroxide, C-S-C from efficient vulcanization or C-S_x-C from conventional vulcanization. Polysulfidic bonds are weaker and consequently can break before the carbon-carbon bonds in the primary rubber backbone and also the mono- or disulfide crosslinks. This will lead to the crack tip blunting and higher energy dissipation from hysteresis [36,37]. Therefore, polysulfidic bonds are preferable to improve the fatigue properties of the products, compared to C-S_{1,2}-C or C-C bonds.

1.2. Fourier-transform rheology (FT-rheology)

1.2.1. Basics of rheology

Rheology is dealing with the relationship between applied force and deformation of materials and applied also in many aspects of the daily life. The term "rheology" is derived from Greek with the prefix *rheo-* means flow and the postfix *-logy* stands for a scientific subject. Therefore, rheology is the science for studying the deformation or flow of materials [38], including liquids and solid materials, when respective stress are applied to them.

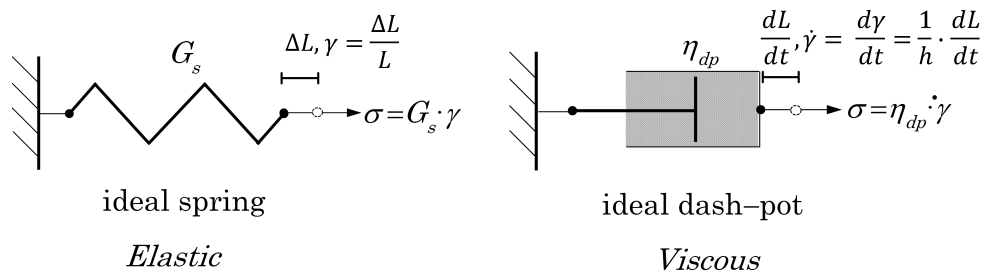


Figure 1.5: An ideal elastic spring under a strain γ with a stress of σ and an ideal viscous dash-pot under a stress of σ to be deformed with strain rate of $\dot{\gamma}$.

The response of materials under a strain of γ (the strain rate is $\dot{\gamma} = d\gamma/dt$) with force per unit area of σ , it can be classified into two ideal cases as demonstrated in Figure 1.5: an ideal elastic and an ideal viscous material. The ideal elastic material like the spring is elongated by ΔL as a linear function of the stress σ , following the Hooke's law (Robert Hooke, 1635–1703, British physicist) $\sigma = G_s \cdot \gamma$, with G_s as the (elastic) modulus or spring constant. Most metallic materials behave closely to this. The ideal viscous material like the dash-pot with liquids, the stretch rate is linearly determined by the applied stress σ , following the Newton's law (Sir Isaac Newton, 1642–1726, English mathematician and physicist) $\sigma = \eta_d \cdot \dot{\gamma}$, with the constant η_d as the viscosity of the dash-pot. Liquids like water can be approximately considered as a Newtonian fluid. After releasing the force, the Hookean spring can fully retreat to the original position by releasing all the applied work history so that the previously input energy can be seen as fully stored by the spring. For the dash-pot, the deformation is kept there since the applied work has been totally dissipated into heat by the fluid. Therefore, the original input energy is fully lost in this process.

With respect to rubber or other polymeric materials, it is neither pure elastic nor pure viscous. It is a combination of both, which is called viscoelastic [39, 40] or elastoviscous. Those

materials can be described simply by the combination of Hookean spring and Newtonian dash-pot [41] as shown in Figure 1.6.

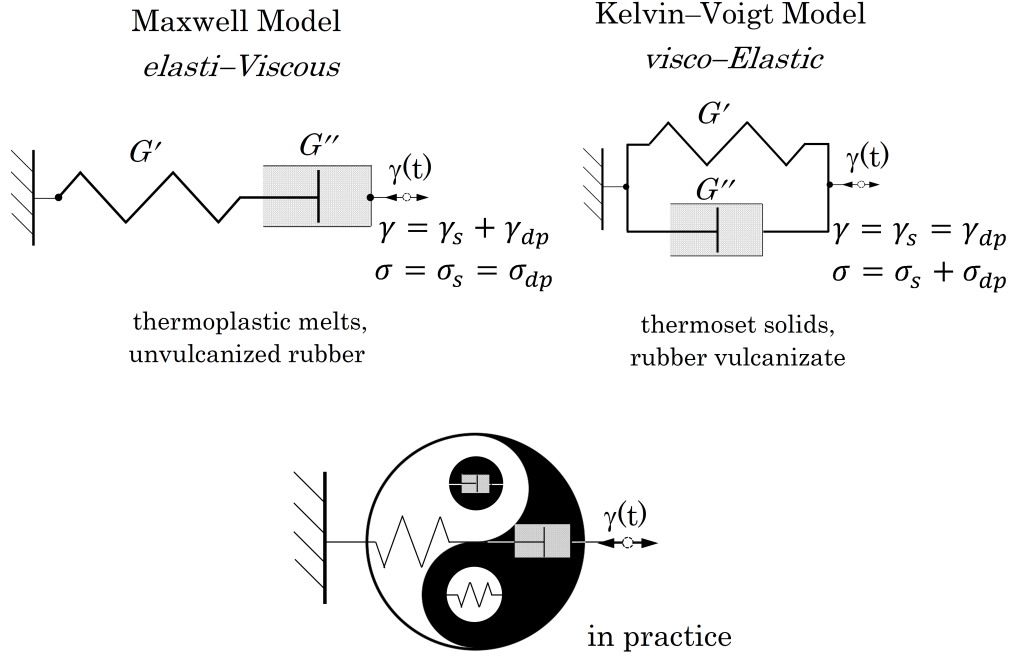


Figure 1.6: The Maxwell and Kelvin-Voigt models stand for viscoelastic materials by combining a Hookean spring and a Newtonian dash-pot in series or in parallel, respectively. While, in practice, the rubber material could be a complex combination of both, with more series of springs and dash-pots combination.

In the Maxwell model (James Clerk Maxwell, 1831–1879, Scottish mathematician and physicist), the spring and dash-pot are connected in series. Let us take the dynamic shear deformation $\gamma(t)$ for explanation. The response of the spring is in phase with the shear strain $\gamma(t)$ as the elastic part of the material. The shear modulus is superscribed with a prime as G' . Conversely, there is the response out of phase with $\gamma(t)$ from the dash-pot, i.e. in phase with the shear strain rate $d\gamma(t)/dt = \dot{\gamma}(t)$. This modulus is the viscous portion and superscribed with a double-prime as G'' . The elastic modulus will store part of the input energy and release it when the deformation is removed, while the viscous modulus will dissipate part of the input energy into heat during deformation. Therefore, G' and G'' are also called storage or loss moduli, respectively. With respect to the Kelvin-Voigt model (William Thomson, Lord Kelvin, 1824–1907, Irish-Scottish mathematical physicist and Woldemar Voigt, 1850–1919, German physicist), the spring and dash-pot are connected in parallel. Different to the Maxwell material, this model can fully recover to unreformed

position after the strain removing.

The Maxwell model can be simply used to describe the thermoplastics in melt state. After the strain there is a plastic deformation in the material so that it is shaped after removing the strain, i.e. processable. For natural rubber, it is the processes of mixing, extrusion, calendaring before the vulcanization. After vulcanization, the rubber chains are permanently linked through covalent bonds and can fully recover after deformation. Therefore, vulcanizates in many conditions can be simply expressed or modeled by the Kelvin-Voigt element with the fully strain-recoverable spring in parallel with time delay controlled by the viscous dash-pot. However, in reality, the rubber compounds and composites are complex combinations of the viscous and elastic properties, which should be generalized via several Maxwell or Kelvin-Voigt elements in the principle of Boltzmann superposition [39].

To access the viscoelastic properties of rubber or polymers, it is favorable to do dynamic rheological (mechanical) analysis of the stress response of the material under oscillatory deformation or vice versa. In this way, both the viscous and elastic properties of the material can be quantified. In comparison, the flow tests such as step strain, creep, stress relaxation, etc., instantaneous (ideally at zero time) step displacement or stress is required, which is challenging for the instruments. Figure 1.7 demonstrates the example of the rheological test of a viscoelastic materials under oscillatory shear on a parallel plate-plate geometry.

The sample is deformed by the motor with a sinusoidal rotation at an amplitude of γ_0 ,

$$\gamma(t) = \gamma_0 \sin(\omega t) \quad (1.2)$$

with

$$\gamma_0 = \frac{\Delta l}{h} \quad (\text{see Figure 1.7}) \quad (1.3)$$

in the unit material element under shear. The torque transducer fixed on the other side is detecting the stress (after proper calculation from the shear torque) signal. The time dependent signals are displayed in the right-hand side. Due the viscosity from the material, the stress response is sinusoidal but with a delayed time, $\sigma(t) = \sigma_0 \sin(\omega t + \delta)$, with δ is the phase delay angle. Based on the character of elasticity and viscosity, the stress can be split

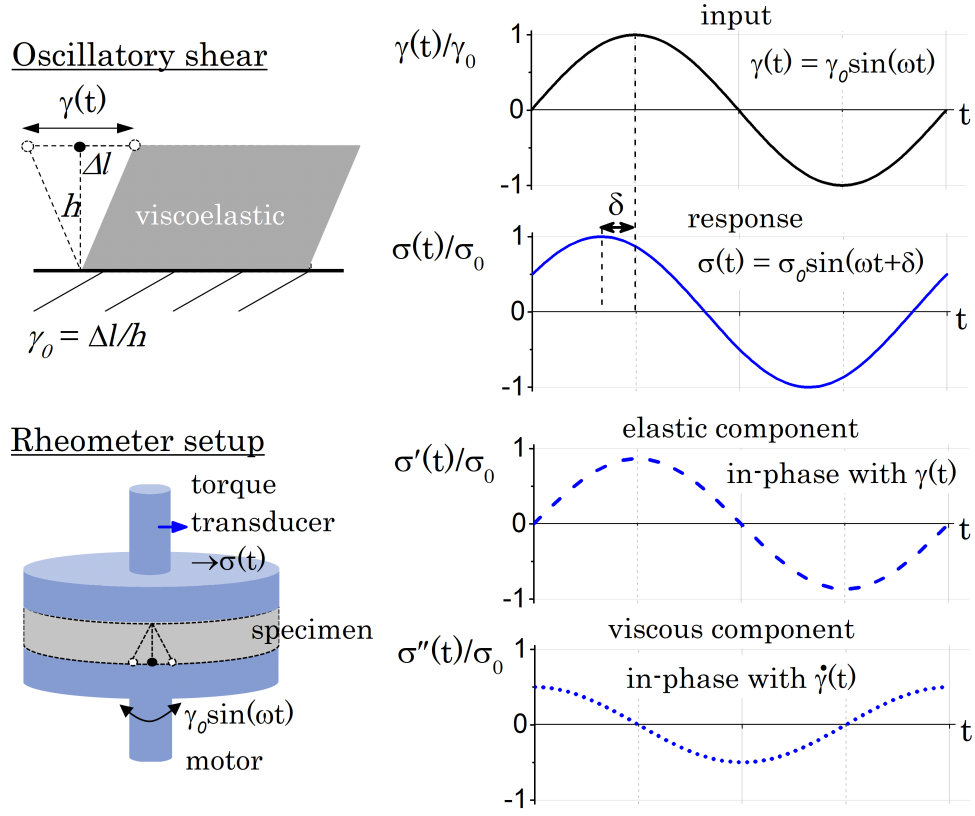


Figure 1.7: The viscoelastic materials under sinusoidal shear deformation $\gamma(t) = \gamma_0 \sin(\omega t)$ and the response stress signal with phase lag of δ . For a simple shear, the strain amplitude is the quotient of the deformation amplitude Δl over the height of the specimen h . During data analysis, the stress signal is decomposed into the in-phase signal and a 90° out-phase signal with the corresponding amplitude.

into the contributions in-phase as the strain and out-phase (phase lag of $\pi/2$) of the strain:

$$\begin{aligned}
 \sigma(t) &= \sigma_0 \sin(\omega t + \delta) \\
 &= \sigma'(t) + \sigma''(t) \\
 &= \sigma'_0 \sin(\omega t) + \sigma''_0 \sin(\omega t + \frac{\pi}{2})
 \end{aligned} \tag{1.4}$$

with σ'_0 and σ''_0 are the amplitudes of the elastic and viscous stress response, respectively. Correspondingly, the storage and loss moduli can be given as:

$$G' = \frac{\sigma'_0}{\gamma_0} \tag{1.5}$$

$$G'' = \frac{\sigma_0''}{\gamma_0} \quad (1.6)$$

The two types of moduli can be expressed by a complex number:

$$G^* = G' + iG'' \quad (1.7)$$

with the absolute value of the complex number,

$$\begin{aligned} |G^*| &= \frac{\sigma_0}{\gamma_0} \\ &= \sqrt{G'^2 + G''^2} \end{aligned} \quad (1.8)$$

The ratio of loss modulus over storage modulus is the mechanical loss factor

$$\tan \delta = G''/G' \quad (1.9)$$

The rheological properties of polymeric materials are highly dependent on the temperature and application frequency (or inversely described by time). For instance, the molecular theory of the viscoelastic homopolymer melt with linear topology and high molecular weight can be expressed by the reptation concept introduced by de Gennes [42] in 1971. Due to the presence of the neighboring molecules, the polymer chains and segments are restricted from lateral movement. As described by Doi and Edwards [43–46], it can be equivalent to put one macromolecule in a "tube" with a length L and a diameter of D . During the reptation of the macromolecule in the tube, the theory can predict the rapid relaxation time of the sub-chain segments, τ_e . With enough long time, τ_d , the whole molecule will fully reptate out from the tube, i.e. the time to relieve the stress from fully disentanglement. Those characteristic relaxation times are functions of temperature, e.g.

$$\tau_d = \frac{12M_e\eta_0}{\pi^2\rho RT} \quad (1.10)$$

with M_e the entanglement molecular weight, η_0 the zero-shear viscosity and ρ the density of the polymer. For the polymer with a molecular weight of M , the total entanglement number $Z = M/M_e$ is associated with the ratio of L/D in Doi-Edwards model.

To investigate the viscoelastic properties of one material covering a big range of time and temperatures with single rheometer, it is convenient to run frequency sweep tests at different temperatures as shown in Figure 1.8, e.g. the complex moduli as function of oscillatory frequency, $G^*(\omega)$. The properties in frequency domain can be seen as the inverse of the time

domain. With commercial rotational rheometers, the typical oscillatory frequency ranges from 0.01 to 100 Hz (0.0628 to 628 rad/s). For most polymeric materials without fillers, those $G^*(\omega)$ acquired from several temperatures can be merged together by horizontally shifting them to one reference temperature via different shifting factors, a_T . This principle is called time-temperature superposition (TTS) [38, 39].

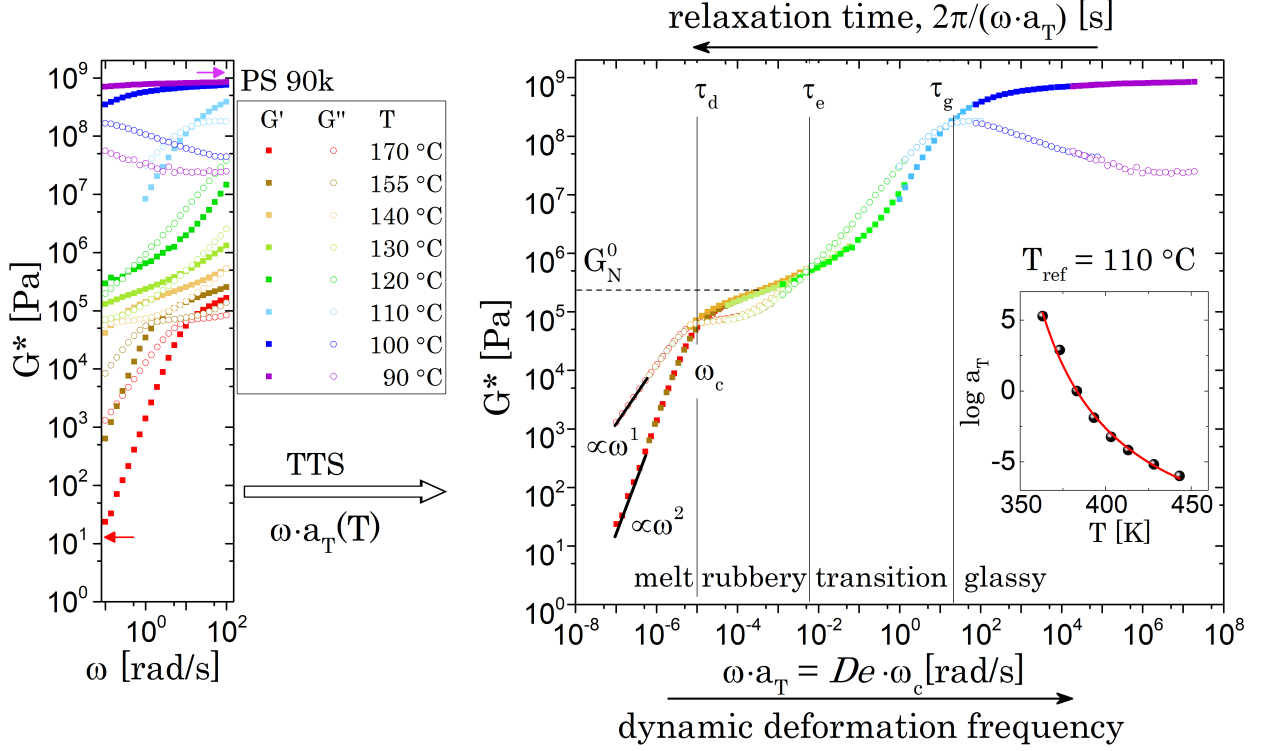


Figure 1.8: The complex shear moduli of mono-dispersed linear polystyrene (PS) with a molecular weight of 90,000 Da from frequency sweeps at different temperatures can be horizontally shifted into a master curve, based on the TTS principle. The shifting factor a_T in the inset graph follows the WLF equation [39, 47] as shown by the fitting line with $C_1 = 13.1$ and $C_2 = 67.4$ K here at the reference temperature of 383 K, close to the T_g of PS. Frequency sweeps were conducted with ARES-G2 rheometer on $D = 13$ mm parallel plates for $T > 120$ °C and width \times thickness \times length = $2 \times 1 \times 10$ mm³ rectangular torsion fixture for lower temperatures.

Afterwards, a single master curve can be built-up, covering a wide range of frequency and the shifting factors follow the WLF(Williams–Landel–Ferry) equation [39, 47],

$$\log(a_T) = \frac{-C_1(T - T_{ref})}{C_2 + (T - T_{ref})} \quad (1.11)$$

with C_1 , C_2 are constants and T_{ref} is the reference temperature in Kelvin. Typically, the T_{ref}

is chosen between $T_g - T_g + 100$ K, which T_g is the glass transition temperature. Obviously, the values of C_1 and C_2 depend on the chosen T_{ref} .

The TTS rule has greatly simplified the description the viscoelastic behavior of polymers covering an extremely wide range of observation time, e.g. it is 15 decades of seconds in Figure 1.8 from single rheometer. From high frequency response to low frequency response (or from short observation time to long), the mechanical status of the materials can be classified as glassy, transition from glassy to rubbery, rubbery and melt for almost all uncrosslinked polymers with enough long chains to entangle each other. The characteristic deformation frequencies (the reciprocal of characteristic relaxation time, τ) between those status are $1/\tau_d$, $1/\tau_e$ and $1/\tau_g$, respectively, with the subscripts "d", "e" and "g" indicate the diffusion, the entanglement and the glassy status.

For viscoelastic fluids or melts, the longest relaxation time at the reference temperature is the reciprocal of the crossover frequency ω_c in before the terminal regime (with the logarithmic slopes of $G'(\omega)$ and $G''(\omega)$ reach to 2 and 1, respectively, see Figure 1.8),

$$\tau_d = \frac{1}{\omega_c} \quad (1.12)$$

and the product of this relaxation time and the characteristic frequency is called the Debroah number,

$$De = \tau_d \omega_c \quad (1.13)$$

which is dimensionless. The rheological properties from different viscoelastic systems can be plotted as a function De , so that the fundamental relationship between the fluidity of the materials and the observation time can be compared.

For crosslinked polymers [39] like rubber vulcanizates, there is no melt status since the polymer chains are experimentally bonded. At long relaxation time, the rubber vulcanizate maintains the rubber plateau modulus, G_N^0 .

1.2.2. FT-rheology and the rheological nonlinearity

The chapter above has mainly described the viscoelastic behavior of polymeric materials under small amplitude oscillatory strain (SAOS) situation, where the response signal is still linear, i.e. a pure sinusoidal wave without extra waveform contributions except from instrumental noise. In this region, the rheological properties like the modulus are independent

of the strain amplitude. This is considered to be the linear viscoelastic regime (LVE) of the material.

However, as the strain amplitude, γ_0 , increase to the large strain amplitude strain (LAOS), the rheological properties will change as a function of γ_0 . Then the material falls into the nonlinear viscoelastic regime (NVE) as indicated by the dashed lines in Figure 1.9. In NVE, the moduli of the materials monotonically decay as a function of γ_0 , known as dynamic strain-softening. For rubber filled with reinforcing fillers, this strain-softening effect is much stronger with a shorter LVE regime [48] due to the introduction of filler-filler and filler-polymer networks. This is called the Payne effect [49].

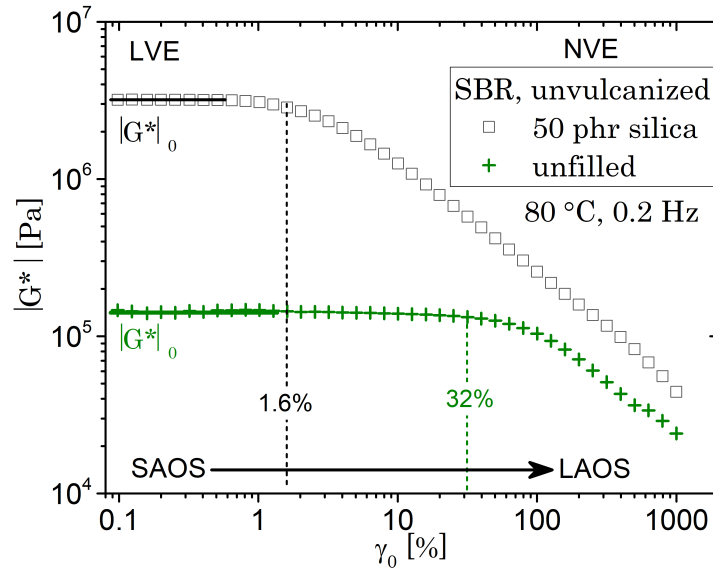


Figure 1.9: The strain dependence of shear modulus $|G^*|$ of unvulcanized SBR rubber (solution polymerization, DSSK 2560 from Sibur, Russia) filled with or without silica (Ultrasil VN3 from Evonik Industries, Germany) from SAOS to LAOS. The dash lines separate the materials between linear and nonlinear viscoelastic regime, defined with a 8% drop of the modulus in linear regime, $|G^*|_0$. Data were acquired from strain sweep on the Scarabaeus SIS V50 rubber rheometer at 80 °C and oscillatory frequency of $\omega/2\pi = 0.2$ Hz.

In the NVE regime of polymeric materials, it is commonly not only showing variation of the stress response amplitude (here for the strain-softening behavior, the stress amplitude is decreasing), but also changing of its waveform as shown in Figure 1.10. The material is the 50 phr silica filled SBR in Figure 1.9. For strain amplitude in SAOS ($\gamma_0 = 2.5\%$), the response signal $\sigma(t)$ is still linear (or at least close to). However, at $\gamma_0 = 250\%$ in LAOS, the response signal has been distorted. For such case, conventional rheometers only do a linear sinusoidal fitting of $\sigma(t)$ to acquire the linear rheological parameters, such as G' and $\tan\delta$ as

describe in last chapter. In linear rheology, only those parameters from linear fitting are used to describe the nonlinear behavior. Substantial information captured in the stress signal is lost, and consequently, missing the physical meaning of the material.

There are several ways to analyze the distorted stress waveform. Qualitatively, one can plot the normalized stress signal $\sigma(t)$ against the normalized strain signal $\gamma(t)$ or strain rate signal $\dot{\gamma}(t)$, i.e. the Lissajous curve (named after Jules Antoine Lissajous, 1822–1880, French physicist). Those Lissajous curves at different strain amplitude are compared so that the patterns of the loops [50, 51] can be identified into different complex fluid categories, such as strain-softening, strain-hardening, strain-overshot, etc.

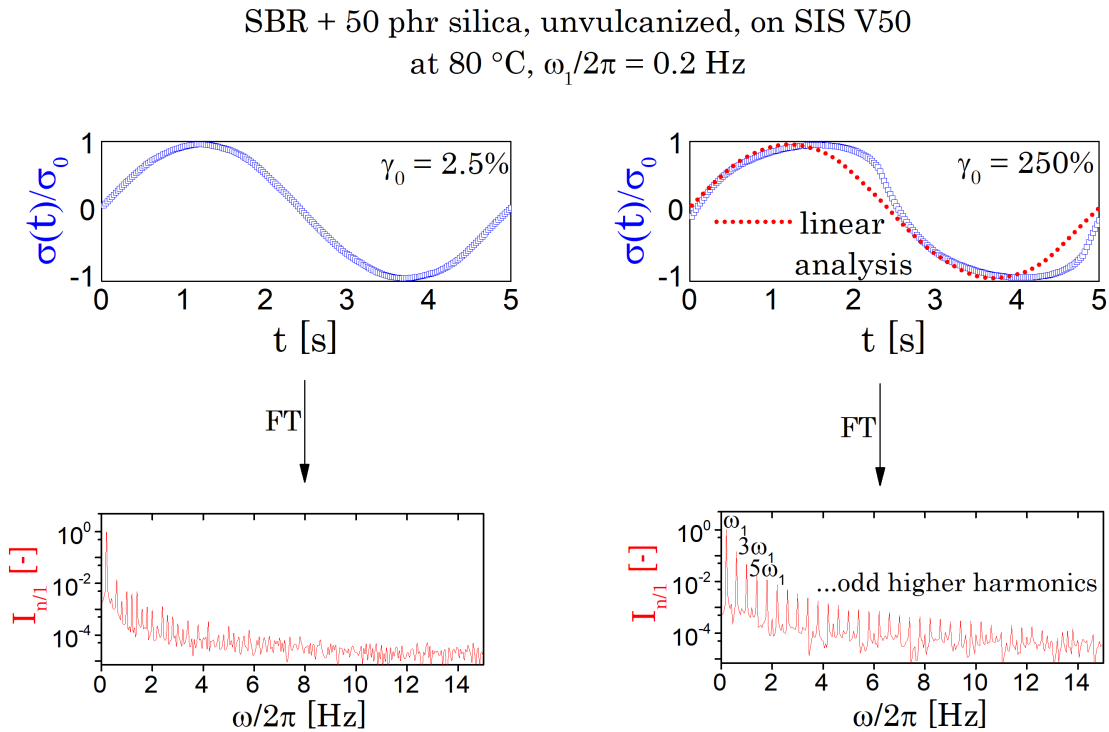


Figure 1.10: The raw stress signals of unvulcanized SBR filled with silica from Scarabaeus SIS V50 rubber rheometer in Figure 1.9 at 80 °C and oscillatory frequency of $\omega_1/2\pi = 0.2$ Hz from SAOS $\gamma_0 = 2.5\%$ and LAOS $\gamma_0 = 250\%$, respectively. The conventional rheometer only doing linear analysis (see the fitting as the dotted line in the graph) for the already distorted waveform at $\gamma_0 = 250\%$ to calculate the rheological parameters, e.g. the G' and G'' , missing some physical information from the signal. However, FT-rheology can Fourier transform the signals into spectra in frequency domain as graph in below, with arising relative intensity of the odd higher harmonics from the signal in LAOS.

Quantitatively, several orthogonal polynomial functions can be adapted for the stress analysis, such as the Chebyshev polynomials of the first kind [52, 53] (named after Pafnuty Lvovich

Chebyshev, 1821–1894, Russian mathematician). However, one of the most straightforward approaches to interpret this distorted response waveform is using Fourier transformation (FT). The theorem [54] is named after Joseph Fourier (1768–1830, French mathematician and physicist). In general, all waveforms, regardless of how scribble they are, can be seen as a sum of simple sinusoids with different frequencies and amplitudes. FT can decompose the signal in the time domain, $s(t)$, into its constituents in the frequency domain, $S(\omega)$:

$$F[s(t)] = S(\omega) = \int_{-i\infty}^{+i\infty} s(t)e^{-i2\pi\omega t} dt \quad (1.14)$$

with the sinusoidal function in Euler's complex form. The coefficients in a discrete $S(\omega)$ are the Fourier series. Figure 1.10 displays the FT spectrum from the stress signal $\sigma(t)$ of rubber materials in LVE ($\gamma_0 = 2.5\%$) and NVE ($\gamma_0 = 250\%$) region. The amplitude of the Fourier series has been normalized by the basic frequency at strain excitation. At higher harmonics, the relative FT intensities of the distorted $\sigma(t)$ are higher than that of the linear $\sigma(t)$. The Fourier series mainly appear at odd harmonics due to the high symmetry of $\sigma(t)$ [55]. While in the case of linear rheology, only linear analysis are applied on the distorted stress signal as indicated by the red dot line, giving parameters such as G' and $\tan\delta$ at the basic frequency.

To explain the mathematical fundamentals of FT-rheology, we can start from the oscillatory shear test as described by Equations 1.2 and 1.4. The sinusoidal shear deformation can be denoted in Euler's complex form to simplify the mathematical expression:

$$\gamma(t) = \gamma_0 e^{i\omega_1 t} \quad (1.15)$$

at the angular frequency of ω_1 , where the subscript "1" to emphasize the basic excitation frequency, distinguished from the higher frequencies (harmonics) in FT-rheology.

Under SAOS where the material is in LVE, the stress response is still linear with a phase lag of δ ,

$$\sigma(t) = G_0 \gamma_0 e^{i(\omega_1 t + \delta)} \quad (1.16)$$

where G_0 is the moduli at the basic excitation frequency.

Once the materials falls into NVE, the stress signal is still periodic but not sinusoidal anymore. The modulus G_0 in Equation 1.16 can be expanded in Taylor's form with even exponents

(only even components due to the symmetric stress amplitude):

$$\begin{aligned}
 \sigma(t) &= [G_1 + G_3\gamma(t)^2 + G_5\gamma(t)^4 + \dots]\gamma_0 e^{i(\omega_1 t + \delta)} \\
 &= G_1\gamma_0 e^{i(\omega_1 t + \delta)} + G_3\gamma_0^3 e^{i(3\omega_1 t + \delta_3)} + G_5\gamma_0^5 e^{i(5\omega_1 t + \delta_5)} + \dots \\
 &= I_1 e^{i(\omega_1 t + \delta)} + I_3 e^{i(3\omega_1 t + \delta_3)} + I_5 e^{i(5\omega_1 t + \delta_5)} + \dots \\
 &\text{(with } G_1\gamma_0 = I_1, G_3\gamma_0^3 = I_3, G_5\gamma_0^5 = I_5 \dots)
 \end{aligned} \tag{1.17}$$

The parameters $G_1, G_3, G_5\dots$ and $\delta, \delta_3, \delta_5\dots$ are the prefactors and phase angles of the Taylor series at the excitation frequency, 3^{rd} higher harmonic, 5^{th} higher harmonics ($\omega_1, 3\omega_1, 5\omega_1, n\omega_1 \dots$) and so on. Consequently, the FT spectra of the stress contains intensities at odd higher harmonics will be $I_1, I_3, I_5, I_n \dots$, where n is an odd number.

In order to compare the output FT signals from different experiments and samples to reduce experimental variations, it is favorable to normalize the absolute intensities of high harmonics I_n by the fundamental intensity I_1 , giving the relative intensity $I_{n/1}$:

$$\boxed{I_{n/1} \equiv \frac{I_n}{I_1}} \tag{1.18}$$

Those relative intensities $I_{n/1}$ from FT-rheology can be seen as the direct quantitative measure for the rheological nonlinearity. Among them, the third relative higher harmonics,

$$\boxed{I_{3/1} \equiv \frac{I_3}{I_1}} = \frac{G_3\gamma_0^3}{G_1\gamma_0} \tag{1.19}$$

is the highest intensity (see Figure 1.10) and thus mostly chosen for FT-rheology studies. Other higher harmonics with lower intensities will be influenced more strongly by the noise, which relays on the raw signals' quality.

The idea of applying FT-rheology for LAOS measurement has been considered and trialed since the 1970s [56, 57]. However, to acquire good enough stress signal from the rheometer for FT was always the obstacle for the development of this technique. Two decades ago, Wilhelm and et al. [55, 57–59] started the upgrading of commercial rheometers for FT-rheology, including the improvement of electronic cable shielding, over sampling of the torque transducer signal, signal analysis in oscilloscope, ADC card reading signal and afterwards home-made Labview software analysis. Since then, FT-rheology has been successfully applied on many viscoelastic systems, including solution micelles [60] polymer melts [61], polymer composites [62], as well as rubber materials in unvulcanized state [9, 63–65]. Nowadays, the

FT-rheology has been implemented in many high end commercial rheometers, including the Scarabaeus SIS V50 (now RPA elite), DHR-3 and ARES-G2 from TA Instruments.

Figure 1.11 demonstrates the development of $I_{3/1}$ as a function of strain amplitude from SAOS to LAOS of the SBR materials from Figure 1.9. The data was acquired from the embedded FT analysis of the stress signal in the rheometer. Increased rheological behavior after filling with fillers has been shown indirectly in Figure 1.9 via G' , a linear rheological parameter. Here, the rheological nonlinearity has been compared in a direct way via $I_{3/1}$, where $I_{3/1}(\gamma_0)$ of the filled SBR has drastically increased at medium strain around $\gamma_0 = 32\%$.

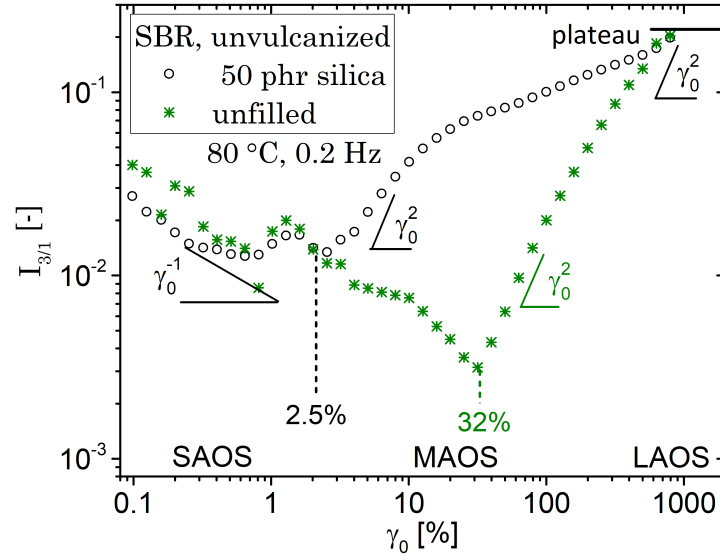


Figure 1.11: The third relative higher harmonic $I_{3/1}$ as the direct rheological nonlinearity parameter was quantified using the example of the unvulcanized SBRs in Figure 1.9 with Scarabaeus SIS V50 rubber rheometer at 80 °C and oscillatory frequency of $\omega_1/2\pi = 0.2$ Hz.

Firstly, let us take the result of the unfilled SBR in Figure 1.11 to explain a typical $I_{3/1}(\gamma_0)$ graph from FT-rheology. In SAOS, when the stress response is small, the $I_{3/1}$ decay as a function of strain amplitude with a order of -1. This is because the FT results mainly from the approximately constant noise of the raw signal. The prefactors I_n in Equation 1.17 at high harmonics are dominated by the absolute noise, which should be a constant value for

identical rheometer at the same torque level of the transducer. Therefore,

$$\begin{aligned}
 I_{3/1} &\equiv \frac{I_3}{I_1} \\
 &\propto \frac{\text{constant noise}}{G_1 \gamma_0} \\
 &= \frac{L_{noise}}{\gamma_0} \\
 &\boxed{I_{3/1} \propto \gamma_0^{-1} \text{ in noise region}}
 \end{aligned} \tag{1.20}$$

with the constant L_{noise} stands for the level of noise during the torque measurement.

After the noisy region of SAOS (after $\gamma_0 = 2.5\%$ and 32% for the filled and unfilled SBR in Figure 1.11), the nonlinearity of the materials arises and $I_{3/1}$ starts to increase. According to Equation 1.19,

$$\begin{aligned}
 I_{3/1} &= \frac{G_3 \gamma_0^3}{G_1 \gamma_0}, \text{ with } \frac{G_3}{G_1} = \text{constant} \\
 &\boxed{I_{3/1} \propto \gamma_0^2 \text{ in MAOS}}
 \end{aligned} \tag{1.21}$$

leading to $I_{3/1}(\gamma_0)$ growth in power order of 2. For filled systems, the $I_{3/1}(\gamma_0)$ seems to maintain two growth regions. At higher strain amplitude in LAOS where $\gamma_0 > 500\%$, $I_{3/1}(\gamma_0)$ reach a plateau. In FT-Rheology, the quadratic growth regime of $I_{3/1}(\gamma_0)$ is usually named as the medium strain amplitude oscillatory strain for the material (MAOS) to distinguish from the LAOS with a plateau.

From the $I_{3/1}(\gamma_0)$ in MAOS, one can extrapolate the rheological nonlinearity at infinite small strain [66], defined as

$${}^3Q_0 \equiv \lim_{\gamma_0 \rightarrow 0} \frac{I_{3/1}}{\gamma_0^2} \tag{1.22}$$

The value of 3Q_0 was found in the literature to be an intrinsic rheological nonlinearity parameter for the unfilled polymer melts since it is not effected by the polymer chemistry but rather by the chain length, the polydispersity and topology of the macromolecules [61]. As shown in Figure 1.12, a master curve of the intrinsic nonlinearity via this parameter can be constructed for many polymer melts, following TTS principle like the linear rheology in last chapter. The 3Q_0 of linear polymers maintain similar function against De , regardless the chemical composition.

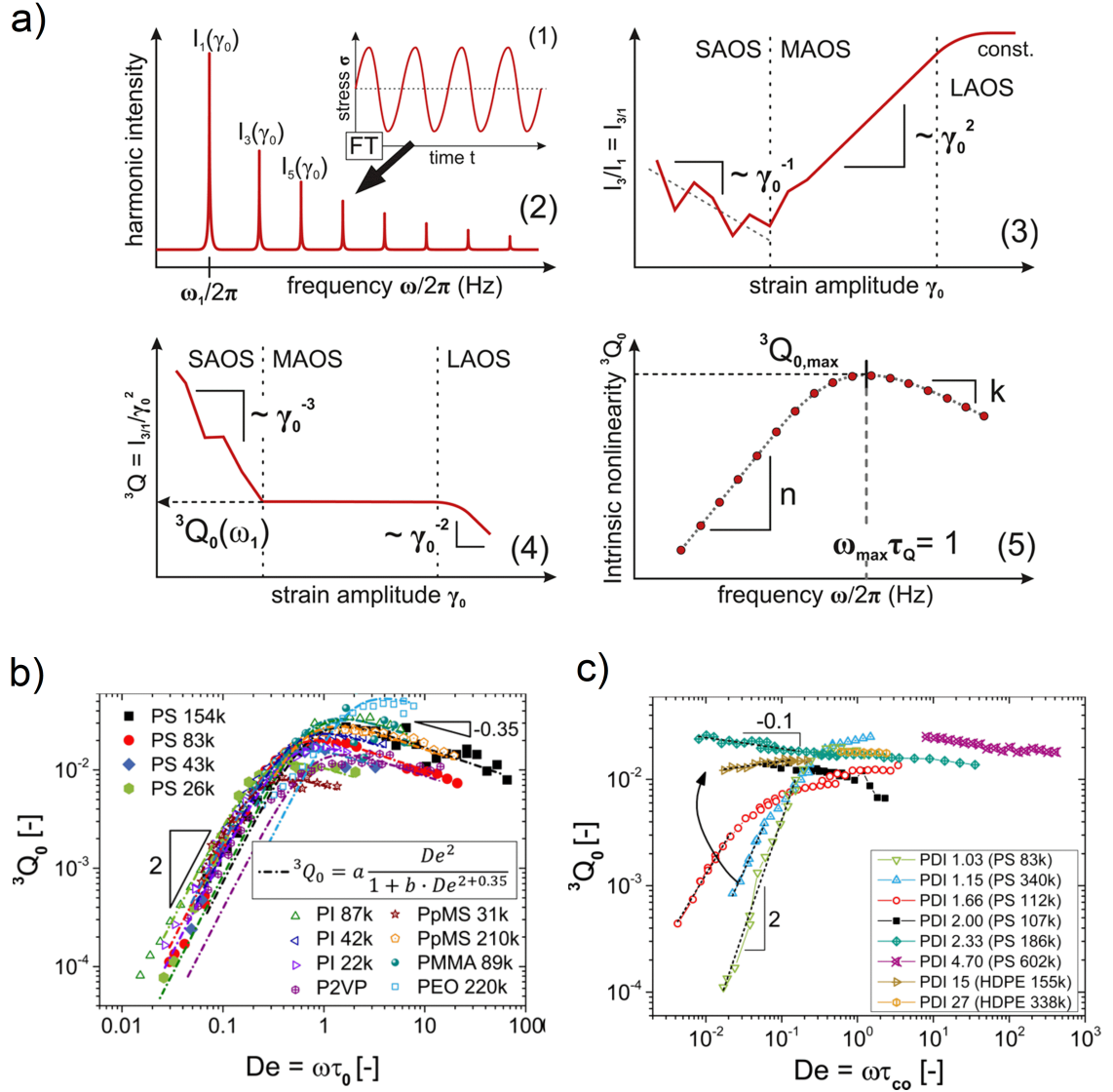


Figure 1.12: a) The scheme to build up the intrinsic nonlinearity master curve in five steps: (1) acquire the nonlinear stress waveform from an oscillatory deformation experiment at strain amplitude of γ_0 and excitation frequency of $\omega_1/2\pi$. (2) Fourier transform the time data into frequency spectrum with odd higher harmonics. (3) The ratio of the first and third harmonic $I_{3/1}(\gamma_0, \omega_1)$ is proportional to γ_0^2 in MAOS. (4) Extrapolate ${}^3Q(\gamma_0, \omega_1)$ to infinite small γ_0 gives the intrinsic nonlinearity ${}^3Q(\omega_1)$. (5) A nonlinear master curve can be created by plotting several ${}^3Q_0(\omega_1)$ from different excitation frequencies, which can be shifted to a reference temperature, utilizing the TTS principle. Two intrinsic nonlinearity master curves from b) mono-dispersed and c) poly-dispersed linear polymer melts are shown as examples, including: polystyrene (PS), Polyisoprene (PI), poly(p-methylstyrene) (PpMS), poly(methyl methacrylate) (PMMA), poly(2-vinylpyridine) (P2VP), poly(ethylene oxide) (PEO) and high-density polyethylene (HDPE). Figures are adapted from [61] with Copyright © 2016 by American Chemical Society. Reprinted by permission.

FT-rheology exhibits some advantages for studying filled rubber materials in comparison with linear rheology. As shown in Figure 1.13, the $I_{3/1}$ from FT-rheology is three times sensitive as $|G^*|$ towards the increasing filler volume in the unvulcanized rubber compounds, ϕ . For crosslinked NR materials, their nonlinearity has not commonly been investigated via FT-rheology yet. Therefore, it would be of high interest to examine FT-rheology technique on this material to directly quantify the rheological nonlinearity and additionally, the response of rheological nonlinearity to the aging effect.

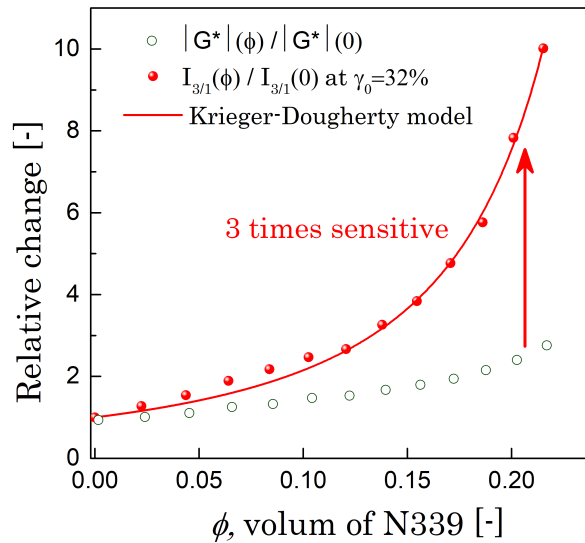


Figure 1.13: The third relative higher harmonic $I_{3/1}$ from FT-Rheology exhibit higher sensitivity than the modulus from linear rheology to the filling volume ϕ of carbon black in SBR. Figure is redrawn according to reference [9].

1.3. Time Domain NMR (TD-NMR)

The self-rotation of atomic nuclei, with charge and mass, possess also an intrinsic property called spin or angular momentum in quantum mechanics and particle physics. A spinning charge is associated with the magnetic moment and the magnetic moment is determined by the angular momentum of the spinning mass. Exposure to a strong constant magnetic field, \vec{B}_0 , the spin will precess (change in the orientation of the self-rotational axis) around the axis of \vec{B}_0 at an intrinsic frequency. The spin in the strong magnetic field can be perturbed (the nutation during procession) by a weak oscillating magnetic radiation, \vec{B}_1 . The resonance will occur when the frequency of \vec{B}_1 matches the intrinsic frequency of the nuclei in the \vec{B}_0 field. Accordingly, this phenomena is called nuclear magnetic resonance (NMR).

Such phenomena had been examined in bulk matter for the first time in 1946 by Purcell et al. [67] at Harvard University and Bloch et al. [68,69] from Stanford University. Afterwards, it attracted the attention of chemists. Nowadays, NMR is known in daily life in many perspectives, such as the magnetic resonance imaging (MRI) in hospitals to diagnose the body of the patients. For scientists and engineers in chemical industry, NMR spectroscopy, i.e. NMR in the frequency domain, is widely known to reveal the detailed chemical structures of the molecules. However, in this thesis, the NMR of the protons ^1H in time domain (TD-NMR) in relatively low \vec{B}_0 field are going to be in focus to study the molecular dynamics of NR during vulcanization and aging.

1.3.1. Fundamentals of NMR

Regarding the fundamentals of NMR, there are several textbooks [70] as references [71–73] in details or compacted version for the basic principles [74].

A rotating nuclei generates a magnetic field as illustrated in Figure 1.14), which the magnet moment is associated with the rotation angular momentum. In particle physics, *spin* is a fundamental property of electrical charge or mass, including the electrons, protons and neutrons. The spin, denoted by I , comes in multiples of $1/2$ and can be positive or negative (with sign of $+$ or $-$). Only the nuclei with unpaired protons or neutrons (odd number of protons and/or odd number of neutrons) have a spin, such as the ^1H with 1 proton and the ^{13}C with 6 protons and 7 neutrons as seen in Table 1.3. Those types of nuclei are detectable by NMR, i.e. spin-active or NMR-active. Nuclei with both an even number of protons and

an even number of neutrons, such as the ^{12}C , have a spin of zero.

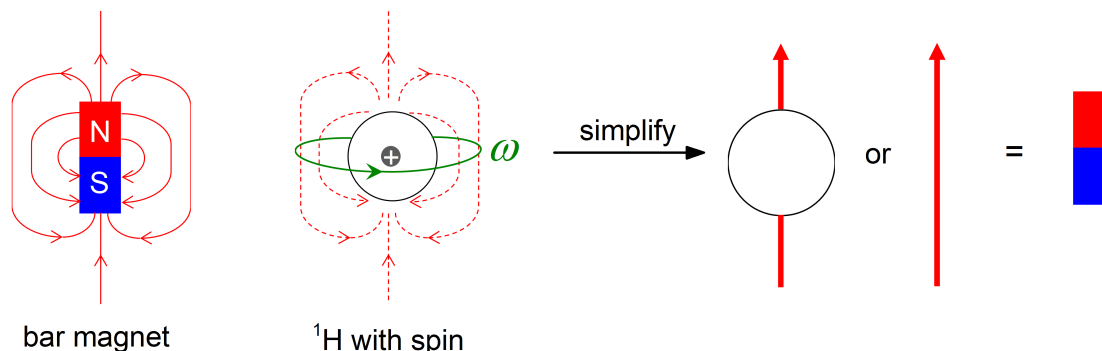


Figure 1.14: The self-rotation of a ^1H nucleus at frequency ω_L with a positive charge can generate a weak magnetic field. It is effective as a tiny magnetic metal bar thus the magnetic field of the nuclei can be simplified as a magnetic vector.

Table 1.3: Properties of some common NMR-active nuclei [73].

Isotope	Natural abundance [%]	Protons, Neutrons	Spin I	Magnetogyric ratio γ [$10^6 \text{ rad}\cdot\text{T}^{-1}\text{s}^{-1}$]	Relative sensitivity to ^{13}C
^1H	99.9844	1, 0	1/2	267.52	5878
$^2\text{H}(\text{D})$	0.0156	1, 1	1	41.07	0.0065
^{11}B	81.17	5, 6	3/2	85.83	777
^{13}C	1.108	6, 7	1/2	67.26	1.0
^{14}N	99.635	7, 7	1	19.33	5.9
^{19}F	100	9, 10	1/2	251.67	4890
^{29}Si	4.7	14, 15	1/2	-53.16	2.16
^{31}P	100	15, 16	1/2	108.29	391

According to quantum mechanics, the potential magnetic quantum numbers, m_I , is given by series of I as

$$m_I = I, (I - 1), (I - 2) \dots - I \quad (1.23)$$

to describe the energy states of the spins. The total number of available spin states N is given by

$$N = 2I + 1 \quad (1.24)$$

from the spin value of I . For ^1H , which $I = \frac{1}{2}$ and thus there are two quantum status of the spin with $m_I = +\frac{1}{2}$ and $-\frac{1}{2}$. In the following section, we only take ^1H , the proton, as an example to simplify the explanation.

Without an external magnetic field, the spins of protons aligned randomly as shown in Figure 1.15a. Once the protons are exposed to the magnetic field \vec{B}_0 with a field strength of B_0 (in unit of Tesla or T), the spins align themselves according to the direction of the magnetic field as Figure 1.15b. Protons with $m_I = +\frac{1}{2}$ spins are in the low energy level and will align along \vec{B}_0 , while the protons of $-\frac{1}{2}$ spins possessing the high energy level can align against the field.

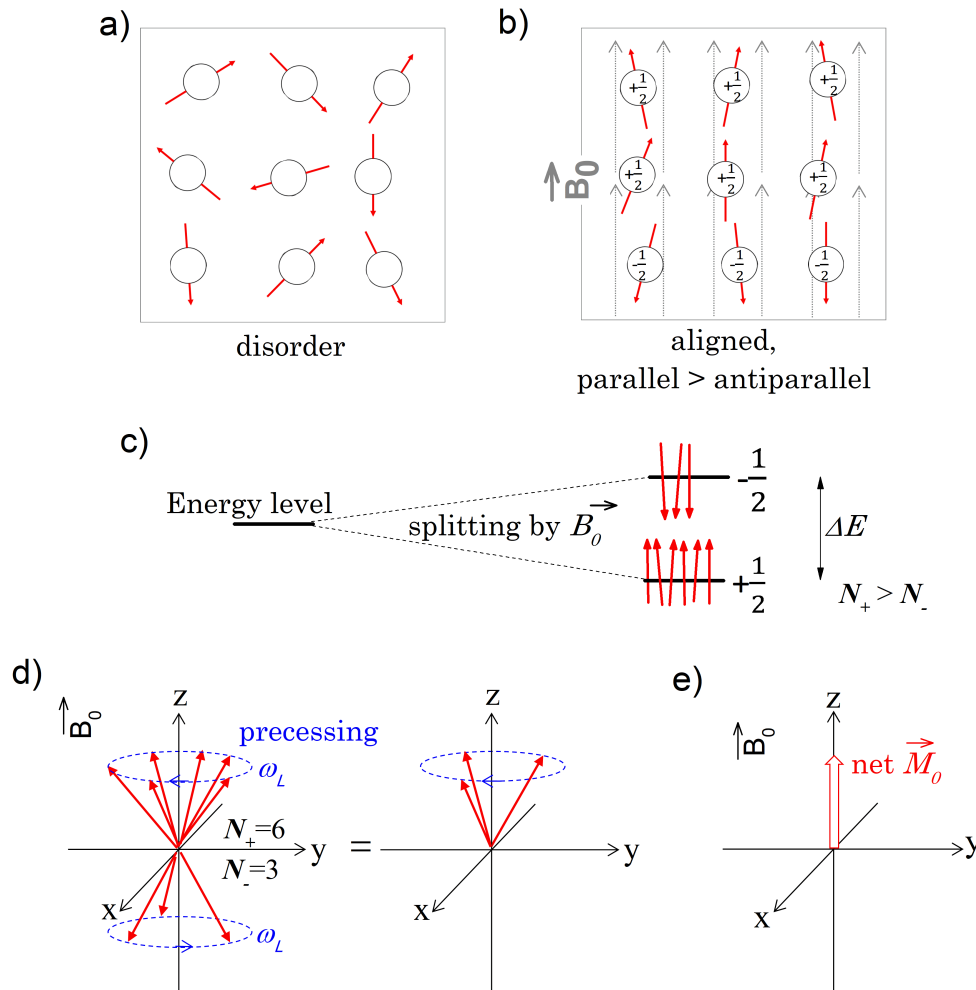


Figure 1.15: The a) disordered spins in the bulk sample will b) be aligned along or against the direction of the applied magnetic field, \vec{B}_0 . Accordingly, c) the energy level of spins $I = \frac{1}{2}$ will be split into two spin states: $-\frac{1}{2}$ with high energy and $+\frac{1}{2}$ with low energy. d) Both types of spins precess along the magnetic field with excess number of low energy spins, leading to e) the effective overall magnetization of the spins is the vector \vec{M} with the direction as same as \vec{B}_0 (+z).

The splitting of the energy levels is called the Zeeman effect (Pieter Zeeman, 1865-1943,

Dutch physicist) with a gap of ΔE , depending on the strength of the external magnetic field

$$\Delta E = \frac{h\gamma B_0}{2\pi} \quad (1.25)$$

with $h = 6.626 \times 10^{-34}$ Js is the Plank's constant. The γ here is called gyromagnetic ratio (or magnetogyric ratio, not to be confused with the same symbol for the shear strain in rheology) in units of $\text{rad}\cdot\text{T}^{-1}\text{s}^{-1}$. From Table 1.3, one can get $\Delta E = 2.82 \times 10^{-26}$ J for ^1H at $B_0 = 1$ T. In bulk, the population difference of $-\frac{1}{2}$ spins and $+\frac{1}{2}$ spins follows the relationship

$$\frac{N_-}{N_+} = e^{-\frac{\Delta E}{kT}} \approx 1 - \frac{\Delta E}{kT} \quad (1.26)$$

with $k = 1.38 \times 10^{-23} \text{ m}^2\text{kgs}^{-1}\text{K}^{-1}$ is the Boltzmann's constant. For ^1H at temperature of 298 K in $B_0 = 1$ T, $N_-/N_+ \approx 0.999993$, i.e. only 7 ppm excess spins are at the low energy level.

Another character of the protons that needs to be clarified is that the individual spinning object precess along the magnetic field lines of \vec{B}_0 as illustrated in Figure 1.15d, which is called Larmor precession (Sir Joseph Larmor, 1857-1942, Irish physicist and mathematician). The protons precess with the Larmor angular frequency ω_L or the resonance frequency

$$\omega_L = \gamma B_0 \quad (1.27)$$

Flowing the Equations 1.25 and 1.27, one can notice that for specified type of spins, stronger the applied magnetic field will split the spins with a higher energy gap and make the spins precess faster inside. In $B_0 = 1$ T, the $\omega_L/2\pi$ of ^1H is 42.6 MHz.

Commonly, a Cartesian coordinate system (x, y, z) is applied to describe the spins and the macroscopic magnetization in space with the direction of \vec{B}_0 vector defined as the z-axis. A pair of a parallel spin and an anti-parallel spin in Figure 1.15d can cancel out each others response, including their components in xy-plane. However, there are excess number of low energy spins precessing along (not against) the magnetic field, leaving the net magnetization of those spins pointing up (towards +z) as the vector \vec{M}_0 in Figure 1.15e.

To detect the precession frequency of a specified type of spins, one can radiate the precessing spins by an electromagnetic wave, \vec{B}_1 . Only when the frequency of \vec{B}_1 matches the ω_L of the spins, some low energy level spins can pick up the energy to transit into a high energy level and start to precess downwards, i.e. resonance.

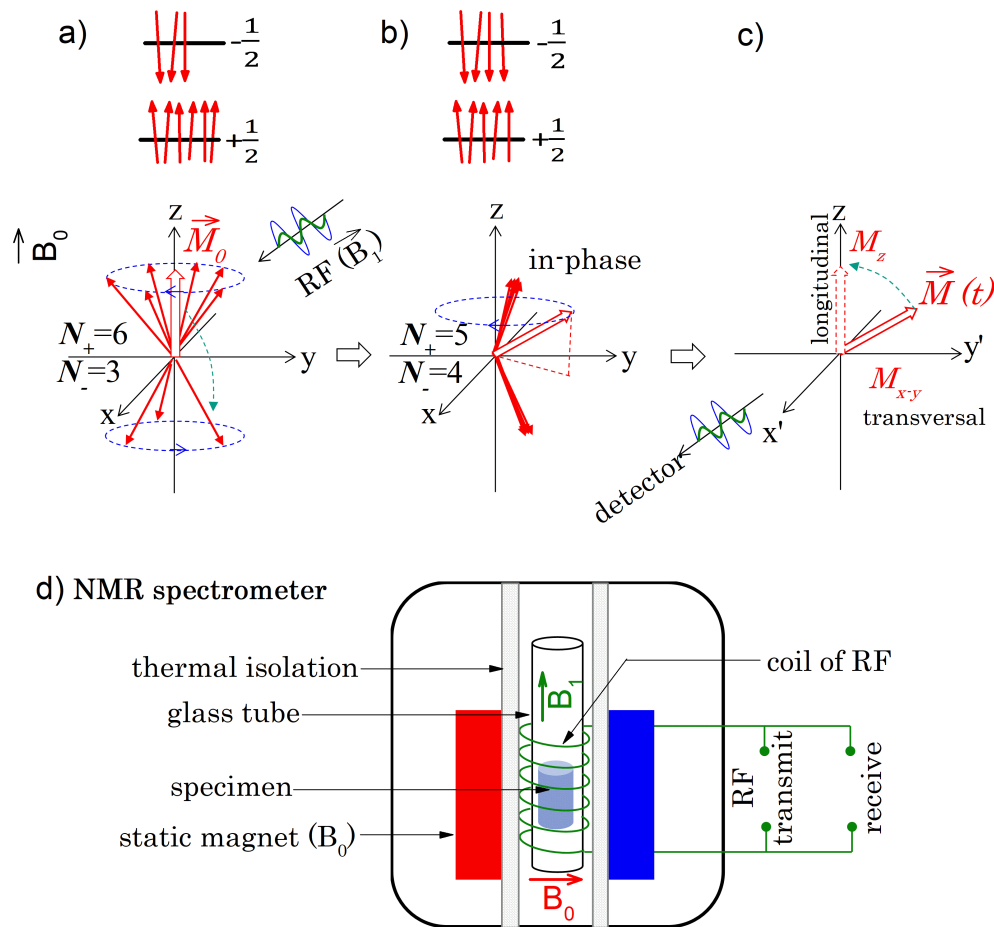


Figure 1.16: a) Exposing to the external strong magnetic field \vec{B}_0 , the spins are splitted into two states and there are more spins aligned with \vec{B}_0 , with a macroscopic magnetization of \vec{M}_0 . Notice here the drawing of the spins is simplified since the Heinsberg uncertainty principle would not allow to draw a single spin. b) After the irradiation of the radio frequency electromagnetic wave, \vec{B}_1 , some low energy spins will take up the energy and flip to high energy status. Meanwhile, the spins are precessing in-phase and the resulting macroscopic magnetization vector has been flipped towards the xy-plane. c) In \vec{B}_0 , the spins will back to the equilibrium status as a) so that the flipped magnetization vector $\vec{M}(t)$ will relax back to \vec{M}_0 , which can be detected as a electromagnetic wave. d) The operation principle and basic construction of a NMR spectrometer.

The working principle of a NMR spectrometer is illustrated in Figure 1.16. The electronic coils can emit impulses of the electromagnetic wave (to generate \vec{B}_1) within the frequency range of the radio waves (weak energy with a wave length of ≈ 100 m) thus named radio frequency (RF). After a short impulse of RF in matched frequency, some low energy spins will take the energy to point downwards. It is commonly referred as pulse in NMR while

strictly speaking it is impulse. Another effect from the RF pulse is that the spins with same energy levels will pointing towards the same direction as Figure 1.16b, called "in-phase" of the spins. This will result in the macroscopic net magnetization, \vec{M}_0 , decreases in longitudinal direction and increases in transversal direction as $\vec{M}(t)$ in Figure 1.16c. If the time duration of the pulse is long enough, all of the excess low energy level spins can have a chance to take the energy and turn into high energy spins, which is in a "saturation" status. The pulse is called 90° pulse since the original magnetic vector has been flipped by 90° from longitudinal direction (+z) to transversal direction (xy-plane) and the duration of the pulse is t_{90} . Similarly, if the duration of the pulse is longer which can invert all spins, it is called 180° pulse with time of t_{180} . In practical, it is cumbersome to visualize this energy exchange in the fixed laboratory coordinate (x, y, z). Commonly, a rotating frame that precesses at ω_L around \vec{B}_0 is adopted as (x', y', z) so the the $\vec{M}(t)$ is observed without the precessing. However, in the following explanation we keep the coordinate labeled as (x, y, z) for simplification.

After the saturation RF pulse, the magnetization will relax back to the original position due to the local magnetic field fluctuations in the sample. The transversal component of $\vec{M}(t)$ will constantly change along with the precessing of the spins thus induce an electric current. The generated electric current can be detected by the coil (in many spectrometers the RF coil and the receiver coil is the same) like an antenna. The signal will follow the precession frequency as the spins in that field. In NMR spectroscopy study of a chemical, varying frequencies of RF pulse will scan over the sample. For a spin in a specified chemical environment, i.e. the shielding by nearby electrons, the coupling with other spins, etc., the splitting energy ΔE is unique for one type of protons in a field of B_0 . Therefore, it only picks up RF energy at a unique frequency. Based on the spectrum of the scanning RF, the possible chemical structures of the spins are deduced.

For the TD-NMR approach in following section, the frequency of RF is fixed. After the NMR pulse perturbation, the relaxation behavior of the magnetization as a function of time [75, 76] is of our interest, based on which the local chain dynamics of the polymers in the melt or solid state can be calculated [77, 78].

1.3.2. NMR relaxometry

Following the perturbation through sequences of electromagnetic pulses, the restoration of the magnetization at thermal equilibrium status occurs in an external static magnetic field. To understand how does the relaxation signal get detected, i.e. to receive the NMR relaxometry,

one can refer to the 90° x pulsed NMR experiment in Figure 1.17 for demonstration. An magnetic field of \vec{B}_1 radiate in x direction for a time of t_{90} (90° x), which is perpendicular to the external magnetic field \vec{B}_0 . This pulse can flip the net magnetization \vec{M}_0 90° to to the y-direction based on the left-hand rule [72]. The spin in the molecules is not entirely isolated but interacted with neighboring nuclei. Due to the inhomogeneities in \vec{B}_0 field and in the sample itself, the flipped magnetization vector start fanning out in the xy-plane as the spins precessing at unequal rates. This result in the decay of $\vec{M}(t)$ in xy-plane. At the same time, the vector is forced back to the z-direction with the external magnetic field \vec{B}_0 . The relaxation function can be expressed by exponential functions as

$$\begin{aligned} M_z(t) &= M_{z\infty} \cdot [1 - \exp(-\frac{t}{T_1})] \\ &= M_0 \cdot [1 - \exp(-\frac{t}{T_1})] \end{aligned} \quad (1.28)$$

and

$$M_{xy}(t) = M_{xy0} \cdot \exp(-\frac{t}{T_2}) \quad (1.29)$$

with the characteristic relaxation times, T_1 and T_2 . The decay of the net magnetization in xy-plane as an electromagnetic wave can be directly detected as the *free induction decay* or FID, where "free" means without further RF radiation ongoing.

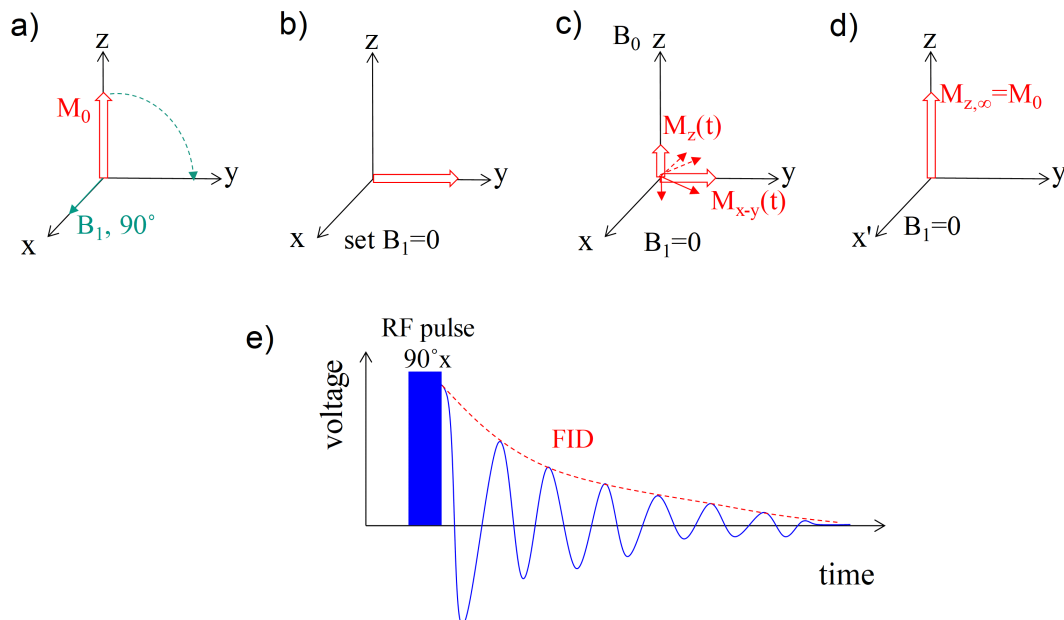


Figure 1.17: a-d) The magnetization in the rotation frame diagrams of the pulsed NMR experiment as a function of time and e) the detection of FID signal.

For the *longitudinal relaxation*, the magnetization process back to z-direction with the characteristic time symbolized as T_1 . It is a process to transfer the energy of the spins to the neighboring molecules, i.e. the lattice. Accordingly, this T_1 process is also called *spin-lattice relaxation*. For the *transversal relaxation*, the magnetization decay in xy-plane with the characteristic time symbolized as T_2 . It is a process mainly governed by the spin-spin dipolar (or quadrupolar) effect for the local \vec{B}_0 field. Therefore, this process is also called *spin-spin relaxation*. The magnitude of the relaxation times depend on the interaction between the spins and with the environment, as modulated by the molecular mobility. For the molecules in motion, the average time of molecular collisions is defined as the *correlation time*, τ_c . The T_1 and T_2 can be well described by BPP (Bloembergen-Purcell-Pound) [79] model

$$\frac{1}{T_1} = \frac{3}{10} \frac{\gamma^4 (h/2\pi)^2}{r^6} \tau_c \left(\frac{1}{1 + \omega_L^2 \tau_c^2} + \frac{4}{1 + 4\omega_L^2 \tau_c^2} \right) \quad (1.30)$$

$$\frac{1}{T_2} = \frac{3}{20} \frac{\gamma^4 (h/2\pi)^2}{r^6} \tau_c \left(3 + \frac{5}{1 + \omega_L^2 \tau_c^2} + \frac{2}{1 + 4\omega_L^2 \tau_c^2} \right) \quad (1.31)$$

where r is the internuclear distance under the assumption of a single correlation time with an exponential autocorrelation function.

Determination of T_1 :

The longitudinal relaxation can not be studied directly along z-direction as the strong static magnetic field \vec{B}_0 inhibits the measurement. By flipping the corresponding or equivalent magnetization M_z into the xy-plane, the relaxation process can be detected. Since the T_1 relaxation involves a variation of the total energy of the system, it implies the energy exchange between the spins and the chemical environment. Analysis of T_1 provides information about faster segmental dynamics of the polymer network as seen in Equation 1.30. It involves the motion of side groups or the rotations in the backbone with a typical rate associated to the reciprocal of the Larmor frequency.

There are mainly two approaches to determine T_1 as seen in Figure 1.18: *inversion recovery* and *saturation recovery* measurements. The former fully invert the magnetization to -z-direction by 180° x pulse, wait for a recovery time variance τ_{rec} and rotate the magnetization into xy-plane by 90° y pulse for signal detection. The recovered magnetization M_{rec} as a function of τ_{rec} are recorded. Before the next recovery measurement, the sample need to be relaxed with enough long time to reach the original equilibrium status, called recycle delay time (RD). The RD is commonly set to be longer than $5T_1$, which allows $\approx 99.33\%$ of M_0 to be relaxed according to Equation 1.28. However, the value of T_1 is unknown prior

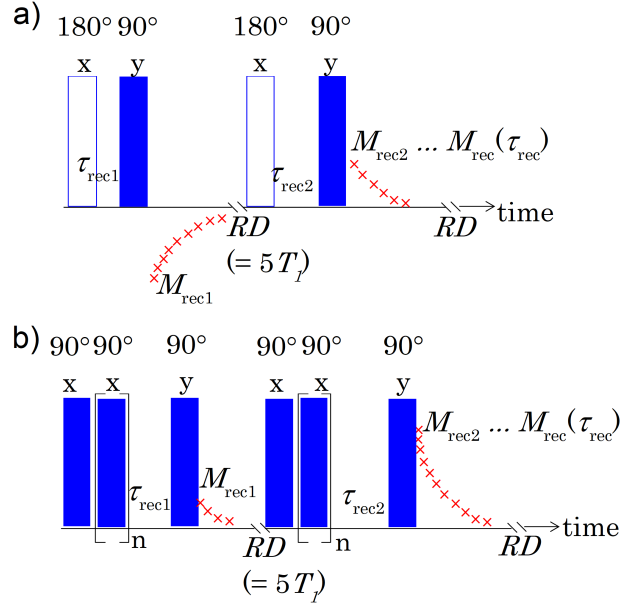


Figure 1.18: The measurement of T_1 via a) inversion recovery pulse sequence or b) saturation recovery pulse sequence.

to the first measurement. For the saturation recover test, the spins are saturated by $90^\circ x$ pulse, wait for a recovery time variance τ_{rec} and then rotate the magnetization into by $90^\circ y$ pulse for signal detection. Instead of one flip by $90^\circ x$, a train of such pulses is preferred for the saturation before the signal detection, which is to make sure most of the magnetization is evenly destroyed for different types of spins in the inhomogeneous \vec{B}_0 field. $M_{rec}(\tau_{rec})$ is recorded accordingly. Finally, the T_1 is given by fitting $M_{rec}(\tau_{rec})$ with Equation 1.28. Inversion recovery provides better quality of the fittings, but is only suitable for liquids. For highly coupled systems with broad spectra, e.g. the crosslinked rubbers in this thesis, the saturation recovery is employed.

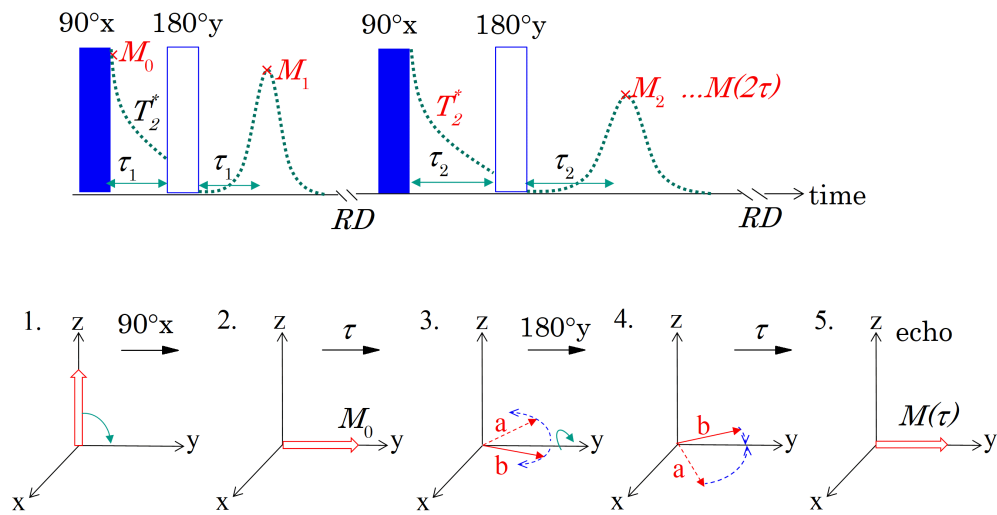
Determination of T_2 :

Theoretically, T_2 should be acquired by flipping the magnetization on the xy -plane with a single $90^\circ x$ and then analyzing the FID signal. However, for the low-field NMR devices with solid polymer samples, inhomogeneities of \vec{B}_0 field cause an additional contribution to the decoherence of the spins. This will shorten the decay time in the FID with $T_2^* < T_2$, which is uncorrelated to the chain dynamics of the polymers.

To remove the effect of inhomogeneous static field, we can apply pulse sequences which can form magnetization echos to equivalently detect the T_2 relaxation signal such as the Hahn echo in Figure 1.19a [80]. The rotation diagrams are depicted from scheme 1 to scheme 5.

The equilibrium magnetization is firstly rotated into y-axis by a 90°_x . The spins follow a FID decay with T_2^* and there are two types of fanning out spins along xy-plane due to the lost of coherence: the faster one a in counter-clock direction and the slower one b in clockwise direction. At time τ , the fanning-out magnets are rotated by a 180°_y pulse along the y-axis so that a and b keep the precessing with their "memorized" direction (scheme 4). After another equivalent time duration of τ , the phase coherence of the magnetization lead to an echo of the magnetization. The echo intensity is the equivalent magnetization at relaxation time of τ . After RD for the system back to equilibrium, the Hahn echo can be applied again with varying τ . Continuing those cycles, the relaxation signal $M(\tau)$ can be obtained from point to point. Fitting $M(\tau)$ with Equation 1.29, the characteristic transversal relaxation time, T_2 , of the polymers can be quantified without the influence of the \vec{B}_0 inhomogeneities.

a) sequece of Hahn-echo



b) sequece of CPMG

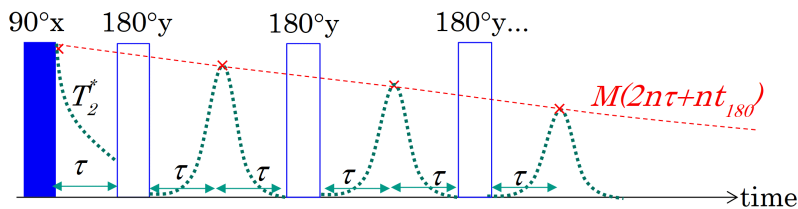


Figure 1.19: The pulse sequences for a) Hahn echo and b) CPMG echo for the measurement of T_2 by 180° rotating the magnetization around the y-axis.

One can notice that the required RDs between each $M(\tau)$ data point from the Hahn echo leave this method very time consuming. An alternative for faster measurement is the CPMG sequence as seen in Figure 1.19. It is named after the inventors [81,82], Carr, Purcell, Meiboom and Gill. Following a 90°_x pulse, the fanning-out magnetization can be continuously coherent by a train of 180°_y pulses with a spacing time of τ . In this way, the full relaxation curve can be acquired by the echos after each 180°_y pulse in single experiment without a waiting of RD. However, the continuous irradiation with the RF wave may substantially heat up the sample while a strong gas flow along the NMR tube is necessary to stabilize temperature. Another effect is the so-called spin-lock effect from a continuous \vec{B}_1 (e.g. here is the 180°_y). At short spacing time τ , there is an extra relaxation mechanism taking place in the sample, the spin-lock $\frac{1}{T_{1\rho}}$, which is determined by the wave frequency, ω_1 . To solve this problem, phase recycling with 180° pulse in alternative directions between each other can be applied, such as a sequence of $180^\circ_y-180^\circ_x-180^\circ_y-180^\circ_x$ and so on. Those phase recycling patterns include xy-4, xy-8, xx-4 (MLEV-4), xy-16, etc. [83].

Concerning rubber and polymeric materials at large, the spin-spin (T_2) relaxation far above glass transition temperature ($> T_g + 100$ K) is of more interest, which is highly sensitive to the slow relaxation process of chain/segmental dynamics involving large spatial scale of molecular motions [84]. The relaxation rate, $\frac{1}{T_2}$, of rubber has been used to study: 1. the swelling of rubber networks [85] and its correlation to tube models; 2. the disentanglement process [86] of long linear rubber chains in a slow diffusion process; 3. the interactions between the rubber chains and reinforcing fillers such as silica [87] and carbon black [88,89]; 4. the crosslink density of rubber vulcanizates. Thereafter, the crosslink density derived from T_2 analysis can be correlated with the concentration of curing agents [90], the elastic modulus from dynamic mechanical test [91], the rubber elasticity in theory [92], the crosslink density measured from solvent swelling equilibrium [93], etc.

For rubber vulcanizates, the crosslink density ν is normally defined as

$$\nu \equiv \frac{\rho}{M_c} \quad (1.32)$$

where ρ is the mass density ($\rho = 0.92$ g/cm³ for unfilled NR) and M_c is the molecular weight between two crosslinks. The crosslink density can be quantitatively represented from T_2 analysis as demonstrated by Gronski and Hoffmann [92], which the values correlated well to the results from traditional methods. Figure 1.20a shows the influence of sulfur concentration on the transversal relaxation curves from Hahn echo experiments on a 90 MHz NMR spectrometer at 100°C. Each experiment took about 1.5 hours. Higher sulfur

concentration vulcanized NR exhibited faster T_2 relaxation.

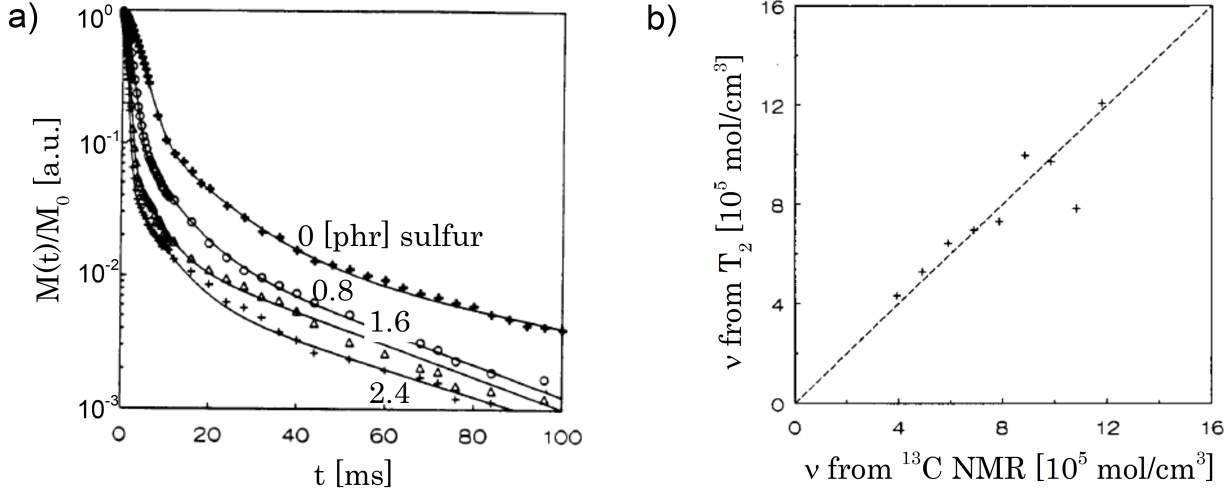


Figure 1.20: a) The T_2 ^1H NMR relaxation from Hahn echo experiments of NR vulcanizates cured with different concentration of sulfur and the corresponding analytical fitting lines. b) The linear correlation between the crosslink densities ν quantified from T_2 relaxation and from ^{13}C NMR spectroscopy. Figures are reprinted with permission from [92] with Copyright © 1992 by John Wiley & Sons, Inc.

The T_2 relaxation contains information about the motional averaging of the spin-spin interactions in a crosslinked rubber network. At temperatures well above T_g , the extent of motional averaging depends on the local dynamics together with the temporary restraint from topological entanglement and permanent constraint from the chemical crosslinks. Different from the fast and isotropic tumbling of small molecules, the fast local motions of chain segments (typically with correlation time of $\tau_c = 10^{-9}$ s) are inherently anisotropic due to the restraints from the polymer chains. However, with a much slower correlation time ($\tau_{cs} = 10^{-3}$ s), the overall motion of inter-crosslink segment is isotropic with a small portion q ($\approx 10^{-4}$) of the second moment of the interaction, M_2 . The decay of the transversal magnetization is mainly a sum of two components, the fast decay of the inter-crosslink segment, M_A , and the slow decay of the dangling chain ends, M_B . The total transversal relaxation of crosslinked rubber can be expressed as [92,94]

$$\frac{M(t)}{M_0} = M_A \exp\left\{-\frac{t}{T_{2A}} - qM_2\tau_{cs}^2\left[\exp\left(-\frac{t}{\tau_{cs}}\right) + \frac{t}{\tau_{cs}} - 1\right]\right\} + M_B \exp\left(-\frac{t}{T_{2B}}\right) \quad (1.33)$$

with the simplified exponential decay for fraction B. The molecular weight between the

crosslinks, M_c , can be calculated by

$$M_c = \frac{3}{5\sqrt{q}}(nM_{unit}) \quad (1.34)$$

where n is the number of the number of backbone bonds in a freely joint statistical segment and M_{unit} is the molar mass of the repeating unit. According to Equation 1.32, the crosslink density of the vulcanizate can be calculated from this M_c . In a direct approach, the crosslink density of sulfur cured NR can be quantified through ^{13}C NMR spectroscopy by assigning the resonances from mono- and polysulfidic linked carbons to the corresponding chemical shifts and calculating those peak intensities in the spectra. The crosslinked density derived from T_2 measurements was almost equivalent to that from ^{13}C NMR spectroscopy as shown in Figure 1.20b. Comparatively, the T_2 approach is more favorable in consideration of the sample treatment and the cost of instrumentation.

The inhomogeneous magnetization decay of two (or even more for a complex rubber network) types of segments can be seen in Figure 1.20a. To simplify the fitting process, the first term in Equation 1.33 can be simplified into a Weibull type of exponential by applying a stretching factor β

$$\frac{M_A(t)}{M_{A0}} = M_A \exp\left\{-\left(\frac{t}{T_2}\right)^\beta\right\} \quad (1.35)$$

where $\beta = 1-2$, i.e. between a Gaussian type and a simple exponential.

Based on those decay functions for the T_2 relaxation analysis of rubbers, there are even commercial NMR analyzers designed for the crosslink density measurement, such as the XLDS NMR crosslink density meter from IIC Dr. Kuhn GmbH [95]. With such devices, vulcanization kinetics [96] or aging process [97] of rubber have been investigated. In addition, NMR imaging technique with the decay function can visualize the crosslink density dispersion in the rubber vulcanizates, which has also been used for the studies of rubber crosslinking and aging [98, 99].

1.3.3. Double quantum NMR (DQ-NMR)

With respect to the crosslink density determination of rubber vulcanizates, there are already several established approaches such as 1. the polymer network equilibrium swelling in solvents [100]; 2. the freezing point depression of the solvent in the swollen rubber network [101, 102]; 3. the stress-strain curve analysis of rubber under uniaxial stretching [103] based

on Mooney-Rivlin [104, 105] representation of the reduced stress; or in a direct way 4. the ^{13}C NMR spectroscopy [92, 106]. However, these traditional methods are either experimentally cumbersome or require a high resolution spectrometer which is not economically efficient. Furthermore, some of those experiments work on the basis of ideal networks and require prerequisite parameters. For instance, the equilibrium swelling test [12, 23] is based on Flory-Rehner statistical mechanics [107] for a perfect network. It may take more than two days to swell the rubber in a suitable solvent to reach equilibrium conditions. Afterwards, the residual solvent on the swollen rubber surface, which might be toxic, has to be mopped up properly so that the mass of take-up solvent can be weighted. Finally, the specified Flory-Huggins interaction parameter, χ_1 , between the examined polymer and solvent must be available in literatures for the calculation of crosslink density. In the ^{13}C NMR spectroscopy, the obtained concentration of crosslinks highly relies on the resolution of the spectrometer and the selectivity of the relevant chemical bonds. All of the above mentioned methods only provide average values of the crosslink density. This information is not enough to describe an inhomogeneous NR network, e.g. crosslinked with different vulcanization systems or broadened network size distribution after aging. Comparatively, the TD-NMR can quantify the crosslink density in a nondestructive way to the rubber samples without toxic solvent through an simple bench-top size NMR spectrometer, such as the T_2 relaxation analysis as explained in last section. The inhomogeneities of the network can be reflected by the multiple decays embedded in the relaxation curve.

However, there are several disadvantages for T_2 relaxation analysis of rubber vulcanizates. The validity of Equations 1.33 and 1.35 on rubbers are still controversial [89, 108]. Additionally, the parameters in those equations are interdependent of each other, giving an unstable fitting results. The criteria of how to cut the tails in the relaxation curve and the definition of the sols, dangling ends and inter-crosslink chains are also uncertain. Thanks to the development of the dipolar-coupling theory and measurement techniques in last decades [109], more reliable information of the rubber network can be acquired from double-quantum NMR (DQ-NMR). With a low field bench-top NMR analyzer and innovative NMR pulses, the buildup intensity related to the pairwise couplings can be selectively analyzed [108, 110, 111]. Accordingly, the crosslink density, the mesh size distribution of the rubber network as well as the amount of network defects (loops, dangling ends and sols) can be quantitatively described. The experimental details can be found in the cited literatures and the explanation in later experimental chapter.

In a crosslinked polymer, topological constraints (entanglements) and permanent crosslinks

hinder the fast and isotropic movement of chain segments. Thus, the segmental fluctuations are anisotropic at long times as mentioned in last section. This leads to the residual local orderness, which will be reflected by a long-time plateau in the orientation autocorrelation function, $C(t)$, of the polymer chains [112] as shown in Figure 1.21a.

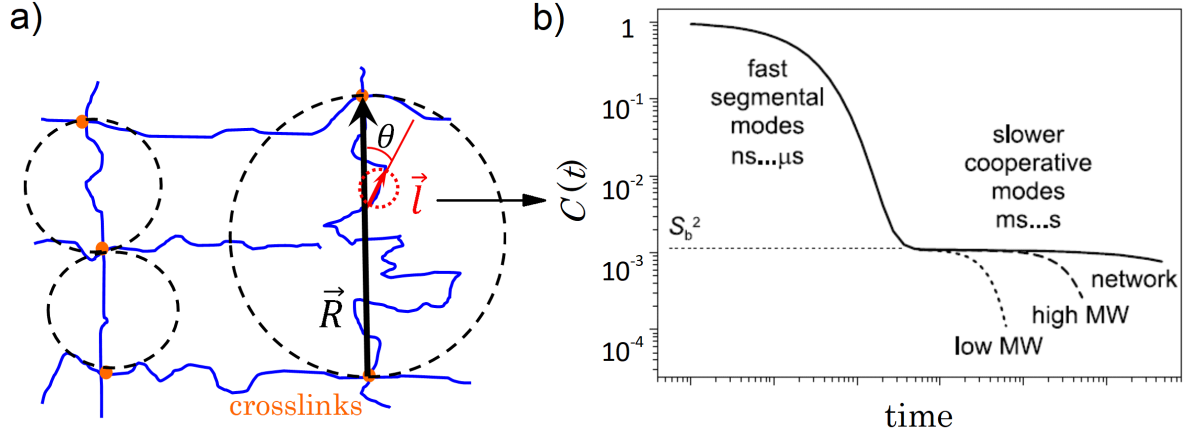


Figure 1.21: a) The orientation angle θ of the statistical freely joint chain segment \vec{l} with respect to the end-to-end vector \vec{R} of the polymer backbone between the two fixed crosslinks is instantaneous and can be reflected as the autocorrelation function $C(t)$. b) Schematic representation of $C(t)$ for the physically entangled polymer melts with different molecular weight (MW) and the chemically crosslinked chains far above T_g . Figure b is adapted from [112].

The plateau value of $C(t)$ in Figure 1.21b is governed by the segmental dynamic order parameter of the polymer backbone, S_b , given by the average of the second order Legendre polynomial [113],

$$\begin{aligned}
 S_b &= \langle P_2(\cos\theta) \rangle \\
 &= \frac{1}{2} [3\cos^2(\theta) - 1] \\
 &= \frac{3}{5} \left(\frac{lR}{R_0^2} \right)^2, \\
 \text{with } \left(\frac{R}{R_0^2} \right)^2 &= \frac{1}{Nl^2} \\
 S_b &= \frac{3}{5N} \propto \nu
 \end{aligned} \tag{1.36}$$

where θ denotes the instantaneous orientation of a statistical segment relative to its average orientation. It should coincide with the end-to-end vector, \vec{R} as depicted in Figure 1.21b. The bracket $\langle \dots \rangle$ in Equation 1.36 indicates the thermal average over all conformations and

[...] indicates the structural average over all segments in the sample [113]. Here, l is the length of the freely jointed Kuhn segment (named after Werner Kuhn, 1899-1963, Swiss physical chemist) [114] for statistical mechanics of chain molecules [115] and N is the number of such segments between the two fixed ends. For a bulk polymer sample, $(\frac{R}{R_0^2})^2 = \frac{1}{Nl^2}$, leading to the S_b proportional to the reciprocal of the average number of N between the effective constraints. The ν here can be seen as the density of physical entanglements for polymer melts or the effective chemical crosslink density for crosslinked networks.

In the network, the dipolar coupling is determined by this chain orientation information and can be reflected by DQ-NMR in term of the residual dipolar coupling constant, D_{res} . This is given by

$$D_{res} = \frac{D_{static}}{k} S_b \propto \nu \quad (1.37)$$

where D_{static} is the effective static limit of the dipolar coupling constant. It is a fixed value for a specified polymer, and k is constant. For NR, $\frac{D_{static}}{k} = 2\pi \times 6.3$ kHz in some results [116]. Overall, D_{res} from DQ-NMR can directly represent the effective crosslink density of a crosslinked rubber.

The exemplary DQ-NMR results of NR vulcanized with increasing amount of sulfur from 1–10 phr [116] are shown in Figure 1.22. The normalized DQ intensity, I_{nDQ} , as a function of the DQ evolution time τ_{DQ} build up faster for the higher crosslinked samples. After the regularization fitting for the buildup curve with a proper kernel function, the residual dipolar coupling constant can be displayed in a distribution fashion. For evolution time τ_{DQ} in unit of [ms] in the raw data, the outcome distribution curve is given by $D_{res}/2\pi$ in unit of [kHz].

Combining Equation 1.37 with the Flory's statistical mechanics [115, 117] and simulation results [118] for *cis*-1,4-polyisoprene, the molar mass M_c between the two crosslinks of NR can be calculated via $D_{res}/2\pi$ via [116]

$$M_c^{(NR)} = \frac{617 \text{ Hz}}{D_{res}/2\pi} [\text{kg/mol}] \quad (1.38)$$

While a narrow distribution of the $D_{res}/2\pi$ reflect a homogeneous network and vice versa.

The D_{res} from DQ-NMR technique has been examined on several rubber materials to compare with the results from solvent equilibrium swelling [119], to probe the rubber crosslinking generation during vulcanization [120] and filler-polymer interactions in rubber composites [121], to prove the correlation with mechanical response [122], etc. It has not been systemically

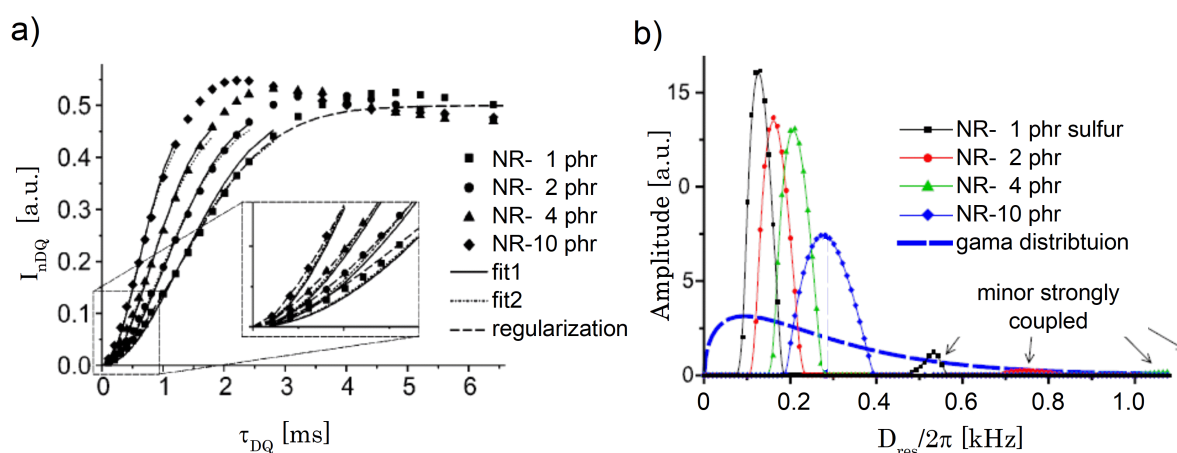


Figure 1.22: a) The normalized DQ buildup intensity I_{nDQ} as a function of DQ evolution time τ_{DQ} of cured NR with different amount of sulfur from DQ-NMR measurement and b) the resulting distribution curves of $D_{res}/2\pi$. Figures adapted from [116]. Copyright © 2005 by American Chemical Society. Reprinted by permission.

applied to investigate the network alternation of rubber vulcanizates during aging. In the present thesis, we are going to employ this robust technique to unveil the aging effect on NR networks in nanometer scale, on which dimension the DQ-NMR relies from the molecular dynamics.

2. Experimental

In the present thesis, several characterization techniques have been used to investigate the crosslinks formation of NR during vulcanization, the network alternation after aging as well as their rheological response. An overview of the sample preparation and the conducted measurements is presented in the flow chart below:

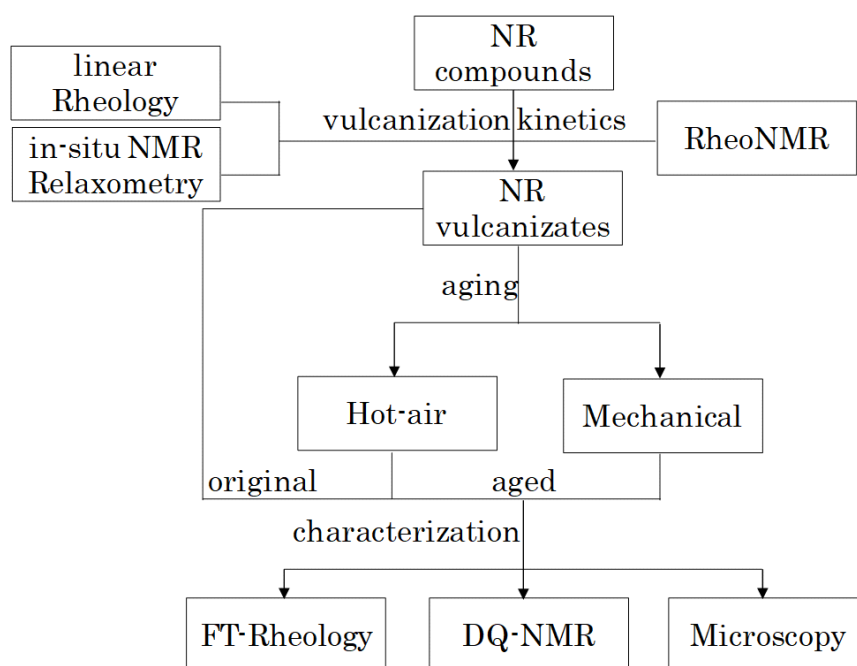


Figure 2.1: Flow chart of the experiments for the studies of NR aging.

Unvulcanized NR compounds were cured in a hyphenated setup of rheology and NMR relaxometry (RheoNMR) to study the crosslinks buildup kinetics for different vulcanization systems. The NR vulcanizates in sheets were submitted for aging either chemically by hot-air or physically by mechanical fatigue. The effect of aging was investigated by comparing the original (unaged) and aged samples in FT-rheology, DQ-NMR and microscopy.

2.1. Sample preparation

There were two sets of NR samples prepared as the formulations listed in Table 2.1 and 2.2. In rubber industry, the amount of each ingredient commonly refers to one hundred parts of pure rubbers by weight so that the unit is "phr" in abbreviation.

Table 2.1: Group 1: unfilled NR samples with different sulfur-accelerator vulcanization systems.

Sample	NR- CVhigh	NR- CVlow	NR- SEVmed	NR- EVhigh	NR- EVlow
vulcanization feature					
Vulcanization	Conventional	Conventional	Semi-Efficient	Efficient	Efficient
Crosslink density	high	low	medium	high	low

Table 2.2: Group 2: NR samples with same vulcanization system (SEVmed) but different filler volume and varying dosage of anti-oxidant, the 6PPD. Notice, the NR1 here is identical as NR-SEVmed in Table 2.1.

Sample	NR1	NRCB1	NRCB0	NRCB2
Ingredients	phr ^a	phr	phr	phr
filler:	unfilled	filled	filled	filled
antioxidant:	normal	normal	zero	double
Natural rubber (NR)	100.0	100.0	100.0	100.0
Carbon black N339 (CB)	0	50.0	50.0	50.0
Zinc oxide (ZnO)	3.0	3.0	3.0	3.0
Stearic acid	1.0	1.0	1.0	1.0
6PPD ^b	1.8	1.8	0	3.6
CBS ^c	1.1	1.1	1.1	1.1
Sulfur	1.1	1.1	1.1	1.1

^a parts per hundred rubber by weight;

^b *N*-(1, 3-dimethylbutyl)-*N'*-phenyl-*p*-phenylenediamine acts as the anti-oxidant, which is also called anti-oxidant 4020;

^c *N*-cyclohexyl-2-benzothiazole sulfenamide, rubber crosslinking accelerator, also called accelerator CZ.

Group 1 were unfilled NR with 5 vulcanization systems and normal dosage of anti-oxidant (1.8 phr of 6PPD with reference to the formulation of tire tread). The vulcanization systems included conventional vulcanization with high or low crosslink density (CVhigh/low), semi-efficient vulcanization with medium crosslink density (SEVmed) and efficient vulcanization

with high or low crosslink density (EVhigh/low). The definition of the vulcanization systems can be found in Chapter 1.1.1.

Group 2 were three extra NR samples filled with 50 phr carbon black (CB) and varying amount of anti-oxidant based on SEVmed sample (NR1) in group1. Samples without and with the CB filler were named as NR, NRCB, respectively. With normal dosage of the anti-oxidant, the samples were labeled with 1 at the end of the name. Otherwise, they were labeled with 0 or 2, indicating the zero or double amount of anti-oxidant. All other ingredients like zinc oxide and stearic acid were the same with each other. All the green compounds (mixed with all ingredients but not yet vulcanized) and the vulcanizates used in this work were kindly prepared by the cooperation partner, Continental Reifen Deutschland GmbH, Hannover, Germany.

Mixing:

All compounds were mixed in a 2 liter internal mixer (Harburg-Freudenberger, Hamburg, Germany) in a two-step mixing process. In the first step, all ingredients except the vulcanization system were mixed for 6 min at a temperature of approximately 150 °C with a rotor speed of 30–40 rpm (revolutions per minute). In the second step, the vulcanization system was added and the compound was finalized by mixing for 2.5 min at 100 °C with a rotor speed of 30 rpm. Green compounds (unvulcanized) of group 1 are delivered as well for vulcanization kinetic studies, each with 100 grams.

Vulcanization:

All green compounds were vulcanized by pressing them into 1.5 mm thick flat sheets at 160 °C within optimum curing time. The optimum curing time is determined by the maximum torque/modulus in the rheo-curves from the curemeter, ranging from 7 to 20 minutes depends on the curing rate of the sample.

2.2. Vulcanization of NR on rheology–NMR combination

The study of curing is carried out on a unique RheoNMR setup constructed by Ratzsch et al. [123] (a new version here) with the combination of a high end rheometer and a lab-made NMR magnet in Halbach design [124] of 16 decagon magnet bars. The schematic RheoNMR setup is shown as Figure 2.2.

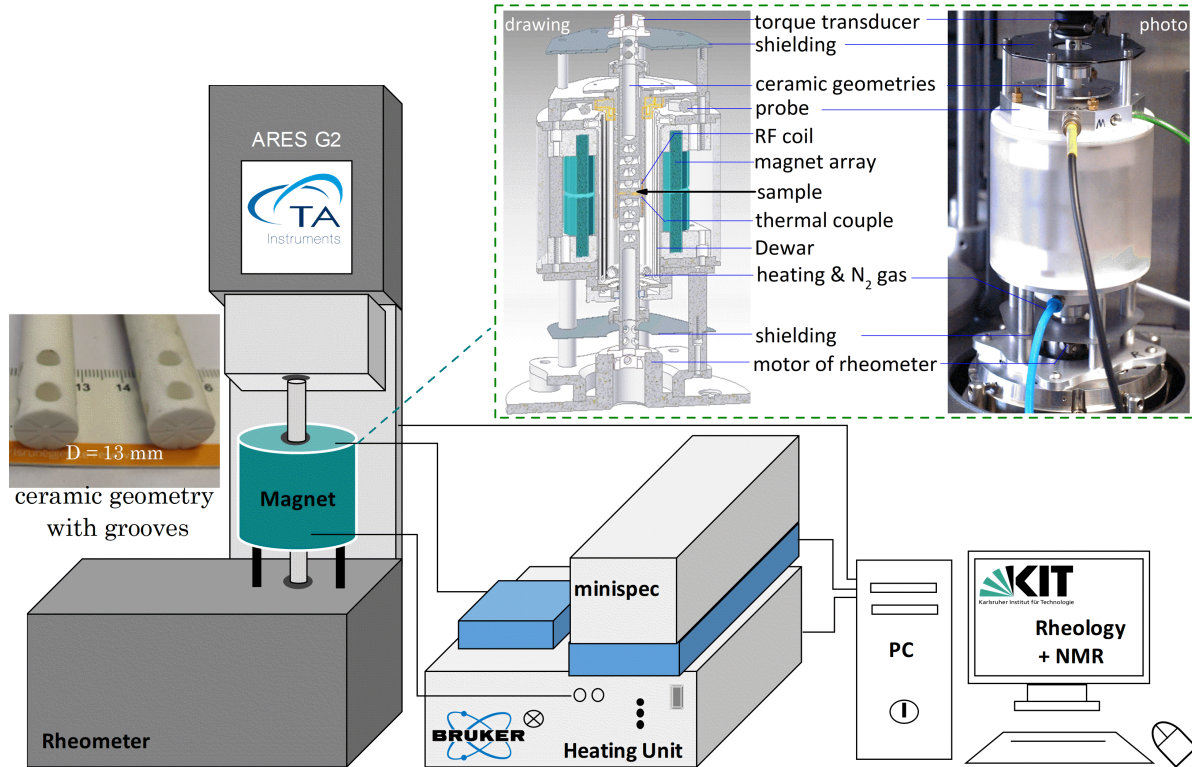


Figure 2.2: Scheme of the RheoNMR setup and the mechanical drawing of the Halbach-arrayed magnet. The photograph of the whole RheoNMR setup as well as the mechanical drawing of the ceramic geometry can be found in Appendix A.

The 2.5 kg magnet with a cylindrical core possesses a static magnetic field of $\vec{B}_0 = 0.59 \text{ T}$ ($\omega_L/2\pi = 25 \text{ MHz}$ as ^1H NMR). The 90° and 180° pulse lengths are $t_{90} = 2.6 \mu\text{s}$ and $t_{180} = 4.9 \mu\text{s}$, respectively, as seen in Figure 2.3b. Such magnet can be mounted on e.g. here the ARES-G2 rheometer from TA Instruments. Shielding materials were covered at both ends of the magnet to protect the metal and electronic parts of the rheometer. The temperature was controlled with a Bruker BVT 3000 Heating Unit by blowing nitrogen gas in to core of the magnet. The magnet is isolated from the heating coil with a glass Dewar. Ceramic geometries with 13 mm diameter were machined and connected to the rheometer. Silver RF coil were self-winded on a ceramic tube outside of the geometry and sample but in the

2. Experimental

center of the magnet. The RF coil together with lab-made probe electronics were ported to a Bruker Minispec amplifier. Furthermore, the magnets were conditioned at 40 °C during the measurement to suppress the drifting of \vec{B}_0 .

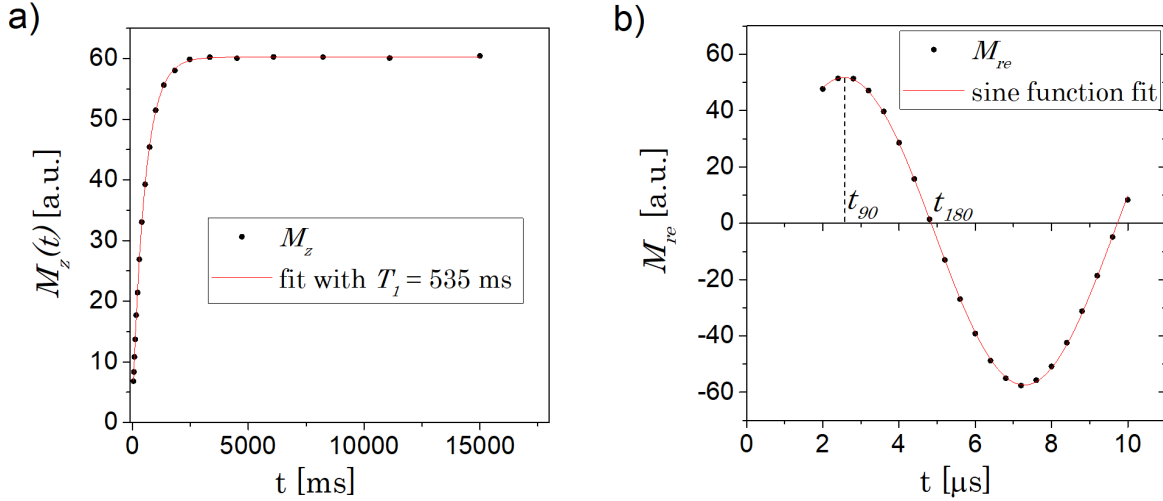


Figure 2.3: a) The longitudinal relaxation time T_1 , b) the saturation time t_{90} and inversion time t_{180} of NR-SEVmed (NR1) in RheoNMR at 140 °C to demonstrate the performance of the setup.

With this novel setup, TD-NMR experiments can be conducted in parallel with rheological characterization. It allows to directly correlate the polymer dynamics on the nanometer scale with the macroscopic rheological response. Such correlations have been already performed on the crystallization kinetics of plastics [123,125] and the hydration of cement paste [126].

RheoNMR is only examined for the green compounds (unvulcanized) of group 1 samples without carbon black. The compounds were hot-pressed in to 1.5 mm thick sheets at 90 °C for 3 min (no observable vulcanization yet) and punched out disk specimens with diameter of 13 mm (approximately 0.3 g). The disk specimens were submitted to the ceramic $D = 13$ mm parallel plates in RheoNMR. Isothermal vulcanization were carried out at 140 °C in nitrogen atmosphere with linear rheology and in situ NMR relaxometry measurements. For temperatures higher than 140 °C, it is challenging to maintain the stability of the magnet temperature thus the data quality of NMR is not guaranteed. The surface of ceramic plates were grooved to avoid the wall-slip during rheological test, which is commonly considered for the rheometry of rubber materials. The vulcanization process took from 3000–10000 s, depending on the curing rate of each sample.

Dynamic time sweep experiment were performed at an oscillation strain amplitude of $\gamma_0 =$

0.5% and frequency of 1 Hz, which is in the LVE regime (see Chapter 1.2.1) of the material. With respect to the in-situ transversal relaxation (T_2) of NMR, xx4 pulse (see Chapter 1.3.2) was applied, following a mixed magic sandwich echo (MSE) with the reference of [127]. The MSE was applied to solve the dead time problem of the NMR as explained in Figure 2.4. Due to the limits of receiver electronics, the beginning part of the magnetization decay can not be acquired by the receiver in a very short period time as the dotted line in Figure 2.4a. This is the so-called dead time, τ_{dead} ($= 11 \mu\text{s}$ for current setup). However, this short period of magnetization decay can be refocused by the MSE sequence so that an equivalent real-time signal is reported. The samples were continuously scanned with MSE-xx4 sequence at a scan numbers of 8. The recycle delay (RD) was set to 2.7 s, which is 5 times of $T_1 = 535 \text{ ms}$ as indicated in Figure 2.3a. It took approximately 23 s to receive one full relaxation curve via MSE-xx4 pulse sequence.

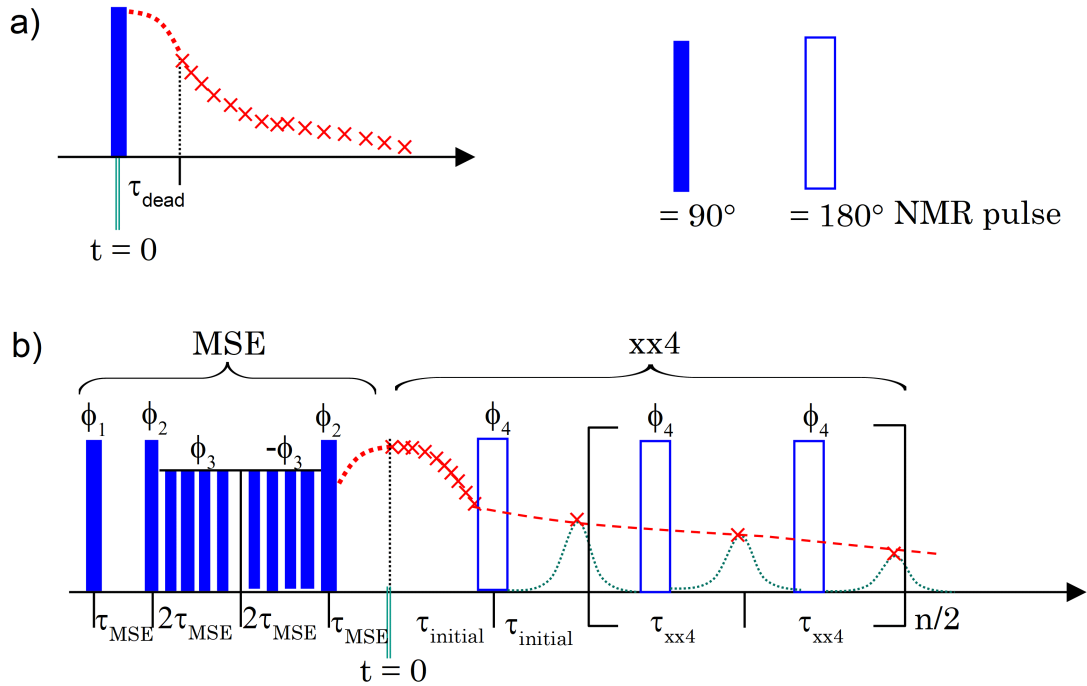


Figure 2.4: a) The dead time problem can be solved by b) adding a MSE pulse sequence before the xx4 sequence during the NMR relaxometry measurements. The phase cycle variables are: $\phi_1 = (x|-x|x|-x)$, $\phi_2 = (-y|y|y|-y)$, $\phi_3 = x$ and $\phi_4 = (y|-y|y|-y|-y|y|-y|y)$. The phase of every other pair of 180° pulse is inverted for the echos, i.e. a xx4 sequence. The explanation in more detail can be found in reference [127].

2.3. Aging of NR vulcanizates

As illustrated in Figure 2.5, the 1.5 mm thick vulcanized rubber sheets were aged either statically at elevated temperatures in the presence of air (hot-air aging) [4] or mechanically fatigued by cyclic stretching at ambient temperature with the reference of the standards from American Society for Testing and Materials (ASTM) [128].

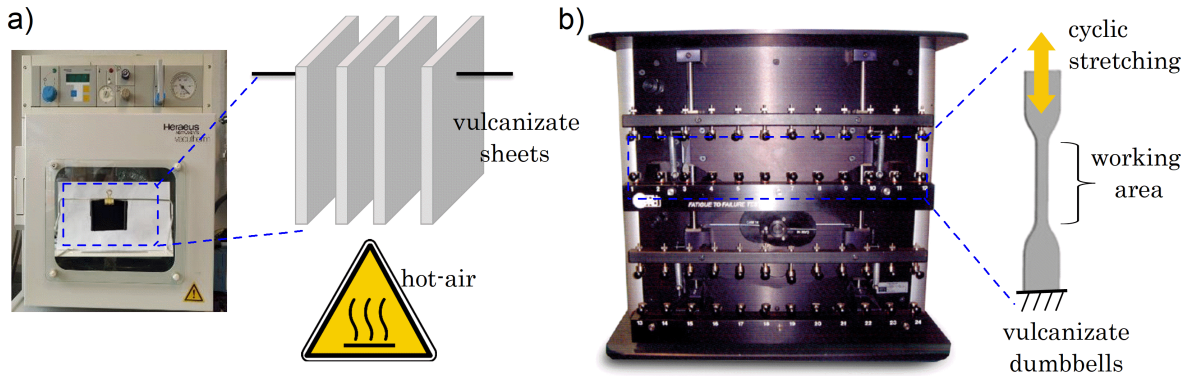


Figure 2.5: Facilities for a) hot-air aging with oven and b) mechanical aging with Fatigue Tester of vulcanized NRs.

2.3.1. Hot-air aging

For hot-air aging, the rubber sheets were hung in Heraeus VT6025 oven (Thermo Scientific, Langensfeld, Germany) at 70 °C for 7–28 days, or at 120 °C for 0.5–3 days in air atmosphere with referential procedures and conditions described in ASTM-D572 [27].

2.3.2. Mechanical aging

For mechanical aging, the rubber sheets of NRCB1 vulcanizates were punched out into dumbbell shape specimen with a sharp cutting die. The dumbbell dimension was described in ASTM-D4482 [33] with a working area of $4 \times 30 \text{ mm}^2$. Under stretching, the force will concentrate on the long working area of the dumbbell to avoid the geometry defects for fatigue. For mechanical aging, the dumbbell specimens were fixed on the fatigue machine (Fatigue to Failure Tester, Alpha Technologies, Hudson, USA) and stretched under an elongation ratio of $\varepsilon_0 = 90\%$ or 140% at frequency of 1.7 Hz (100 cycles per minute) and varying kilocycle

numbers at ambient temperature. It was suggested to run fatigue test below 5 Hz for CB filled rubbers to reduce the self-heating of the specimens during fatigue [129], which would superimpose thermal-oxidation aging effect. All of the specimens were removed before failure, i.e. before cracks were visually observable on the specimens or the initial modulus dropped more than 50%.

2.4. Characterization of NR vulcanizates

The characterization of the vulcanized NR sheets, both before and after aging, were characterized via the instruments as listed in Figure 2.6: the strain-controlled rheometer ARES-G2 (TA Instruments, New Castle, USA) for linear and FT-rheology measurements to detect the mechanical response in millimeter scale [mm]; the 20 MHz NMR analyzer Minispec mq20 (Bruker BioSpin GmbH, Rheinstetten, Germany) for DQ-NMR measurement to study the rubber chain dynamics in nano/sub-nanometer scale [nm]; and the light reflection microscope VHX 900F (Keyence Corporation, Osaka, Japan) to probe the potentially generated cracks on the surface or the cross-section of the samples with a resolution down to 1 micrometer [μm].

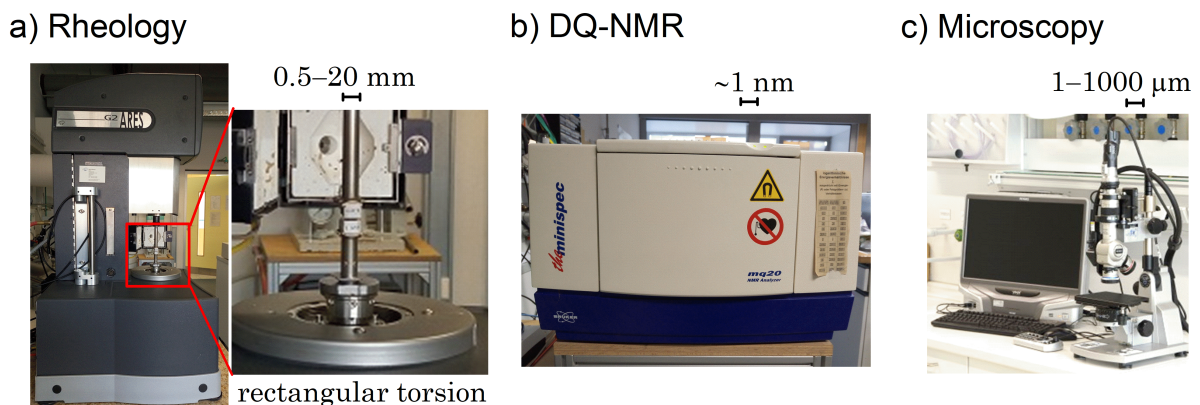


Figure 2.6: a) An ARES-G2 rheometer with rectangular torsion fixture, b) a mq20 NMR analyzer and c) a VHF 900F reflection light microscope for rheological, DQ-NMR and morphology characterization of the NR vulcanizates with the response from different dimension scales. Photographs of other sample preparation apparatus can be found in Appendix A.

2.4.1. Rheology

To conduct rheological or mechanical measurements of relative solid or slippery materials, it is of critical importance to fix or glue the specimen properly on the rheometer geometry. This can avoid the stress contribution from wall-slip or tribological phenomena between the sample and the fixture during deformation. For the vulcanized rubber sheets, we utilized the rectangular torsion geometry. There are many other common dynamic mechanical geometries or instruments that could be employed. However, for the rubber aging studies, we selected torsion on rubber samples in thin sheet shape (1.5 mm) and an ARES-G2 rheometer based on several considerations as below.

Compared to common dynamic mechanical analyzer (DMA) with a linear motor in vibration mode, the ARES-G2 is a high end rheometer with rotational brushless motor and force rebalance torque transducer. FT-rheology technique requires or at least prefers accurate control of the sinusoidal strain as well as the precise measurement of the stress response to suppress the spectra noise from the instruments [130]. Even on a well controlled DMA, it is not recommended to adopt tension or double shear geometry for FT-rheology on rubber. In a uniaxial tension geometry, the rubber undergoes dynamic stretching with a fixed static elongation. Due to intrinsic asymmetry of the specimen under uniaxial tension (the elongation will shrink the cross-section area), the stress signal is an engineering stress and exists higher harmonics already. In a double shear geometry, two testing pieces are sandwiched between three parallel plates with the middle plate oscillating thus double-shearing the samples. However, the rubber vulcanizates have to be bonded on the double shear geometry by glue, introducing an uncertain contribution to the stress at large strain amplitude (LAOS) conditions. In addition, the geometric symmetry of such testing assembly is difficult to be guaranteed. Therefore, the torsion fixture is preferred here. Concerning the chemical aging process of rubber, rubber sample in sheet is thinner than cylindrical shape with same volume, where the later would go through an inhomogeneous aging from the surface to inside. Additionally, the fixing mechanism of rectangle torsion geometry is more practical and operable.

Both the original and the aged 1.5 mm thick rubber sheets were cut into 3 mm wide strips and then fixed on ARES-G2 rectangle fixture at a gap distance of 2 mm. For the dumbbell shape samples after mechanical aging, only their working areas were selected to cut into rectangle strips for measurements. The specimens were strain swept from strain amplitude $\gamma_0 = 0.01$ to 200% at an oscillatory frequency of $\omega_1/2\pi = 1$ Hz and room temperature to

obtain both linear rheological results and the FT-rheology parameter, $I_{3/1}$, as a function of γ_0 . Twenty data points per decade of the strain amplitude were measured with ten oscillation cycles during the acquisition of each data point. It was found that the strain amplitude density has no obvious effect to the strain sweep results between 10–20 data points per decade (see Appendix B). At least three specimens were tested for each sample to evaluate the reproducibility.

2.4.2. DQ-NMR

Proton double quantum NMR (^1H DQ-NMR) is a versatile and robust technique to characterize the structure of crosslinked rubber materials [109, 131] by measuring the polymer chain dynamics. The content of network defects, the network density and its distribution can be quantitatively described.

The 1.5 mm thick rubber sheets were cut into 8 mm diameter disks and piled into O.D. = 10 mm NMR glass tubes. For the dumbbell shape samples after mechanical aging, only the working areas were selected and cut into roughly $2 \times 2 \times 1.5 \text{ mm}^3$ cubes before filling into the NMR glass tubes as above. All of the pile height of the samples in the glass tubes are lower than 8 mm for good RF homogeneity. The DQ-NMR measurements were conducted on a Minispec mq20 by applying a Baum-Pines NMR pulse sequence [119, 132] as the scheme shown in Figure 2.7.

As indicated in the Figure 2.7, τ_c and n_c denote the time for one cycle and the number of cycles, respectively. The timings of the sequence are $\tau_1 = \tau_c/24 - t_{90}/2$ and $\tau_2 = \tau_c/12 - 3t_{90}/2$. Then during the measurement, τ_c and n_c were varied for different τ_{DQ} .

To measure the residual dipolar coupling constant D_{res} as caused by the entanglement, it is required to condition the materials far above the glass transition temperature [109], i.e. at least $T_{measure} > T_g + 100^\circ\text{C}$. The onset T_g of unvulcanized cis-polyisoprene was -67°C according to the differential scanning calorimetry (DSC) analysis in literature [133]. The onset T_g of the NR1 and NRCB1 was confirmed as close to -62°C from the temperature ramp data at dynamic mechanical frequency of 1 Hz (see Appendix B). The DQ-NMR experimental temperature was selected as 60°C , which is already $T_{measure} > T_g + 100^\circ\text{C}$ of NR but below the hot-air aging temperature (70 and 120°C) to avoid extra aging effect during the 2 hours measurement.

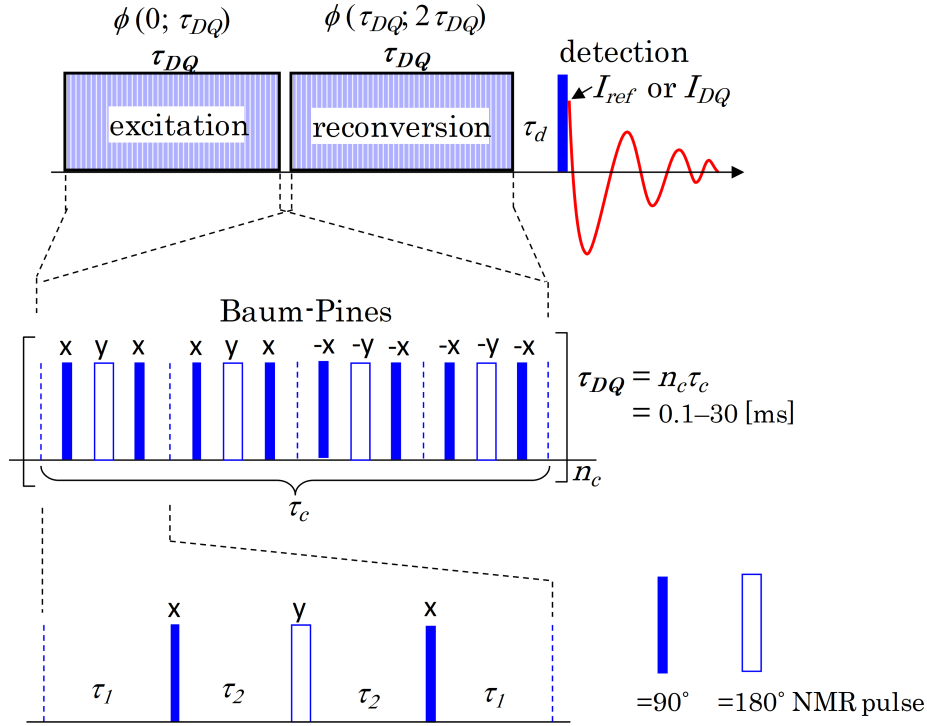


Figure 2.7: Scheme of the DQ-NMR measurement with a Baum-Pines sequence [109,132] for dipolar coupling excitation and reconversion.

The 90° and 180° ^1H pulse lengths of the crosslinked NR were $t_{90} = 2.7 \mu\text{s}$ and $t_{180} = 4.9 \mu\text{s}$, respectively. The conditioned sample were excited and reconverted at different evolution time intervals, τ_{DQ} , from 0.08 to 30 ms at a scan number of 128. The corresponding reference intensity and double quantum build-up intensity, I_{ref} and I_{DQ} , were acquired separately. Each sample was measured three times to evaluate the reproducibility. The data treatment followed the procedure described in the reference [134].

2.4.3. Microscopy

The surface and internal section of both the aged and unaged samples were investigated under a VHX 900F (Keyence Corporation, Osaka, Japan) light reflection microscope at magnifications of up to 1000 times. To check the internal cross-section area, the samples were cut through with a sharp scalpel. For the mechanically fatigued samples, only the working area of the dumbbell specimens were used for observation and analysis.

3. Vulcanization Kinetics

During the vulcanization of NR in the presence of sulfur and accelerator, several types of sulfidic crosslinks can be formed, depending on the sulfur/accelerator ratio as mentioned in Chapter 1.1.1. It is of importance to understand the crosslinks formation kinetics since the nature of those chemical bonds determines the aging properties of NR vulcanizates.

The crosslinking or vulcanization kinetics of rubber have been intensively studied with a variety of methods, including the development (the time dependent) of moduli via rheology or the decrease of chain mobility via NMR relaxometry. However, those experiments are usually conducted separately so that a direct correlation between the results is questionable since there are non-neglectable errors between the sample size and the curing environment for such fast kinetics. It requires lots of additional efforts to ensure the identical environment for the vulcanization process in different instruments. Here, we present the results from a unique hyphenation of a low field NMR with a high-end rheometer (RheoNMR) as illustrated in Chapter 2.2. It is the first time to conduct such experiment to this material class. During vulcanization, the ^1H NMR relaxometry can be carried out in parallel with the rheological characterization. It enables the direct correlation between the macroscopic rheological properties and the local molecular dynamics.

3.1. Rheology curve with in-situ NMR relaxometry

The NR samples of group 1 of Table 2.1 were submitted to RheoNMR for isothermal crosslinking (curing or vulcanization) measurements. Time sweep experiments using oscillatory shear were carried out with small strain amplitude in LVE regime. This is commonly adapted approach in rubber industry for the determination of optimum vulcanization time and quality control.

The raw output of sample NR-CVhigh from RheoNMR is shown in Figure 3.1 as an example.

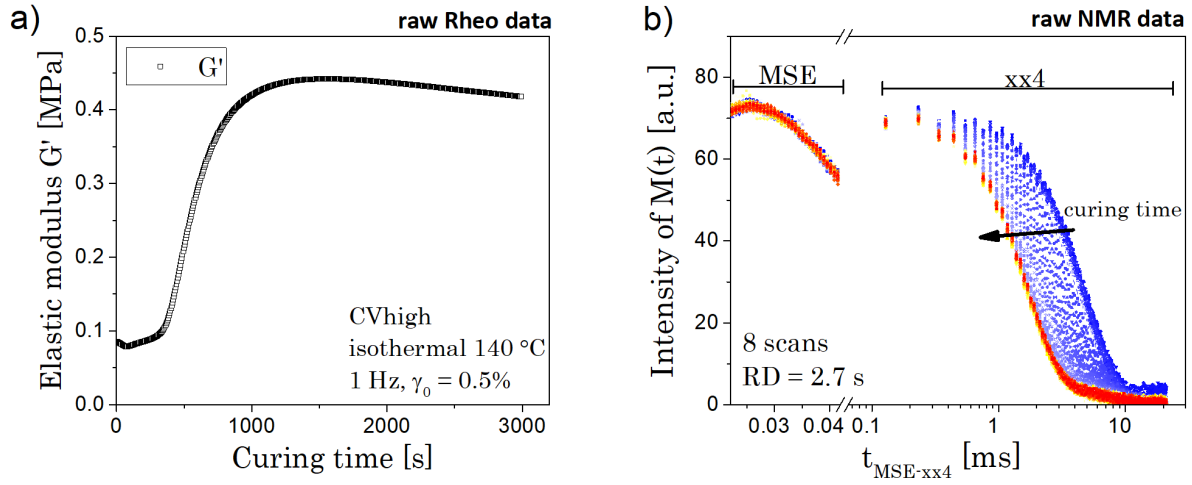


Figure 3.1: There are two groups of time dependent raw data from a RheoNMR measurement, such as a) the evolution of the macroscopic properties from elastic modulus G' in rheology (the rheo-curve) and b) the molecular level information from the T_2 relaxation curves in NMR.

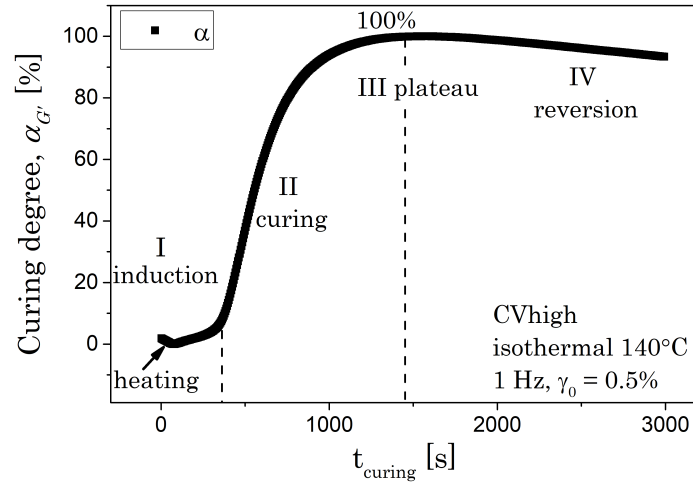


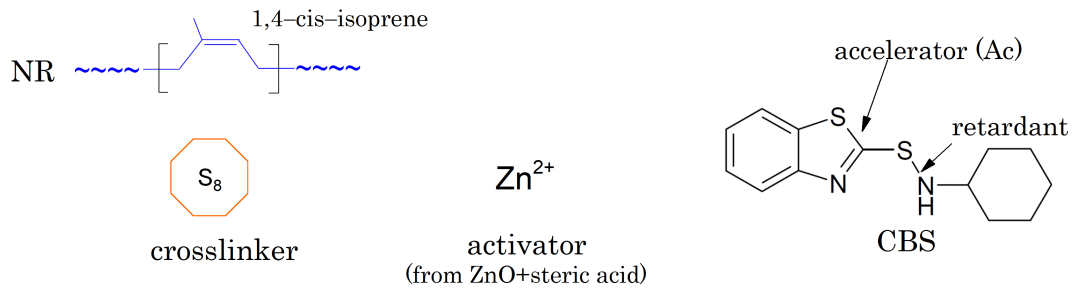
Figure 3.2: The curing degree α as a function of curing time and the typically categorized curing periods.

The torque or moduli data plotted against the curing time is commonly called rheo-curve. The elastic modulus increased along the vulcanization, but started to decrease at the end. This behavior is typical for conventional vulcanized NR with high sulfur/accelerator ratio. Normally, the degree of curing can be defined by the relative increase of the elastic moduli:

$$\alpha \equiv \frac{G'_{max} - G'(t_{curing})}{G'_{max} - G'_{min}} \times 100\% \quad (3.1)$$

where G'_{max} and G'_{min} are the minimum and maximum modulus along the course of vulcanization. In this way, the vulcanization rates for samples with different moduli could be directly compared. The curing course of sulfur-NR system can be separated into four periods as indicated in Figure 3.2: I) induction, II) curing, III) plateau and IV) reversion. The drop of the moduli at the very beginning is due to the heating up of the materials from room temperature (RT) to 140 °C.

Formulation:



Reaction scheme:

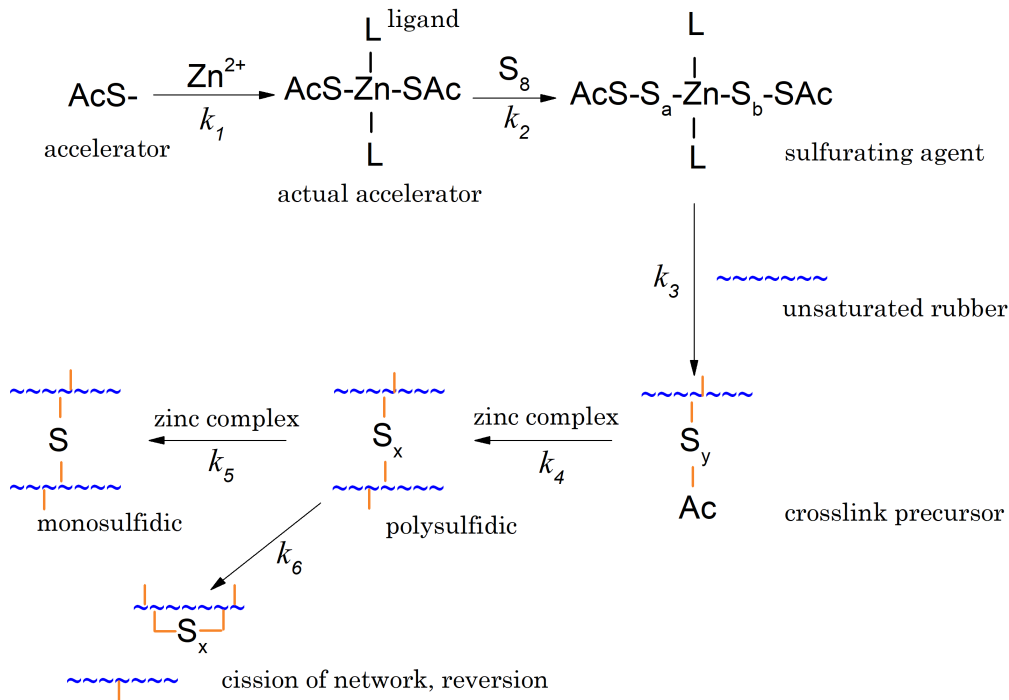


Figure 3.3: The influence of the curing chemicals on the reaction scheme of the accelerated sulfur-NR systems in presence of zinc oxide. The scheme is modified according to [25].

There are several chemicals and mechanisms involved during the crosslinking in sulfur-accelerator-NR formulations. The details can be referred in books and review articles [25,135].

Here, only the main reactions are explained briefly. Consider the formulation of NR-SEVmed (NR1) as an example, it can be classified into 4 chemical systems: 1) the sulfur as crosslinker to bond two neighbor NR chains via C=C bonds, 2) CBS as accelerator to speed-up the curing reaction, 3) retardation of the reactions at the very beginning and 4) ZnO and fatty acid as activator to catalyze the crosslinking reaction. The chemical structure and chemical reaction schemes can be found in Figure 3.3.

The early stage crosslinking is called scorch in the rubber industry, which should be avoided before vulcanization to allow the processibility of rubber for mixing and calendaring. The -S-N- bonds in CBS inhibit k_1 and k_2 in the reaction scheme, which is the induction time for the crosslinking. After that period, the zinc ions continuously form a ligand with the accelerator (Ac, the -N=CR-S- in CBS) and the free sulfur. The sulfurating agent attacks the -C=C- in NR to form the crosslink precursor with a dangling polysulfide-Ac. In the presence of a zinc ligand complex, the precursor reacts with neighboring -C=C- bonds and links two chains with polysulfidic bridges. This crosslinks-forming period, with constant speed, is the curing period. The polysulfidic crosslinks are not stable due to the low bond energy. They can be easily modified into more number of mono-/disulfidic bridges, which slows down the crosslinks-forming as shown by the plateau period. In longer time, cyclic-sulfidic bridges formation from the polysulfidic bonds dominates the reaction, resulting in the network scission as reflected by the drop-down of the elastic modulus. This is called network reversion.

The rheo-curves of the five NRs containing different crosslinking agents compositions are plotted in Figure 3.4. The evolution of other characteristic data can be found in the Appendix B. As expected, the amplitude of optimal storage moduli, G'_{max} , followed the order of crosslink density as design, high>medium>low, as listed in Table 2.1 of Chapter 2.1. CV samples exhibited strong degree of curing reversion after 1500 s while the EV samples maintained a distinctively long plateau. The SEV sample is in between.

During the NMR relaxometry measurements as Figure 3.1b, MSE-xx4 pulse was continuously scanned on the sample with 8 scans as in-situ to the rheology test. The data sampling duration for NMR and rheology were about 23 and 6 seconds per data set or per data point, respectively. The signal to noise ratio of the relaxation curves was around 120. The short time intensity of MSE was stable during curing, as it reflects the total number of protons within the sample. The MSE signals decayed along the evolution time $t_{MSE-xx4}$, mainly due to the inhomogeneities of the static magnetic field, \vec{B}_0 . The initial intensity of xx4 part (evolution time 0.1–0.3 ms) was also close to the stable MSE peak intensity. This implies there is no such fast relaxation motion mode (at a temperature far above T_g) in the rubber

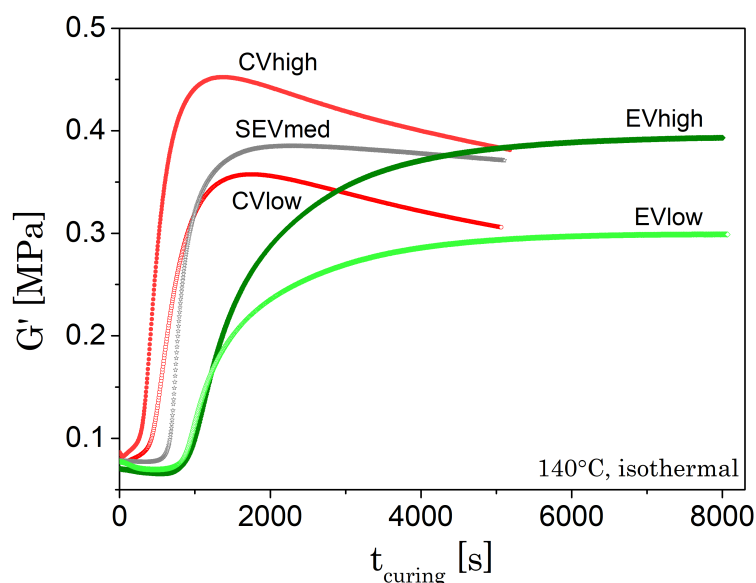


Figure 3.4: The rheo-curves of crosslinking NRs with different vulcanization systems. All data were acquired from the rheological part in the RheoNMR measurements.

segments even after crosslinking. Or in other words, the chemical permanent crosslinks would not change the sub-segmental vibrations, in comparison with the physical transient entanglement. However, the xx4 signals shifted towards shorter relaxation time during curing. This indicates the fluctuation of the rubber sub-chain segments are more constrained by the crosslinks, leading to a faster T_2 relaxation rate of the spins on the segments. Therefore, the newly generated crosslinks constrain the molecular mobility in the range of chain segments other than the sub-segmental sections as shown in Figure 1.21a.

3.2. Analysis of the transversal relaxation time

3.2.1. Fitting procedures

Regarding the raw data from the in-situ ^1H NMR relaxometry as above, we have to find a way to extract the T_2 time embedded in the transversal relaxation curves, especially the xx4 part. They are related to cooperative chain dynamics and is influenced by constraints such as crosslinked points. The net magnetization intensities were different from each experiments since the sample quantity and the receiver gain for NMR signal were varying. Therefore, the raw intensity in Figure 3.1 was normalized as $I(t)$ by the initial intensity of xx4 part

or the peak intensity of MSE part for analysis. For rubber materials or elastomers, it is known that the transversal relaxation can not be simply expressed by a single exponent or Gaussian function due to the heterogeneity of the molecular dynamics. The decay behavior is intermediate, and should mostly be decomposed into multiple components. However, bi-exponential function still did not fit well on the experimental data as seen in Figure 3.5.

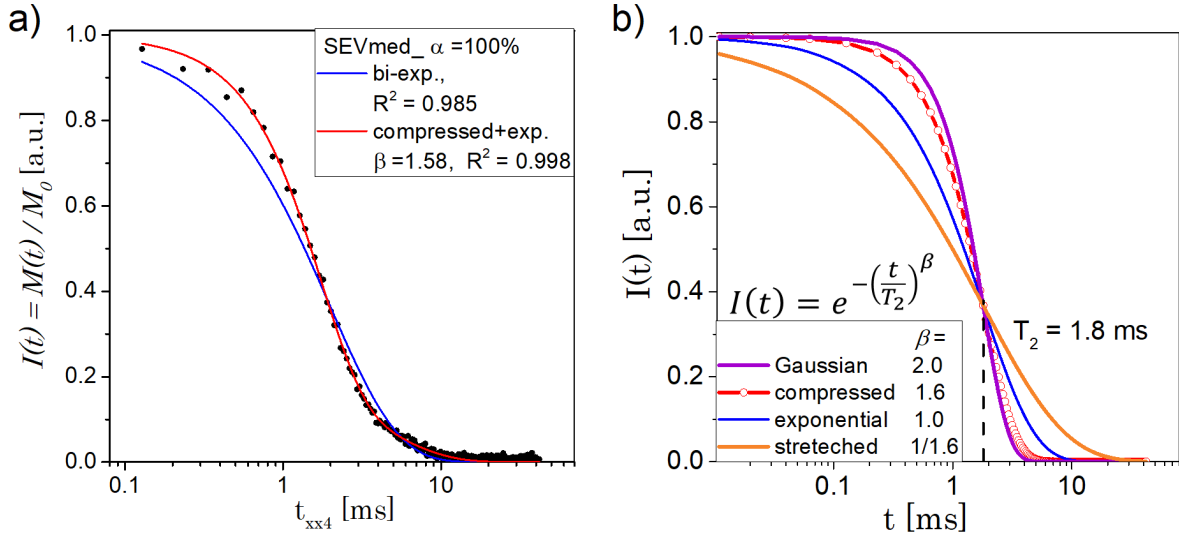


Figure 3.5: a) The fit performance of Equation 3.2 on 100% cured SEVmed sample and b) the shapes of the exponential decay function with same T_2 but different factor of β . With $1 < \beta < 2$, the function is compressed and with $0 < \beta < 1$, the function is stretched.

As discussed in Chapter 1.3.2, one can impose a compression factor, $1 < \beta < 2$, to the exponential functions. It is found that a combination of one exponential and one compressed-exponential (Weibull type) can make a satisfying fit,

$$I(t) = \frac{M_{xx4}(t)}{M_0} = I_R \exp\left[-\left(\frac{t}{T_{2R}}\right)^\beta\right] + I_M \exp\left(-\frac{t}{T_{2M}}\right), \quad (3.2)$$

with boundaries:

$$I_R + I_M = 1, \quad T_{2R} < T_{2M}, \quad 1 < \beta < 2.$$

with R and M representing the relative rigid segments close to the crosslinks and the relative mobile segments in middle of the crosslinks, respectively. This model works for samples along the course of vulcanization from the unvulcanized to the fully vulcanized status.

In Equation 3.2, the five free parameters, I_R , I_M , T_{2R} , β and T_{2M} , are interdependent with each other, causing fitting instabilities for the whole set of curing data. The target is to use one polymer dynamic parameter from above to correlate with the rheological response. Thus

it is preferable to reduce the number of fitting variables and select the most representative one. According to the raw NMR signals evolution in Figure 3.1, the most distinctive change after crosslinking is the relaxation time at the short t_{xx4} , i.e. the T_{2R} . Therefore, the fitting quality of T_{2R} is considered as the most relevant.

Table 3.1: Fitting results with Equation 3.2 on all the NR samples at the zero($\alpha = 0\%$) or fully($\alpha = 100\%$) vulcanized status.

Parameters samples	I_R -	I_M -	T_{2R} [ms]	T_{2M} [ms]	β -	R^2
<i>free fitting:</i>						
CVhigh-0%	0.701	0.299	5.269	5.939	1.630	0.99874
CVlow-0%	0.821	0.179	5.014	5.802	1.579	0.99851
SEVmed-0%	0.833	0.167	4.688	5.271	1.691	0.99765
EVhigh-0%	0.883	0.117	4.967	5.483	1.638	0.99811
EVlow-0%	0.832	0.168	4.902	5.460	1.654	0.99842
CVhigh-100%	0.859	0.141	1.483	3.719	1.557	0.99734
CVlow-100%	0.803	0.197	1.782	3.737	1.599	0.99768
SEVmed-100%	0.765	0.235	1.717	3.905	1.574	0.99774
EVhigh-100%	0.737	0.263	1.545	3.605	1.615	0.99771
EVlow-100%	0.810	0.190	2.148	5.824	1.556	0.99711
average	0.804	0.196	3.351	4.875	1.609	
<i>fix $T_{2M} = 5$ ms and $\beta = 1.6$:</i>						
CVhigh-0%	0.638	0.362	5.044	5	1.6	0.99592
CVlow-0%	0.784	0.216	5.025	5	1.6	0.99839
SEVmed-0%	0.893	0.107	4.689	5	1.6	0.99767
EVhigh-0%	0.936	0.064	5.020	5	1.6	0.99809
EVlow-0%	0.888	0.112	5.021	5	1.6	0.99817
CVhigh-100%	0.894	0.106	1.544	5	1.6	0.99648
CVlow-100%	0.865	0.135	1.863	5	1.6	0.99701
SEVmed-100%	0.825	0.175	1.794	5	1.6	0.99703
EVhigh-100%	0.825	0.175	1.642	5	1.6	0.99700
EVlow-100%	0.762	0.238	2.116	5	1.6	0.99697

The Equation 3.2 has been examined without extra boundaries (free fitting) on the five NRs at both unvulcanized ($\alpha = 0\%$) and fully vulcanized ($\alpha = 100\%$) status. The results are listed in the upper-half of Table 3.1. For all of the NRs, the most changed parameter between $\alpha = 0\%$ and 100% was T_{2R} . The compression parameter, β , was similar at both status around 1.6. The unvulcanized rubber shared similar value (close to 5 ms) between T_{2R} with T_{2M} ,

which is reasonable that the "rigid" components should be similar as the "mobile" ones before crosslinking.

To reduce the fitting variables, T_{2M} was fixed to the averaged value, 5 ms, assuming the dynamics of mobile segments before and after crosslinking were similar. The compression factor β was set to the average value of 1.6. In this way, the five fitting parameters had been reduced into three. Using the fixed T_{2M} and β for Equation 3.2, the fit still worked well since $R^2 > 0.996$ as seen in the lower-half of Table 3.1. A corresponding MATLAB code was constructed for the batch processing of the intensive NMR raw data sets, setting $T_{2M} = 5$ ms and $\beta = 1.6$ for Equation 3.2. The most drastically changed parameter along the vulcanization, T_{2R} , was selected as the tracking parameter from NMR experiment during vulcanization.

The comparison of T_{2R} of the five types of NR samples at fully cured status is shown in Figure 3.6. The results follows the experimental design, which high crosslink density formulation results in more rigid segments (lower T_{2R}) and vice versa for the same vulcanization system. The T_{2R} of SEVmed was in between of both types of systems. The T_{2R} of EV samples were higher than that of CV samples. This is attributed to the more rigid crosslinks, mono- and di-sulfidic bonds, generated from EV vulcanization, which is going to be discussed later.

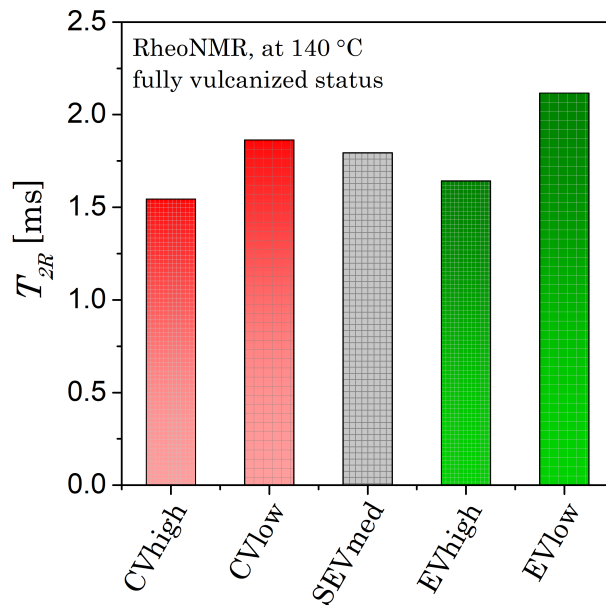


Figure 3.6: The comparison of T_{2R} of the five fully vulcanized NRs ($\alpha = 100\%$), from fitting with fixed parameters $T_{2M} = 5$ ms and $\beta = 1.6$.

3.2.2. Correlation: $1/T_{2R}$ vs G'

Following the above fitting procedure, the macroscopic elasticity, G' , reflected by rheology and the nanoscale mobility of the relative rigid chain segments determined from NMR was able to be tracked in parallel. The rigidity of the molecules was represented by the the relaxation rate, $1/T_{2R}$, in unit of kHz for a revolution time in ms. Such comparative results are shown in Figure 3.7 with the NR-CVhigh sample as an example. The time resolution for the rheological data was 6 s per data point, while for the NMR data was around 23 s. It is seen that the evolution curve of NMR, $1/T_{2R}(t)$, overlays well with $G'(t)$ in a proper scale of the vertical axis, although the NMR data was more noisy. Data of other samples can be found in Appendix B.

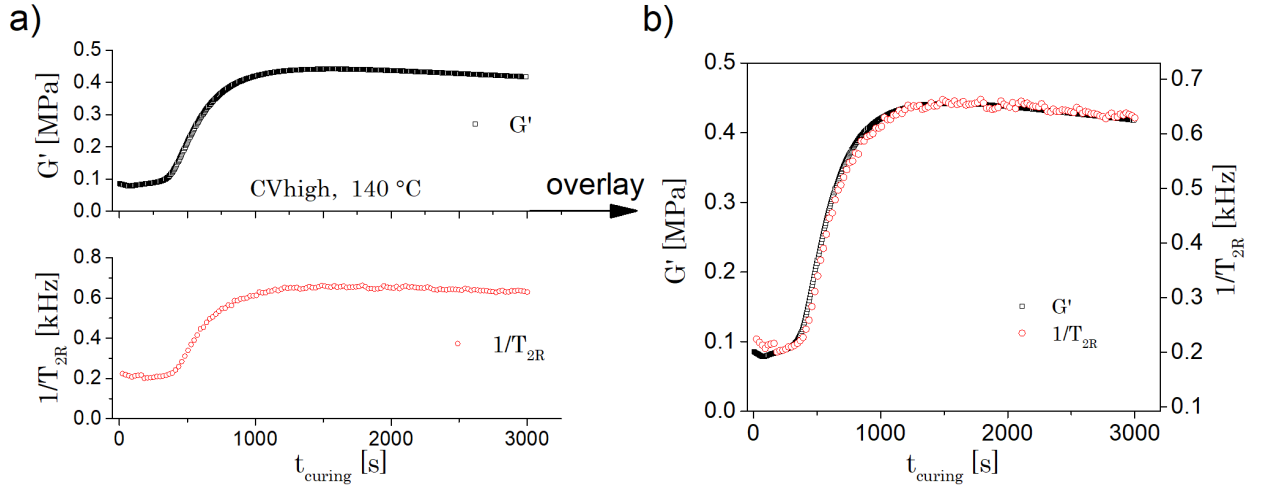


Figure 3.7: The evolution of G' and $1/T_{2R}$ of NR-CVhigh compared in parallel, which maintains good overlay.

The parallel data, from rheology and NMR, can be compared at the same time of the experiment to generate a correlation curve as Figure 3.8. To easy guide the eye, data only from curing degree between $\alpha = 0\%$ and 100% was plotted, without the heating softening and network reversion period. It was found that the segmental rigidity built up together with the macroscopic elasticity in a slope of 1.36 kHz/MPa as indicated in Figure 3.8.

However, the above correlation only took account of the rigid rubber segments for the NMR data, while the assignment of $1/T_{2M} = 5$ ms for the whole vulcanization process could be controversial. Meanwhile, other fitting parameters, I_R and I_M , were also interdependent to each other as shown in Figure 3.9 with the jump in intensity after the vulcanization induction period. Based on expectation, I_R should increase during vulcanization as the population of

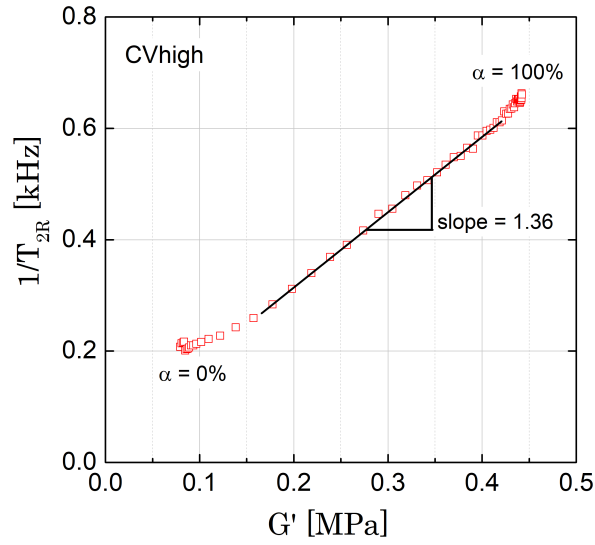


Figure 3.8: The $1/T_{2R}$ - G' correlation curve of NR-CVhigh from RheoNMR results.

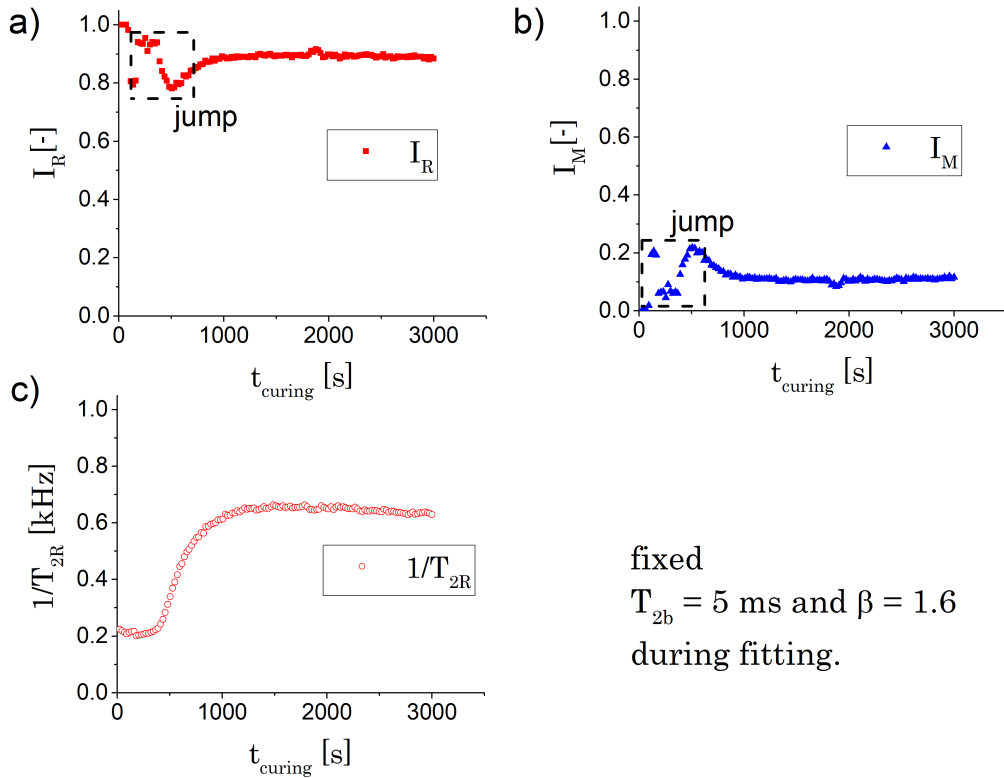


Figure 3.9: The jump of fitted I_R , I_M data near the induction period of vulcanization.

crosslinked segments grows, and I_M should decrease. Therefore, $1/T_{2R}$ is not single and only parameter that represents the dynamic status of overall segments in the sample.

3.3. Analysis via inverse Laplace transformation

An alternative way to analyze the transversal relaxation data from NMR is the inverse Laplace transformation (ILT). The multiple relaxation rates in the complex network, $1/T_2$, can be regularized via ILT with proper kernel function. Consequently, the distribution of $1/T_2$ [136] or similar form are deduced. Based on this distribution, the number averaged or logarithmic averaged value of $1/T_2$ [137] can be chosen as the single parameter to represent the molecular dynamic status of the whole rubber sample.

3.3.1. Inverse Laplace transformation

The Laplace transformation is named after Pierre-Simon Laplace (1749-1827, French scholar) [138], which can describe the exponential functions. The intrinsically embedded exponential functions in a decay signal can be deconvolved using the inverse Laplace transformation [139,140]. The path integral can be evaluated for any real value re in the region of convergence, described as

$$L^{-1}[F(s)](t) = \frac{1}{2\pi i} \int_{re-i\infty}^{re+i\infty} F(s) \exp(st) ds \quad (3.3)$$

However, this is an ill-proposed problem that prior assumptions are required to solve the function. This can be realized by the regularization with numerical computing program such as MATLAB.

The ILT approach has been successfully implemented on the strongly swollen networks such as hydrogels [141,142] with simple exponential function as kernel,

$$\frac{M(t)}{M_0} = \sum_i g_i \exp\left(-t \frac{1}{T_{2,i}}\right) \quad (3.4)$$

where g_i is the distribution amplitude of $1/T_{2,i}$. Consequently, the distribution of transversal relaxation rate $g_i(1/T_{2,i})$ was described. However, ILT based on above kernel can not converge properly for current NR samples, which are non-swollen and narrowly distributed networks covering a short range of $1/T_2$.

In quantitative terms, the transversal relaxation rate, $1/T_2$, depends mainly on the dipolar coupling strength of the surrounding spins [141]. The dipolar interaction from neighboring spins is controlled by the molecular motions. Thereby the relaxation path of the magnetization relies on the orientation autocorrelation function $C(t)$, see chapter 1.3.3. The spectral density

$J(\omega, \tau_c)$ from the T_2 relaxation curve (via Fourier transformation) can be connected to $C(t)$. According to the BPP model [79] described in Equation 1.30, $J(\omega, \tau_c)$ determines the T_2 relaxation via

$$\frac{1}{T_2} = \frac{3}{40} \frac{\gamma^4 (h/2\pi)^2}{r^6} [3J(\Delta\omega) + 5J(\omega_0) + 2J(2\omega_0)] \quad (3.5)$$

where $\Delta\omega$ is the dipolar coupling frequency width, typically 0–20 kHz.

In a crosslinked rubber network far above the glass transition temperature, the T_2 relaxation is sensitive to the slow motions of the crosslinked chain segments, i.e. the term of $J(\Delta\omega)$. As observed in many spin diffusion processes, it is not necessarily a pure Gaussian distribution but also includes both Markoffian and non-Markoffian distributions [143]. Based on the Anderson-Weiss approximation [144], the second moment M_2 in Equation 1.33 can be described by the residual dipolar coupling constant D_{res} ,

$$qM_2 = \frac{9}{20} D_{res}^2 \quad (3.6)$$

here D_{res} is in unit of rad/s and q is the residual part of the M_2 of dipolar interaction. For networks of rubber materials or elastomers, it is found [108] that with the limit of t in Equation 1.33, the term $-t/T_{2A} \rightarrow 0$. The relaxation function is reduced to

$$M_A(t) = M_{A0} \exp\left(-\frac{1}{2} q M_2 t^2\right) = M_{A0} \exp\left(-\frac{9}{40} D_{res}^2 t^2\right) \quad (3.7)$$

That is one possible reason that why only a simple exponential kernel does not fit the data of NR samples. Accordingly, the T_2 relaxation curve can be described by this Gaussian-type dipolar dephasing function. Thus Equation 3.4 was customized here as

$$\frac{M(t)}{M_0} = \sum_i g_i \exp\left(-\frac{9}{40} D_{res,i}^2 t^2\right) \quad (3.8)$$

for the ILT. In this way, the the relaxation data $I(t)$ of NRs will be translated into the distribution of residual dipolar coupling $g_i(D_{res,i})$, instead of the transversal relaxation rate.

3.3.2. Correlation: D_{res} vs G'

ILT based on Equation 3.8 was performed on the sets of NMR raw data in MATLAB code. For the xx4 echo time from 0.06 to 21 ms, accordingly, the ILT was set to a range of $D_{res,i} =$

0.01 to 50 krad/s in a logarithmic spacing. The results from NR-CVhigh as an example was shown in Figure 3.10. The unit of $D_{res,i}$ was transformed from [krad/s] into [Hz].

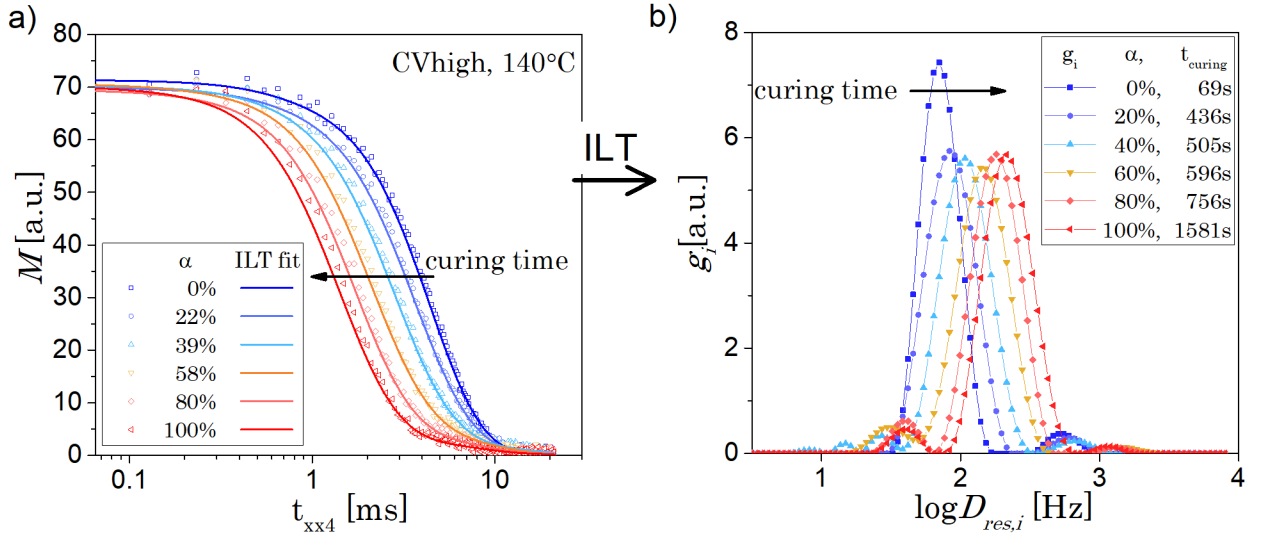


Figure 3.10: a) The raw NMR data of NR-CVhigh selected at different curing degrees and the fitting from ILT results. b) The corresponding distribution curves of $g_i(D_{res,i})$.

As expected for the shortening T_2 along the curing, the $D_{res,i}$ shifted towards a higher coupling frequency. At $\alpha = 100\%$, there were still small portion of the sample with low $D_{res,i}$. This might be the small molecules in the rubber sample, the left sol molecules and/or network detects.

From the distribution curve, we need to define a single representative parameter to correlate with the rheological properties. Saalwächter and coworkers have adapted probability functions $P(D_{res,i})$ [145], such as a Γ distribution or a lognormal distribution function to extract the median value. The median D_{res} is adapted to represent the chain dynamic of the network. However, those functions can not fulfill the distribution shape, in particular the small peaks or tails at high or low D_{res} range. In oil exploration industry, the logarithmic mean of T_2 distribution curves from a low-field NMR well-logging tools, $T_{2,log}$, were suggested to estimate the oil saturation [137, 146] in the porous rock cores. The $T_{2,log}$ correlated well to the oil viscosity in a defined power law relationship.

Another approach we could refer to is the number averaging in a normalized probability, such as the molecular weight calculation of macromolecules in size exclusion chromatography (SEC). The raw distribution curves from ILT translation, $g_i(D_{res,i})$, can be normalized in an

integral fashion by setting the area under the discrete curve as one.

$$\frac{g_i}{\sum_i g_i \times \Delta \log D_{res,i}} \Rightarrow P_i(\log D_{res,i}), \text{ so that } \sum_i P_i \times \Delta \log D_{res,i} = 1 \quad (3.9)$$

with $\Delta \log D_{res,i}$ is the spacing of the discrete $\log D_{res,i}$ and $P_i(\log D_{res,i})$ is the normalized distribution. The P_i can be seen as the "weight" portion for the coupling constants between $\log D_{res,i}$ and $\log D_{res,i+1}$. The averaged dipolar coupling strength, e.g. the number-averaged value $D_{res,n}$, can be received by

$$\begin{aligned} \log D_{res,n} &= \frac{\sum_i P_i}{\sum_i n_i} \\ &= \frac{\sum_i P_i}{\sum_i (P_i / \log D_{res,i})} \\ D_{res,n} &= 10^{\log D_{res,n}} \end{aligned} \quad (3.10)$$

with n_i seen as the "number" portion between $\log D_{res,i}$ and $\log D_{res,i+1}$. In this way, the single representative parameter of network dynamic is obtained.

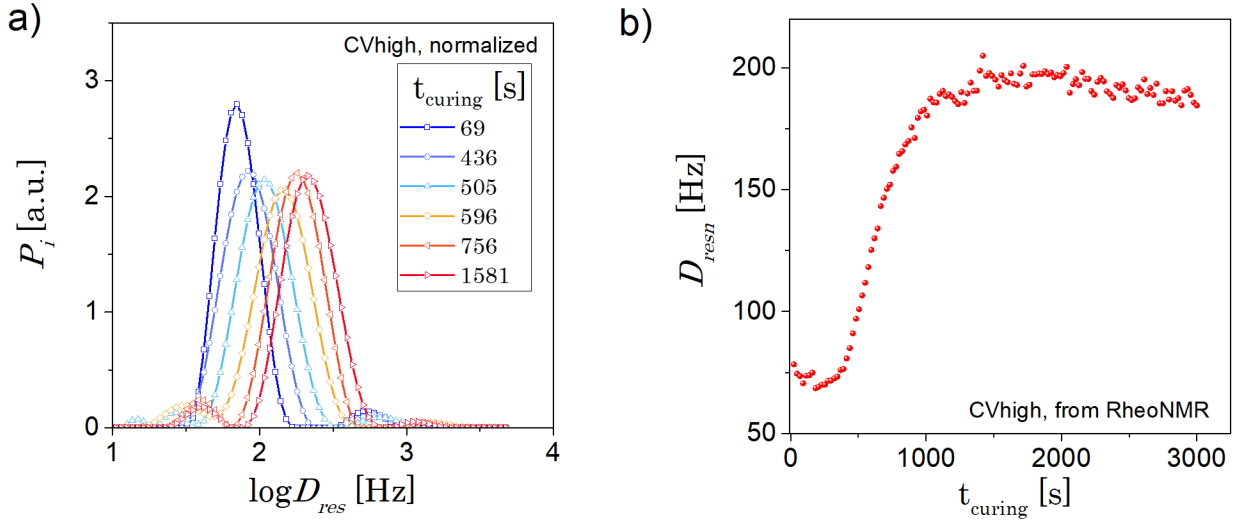


Figure 3.11: a) The normalized $\log D_{res,i}$ distribution of NR-CVhigh and b) the calculated number-averaged dipolar coupling constant $D_{res,n}$ along the vulcanization process.

Figure 3.11a is the normalized distribution curves of Figure 3.10b. The $D_{res,n}$ of NR-CVhigh during curing were calculated between $\log D_{res,i} = 1$ to 3.5 Hz, neglecting the curve tails. During crosslinking, the $D_{res,n}$ exhibited similar evolution trend as G' . The $D_{res,n}$ is considered as the overall averaged chain/segmental dipolar coupling strength of the sample. Therefore, this parameter can solely represent the molecular dynamics at the nanometer scale and be

used for the correlation to macroscopic properties.

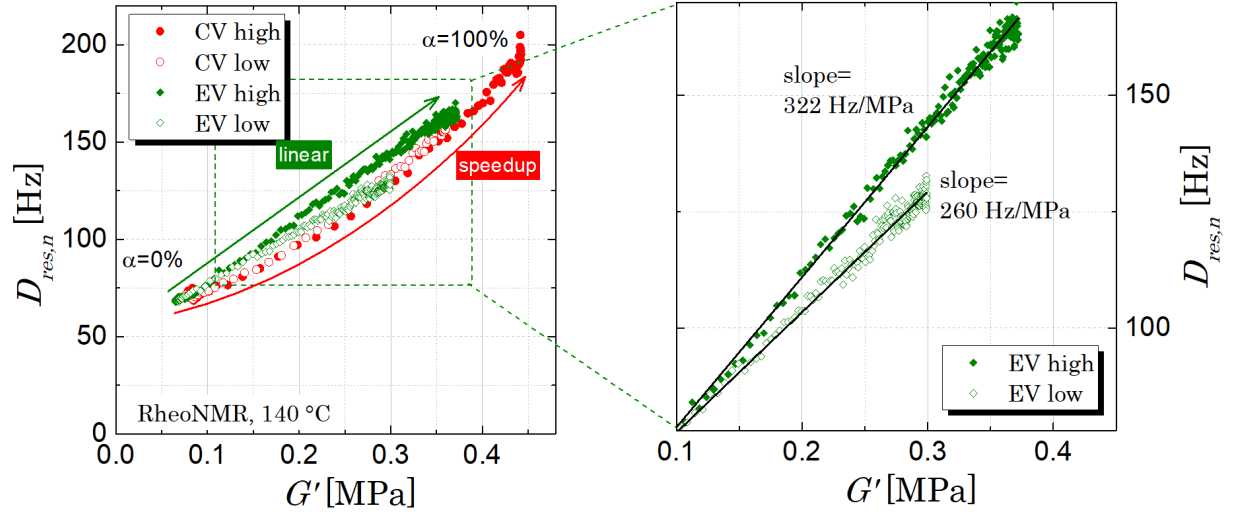


Figure 3.12: Correlation plot of the nanoscale chain dynamic parameter $D_{res,n}$ to the macroscopic elasticity of the conventional and efficient vulcanization process.

The correlation features of $D_{res,n}$ against G' of different NR samples are compared in Figure 3.12. Assuming that those rubbers were only forming ideal networks (no topological complex), the elastic moduli in rubber plateau G' would be proportional to the number of crosslinks per volume (the crosslink density ν) [39]

$$G' = \nu RT \quad (3.11)$$

where R is the universal gas constant and T is the temperature. Due to the growing number of crosslinks formed during vulcanization, G' increased. The $D_{res,n}$ reflects the level of local chain dynamics in both transient or permanent networks. The crosslinks generated permanent networks and induced more constraints to the segmental movement, leading to the increase of $D_{res,n}$. Therefore, $D_{res,n}$ is always positively associated with G' .

For NR with different vulcanization systems, $D_{res,n}(G')$ of EVs maintained a linear correlation, while $D_{res,n}(G')$ of CVs was nonlinear with a increased slope towards the curing plateau period (close to $\alpha = 100\%$). The formation of sulfidic crosslinks in EV and CV samples are illustrated in Figure 3.13. As introduced in Chapter 1.1.1 for the efficiency of utilizing sulfur to form networks, EV systems preferably generates mono-sulfidic crosslinks and in CV formulations the polysulfidic bridges dominate [25]. Furthermore, the low energy polysulfidic bonds tend to be modified into di-/mono-sulfidic bonds at high temperatures. A reasonable

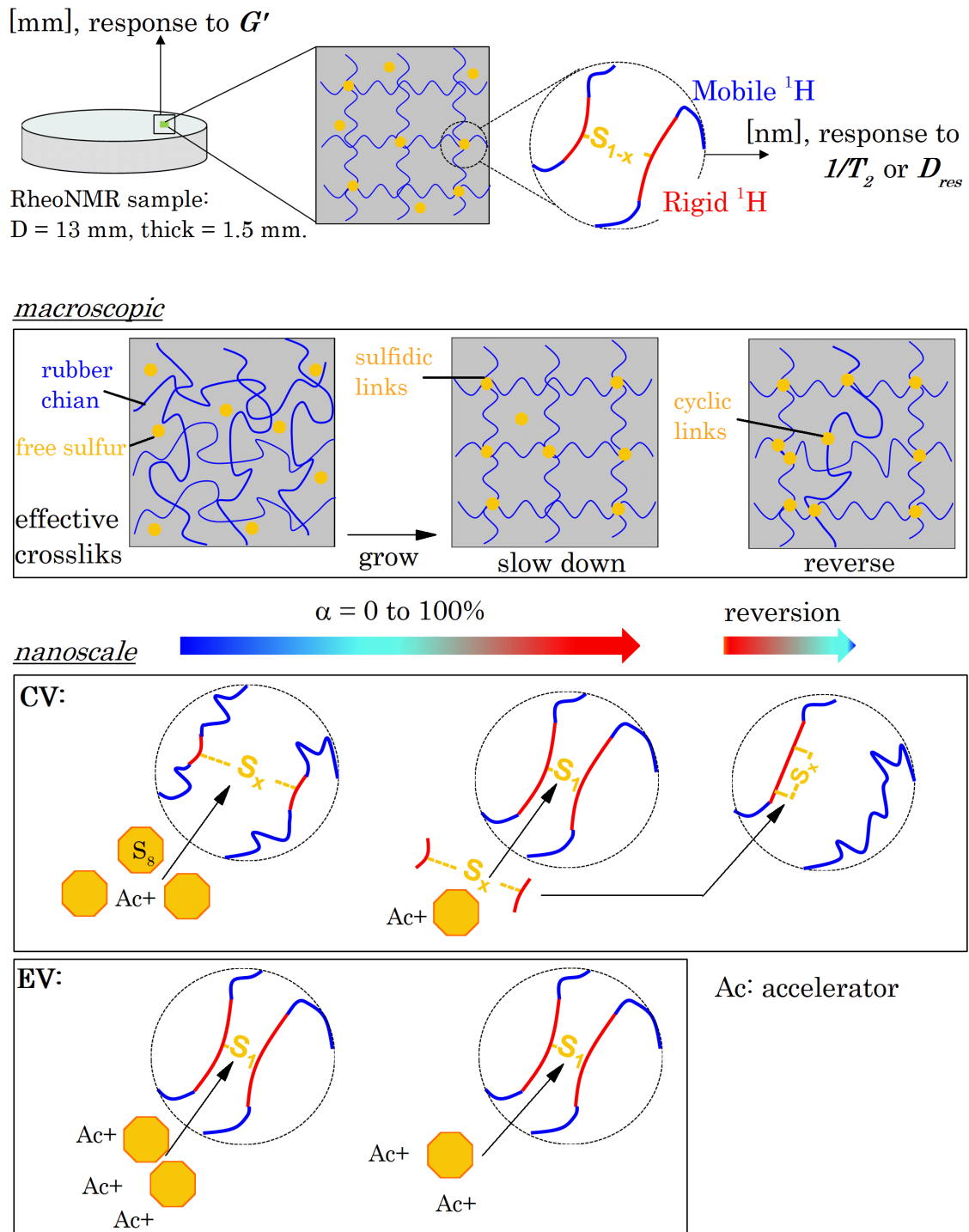


Figure 3.13: Schematic illustration for the build-up and modification processes of sulfidic crosslinks in conventional or efficient vulcanization systems and their influence on the nanometer scale polymer chain dynamics as well as on the macroscopic elasticity. This kinetic agrees with the results from RheoNMR.

hypothesis is that the protons from mono-sulfidic linked networks possess a higher $D_{res,n}$ than that from polysulfidic linked networks. Close to the curing plateau period, the polysulfidic bridges in CV samples were shortened into mono-sulfidic ones. Such reaction introduced highly rigid chain/segmental near the crosslinks rather than substantial numbers of effective crosslinks. In other words, it resulted in a more effective increase of $D_{res,n}$ than the growth of G' . With regards to the EV samples, only one type of crosslinks was built up gradually, the mono-sulfidic bonds. Therefore, in comparison with the development of G' , the increasing amplitude of $D_{res,n}$ in EV should be constant along the vulcanization, i.e. a linear correlation as expected.

Additionally, with similar final crosslink density, $D_{res,n}(G')$ of EV samples were always higher than their counterparts (NR-EVhigh vs NR-CVhigh, or NR-EVlow vs NR-CVlow). This phenomenon supports the hypothesis above that with the same number of effective crosslinks, mono-sulfidic bonds result in more rigid chains than the polysulfidic bonds, especially around the bonding points as the sulfur atom is not NMR active. For EV with only mono-sulfidic crosslinks, a high concentration of vulcanization chemicals increased the chain rigidity more effectively with 322 Hz/MPa of NR-EVhigh. While NR-EVlow possessed a slope of 260 Hz/MPa. However, this effect was not obvious for the CV samples as seen that the $D_{res,n}(G')$ of NR-CVhigh and NR-CVlow were similar.

The $D_{res,n}(G')$ correlation data of the reference sample in this work, NR-SEVmed, were plotted in Figure 3.14. The evolution line of NR-SEVmed fell in between that of the NR-EVhigh and the NR-CVhigh. Comparatively, the $D_{res,n}(G')$ of NR-SEVmed fluctuated more. It implies that both polysulfidic and short bridges were formed in the SEV system, generating both relative rigid and relative mobile networks along the vulcanization course.

The speculation of the buildup and modification of sulfidic crosslinks in rubber vulcanization agrees with the results from ^{13}C NMR spectroscopy or selective cleavage of the crosslinks by solvent in literature [25]. In this chapter, the kinetics of the crosslinks buildup and its influence on both nanometer scale molecular dynamics and macroscopic scale dynamic elasticity were observed and correlated. With the correlation curves of $D_{res,n}(G')$, the differences in crosslink structures and the evolution process in varying NR vulcanization systems were confirmed. Those structures existing in NRs would be supportive for later aging analysis.

With respect to the analysis shown above, the combined setup RheoNMR has assured the unique validity of correlation with the concurrent responses to rheology and NMR relaxometry from NR crosslinking process. However, in case of the separately conducted measurements on

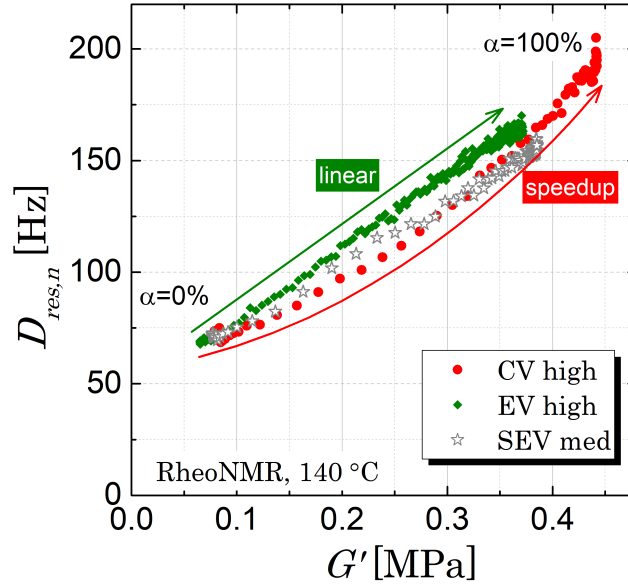


Figure 3.14: Correlation plot of SEVmed in comparison with EVhigh and CVhigh.

rheometer and NMR analyzer, the plot of $D_{res,n}$ as a function of G' would be controversial due to the nonidentical experimental conditions: 1) there would be errors for the mass and chemical ingredients from different specimens; 2) the loading time of specimen before starting the tests may differ; 3) the environment for the crosslinking reaction varies, including the thermocouples in the rheometer oven and in the NMR core, the air or nitrogen flow around the specimen and heating conductivity through the specimen. With those challenges and error sources in the separated methods, the differences between the NR samples in Figure 3.12 and Figure 3.14 might be smeared out or be arbitrary.

Moreover, the evolution time in the raw data, t_{xx4} , was in linear spacing for the ILT into $D_{res,i}$ (or $T_{2,i}$) [Hz] on logarithmic scale. The instability of the first few data points at short t_{xx4} may cause strong calculation artifacts in the resulting distribution curve of $g_i(\log D_{res,i})$, such as the small peaks at high rate (see Figure 3.11a, at logarithmic 2.5–3.5 Hz). A possible improvement is to manipulate the raw $M(t_{xx4})$ data into logarithmic spacing before ILT. Firstly, fit the raw data with Equation 3.2 with a high quality ($R^2 > 0.997$ as seen in Table 3.1). Secondly, translate the data into logarithmic spacing for t_{xx4} from the fitting results. Finally, submit the manipulated data for ILT process. It is worth to compare the $g_i(\log D_{res,i})$ results from this way of data treatment with the non-manipulated ones.

4. Hot-Air Aging

In this chapter, the FT-rheology and ^1H DQ-NMR as recently developed techniques were validated on the NR vulcanizates before aging. The rheological nonlinearity of crosslinked NR network as well as the filler network were quantified directly via FT-rheology. Using DQ-NMR, the rubber network density, the mesh size distribution as well as the amount of defects of the network were revealed. Thereafter, the effect of high temperature aerobic aging on NR vulcanizates were investigated with the respects of rheological nonlinearity and network structures.

4.1. Validation of the characterization protocol

The NR vulcanizates in unaged status were used to examine the feasibility of FT-rheology and the DQ-NMR on crosslinked rubbers. Compared to polymer melts [57,61] and rubbers in unvulcanized status [9,10,63], FT-rheology is rarely used for rubber vulcanizates so that few referential experimental procedures and results can be found in literature. In the following chapter, through FT-rheology of NR vulcanizate, the rheological nonlinearity characters of rubber network as well as filler network are going to be unveiled. In Chapter 4.1.3, the data treatment process of DQ-NMR for NR vulcanizate is going to be demonstrated. Since then, the characterization protocol is established.

4.1.1. FT-rheology of NR vulcanizate

Strain sweep measurements were performed on the NR vulcanizates with a rectangular torsion fixture at room temperature and $\omega_1/2\pi = 1$ Hz from low to high strain amplitudes. Both linear and FT-rheological results were obtained as shown in Figure 4.1. The subscript "1" on the frequency refers to the basic frequency for exciting the sinusoidal strain.

For linear rheological properties, the G' and $\tan\delta$ of the unfilled NR (NR1) were independent of the strain amplitude in a long range, i.e. a broad linear viscoelastic (LVE) regime. Distinctively, the G' of the 50 phr N339 filled NR (NRCB1) exhibited strong strain softening above $\gamma_0 = 0.2\%$, known as the Payne effect [49,147]. This is commonly observed in reinforcing filler filled composites. The mechanical loss factor, $\tan\delta$, was also increased by the fillers and developed a maximum at around $\gamma_0 = 10\%$. The average values of the elastic moduli and loss factor in LVE regime, G'_0 and $\tan\delta_0$, as indicated by the solid lines in Figure 4.1, were selected to represent the linear rheological properties for the aging analysis of NR vulcanizates afterwards.

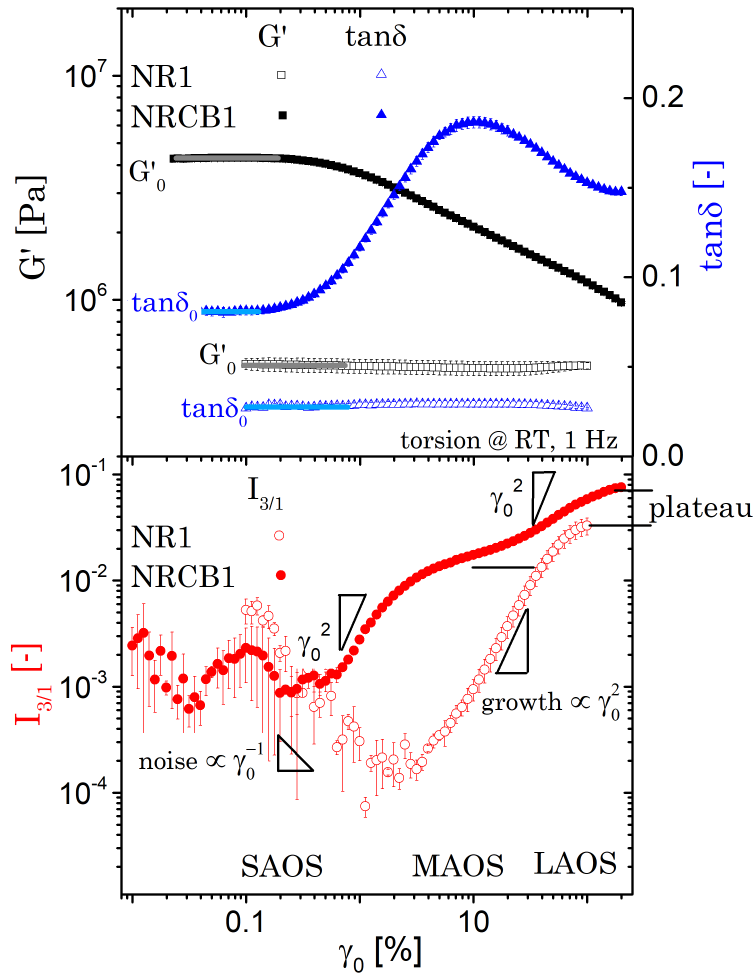


Figure 4.1: The strain dependence of the linear and FT-rheological parameters of NR vulcanizates with and without 50 phr CB (NRCB1 and NR1) obtained from ARES-G2 oscillatory torsion at frequency of $\omega_1/2\pi = 1$ Hz and room temperature (RT).

There are several contributions to the storage moduli at low strain amplitude, according to

the dynamic network model for the fillers [148] or the dynamic adhesion model for the rubber chains adsorbed on the filler surface [149]. The origins could be described in Figure 4.2 in a semi-logarithmic plot. The strain independent components include the plateau storage modulus of crosslinked rubber, G_N^0 , and the hydrodynamic reinforcement from the rigid fillers, following the Einstein equation for a suspension system $G' = G_N^0(1 + 2.5\phi)$. The strain softening behavior originates from the mechanically instable filler-filler interaction and the deformation or sliding of the rubber chains on the immobilized rubber surface [7, 150, 151].

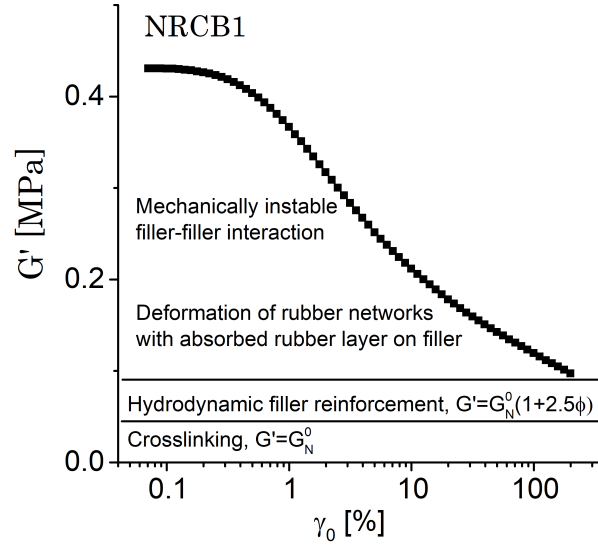


Figure 4.2: The storage moduli consists the contributions [151] from the reinforcement and crosslinking effect in filled rubber vulcanizate, according to the concept of dynamic de- and re-agglomeration of filler networks [7, 148] and immobilized rubber layer on the filler surface [150, 152]. Some components exhibit strain softening, i.e. the Payne effect.

Conventionally, the rheological nonlinearity is quantified in an indirect way via e.g. the drop of G' at specified strain amplitude range. In present work, the direct quantitative parameters from FT-rheology were employed, such as the relative intensity of third harmonics, $I_{3/1}$, as explained in Chapter 1.2.2. Following the theory of FT-rheology and the observations from other polymeric materials, the $I_{3/1}(\gamma_0)$ of NR vulcanizates also passed a noise region at small amplitude oscillatory strain (SAOS) as indicated in Figure 4.1. The noise dominated data dropped with a slope of -1 in the logarithmic plot. Afterwards, $I_{3/1}$ increased quadratically ($I_{3/1}(\gamma_0) \propto \gamma_0^2$) at the medium amplitude oscillatory strain (MAOS) until reaching a plateau or level-off at large amplitude oscillatory strain (LAOS). Compared to the unfilled NR, the introduction of CB network in NRCB1 increased $I_{3/1}$ drastically in MAOS region. Additionally, there were two quadratic growth regions of $I_{3/1}(\gamma_0)$ in NRCB1.

In SAOS, only the noise dominates the intensity of $I_{3/1}$ with a relationship of $I_{3/1}(\gamma_0) \propto \gamma_0^{-1}$. Assuming the level of noise, L_{noise} , is a constant for the same rheometer on similar materials, one can deduce

$$I_{3/1}(\gamma_0) = \frac{L_{noise}}{\gamma_0} \text{ in SAOS} \quad (4.1)$$

After the SAOS region, $I_{3/1}(\gamma_0)$ grows quadratically in MAOS and levels off in LAOS. To phenomenally describe this behavior, two types of sigmoidal functions with squared exponents were proposed for a pure polymer network:

$$\text{Type I: } I_{3/1}(\gamma_0) = \frac{L_{noise}}{\gamma_0} + n_P \frac{(\gamma_0/\gamma_{cP})^2}{(1 + \gamma_0/\gamma_{cP})^2} \quad (4.2)$$

$$\text{Type II: } I_{3/1}(\gamma_0) = \frac{L_{noise}}{\gamma_0} + n_P \frac{(\gamma_0/\gamma_{cP})^2}{1 + (\gamma_0/\gamma_{cP})^2} \quad (4.3)$$

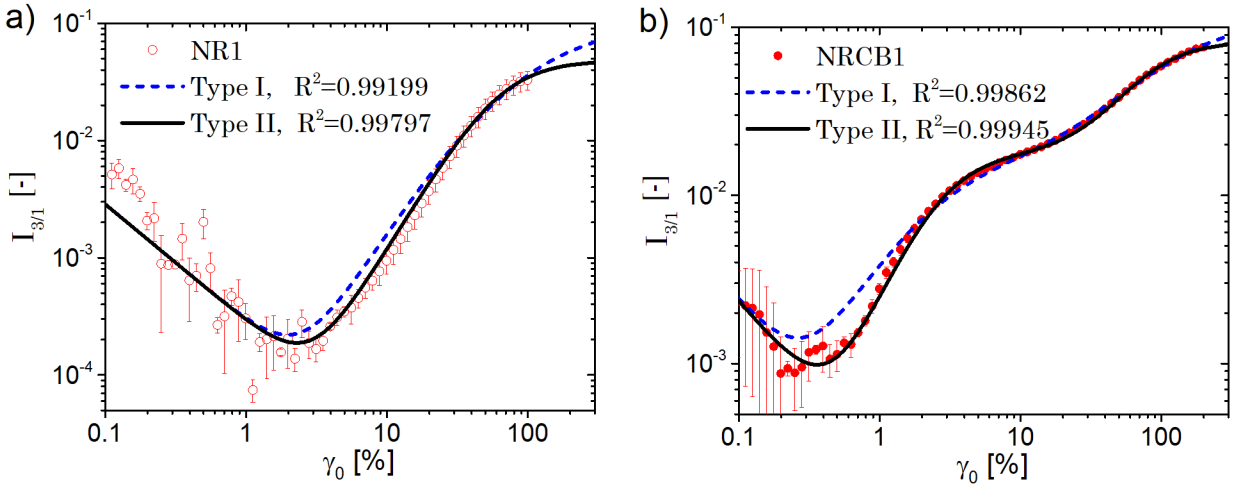


Figure 4.3: The fitting performance of two types of quadratic growth function for $I_{3/1}(\gamma_0)$ with limiting plateau on a) unfilled and b) CB filled NR vulcanizates.

While for NRCB1 sample, there are two types of networks, the filler network and polymer network, with two quadratic growth regions of the $I_{3/1}(\gamma_0)$. It leads to the idea that the $I_{3/1}(\gamma_0)$ of a filled system could be seen as the superposition of above functions with two critical strain amplitudes,

$$\text{Type I: } I_{3/1}(\gamma_0) = \frac{L_{noise}}{\gamma_0} + n_F \frac{(\gamma_0/\gamma_{cF})^2}{(1 + \gamma_0/\gamma_{cF})^2} + n_P \frac{(\gamma_0/\gamma_{cP})^2}{(1 + \gamma_0/\gamma_{cP})^2} \quad (4.4)$$

$$\text{Type II: } I_{3/1}(\gamma_0) = \frac{L_{noise}}{\gamma_0} + n_F \frac{(\gamma_0/\gamma_{cF})^2}{1 + (\gamma_0/\gamma_{cF})^2} + n_P \frac{(\gamma_0/\gamma_{cP})^2}{1 + (\gamma_0/\gamma_{cP})^2} \quad (4.5)$$

where the prefactor n is the limiting nonlinearity at the plateau and γ_c is the critical strain amplitude to excite nonlinear response. The subscripts, "F" and "P", stand for the filler- and polymer-involved networks, respectively.

The fitting quality of two types of sigmoidal functions on NR1 and NRCB1 are compared in Figure 4.3. The fit line of Type I deviated more from the experimental data thus the Type II function was more suitable to describe $I_{3/1}(\gamma_0)$. Therefore, Equations 4.3 and 4.5 (both Type II) were selected to fit the $I_{3/1}(\gamma_0)$ data of unfilled and filled NR vulcanizates.

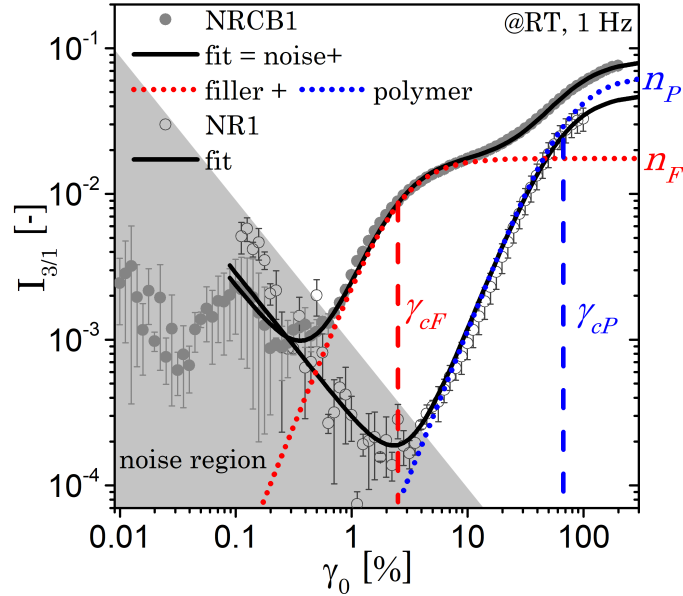


Figure 4.4: Fitting of Equations 4.3 and 4.5 on unfilled and filled NR vulcanizates with critical strains γ_{cF} , γ_{cP} and superposition of the limiting rheological nonlinearity n_{cF} , n_{cP} .

Table 4.1: FT-rheology fitting parameters for crosslinked NR network with and without filler network in Figure 4.4.

Sample	Filler network		Polymer network	
	n_F	γ_{cF}	n_P	γ_{cP}
NR1	n.a.	n.a.	0.049	64%
NRCB1	0.0176	2.5%	0.065	75%

The critical strain amplitudes and the limiting rheological nonlinearity are illustrated in Figure 4.4 with the fitting results listed in Table 4.1. The noise region has been colored in

gray background, indicating the data from this zone is out of interest for analysis.

The fit line for NRCB1 was decomposed into two dotted lines, representing the filler network in red and polymer network in blue, respectively. The critical strains were indicated as well in dashed lines. Neglecting the noise contribution, at critical strain amplitude $\gamma_0 = \gamma_c$, the rheological nonlinearity is

$$I_{3/1}(\gamma_c) = n \frac{(\gamma_c/\gamma_c)^2}{1 + (\gamma_c/\gamma_c)^2} = \frac{n}{2} \quad (4.6)$$

indicating the network has reached half its limiting nonlinearity. For the same polymer matrix, it is found that NR1 and NRCB1 share a critical strain amplitude at $\gamma_{cP} \approx 70\%$ and similar limiting nonlinearity for the polymer term, n_P . The critical strain amplitude of filler network is much lower, at $\gamma_{cF} \approx 2.5\%$. In the following chapters within the NR aged samples, the half-limiting rheological nonlinearities at γ_c , $I_{3/1}(\gamma_0=2.5\%)$ and $I_{3/1}(\gamma_0=70\%)$, were selected to evaluate the rheological nonlinearity of filler and polymer networks, respectively.

In summary for the proposed model to describe the $I_{3/1}(\gamma_0)$ of NR vulcanizates with and without fillers:

- In small amplitude oscillatory strain (SAOS), $I_{3/1}$ is dominated by noise. The $I_{3/1}(\gamma_0)$ decreases in relationship of γ_0^{-1} with a constant prefactor, L_{noise} , which is the noise level of the experiments (the sensitivity of the rheometer and the moduli of the sample).
- In medium amplitude oscillatory strain (MAOS), the $I_{3/1}(\gamma_0)$ starts to increase quadratically. At the critical strain amplitude, γ_c , the growth of $I_{3/1}(\gamma_0)$ start to level-off. The γ_c can be seen as the characteristic strain amplitude, at which the rheological nonlinearity of the network reaches the half of the limitation, $\frac{n}{2}$.
- In NR filled with reinforcing fillers, two critical strain amplitudes are specified for the filler network and polymer network as γ_{cF} and γ_{cP} . Their $I_{3/1}(\gamma_0)$ terms are linearly superposed, with the γ_{cF} being smaller than γ_{cP} .
- In large amplitude oscillatory strain (LAOS), the $I_{3/1}$ of the filler and polymer networks reach their corresponding limitations as plateaus, n_{cF} and n_{cP} .
- With regards to the NR vulcanizates in the presented work, it is found that $\gamma_{cF} \approx 2.5\%$ and $\gamma_{cP} \approx 70\%$. For the aging results in following chapters, the $I_{3/1}$ at those critical

strain amplitudes are chosen as the direct indicators of the rheological nonlinearity of the filler network and polymer network, respectively.

The assumption of the critical strain amplitude and the limitation of rheological nonlinearity have been verified on other networks systemically as follows.

4.1.2. $I_{3/1}(\gamma_0)$ of filled networks

Two growth regions in $I_{3/1}(\gamma_0)$ of filled systems have also been observed in unvulcanized rubbers with reinforcing fillers, such as CB or silica as shown in Figure 4.5 and Table 4.2 [9,10]. One group of SBR were filled with same type of filler, the N339 carbon black, while increasing the filling ratio in volume, ϕ . Another series of SBR were filled with the same amount of silica (50 phr) but tuned the filler-filler interaction by surface modification via silane. The surface of silica particles are covered by numerous silanol groups, which is different from the surface of CB. This leads to strong polar and hydrophilic characteristics. In consequence, the interparticle interaction of silica is strong. During the mixing process, an alkyl silane such as 3,3'-tetrathioisobutyltriethoxysilane is commonly blended into the compounds to functionalize the particle surface via a condensation reaction with the silanol groups. This reduces the hydrogen bonding thus, the strength of inter-particles interaction of silica [153,154].

Interestingly, the $I_{3/1}(\gamma_0)$ in MAOS (near the γ_{cF}) was sensitive to both the volume fraction of the filler and the strength of filler-filler interaction as indicated by the arrows in Figure 4.5. The increased filling ratio, ϕ , of N339 resulted in higher $I_{3/1}$ at strain amplitude around $\gamma_{cF} = 42\text{--}91\%$ with the increase of n_F from 0.059 to 0.11. However, the limiting nonlinearity of the rubber matrix, $n_P = 0.15\text{--}0.16$, was stable for the same polymer matrix. The n_F of silica filled SBR in Figure 4.5b decreased as a function of silane concentration because the filler-filler interaction had been suppressed by the silanization. The limiting nonlinearity of the rubber network, n_P , of silica filled SBR increased as the filler-polymer interaction was enhanced through the silanization. In summary, the build-up of rheological nonlinearity in filled rubbers occurs at two distinctive strain amplitudes, which correlates to the dimension and strength of filler- and polymer-involved networks as the functions proposed before.

As suggested by Kraus [7,148], the carbon black aggregates or the silica clusters in the rubber matrix can be seen as soft spheres with the arms entangled each other. During the dynamic deformation, the de-agglomeration and re-agglomeration reaches equilibrium thus

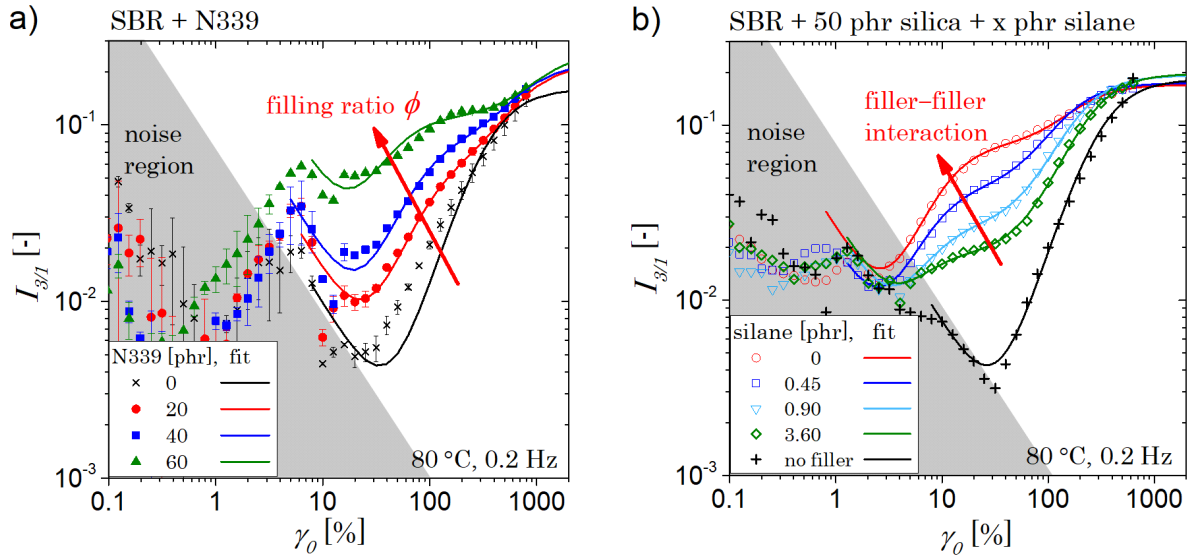


Figure 4.5: $I_{3/1}(\gamma_0)$ of unvulcanized SBR filled with a) increasing filler fraction in volume (filling ratio), ϕ , of CB N339 from 0 to 60 phr (data from Schwab [155]) and b) fixed volume fraction of silica, 50 phr, but decreased filler-filler interaction by silanization (the dosage of silane was 0–3.60 phr, data from Nie [10]). The solid lines are fitting by Equations 4.3 or 4.5.

Table 4.2: The changing of FT-rheological parameters for the filler filled SBR rubbers in Figure 4.5.

FT-rheological parameter	n_F	γ_{cF}	n_P	γ_{cP}
a) N339: 20→60 phr filler network volume ↑ changing trend:	0.059→0.11	91%→42%	0.15–0.16	355%→1000%
b) silane: 0.45→3.60 phr filler-filler interaction ↓ filler-polymer interaction ↑ changing trend:	0.077→0.018	9.7%→6.1%	0.093→0.18	230%→140%

the dynamic moduli as a function of the strain amplitude $G^*(\gamma_0)$ can be simulated. In the Kraus model or its modified version [156], there is also one critical strain amplitude, γ_c . It is the strain amplitude at which the tear down rate and reform rate of filler networks stay in equilibrium, i.e. similar physical meaning as the γ_{cF} in MAOS [10]. Nevertheless, in those models, only the filler-involved network is taken into consideration, not the larger deformation of polymer network in LAOS close to γ_{cP} . However, the polymer-involved network also exhibit strain softening and rheological nonlinearity in LAOS. It would be reasonable to propose two distinct strain amplitudes for the structural changes of both the filler and polymer networks

in the composites as sketched in Figure 4.6. In the rubber matrix, the filler aggregates or clusters can be considered as "soft spheres" with effective radius of the branches, R_{eff} .

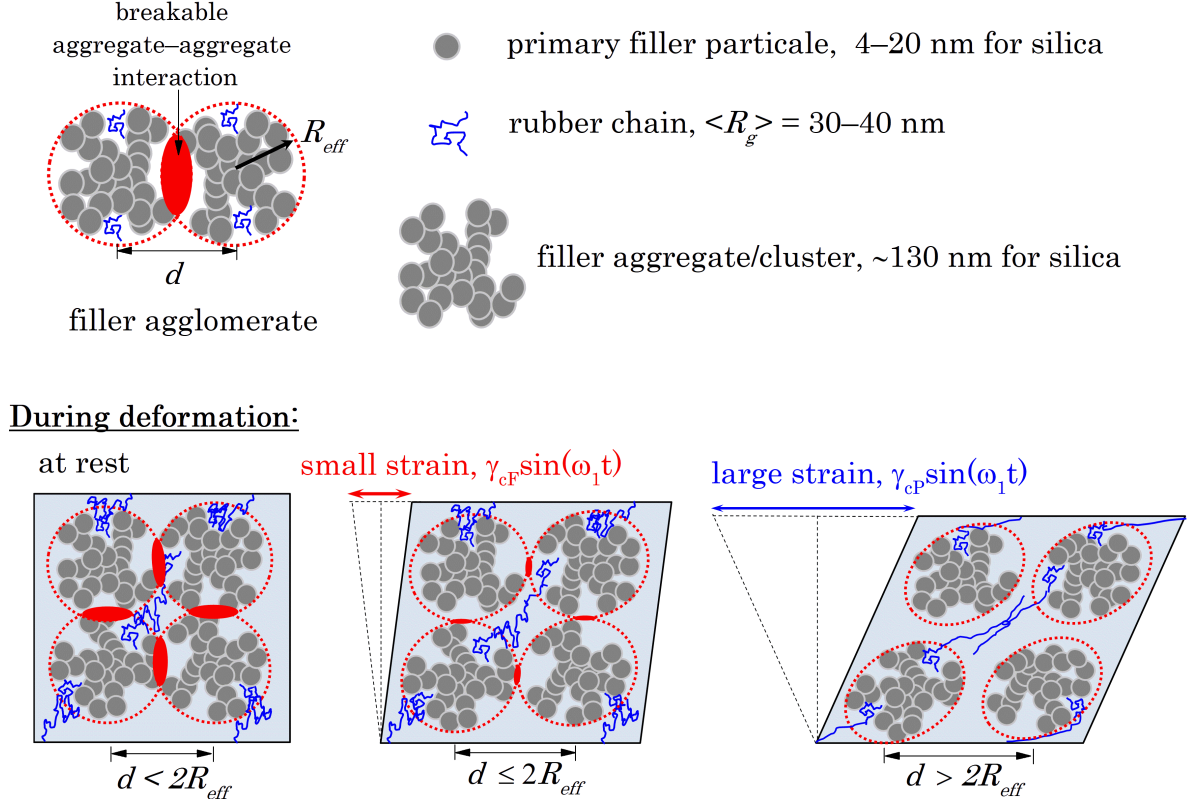


Figure 4.6: Proposed structural status of rubber chains and agglomerated filler aggregates or clusters at rest, at small and large oscillatory strain deformation. The size of silica particle and the radius of gyration, $\langle R_g \rangle$, of SBR are from literatures [157–159].

At rest, the aggregates or clusters are in favor of agglomeration in the rubber matrix within a distance of $d < 2R_{eff}$. The interaction between the soft spheres are represented by the overlay area in red in Figure 4.6. Once there is an external dynamic strain applied on the material, it is the agglomerate that will firstly deform without tearing down, while the rubber networks are still in a relaxed form. At this small strain amplitude, the deagglomeration and reagglomeration of the filler network produces rheological nonlinearity due to the nonlinear particle-particle interaction [160]. Under large dynamic deformation, the agglomerate will be totally broken down when $d > 2R_{eff}$. Then the entangled polymer network starts to respond by changing the chain orientation and conformation. In this region, the polymer-involved network superpose the filler network to generate rheological nonlinearity.

Equations 4.3 and 4.5 are also applicable for other model networks as shown in Figure 4.7,

including the physically bonded transient networks or the chemically linked permanent networks. For the polydispersed SBR, the function was fitted by order of $k < 2$ instead of quadratic, which is going to be discussed later. Evidently, for materials possessing different grades of networks, the critical strain amplitudes to build up the $I_{3/1}$ vary. This might be relevant to the size and the deformability of the network.

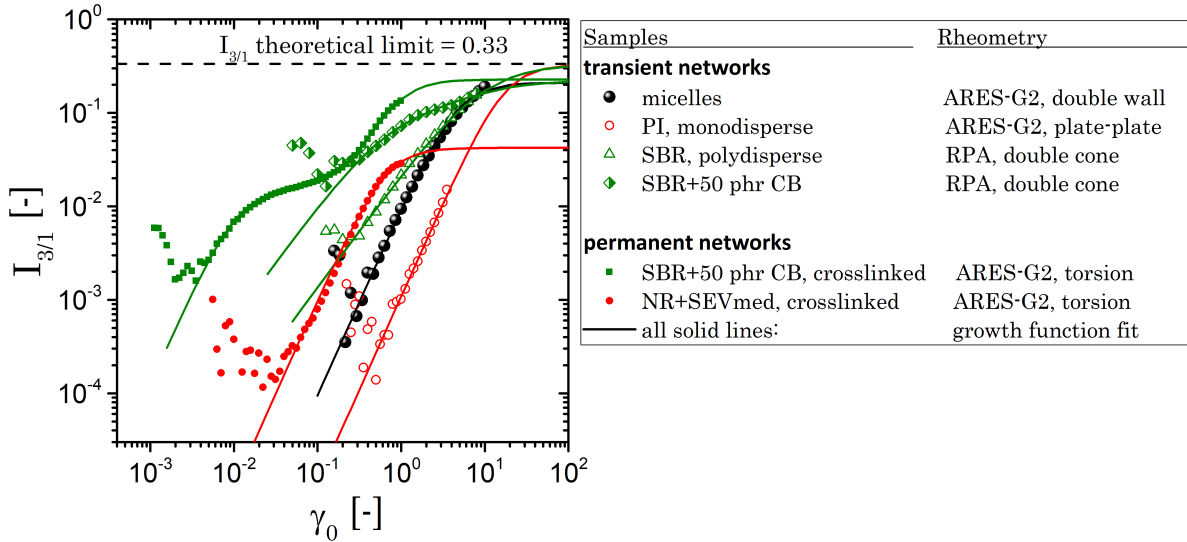


Figure 4.7: The comparison of $I_{3/1}(\gamma_0)$ for materials possessing different types of networks. This includes the transient networks: micelles [60], polyisoprene melts (PI) [61] and unvulcanized SBR rubber without/with filler [155]; permanent networks: vulcanized SBR with filler or NR1 in this work. The solid lines are fitting from Equations 4.3 and 4.5 without the term for noise.

The structure of a 3D network can be simplified as a square mesh with four fixed joints as seen in Figure 4.8a. The elements on the four joints are considered to be nondeformable with a radius of r . The four elements are interacted or bonded by a maximum contour length of L as the red links of the square mesh. Beyond the distance of L , there is no or neglectable interactions between the two elements. Therefore, the mesh would be a square in a side length of $2r + L$. The r can be seen, for example, as the radius of an aggregate of CB, the radius of the nondeformable filler particles, the radius of the micelles, the entangled section of the polymer melts or the crosslinks in the rubber vulcanizates.

During the fabrication of CB [35], the primary particles fused together as an aggregate. As proposed in Figure 4.6, the aggregate can not be broken down during deformation with the rubber matrix, which may be seen as nondeformable or close to. While many aggregates entangled to each other to form a network mesh as an agglomerate, with an effective radius

$R_{eff} \approx r$. The maximum distance of effective interaction L between the aggregates in one agglomerate mesh is the maximum width of the red area in Figure 4.6. Similar concept could be employed to the micelles in the emulsion. During equilibrium of a specified emulsion, the size of micelles and the maximum effective interaction distance is almost fixed.

For a crosslinked rubber network, the status in Figure 4.8a can be seen as the fully expansion of the rubber network before deformation. It is hard to define the radius of the nondeformable elements r in the mesh, however, the mesh side length $2r + L$ can be seen as the contour length of the rubber chain segments between the crosslinks, which the molecular weight is M_c .

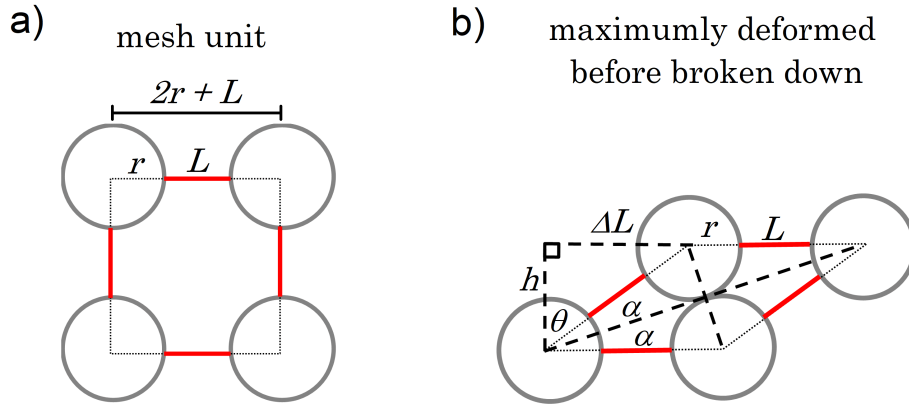


Figure 4.8: a) A simplified model square mesh in a 3D network with nondeformable elements, in radius of r , at four joints. The elements are bonded with an interaction contour length of L . b) The position of the four elements at maximum strain amplitude γ_{max} of the bonded network (before the break of the effective interactions with maximum length of L).

Taking the whole mesh as a unit body, the maximum deformation before breaking down the bonds would be the scenario depicted in Figure 4.8a. The mesh is deformed into a diamond shape, with two of the unlinked elements touching each other. The maximum strain can be derived as

$$\gamma_{max} = \frac{\Delta L}{h} = \tan\theta \quad (4.7)$$

To calculate the angle of θ , one can rely on the acute angle of the diamond, 2α , since

$$2\alpha + \theta = 90^\circ \quad (4.8)$$

and

$$\sin\alpha = \frac{r}{2r + L} \alpha = \arcsin\left(\frac{r}{2r + L}\right) \quad (4.9)$$

Therefore,

$$\begin{aligned}
 \gamma_{max} &= \tan\theta \\
 &= \tan(90^\circ - 2\alpha) \\
 &= \tan \left[90^\circ - 2\arcsin \left(\frac{r}{2r + L} \right) \right]
 \end{aligned} \tag{4.10}$$

When $r \gg L$,

$$\frac{r}{2r + L} = \frac{1}{2} \tag{4.11}$$

leading to $\alpha = 30^\circ$

$$\gamma_{max} = \tan\theta = \tan(90^\circ - 2\alpha) = \tan 30^\circ = 57\% \tag{4.12}$$

Assuming that the carbon black agglomerates are in the case as above, i.e. $r \gg L$ and $\gamma_{max,F} = 57\%$, from the $\gamma_{cF} = 2.5\%$ of NRCB1 one can deduce the maximum strain amplitude to break down the filler network of CB as

$$\gamma_{max,F} \approx 20\gamma_{cF} \tag{4.13}$$

When $r \ll L$,

$$\gamma_{max} \rightarrow \infty \tag{4.14}$$

When $r = L$,

$$\frac{r}{2r + L} = \frac{1}{3} \tag{4.15}$$

leading to $\alpha = \arcsin(1/3) = 19.47^\circ$, and

$$\gamma_{max} = \tan 2.83^\circ = 283\% \tag{4.16}$$

If the relationship in Equation 4.13 is applicable to the mesh grid of crosslinked NRs, with $\gamma_{cP} = 70\%$ one can get the maximum strain amplitude of the crosslinked polymer network in NRCB1

$$\gamma_{max,P} = 20 \times 70\% = 1400\% \tag{4.17}$$

giving

$$\tan\theta = 14, \theta = 85.914^\circ, \alpha = 2.043^\circ \quad (4.18)$$

$$\frac{r}{2r + L} = \sin 2.043^\circ = 0.03556 \quad (4.19)$$

This yields

$$L \approx 26r \quad (4.20)$$

for the crosslinked NR networks.

The above discussion for the growth function of $I_{3/1}(\gamma_0)$ in Equations 4.3 or 4.5 is based on the assumption that each elements or particles in the mesh is linked to others by effective interactions. However, for fillers with little interparticle interaction, such network mesh does not exist or at least is not obvious. Those fillers are non-reinforcing fillers and can only expand the volume of the polymer matrix. The $I_{3/1}(\gamma_0)$ of polymer matrix with such fillers would behave differently from reinforcing fillers as proven by the results in Figure 4.9.

The mono-dispersed PS melts with a molecular weight $M_n = 90$ kg/mol (PS90k) were filled with crosslinked polystyrene (PS) beads (in spherical shape) in a diameter of 50–100 μm . The PS beads were lab-synthesized by Rantszch and Klein [161] via emulsion polymerization in a double-walled cylindrical glass reactor (Rettberg GmbH, Gottingen, Germany). Distilled styrene, divinylbenzene and azobisisobutyronitrile (AIBN) were added consecutively to the aqueous phase with hydroxypropyl cellulose. The mixture was stirred at 300 rpm to form an emulsion, and polymerized for 3 h at 70 $^\circ\text{C}$ under reflux. The product was sonicated in a beaker for 30 min, decanted, washed several times with deionized water to remove all the stabilizer, then dried at 80 $^\circ\text{C}$ under vacuum overnight. The micro-particles in powder form were sieved into several grades with different particle size. The $D = 50\text{--}100$ μm grade PS beads were utilized to blend with PS90k in solvent of tetrahydrofuran (THF) and dried under rotary evaporation. In this mixture, the specific filler-filler interaction can be neglected for the PS beads in μm size and the adhesion between PS beads and melts is rather small in comparison with the melt-melt entanglement.

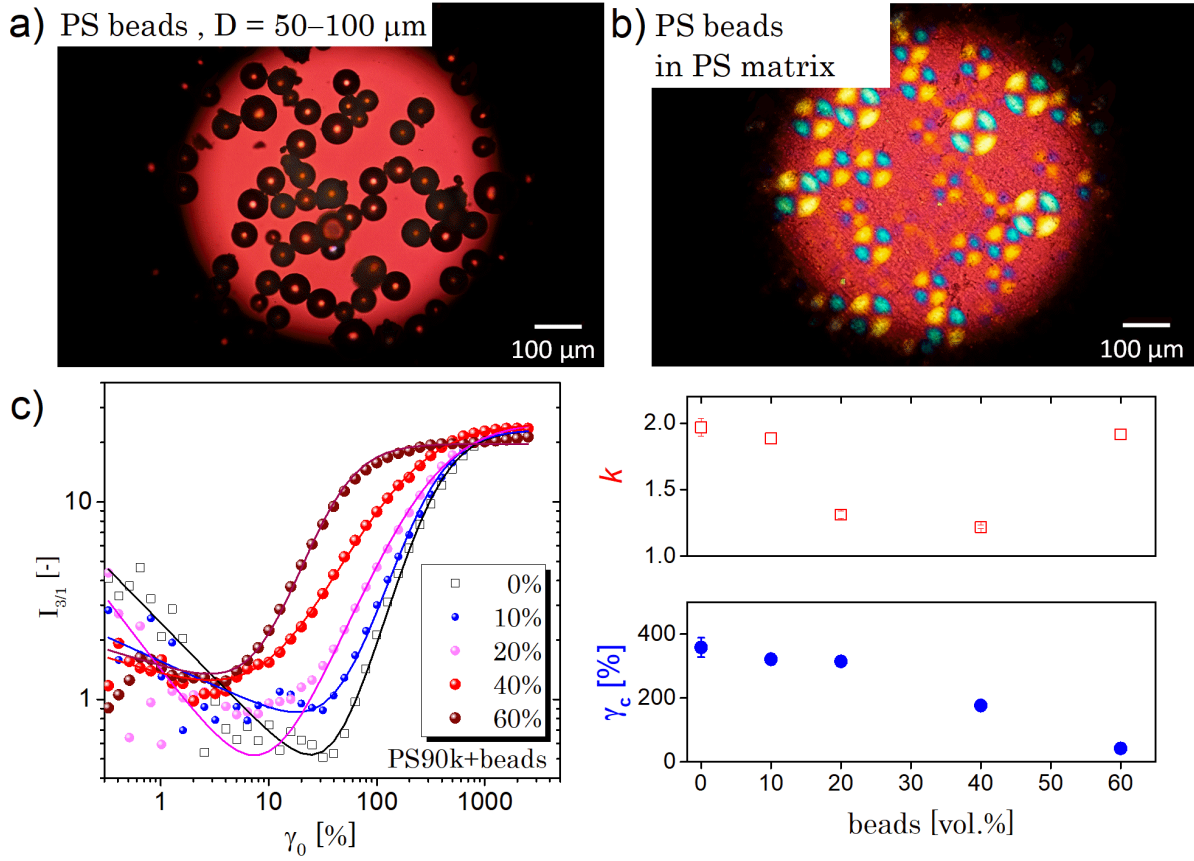


Figure 4.9: a) The 50–100 μm spherical crosslinked PS beads as volume filler in b) PS matrix under polarized light transmission microscopy and c) the $I_{3/1}(\gamma_0)$ development of PS melts from FT-rheology (at $De = 1$ of the pure melt, 155 $^\circ\text{C}$ and 0.145 Hz). As the chemical structure of the bead filler and the matrix are same so that the interfacial interaction between filler-matrix could be identical as that within the matrix. The fitting lines and parameters, k and γ_c , are obeying Equations 4.21. Rheological measurements were performed on SCARABAEUS SIS V50 rheometer with sealed geometry and grooved surface to suppress the wall-slip.

As shown in Figure 4.9, the increase of $I_{3/1}(\gamma_0)$ in those composites were not quadratic anymore but rather grew with a smaller growth power order, $k < 2$. In analogy, Equation 4.5 was modified into

$$I_{3/1}(\gamma_0) = \frac{L_{noise}}{\gamma_0} + n_{F-P} \frac{(\gamma_0/\gamma_{cF-P})^k}{1 + (\gamma_0/\gamma_{cF-P})^k} \quad (4.21)$$

and $1 < k < 2$

with only one growth term at γ_{cF-P} , as the shared critical strain amplitude for both the filler and the polymer matrix. The γ_{cF-P} shifted to the lower range with higher PS beads loading

(see the plot of γ_{cF-P} in Figure 4.9c, for PS melts filled with beads 0 vol% \rightarrow 60 vol%, the γ_{cF-P} moved from 392% \rightarrow 48%). It implies that under shear, the mobility of the polymer melts was hindered by the filler obstacles and the rheological nonlinearity started to build up at lower strain amplitudes.

4.1.3. DQ-NMR of NR vulcanizate

As explained in Chapter 1.3.3, the topological constraints like entanglements and the permanent crosslinks in the polymer network prevent the free movement of chain segments. This will leave the segmental fluctuations anisotropic at long observation time thus, the local residual orientation persists. It is reflected by the long-time plateau in the orientation autocorrelation function of the polymer chains [162], $C(t)$ (see Figure 1.21). The value of this plateau is governed by the dynamic order parameter of the polymer backbone, S_b , which is proportional to the crosslink density, ν , according to statistical mechanics. In DQ-NMR, the residual dipolar coupling (RDC) of the protons on the chain segments is also determined by the chain orientation. For the networks far above the glass transition temperature, the residual dipolar coupling constant, D_{res} , is proportional to the dynamic order parameter thus the crosslink density, $D_{res} \propto S_b \propto \nu$ (see Equation 1.37). Therefore, the D_{res} from DQ-NMR, measured at a temperature far above the glass transition ($T > T_g + 100$ K) of rubber, is considered to be a quantitative parameter of the effective crosslink density.

The D_{res} is not directly obtained from the DQ-NMR measurements, but requires a procedure of the data treatment of the raw NMR signals in several steps. Figure 4.10 illustrates the data treatment process for the raw data of NR1 sample acquired from the Bruker mq20 NMR analyzer at $T = 60^\circ\text{C}$ with Baum-Pines sequence, following the procedure in literature [109, 134].

The raw DQ-NMR results in step 1 consists of two sets of data, the reference intensity, I_{ref} , and the excited double quantum filtered intensity, I_{DQ} , measured at different evolution time of τ_{DQ} . The raw data was normalized into nI_{ref} and nI_{DQ} as step 2 by the full magnetization of the sample after the 90° pulse, i.e. I_{ref} at $\tau_{DQ} = 0$ from the extrapolation of $I_{ref}(\tau_{DQ})$. In the $nI_{DQ}(\tau_{DQ})$, there are interferential contributions from the network defects, such as the small molecules, uncrosslinked sols, dangling ends and crosslinked loops. If there are no network defects, in the long evolution time range, the referential signal and DQ signal should be equal. Subtracting nI_{DQ} from nI_{ref} , the contribution from network defects appears in the long evolution time, more distinctively in a semi-logarithmic scale as shown in step 3. The

jump-up tail in $nI_{ref}(\tau_{DQ}) - nI_{DQ}(\tau_{DQ})$ can be fitted by a single exponential decay function

$$\text{the tail in } nI_{ref}(\tau_{DQ}) - nI_{DQ}(\tau_{DQ}) = I_{def} \exp\left(-\frac{2\tau_{DQ}}{T_2}\right) \quad (4.22)$$

with the intensity from network defect, I_{def} , at an apparent transversal relaxation time, T_2 . The value I_{def} in this normalized intensity curve can be seen as the fraction of the network defects in percentage ($I_{def} \times 100\%$).

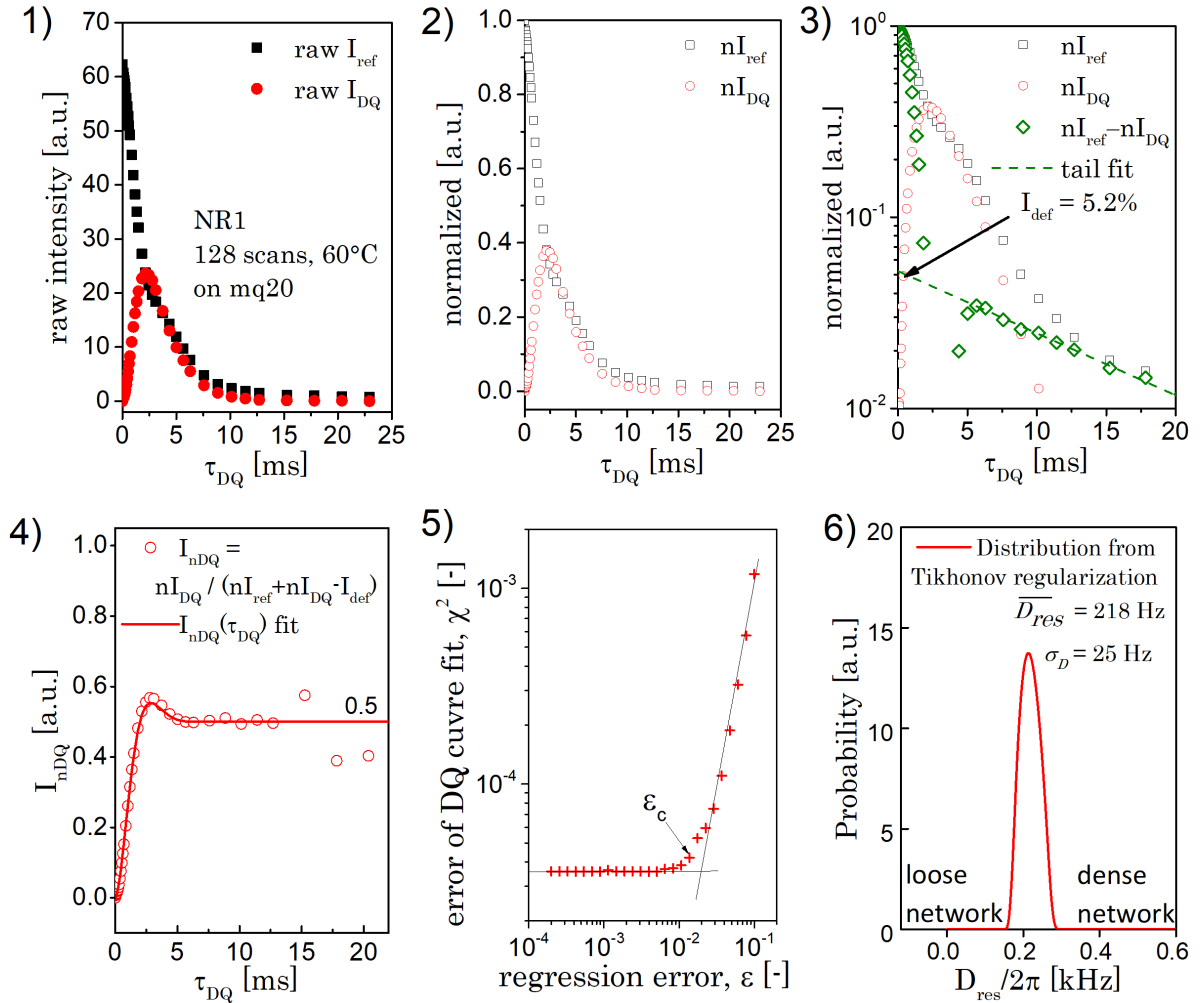


Figure 4.10: The exemplary DQ-NMR raw data treatment of NR vulcanizate (sample NR1) in six steps to receive the portion of network defects, I_{def} , the residual dipolar coupling constants, D_{res} , and the standard deviation of the distribution, σ_D , as the quantitative parameters to describe the structure of a rubber network.

The nI_{DQ} collects the signal from dipolar coupled segments (strictly speaking, it is multiple quantum since it also includes signal from $4n+2$ quantum orders [116]). The nI_{ref} contains

the contributions of all double quantum magnetization plus all that from the uncoupled protons in the isotropically mobile chain segments. Therefore, the sum intensity in the corrected version is $nI_{ref} + nI_{DQ} - I_{def}$. The normalized DQ buildup data reads

$$I_{nDQ}(\tau_{DQ}) = \frac{I_{nDQ}(\tau_{DQ})}{nI_{ref}(\tau_{DQ}) + nI_{DQ}(\tau_{DQ}) - I_{def} \exp\left(-\frac{2\tau_{DQ}}{T_2}\right)} \quad (4.23)$$

At long τ_{DQ} , the reference term and DQ term should be equal, leading to $I_{nDQ}(\tau_{DQ}) = 0.5$. This normalized DQ intensity, $I_{nDQ}(\tau_{DQ})$, is temperature independent at $T > T_g + 100$ K, as proven by Figure 4.11. In the following rubber aging studies, DQ-NMR measurements were conducted at 60 °C, which is far above T_g but lower than the lowest aging temperature (70 °C).

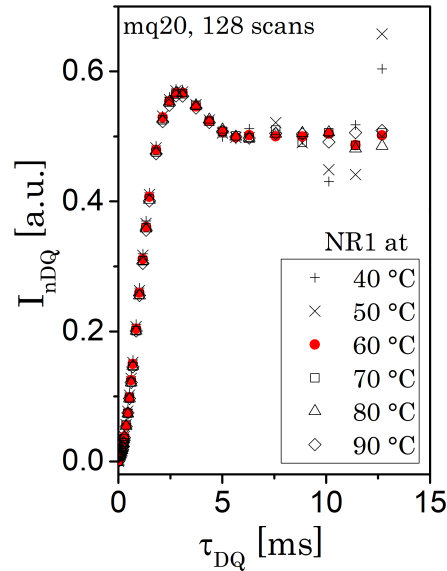


Figure 4.11: The $I_{nDQ}(\tau_{DQ})$ build-up curves of NR1, measured on mq20 NMR analyzer at different temperatures above $T > T_g + 100$ K, are almost identical. Other test conditions are same.

For a homogeneous network, such as the sulfur-accelerator vulcanized NR as above, the $I_{nDQ}(\tau_{DQ})$ curve presents not only a typical buildup behavior to a plateau of 0.5, but also a local maximum, as seen Figure 4.10-4 at around $\tau_{DQ} = 2.8$ ms. This maximum results from the growing importance of four-quantum coherences during the primary DQ buildup. To fulfill this maximum in the $I_{nDQ}(\tau_{DQ})$, Chassé et al. [134] proposed a model for the

homogeneous network,

$$I_{nDQ}(\tau_{DQ}, D_{res}) = \frac{1}{2} \left\{ 1 - \exp \left[- (D_{res} \tau_{DQ})^{1.5} \right] \right\} \times \cos(0.583 D_{res} \tau_{DQ}) \quad (4.24)$$

where D_{res} determines the DQ buildup rate. Networks with dense mesh grids will exhibit a steep slope before the maximum in the $I_{nDQ}(\tau_{DQ})$ curve.

In an inhomogeneous network, the DQ intensity of the mesh grids at different density will linearly superpose on the DQ curves with their intrinsic buildup slope. Compared to the homogeneous network with a maximum, the $I_{nDQ}(\tau_{DQ})$ of a broadly distributed mesh size would not show the typical maximum as in Figure 4.10-4. Generally, one can fit this type of data by multiple linear superpositions of Equation 4.24. However, this is an ill-posed problem. Therefore, Saalwächter and Weese [109, 163] developed a program for regression analysis with a Tikhonov regularization algorithm. With Equation 4.24 as kernel function, the distribution of D_{res} , as shown in Figure 4.10 step 6, can be deduced properly at the transition point of the regression error, ε_c . This protocol has been verified on rubber materials with model networks [134]. The average value of the RDC constant, $\overline{D_{res}}$, and its standard deviation, σ_D , are obtained from the distribution curve as well.

4.2. Hot-air aging of unfilled NR

The characterization tools, FT-rheology and DQ-NMR, have been successfully validated on the NR vulcanizates in an unaged status to analyze the linear, nonlinear rheological properties and the rubber network structure. In the following, the effect of aerobic aging at elevated temperature (hot-air aging) on NR vulcanizates is discussed based on the two methods. For linear rheological properties, the elastic moduli and the mechanical loss factor in LVE regime, G'_0 and $\tan\delta_0$, are compared after aging. From FT-rheology, the $I_{3/1}$ at the critical strain amplitudes, $I_{3/1}(\gamma_0 = 70\%)$ and $I_{3/1}(\gamma_0 = 2.5\%)$, are used to represent the rheological nonlinearity of the polymer and filler network, respectively. The alternation of rubber networks are uncovered through the DQ-NMR measurement.

Here the aging effect was firstly investigated on the unfilled NR samples, without concerning the influence of the fillers on the rheological data as well as the effect of aging. The unfilled NRs only possess one critical strain amplitude for the development $I_{3/1}$ at around $\gamma_0 = 70\%$.

4.2.1. Influence of aging temperature

The NR from the controlled vulcanization formulations (the SEVmed) without filler, NR1, are selected to investigate the influence of hot-air temperature. In the hot-air aging process, the NR1 vulcanizates in sheets were hang in the oven at 70°C for several weeks, or at 120 °C for several days. The rheological data of NR1 after two typical aging conditions, 70 °C for 14 days (sample named as NR1-70C14d) and 120 °C for 3 days (sample named as NR1-120C3d), are compared with the unaged sample (the original) in Figure 4.12.

After the hot-air aging at a moderate temperature, 70 °C, for 14 days, NR1 turned into a more elastic material (G' increased 42%) with lower mechanical loss factor $\tan\delta$ (lower than the half of the original). After exposing in the 120 °C hot-air for 3 days, the mechanical loss factor $\tan\delta$ strongly increased (more than doubled), i.e. it turned into high relative viscous material. The rheological nonlinearity of NR1-70C14d was lower than the unaged with lower $I_{3/1}$ after non-noise region.

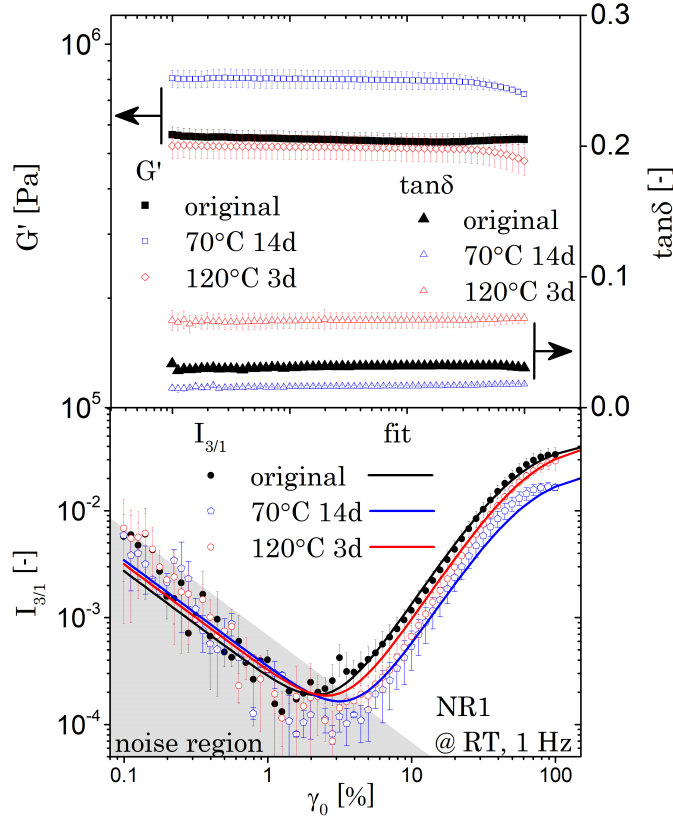


Figure 4.12: The linear and nonlinear rheological properties of NR1 before and hot-air aging at 70 °C for two weeks and 120 °C for 3 days. The measurements were conducted on ARES-G2 oscillatory torsion at frequency of $\omega_1/2\pi = 1$ Hz and RT. The fitting line for $I_{3/1}(\gamma_0)$ is based on Equation 4.3.

As proposed in Chapter 4.1.1, the representative rheological parameters, G'_0 , $\tan\delta_0$ and $I_{3/1}(\gamma_0 = 70\%)$ were selected to track the linear and nonlinear properties of the polymer network. Their evolution during hot-air aging at two temperatures are drawn in Figure 4.13. Under 70 °C hot-air aging conditions for 28 days, G'_0 of NR1 increased along the aging time before 14 days and then levels off, accompanying the decline of $\tan\delta_0$ accordingly. This indicates that new crosslinks formation reactions dominate in NR1 during the hot-air aging at 70 °C since $G'_0 \propto \nu$. The $I_{3/1}(\gamma_0 = 70\%)$ decreased so the rheological nonlinearity was lower for the aged networks.

With respect to the hot-air aging process of NR1 at 120 °C for 3 days, there likely exists a time point for the transition of rheological properties at around 0.5–1 days. In the early aging period, the developments of both linear and nonlinear rheological parameters were similar as the 70 °C aging process for 28 days. The $\tan\delta_0$ and $I_{3/1}(\gamma_0 = 70\%)$ reached a minimum at 0.5 days. Afterwards, the elasticity of the network, G'_0 , started to drop down, accompanied

by the rising of the loss factor $\tan\delta_0$ and nonlinearity $I_{3/1}(\gamma_0 = 70\%)$. This implies that for NR1 in the 120 °C hot-air, the generation of new networks occurred at the beginning and then the chain scission reactions might prevail.

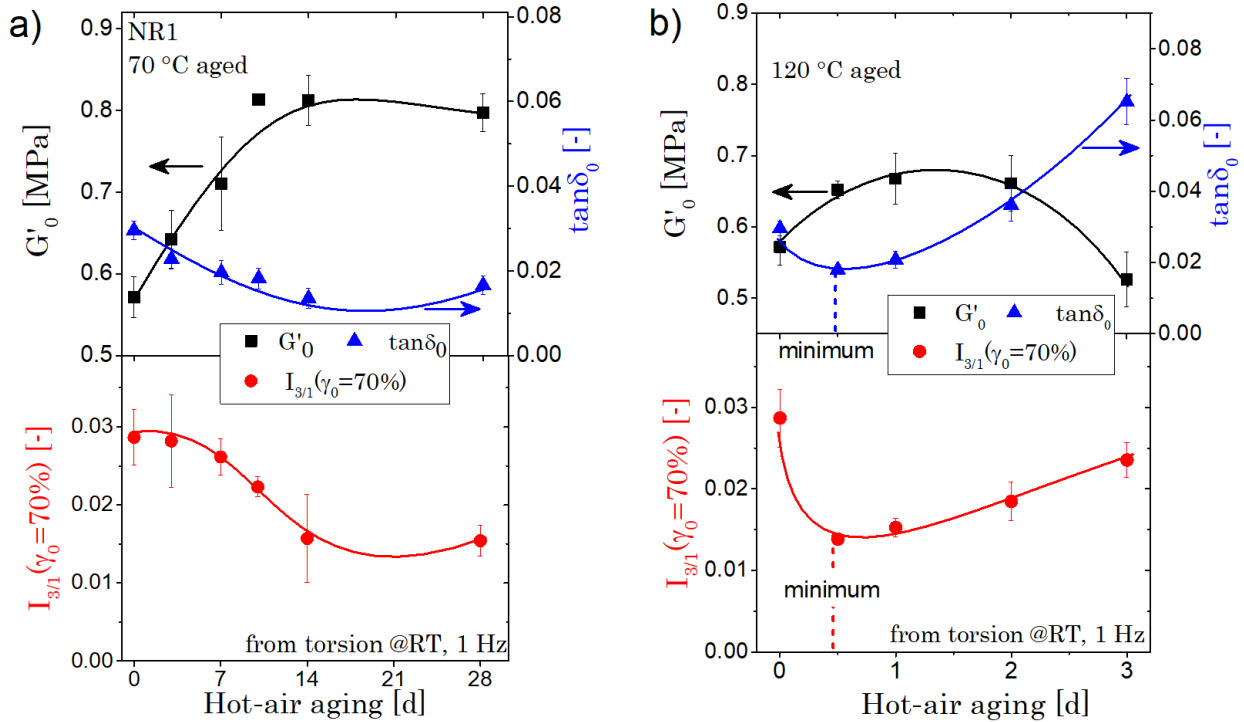


Figure 4.13: The development of linear- and FT-rheological properties of NR1 during aerobic aging at a) 70 °C and b) 120 °C, respectively. The rheological parameters are acquired from oscillatory torsion at room temperature. The solid lines are manually drawn just to guide the eyes.

The crosslink density of the polymer network as well as the network defects were monitored by DQ-NMR. In Figure 4.14, the DQ buildup curve of NR1 are compared after two aging processes. At 70 °C aging, the DQ buildup displays a high rate, implying that the network became more and more dense. At 120 °C aging, the DQ buildup turned over from the faster rate at the beginning but slowed down after 0.5–1 day.

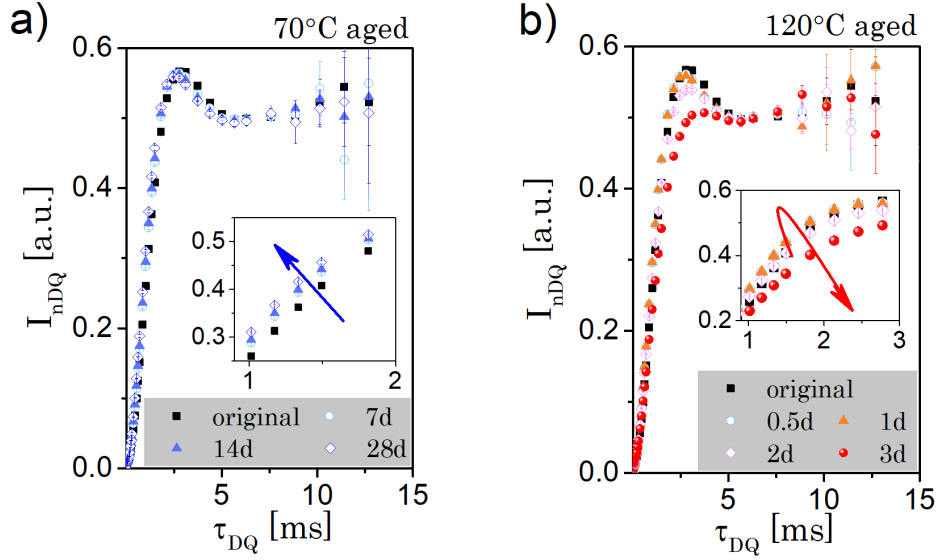


Figure 4.14: The DQ buildup, $I_{nDQ}(\tau_{DQ})$, of the original and the hot-air aged NR1 at a) 70 °C and b) 120 °C, respectively. The DQ-NMR results were obtained from a mq20 NMR analyzer at 60 °C.

Table 4.3: Network density, distribution broadness and defects of hot-air aged NR1 at 70 °C and 120 °C according to the DQ-NMR results.

Sample	$\overline{D_{res}}$ [Hz]	σ_D [Hz]	I_{def} - [%]
Original	218	24.6	5.11
70 °C-7d	236	30.4	4.70
-14d	240	31.0	4.65
-28d	251	35.9	4.48
120 °C-0.5d	236	32.3	5.66
-1d	241	37.6	5.87
-2d	230	65.8	7.91
-3d	203	91.3	11.26

The D_{res} distribution from the Tikhnov regularization and the contents of network defects are shown in Figure 4.15 and summarized in Table 4.3. Along the hot-air aging time at 70 °C, the D_{res} shifted to higher coupling rates as seen from the distribution curves. The average RDC constants $\overline{D_{res}}$ increased from 218 Hz to 251 Hz. This indicates that in average high dipolar-coupled chain segments, consequently less mobile, were produced. Meanwhile, the deviation in the distribution curves, σ_D maintained the similar level at 24.6–35.9 Hz. The network defects, I_{def} , reduced slightly from 5.11% to 4.48%. It proved that in 70 °C

hot-air, the rubber network of NR1 became more and more dense without generating network defects. This is reflected in the increased elasticity and decreased rheological nonlinearity of the network as discussed above.

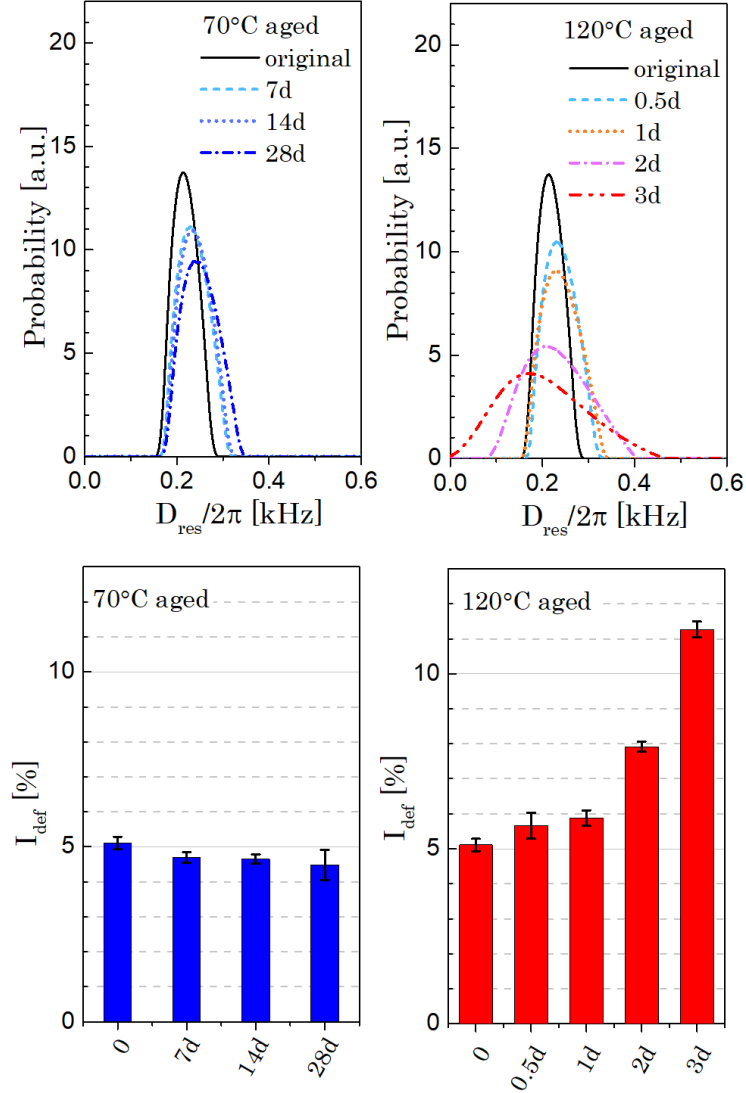


Figure 4.15: The evolution of D_{res} distribution and the network defects I_{def} (see Equation 4.22 and 4.24) of NR1 under hot-air aging at two temperatures, 70 °C and 120 °C. The distribution curves were acquired from the Tikhnov regularization of the data in Figure 4.14.

For hot-air aging at 120 °C, there also existed a transition time for the network structures. At 0.5 days, the $\overline{D_{res}}$ reached a maximum value at the similar level as the NR1-70C14d sample did. Afterwards, $\overline{D_{res}}$ declined with a broadening of the distributions from $\sigma_D = 24.6$ to 91.3 Hz. Furthermore, the network defects soared up after 1 day. The I_{def} of NR1-120C3d

was more than doubled than that of the original. The broadening of mesh size distribution and the raise of network defects are responsible to the increase of $\tan\delta_0$ and rheological nonlinearity.

In summary, a denser network with less defects responds rheologically with higher elasticity, lower loss factor and less rheological nonlinearity in term of $I_{3/1}(\gamma_0 = 70\%)$. On the contrary, a loose network leads to low elasticity. The broadening mesh size distribution and the increasing fraction of defects results in high loss factor and strong rheological nonlinearity of the network.

With regards to the tested sample above, NR1 was vulcanized with SEV system, which would partially generate polysulfidic crosslinks during the vulcanization [24,25]. As suggested in the literatures [28,164], the polysulfides in the starting material can transfer into more crosslinks with shorter linkages as mono- or disulfidic bonds under long term heating process. Correspondingly, there are more rubber chains/segments with high D_{res} appeared in the distribution curves of Figure 4.15 after hot-air aging. In addition, a small portion of the polysulfidic bridges can transfer into cyclic sulfides [165], which is probably the reason for the appearance of very high D_{res} rubber segments after aging ($D_{res}/2\pi > 0.35$ kHz in Figure 4.15, especially in sample NR1-120C3d). Another common chemical reaction in NR vulcanizate under hot-air aging process is the thermal-oxidation of the unsaturated backbones (C=C bonds), resulting in network scission [166,167] with alcohol and carbonyl groups at the broken chain ends as confirmed from FTIR spectroscopy [168–170]. It is also found the chain scission also take place on the sulfidic linkages [165,166].

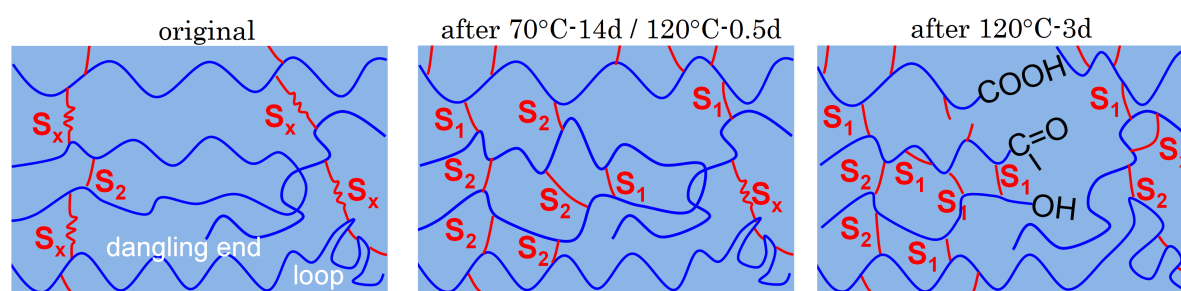


Figure 4.16: Schematic illustration for the evolution of network structures in NR vulcanizates under progressive aerobic aging at elevated temperatures.

Based on the rheological and DQ-NMR results, the evolution scheme of NR1 networks under hot-air aging at two examined temperatures can be depicted as Figure 4.16. At relative low temperature like 70 °C for 14 days or high temperature but short period of time like

120 °C for 0.5 days, the polysulfidic crosslinks transform mainly into more linkages in type of mono- or disulfidic bonds without network defects. This sample exhibits higher elasticity and lower rheological nonlinearity than the original. However, for high temperature and long time hot-air aging like at 120 °C for 3 days, the network scission reactions on the unsaturated backbones and the sulfidic bonds dominate. This results in the loss of effective elasticity of the sample. The produced dangling ends behave as network defects, leading to a higher mechanical dissipation ($\tan\delta$) and stronger rheological nonlinearity of the network. Additionally, a small portion of polysulfidic bonds transfer into cyclic sulfides on the neighbor chain segments or crosslinks. This generates highly dipolar-coupled chain segments but not effective crosslinks for the macroscopic elasticity.

4.2.2. Influence of vulcanization system

The hot-air aging effect was also tested on the five unfilled NRs vulcanized with different vulcanization systems (see Table 2.1) to see the influence of the type of crosslinks. The samples were the referential sample NR1 with semi-efficient vulcanization and medium dosage of agents (named SEVmed here, identical as sample NR1), conventional/efficient vulcanization with varying dosage of agents (CVhigh, CVlow, EVhigh, and EVlow). Two aging conditions, relative low temperature aged 70 °C for 14 days (termed as 70C14d) and relative high temperature aged 120 °C for 3 days (termed as 120C3d), were selected to study.

In Figure 4.17, the relative rheological properties of the five NRs after hot-air aging at the two selected conditions are compared. All of the linear rheological parameters, G'_0 and $\tan\delta_0$, and nonlinear rheological parameter, $I_{3/1}(\gamma_0 = 70\%)$, of the aged samples were normalized by the values from the unaged counterparts (the original), symbolized as nG'_0 , $ntan\delta_0$ and $nI_{3/1}(\gamma_0 = 70\%)$, respectively. In this way, the rheological properties can be compared in a relative fashion to eliminate the differences between the starting materials. The retention of those parameters were considered as the criteria to evaluate their resistance to hot-air aging.

With respect to the chemical structures of the crosslinks and their contents in those vulcanized samples, please refer to Table 1.2. After vulcanization at optimal curing time (e.g. at the time of curing degree $\alpha = 97\%$), there would be mainly polysulfidic crosslinks (90%) in CV samples, mono-/disulfides (95%) in EV samples and half of both types in SEV systems [25]. The expected compositions of those crosslinks had been further supported by the D_{res} distribution curves of the original samples (black solid lines) in Figure 4.18 from the DQ-NMR measurements. In the original samples, the distribution of D_{res} from broad to narrow

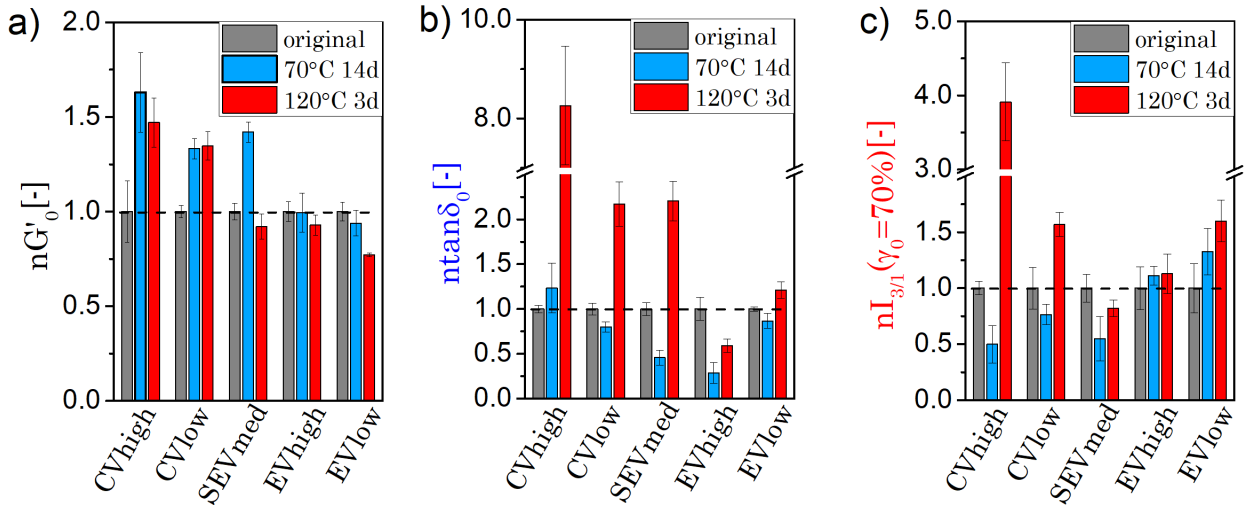


Figure 4.17: The hot-air aging effect on the normalized rheological parameters, a) nG'_0 ($nG'_0 = G'_0$ of the aged/ G'_0 of the original), b) $n \tan \delta_0$ and c) $n I_{3/1} (\gamma_0 = 70\%)$ of the five unfilled NRs vulcanized with different systems. Notice the SEVmed here is identical as the NR1 in Chapter 4.2.1.

generally followed the order of $CV > SEV > EV$. In CV samples, particularly the CVhigh, the polysulfidic crosslinks could range from long to short bridges ($-S_x-$, $x = 3-8$). Additionally, there were portions of mono-/disulfidic bonds or complex cyclic sulfides, resulting in a high dipolar-coupled chain segments. Thus, their network mesh size was rather broadly distributed. On the contrary, there would be only one type of links (short mono- or disulfidic) formation in EV samples, leaving their D_{res} distributions very narrow. The SEVmed sample possessed a medium distribution. Those crosslinks with different levels of chemical bond energy determine the resistance of NR vulcanizates to thermal-oxidative reactions, i.e. hot-air aging.

For the retention of the three rheological properties against hot-air aging in Figure 4.17, overall they follow in the order of, from good to bad, $EVhigh > EVlow > SEVmed > CVlow > CVhigh$. This is consistent with the results from other studies [28, 165]. This order is also reflected by the DQ-NMR results in Figure 4.18, in particular, if one compares the change of D_{res} distribution broadness of the 120C3d aged samples. High amount of long polysulfidic bridges in CVhigh possessing low bond energy is easily modified into more crosslinked or rigid networks after hot-air treatment, resulting in the increase of elasticity after aging. On the other hand, the severely inhomogeneous networks in CVhigh-120C3d with high amount of network defects lead to a strong rheological nonlinearity of the material and also a drastic increase of the loss factor. The EV samples exhibit better hot-air aging resistance than the CV samples, owing to the high energy of the mono- or disulfidic bonds. Additionally,

the EVhigh shows better retention than EVlow in term of the three rheological parameters. One possible explanation is that for EV systems, high crosslink density can slow down the

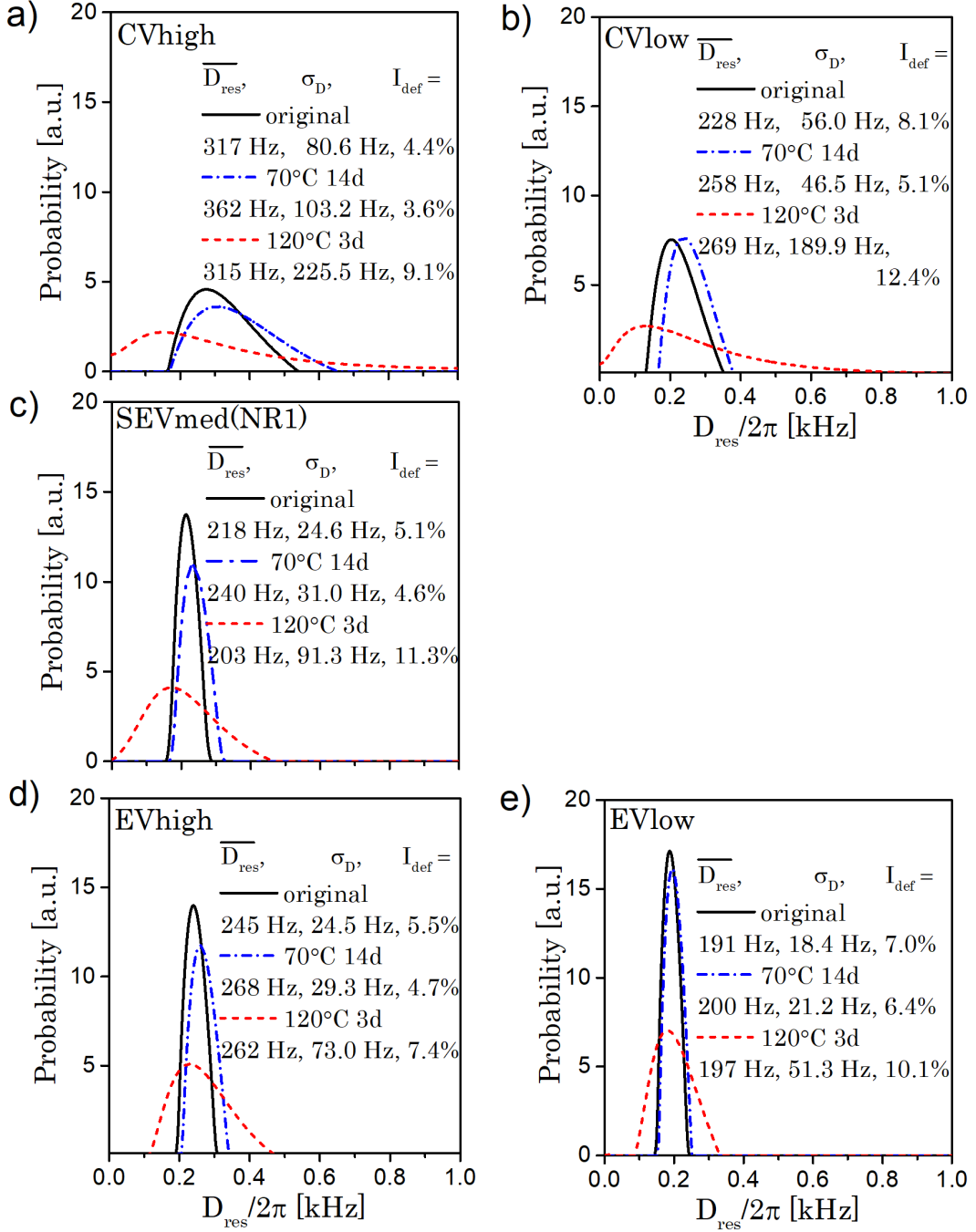


Figure 4.18: The hot-air aging effect on the D_{res} distribution and network defects I_{def} of the five unfilled NRs vulcanized with different systems: CVhigh, CVlow, SEVmed, EVhigh and EVlow.

diffusion of oxygen thus reduced the opportunities for thermal-oxidation on the unsaturated rubber backbones.

Within the examined samples and conditions in Figure 4.17, $\tan\delta_0$ exhibits the maximum relative change (relative value = 8.2) in the case of 120C3d aged CVhigh, followed by $I_{3/1}(\gamma_0 = 70\%)$ (relative value = 3.9).

4.3. Hot-air aging of filled NR

In the following, the hot-air aging on NR filled with 50 phr N339 carbon black (CB), is going to be investigated. It should be emphasized again that the CB filled polymers exhibited another $I_{3/1}$ quadratic growth region at γ_{cF} due to the filler-involved network, based on the study in Chapter 4.1.2. In the case of NRCB1, we can use $I_{3/1}(\gamma_0 = 2.5\%)$ and $I_{3/1}(\gamma_0 = 70\%)$ to present the rheological nonlinearity of the filler- and polymer-involved networks, respectively.

4.3.1. Influence of carbon black

The strain sweep data comparison of NRCB1 (NR1 filled with 50 phr N339) before and after two typical hot-air aging conditions, 70 °C for 14 days (termed as 70C14d) and 120 °C for 3 days (termed as 120C3d), are shown in Figure 4.19. The corresponding crosslink density distribution and network defects are displayed in Figure 4.20.

The alteration of rheological properties and network structures after aging were similar to the unfilled NR as seen in Figure 4.12 and Figure 4.15. After 70C14d aging, the sample became more elastic with higher G'_0 and smaller $\tan\delta_0$, due to the increased crosslink density. The rheological nonlinearity of the polymer-involved network, the $I_{3/1}$ at high strain ($\gamma_0 = 70\%$), dropped to a lower level. After 120C3d aging, as the crosslink density became broadly distributed with doubled amount of defects, $\tan\delta_0$ had distinctively increased. The rheological nonlinearity $I_{3/1}$ at high strain amplitude was elevated for this inhomogeneous polymer network with high amount of defects. However, for the filler-involved network, the rheological nonlinearity $I_{3/1}(\gamma_0 = 2.5\%)$ always declined, as indicated by the arrows in the graph.

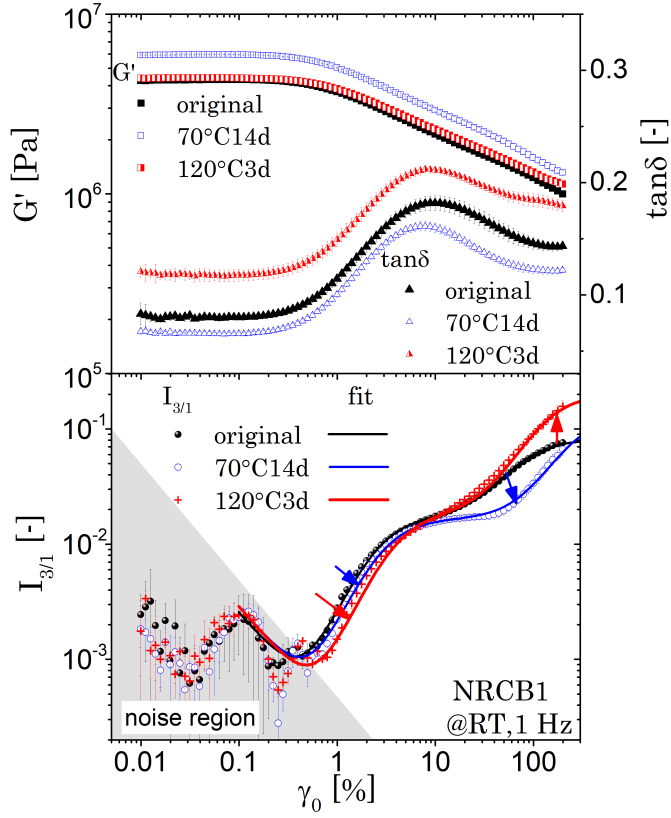


Figure 4.19: The linear and nonlinear rheological properties of NRCB1 before and hot-air aging at 70 °C for 14 days and 120 °C for 3 days. The solid lines are the fittings for $I_{3/1}(\gamma_0)$, based on Equation 4.5.

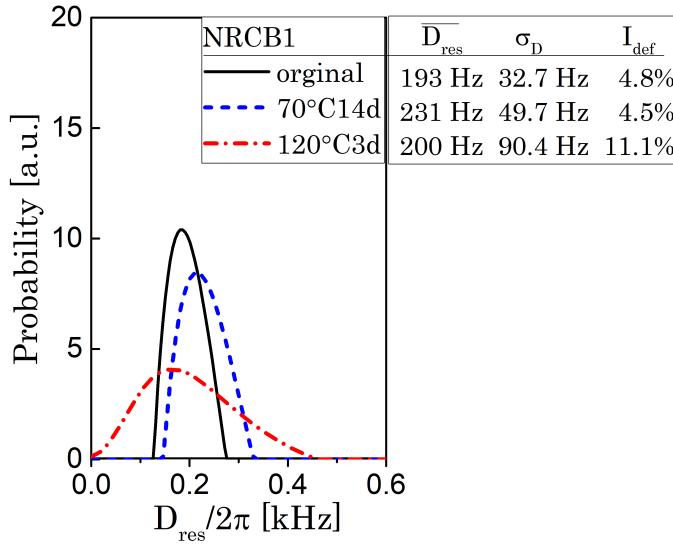


Figure 4.20: The alternation of the D_{res} distribution and the network defects, I_{def} , of NRCB1 under hot-air aging at two conditions, 70 °C for 14 days and 120 °C for 3 days. Data were derived from DQ-NMR measurements on a mq20 NMR analyzer at 60 °C.

The evolution of the characteristic rheological parameters in progressive hot-air aging of NRCB1 is shown in Figure 4.21. The trend is similar at unfilled system, the sample of NR1. At 120 °C aging, both NR1 and NRCB1 exhibit a turn over of the rheological properties. However, the turn-over of $\tan\delta_0$ and $I_{3/1}(\gamma_0 = 70\%)$ for NRCB1 occurred close to 1 day, as indicated by the dash lines. This turn over time is half days postponed in comparison with

NR1 as in Figure 4.13b. The filler, carbon black, may act as a free radical acceptor, which can absorb the resulting free radicals at high temperatures in air atmosphere. This reduces the chance of the unsaturated C=C bonds get attached thus, slows down the thermal-oxidation process of the polymer chains. Furthermore, some studies [171] has suggested that the good filler-polymer interaction could enhance the thermal conductivity as well as the thermal stability, owing to the high surface energy of the small CB particles.

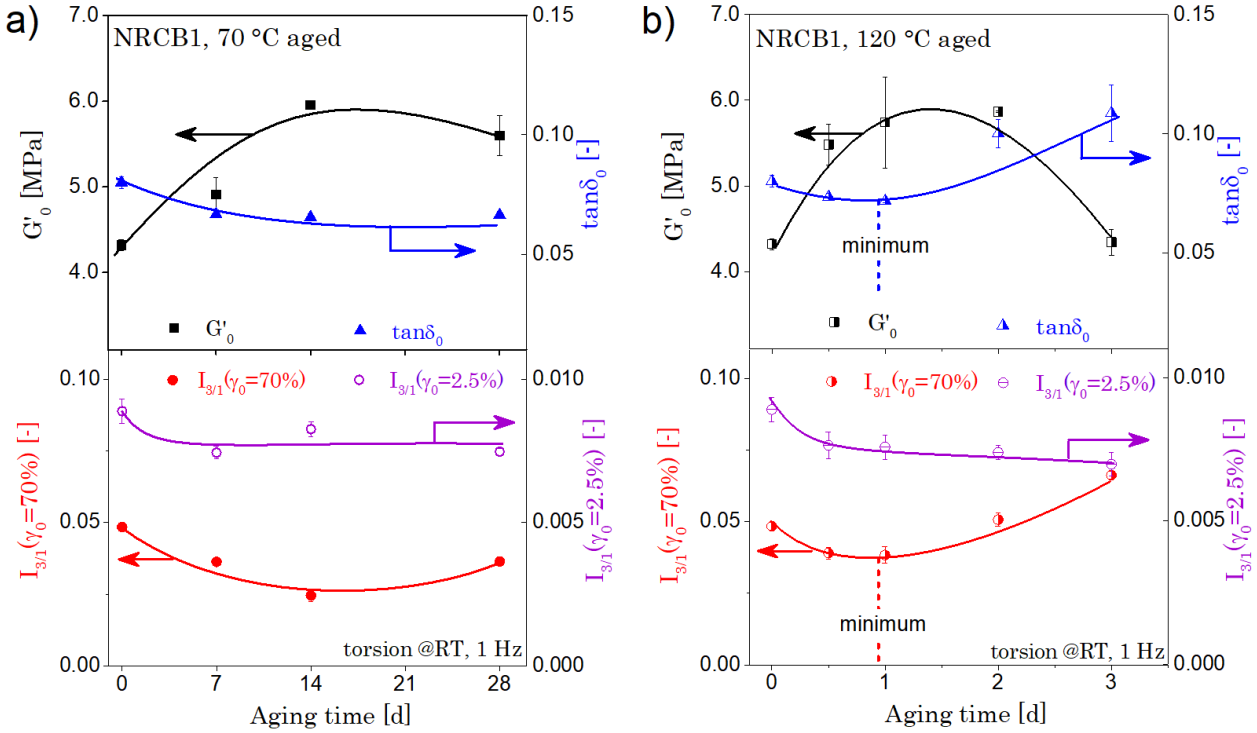


Figure 4.21: The development of linear- and FT-rheological properties of NRCB1 during aerobic aging at a) 70 °C and b) 120 °C, respectively. The rheological parameters are acquired from oscillatory torsion at room temperature. The solid lines are manually drawn just to guide the eyes.

In addition, the $I_{3/1}$ of filler-involved network at $\gamma_0 = 2.5\%$ always declined after aging, particularly in the aging process at 120 °C. As mentioned before, the CB particles with high surface energy absorb the rubber chains during mixing, leaving the polymer networks partially entrapped in the filler aggregates as bound rubber. The bound rubber moves together with the filler agglomerates under deformation. The layer of polymer chains on the filler surface is considered as "glassy" and is not as mobile as the chains in the polymer matrix [7, 149]. These external linkages between the filler aggregates or agglomerates through the rubber chains could contribute an extra rheological nonlinearity. After heat treatment of the composites, part of the bounded polymer chains may desorb from the filler surface [172–174], i.e. the

bound rubber is partially reversible. The thermal desorption of rubber chains leads to a disconnection between the big filler aggregates and the polymer network thus, the $I_{3/1}(\gamma_0 = 2.5\%)$ declines.

4.3.2. Influence of anti-oxidant

In order to protect the rubber products from thermal oxidation and degradation, particularly for the unsaturated diene rubbers like NR, a small amount (1–2 phr) of anti-aging chemicals is commonly added into the materials. Those chemicals work either in a physical way to insulate the rubber from oxygen, e.g. through a layer of wax immigrated to the product surface, or in a chemical approach by reacting with the free radicals more actively during thermal-oxidation. The chemical in latter case is called anti-oxidant.

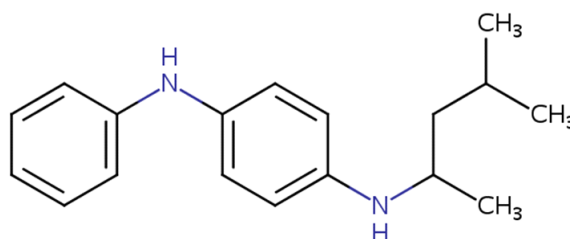


Figure 4.22: The chemical structure of 6PPD (*N*-(1, 3-dimethylbutyl)-*N'*-phenyl-*p*-phenylenediamine), used as the anti-oxidant in present work. The functioning groups are highlighted in blue.

To mimic the tire tread formulation, a normal dosage of anti-oxidant (1.8 phr *N*-(1, 3-dimethylbutyl)-*N'*-phenyl-*p*-phenylenediamine, namely 6PPD in rubber industry) had been blended into NR1 and NRCB1. Based on NRCB1, two extra samples, NRCB0 without 6PPD and NRCB2 with double amount of 6PPD, were prepared to study the influence of anti-oxidant amount on hot-air aging. The chemical structure of 6PPD is depicted in Figure 4.22. It is widely used in tire industry with the good anti-ozonants and anti-fatigue effects. In the hot-air aging process, the concentration of the oxygen centered free radicals, such as ROO· and RO·, determines the rate of oxidation process. Prior to the oxidation on the -C=C- bonds on the rubber backbone, the free radicals react with the hydrogen on the phenylenediamine -NH- of 6PPD, forming benzoquinondiimine and nitroxide radicals [175–177].

The crosslink density and amount of network defects of NRCB1, NRCB0 and NRCB2 after hot-air aging at 70 °C for 14 days (70C14d) and 120 °C for 3 days (120C3d) are shown in

Figure 4.23. With similar D_{res} distributions and defects of the starting materials, the 70C14d aged samples were still alike each other. At the relatively low temperature aging conditions (70 °C) for 14 days, the dosage of anti-oxidant does not show obvious impact on the chemical structure retention of the vulcanizates. After 120C3d aging, the crosslink density of NRCB0 dropped distinctively in comparison with the rest, including a higher amount of defects. According to the DQ-NMR results, doubling the dosage of 6PPD does not further improve the hot-air aging resistance even after 3 days at 120 °C.

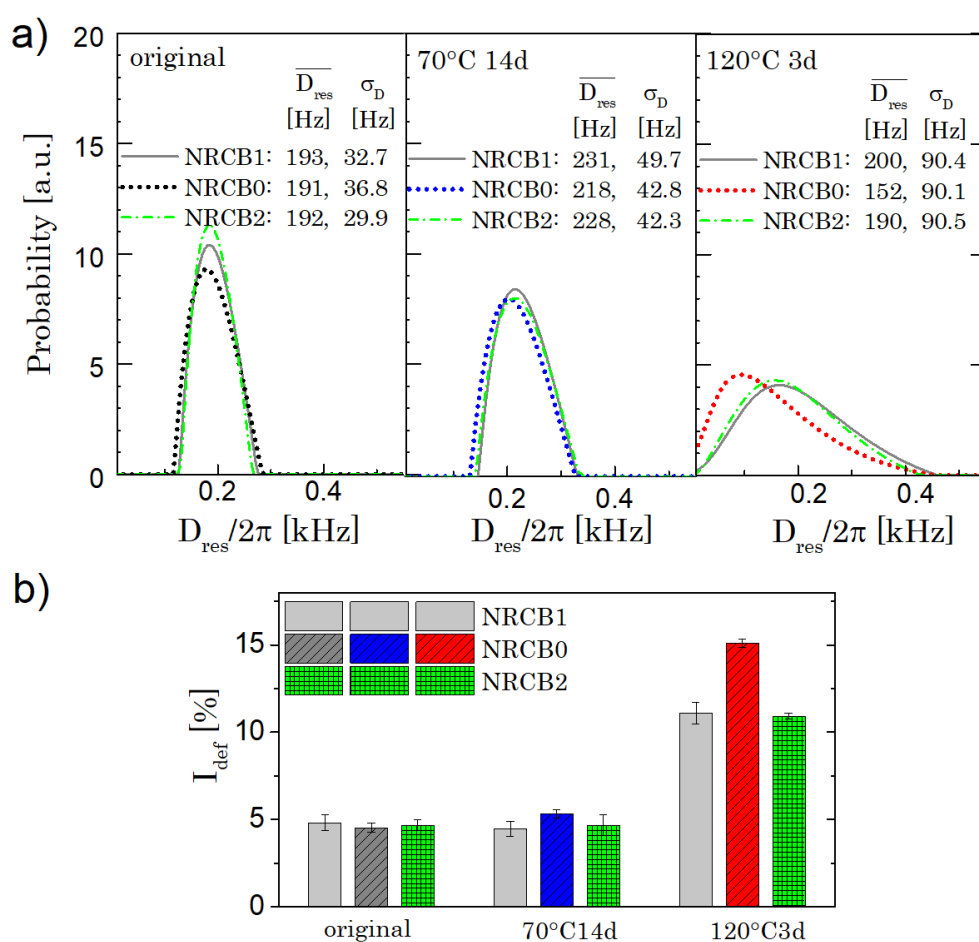


Figure 4.23: The alternation of a) D_{res} distribution and b) network defects I_{def} of NRCBs with different dosage of anti-oxidant after hot-air aging at two conditions, 70 °C for 14 days and 120 °C for 3 days. Data were derived from DQ-NMR measurements on mq20 NMR analyzer at 60 °C.

Since there were no obvious differences for all the 70C14d aged samples in the DQ-NMR results, hereby only the rheological results from the 120 °C hot-air aging were compared in Figure 4.24. The linear and nonlinear rheological parameters of NRCB1, NRCB0 and NRCB2

were normalized by their unaged status (aging time for 0 day in the plots) for comparison to eliminate the differences between the starting materials.

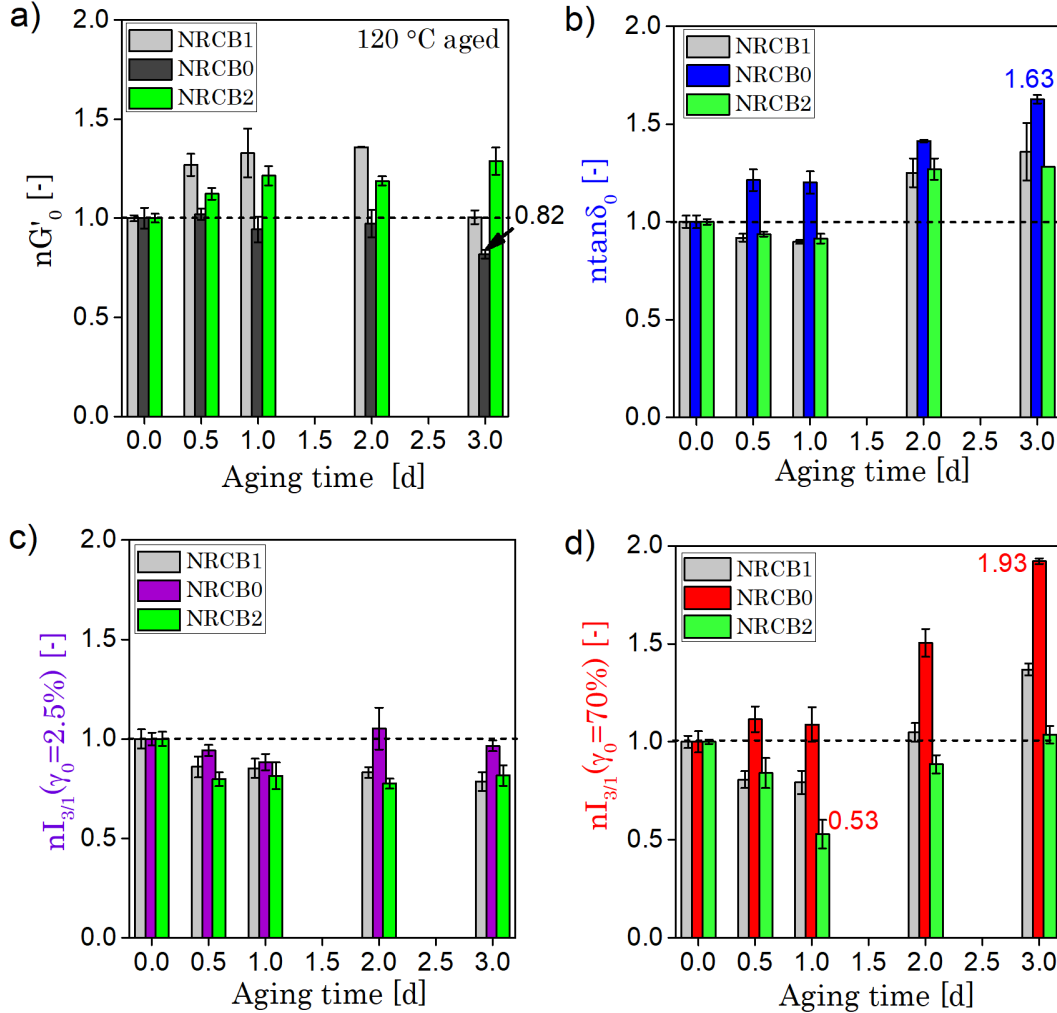


Figure 4.24: The hot-air aging effect on the normalized rheological parameters, a) nG'_0 ($nG'_0 = G'_0$ of the aged/ G'_0 of the original, so as other parameters), b) $n \tan \delta_0$, c) $nI_{3/1}(\gamma_0 = 2.5\%)$ and d) $nI_{3/1}(\gamma_0 = 70\%)$ of the NRCBs added with different dosage of the anti-oxidant, 6PPD. All rheological data were acquired from ARES-G2 oscillatory torsion experiments at RT and 1 Hz.

For most rheological parameters, NRCB0 exhibited faster aging process from 0.5 to 3 days than other two samples. The elasticity G'_0 of NRCB0 did not show an increase at the early aging period, indicating there was no increase of the crosslink density along the 120 °C aging. In absence of anti-oxidant, the new crosslinks formation reaction is not competitive as the chain scission reaction. There were also no turn over points of the $\tan \delta_0$ and the $I_{3/1}(\gamma_0 = 70\%)$ of NRCB0 around 0.5–1 days like the NRCB1 and NRCB2. This implies NRCB0

degrades into more inhomogeneous network with more defects. The nonlinearity of filler networks of NRCB0 did not decline as much as the rest samples. The bound rubber in NRCB0 might under more severe aging effect other than the thermal desorption from the filler surface. The filler network of NRCB0 maintains a high level of rheological nonlinearity. In summary, at 120 °C hot-air aging, the anti-oxidant 6PPD takes affect already at early period based on the comparison of the rheological properties between NRCB0 and NRCB1.

Although there is no obvious improvement by the double-loading of 6PPD, according to the DQ-NMR results as shown in Figure 4.23, some differences between the aged NRCB1 and NRCB2 in term of the rheological properties can be found. NRCB2 maintained better retention of G'_0 in long period of aging (after 2 days). Additionally, the $I_{3/1}(\gamma_0 = 70\%)$ of NRCB2 reduced to a lower level at 120 °C for 1 day, implying a more homogeneous rubber network than the aged NRCB1 at the same condition. The decreasing behavior of $I_{3/1}(\gamma_0 = 70\%)$ in the early aging period may be enhanced by the extra amount of 6PPD so that NRCB2 had suppressed more of the thermal-oxidation than NRCB1. After 1 day aging, the rise of $I_{3/1}(\gamma_0 = 70\%)$ of NRCB2 was not as severe as that of NRCB1. To conclude, doubling the dosage of 6PPD is helpful for 120 °C hot-air aging after 1 day.

Under the examined samples and aging conditions, the most drastic relative changes (both decrease and increase behaviors) of the linear and nonlinear rheological properties are indicated with the values in Figure 4.24. The parameter of polymer network nonlinearity obtained from FT-rheology, $I_{3/1}(\gamma_0 = 70\%)$, presents the most relative changes, by 93% in the case of the 120C3d aged NRCB0. This is followed by the linear parameter $\tan\delta_0$ by a relative change of 63% also occurred on the case of 120C3d aged NRCB0.

5. Mechanical Aging

Apart from the static aging process like the hot-air aging experiments in Chapter 4, NR vulcanizates used in engineering products also widely endure large deformation or dynamic loading of stress such as the running tires, the conveying belts, etc. The mechanical aging or fatigue of the materials deteriorates the dynamic mechanical properties of the products and finally into mechanical failure. Therefore the mechanical aging (fatigue) properties of NR vulcanizates are also of critical importance. In this chapter, the mechanical aging behavior of reinforced NR vulcanizates are analyzed through their linear and nonlinear macroscopic rheological properties as well as their micro-/nano-scopic structures of the composites.

Commonly, rubber materials used in engineering products are not used solely but rather filled with reinforcing fillers to improve the moduli and dynamic mechanical properties. For this reason, on the CB filled NR vulcanizate (NRCB1) was submitted to mechanical aging in this work. Carbon black filled rubber materials are known to have a short shelf life. Therefore, a new batch of NRCB1 were prepared for mechanical aging studies (the same formulation as the NRCB1 used for hot-air aging). To reduce the influence of sample fabrication errors, the corresponding experiments only conducted and compared within the new batch. Otherwise, the reused hot-air aging results will be indicated in the following figures or texts.

Mostly, the mechanical aging mechanism of rubber materials is studied by tracking the crack initiation and propagation during fatigue [178, 179]. Sometime, the specimen is even initially cut with a sharp blade tip thus it is easy to track the location of an artificial crack [180, 181]. In this study, the intention is to study the mechanical aging of NRCB1 in an earlier fatigue period, i.e. before the appearance of visually observable cracks on the specimen's surface or a plunge of the modulus (50% drop of the initial G'). The response of linear and nonlinear rheological properties of the unaged and the fatigued samples are compared. On one hand, we can evaluate the sensitivity of the FT-rheological parameters in comparison with the linear rheological counterparts towards the mechanical aging effect. Meanwhile, it delivers the information regarding the relationship between the fatigue process and the rheological

nonlinearity.

5.1. Aged at different fatigue cycles

The punched out dumbbell shape specimens from NRCB1 vulcanizate sheets were stretched on the Fatigue Tester at stretch ratio of $\varepsilon_0 \equiv (l - l_0)/l_0 = 90\%$ at frequency of 1.7 Hz (100 cycles per minute) and varying kilocycles (kc), at ambient temperature. When the samples got ruptured or the initial stress amplitude loaded at the first cycle had decreased 50%, it was defined as a failure.

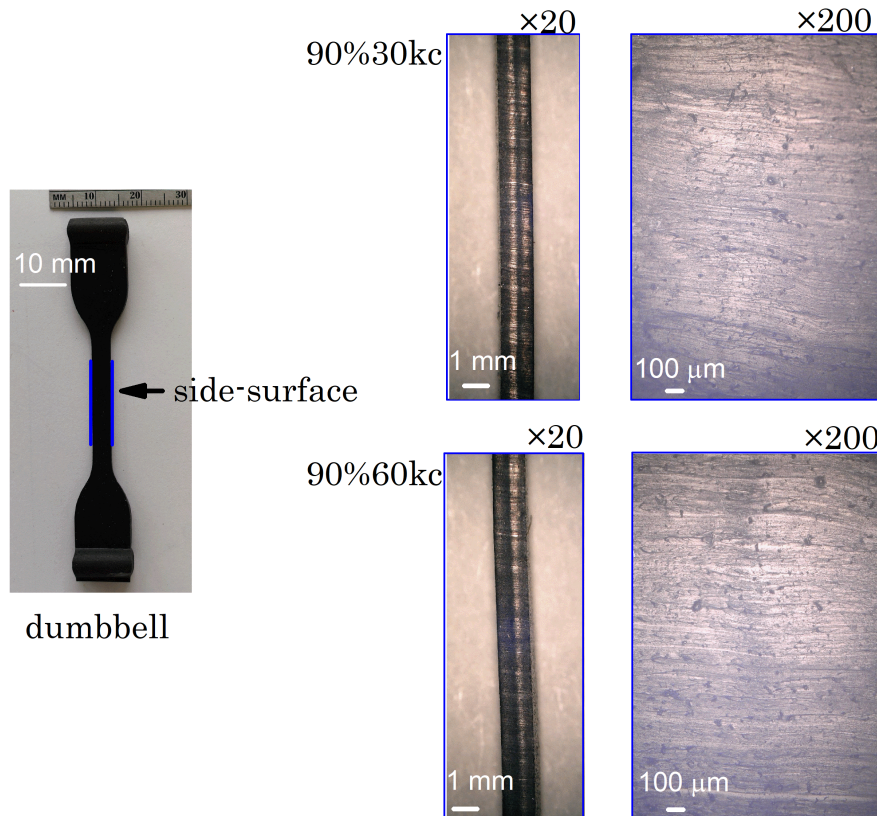


Figure 5.1: The fatigued sample in a dumbbell shape and the selective images of the side surface in the middle working area of NRCB1-90%30kc and NRCB1-90%60kc at magnifications of 20 and 200 times via the VHX 900F microscope. There were no observable cracks on the examined surface.

The averaged cycle numbers of failure for NRCB1 is $N_f = 120$ kc at such aging condition. However, the fatigue tests were interrupted at 30 kc or 60 kc before failure, i.e. aged at one quarter or half of the failure life, $0.25N_f = 30$ kc or $0.50N_f = 60$ kc. The specimens were

collected for the aging studies and there were no observable cracks on the surface of those specimens. They were labeled with the stretch ratio and fatigue cycles as NRCB1-90%30kc and NRCB1-90%60kc, respectively.

The representative images of the surfaces of the aged specimens under a light microscope are shown in Figure 5.1. The side surfaces were checked along the dumbbell die-cutting side as indicated by the blue lines in the picture. The leftover surface from the cutting die was relatively smoother than the front surface with many rough marks, which were resulted from the demoulding films during vulcanization in the hot-pressed mold. There were no defects and cracks found from the surface of NRCB1-90%30kc and NRCB1-90%60kc even at large magnification, excluding the cutting striations from the blade of the cutting die.

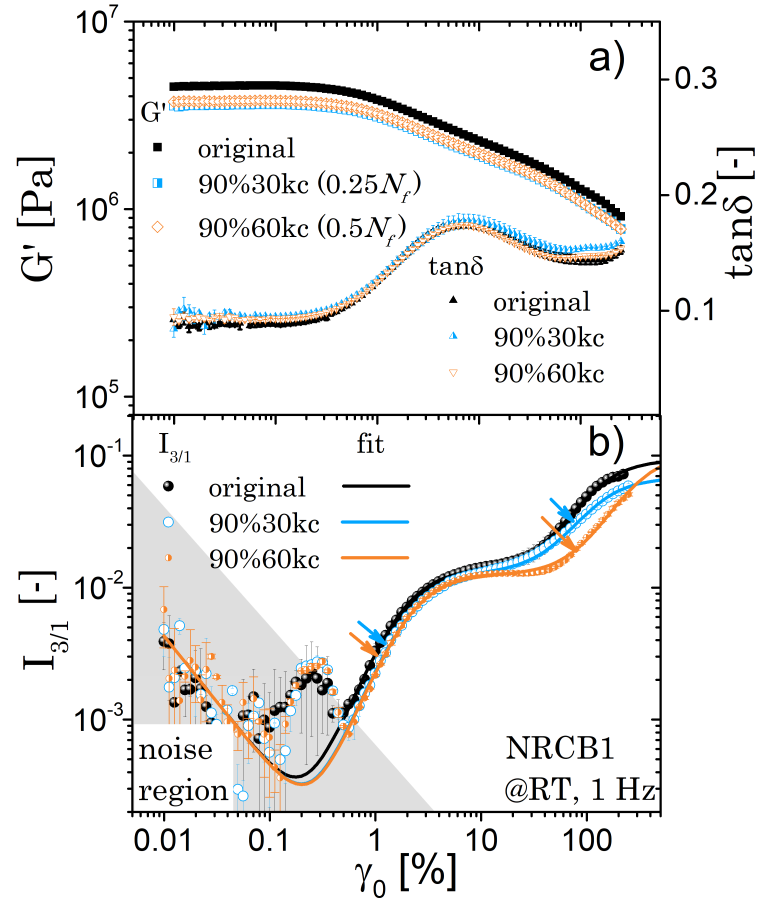


Figure 5.2: The strain dependence of the linear and FT-rheological parameters of NRCB1 before and after mechanical aging at same stretching ratio but different fatigue life. Data was acquired from oscillatory torsion on ARES-G2 at $\omega_1/2\pi = 1$ Hz and room temperature.

For the mechanically aged specimens, the working area in the middle was cut into rectangular specimens and submitted to oscillatory torsion on ARES-G2 for FT-rheology characterization

the say way as before. The strain sweep results of the unaged NRCB1 (original), NRCB1-90%30kc and NRCB1-90%60kc are compared in Figure 5.2.

In the LVE regime, the G' only slightly declined after fatigue and the $\tan\delta$ increased with minor magnitude after the fatigue for 30 kc. At longer fatigue cycles, there were no obvious deferences between the 90%30kc and the 90%60kc fatigued samples in term of the linear rheological parameters, G' and $\tan\delta$. This drop of moduli between the original NRCB1 and the stretched samples may result from the irrecoverable structures in filler-filler and filler-polymer connections after the large deformation of $\varepsilon_0 = 90\%$. Such networks, in reinforced rubbers, are thioxtropic thus can be broken at the first few cycles of stretching. This is known as the Mullins effect [182]. The Mullins effect claims that during the first cycle of uniaxial stretching, ruptures of the filler agglomerates occur and the polymer chains retract [183]. There were also network rearrangement and some other composite micro-structure formation. A fraction of the formation can only be healed when the materials are exposed to high temperatures in vacuo or to solvent swelling.

On the contrary to the weak response of the linear rheological properties, the nonlinear rheology parameter $I_{3/1}$ decreased pronouncedly at large strain amplitude (around $\gamma_0 = 70\%$) as indicated by the arrows in Figure 5.2b. In addition, more fatigue cycles resulted in a stronger decline of $I_{3/1}$ at large strain amplitude. As explained in the last chapter, the $I_{3/1}$ at around $\gamma_0 = 70\%$ is considered to be the rheological nonlinearity of the polymer network. The decrease of $I_{3/1}$ of a polymer as a function of the fatigue cycles has also been observed in thermoplastics below T_g , before failure [184]. The polystyrene (PS) was continuously aged in oscillatory torsion at room temperature (80 K below the T_g). The $I_{3/1}$ of PS decreased steadily to a minimum (see Figure 6, 7 and 8 in [184]) during the micro-cracks initiation and propagation period. In comparison with the NRCB1 composites in black color, the micro-cracks on PS are more visually observable, owing to the high transparency of PS and the the whitening around the cracks during mechanical aging.

The rheological nonlinearity of the filler-involved network in NRCB1, the $I_{3/1}$ at around $\gamma_0 = 2.5\%$ also declined after mechanical aging. However, there is no influence of the number of fatigue cycles. This implies that the change of filler involved networks followed the Mullins effect as discussed above. During the fatigue at the first few cycles, the polymer chains adsorbed by the filler retract from the particle surface of the filler. Additionally, the entangled filler agglomerates/clusters may rapture into a smaller size under stretch. All of the above effects result in the disconnection between filler-filler, leading to a reduced rheological nonlinearity.

The relative changes of the rheological parameters after mechanical aging at $\varepsilon_0 = 90\%$ are compared in Figure 5.3. The parameters were normalized by the values of the starting materials (the original). The change amplitudes of long term fatigued sample (NRCB1-90%60kc) are indicated by the arrows with the labeled values in the graph. It is found that the $I_{3/1}(\gamma_0 = 70\%)$ from FT-Rheology is the most sensitive parameter with a relative change of 50%. While the relative changes of linear rheological parameters are much lower with a decrease of G'_0 by 15% and a increase of $\tan\delta_0$ by 7%.

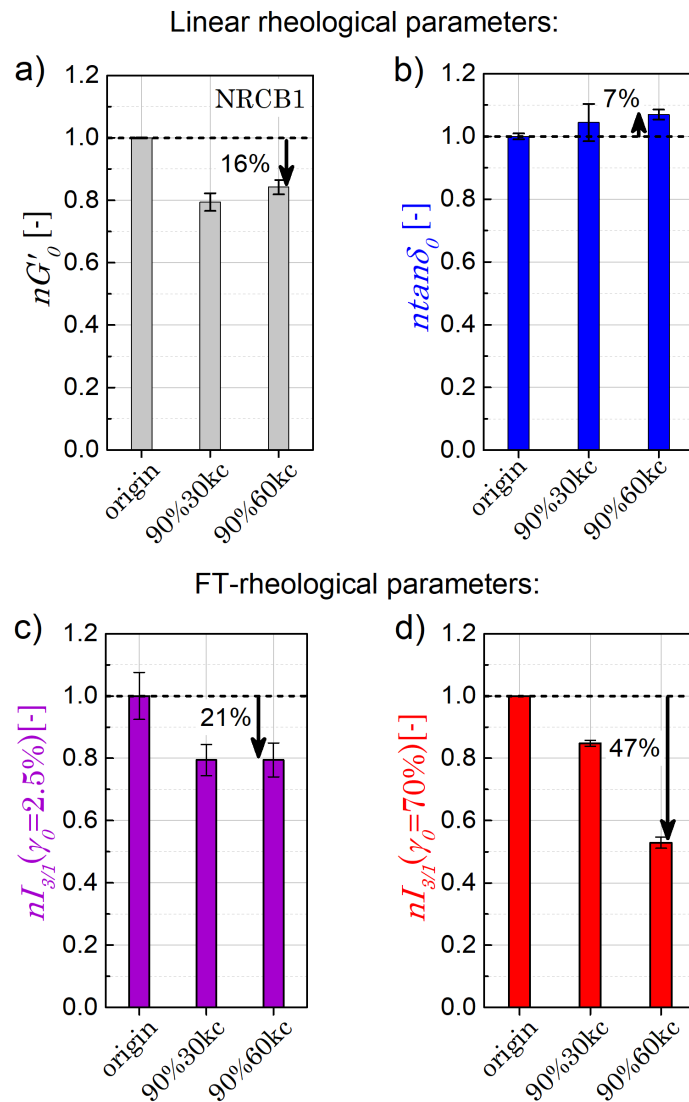


Figure 5.3: The normalized values of linear and nonlinear rheological parameters, a) nG'_0 , b) $n \tan \delta_0$, c) $nI_{3/1}(\gamma_0 = 2.5\%)$ and d) $nI_{3/1}(\gamma_0 = 70\%)$ of NRCB1 after mechanical aging at $\varepsilon_0 = 90\%$ and different fatigue cycles. Data were acquired from Figure 5.2. The arrows and labeled data indicate the highest relative changes for each parameter.

The polymer network structure of the fatigued samples was characterized via the DQ-NMR technique as the results shown in Figure 5.4. Compared to NRCB1-original, the DQ buildup rate in $I_{nDQ}(\tau_D Q)$ of NRCB1-90%30kc and NRCB1-90%60kc only slightly slowed down. Meanwhile, the amount of network defects, I_{def} , were almost stable. After the Tikhonov regularization [134], the distribution of the residual dipolar coupling constant, D_{res} , only slightly shifted to the lower frequency range (less than 3% of the $\overline{D_{res}}$), without changing the broadness of the distributions. However, there was a distinguishable change in the FT-Rheological parameter $nI_{3/1}(\gamma_0 = 70\%)$.

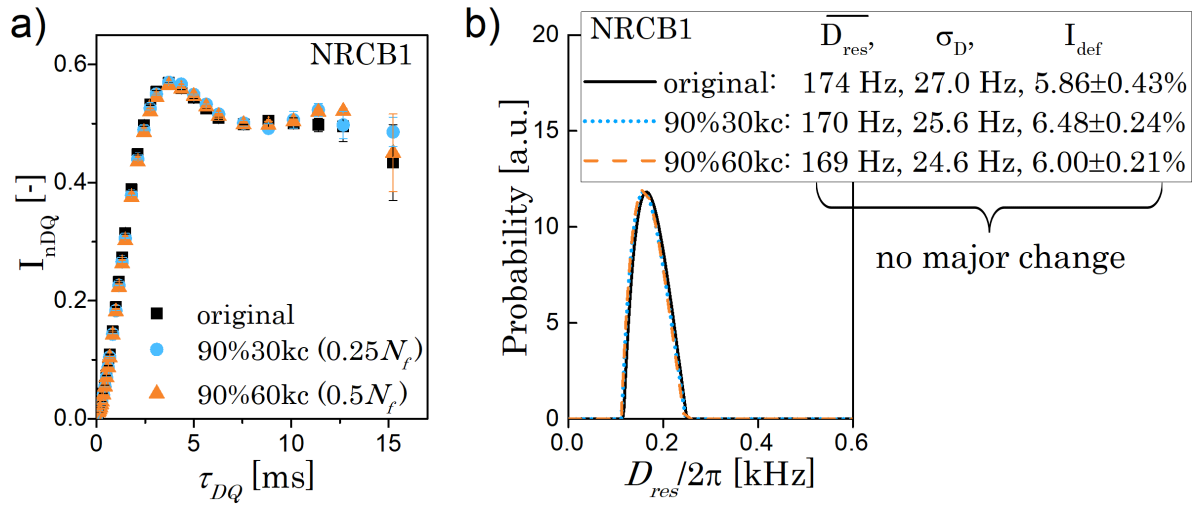


Figure 5.4: a) The normalized DQ build-up curves and b) the distribution of D_{res} of original NRCB1 and its mechanically aged counterparts after $\varepsilon_0 = 90\%$ stretching at 30 kc or 60 kc, where no major change could be detected. The DQ-NMR raw data were acquired from mq20 NMR analyzer at 60°C.

Since there were no observable cracks or defects on the surface of the $\varepsilon_0 = 90\%$ fatigued samples even under microscope (see Figure 5.1), the internal section of the fatigued specimens were checked. The middle working area of NRCB1-90%30kc and NRCB1-90%60kc were cut through with a sharp blade and the cut-off cross sectional surfaces were observed under a VHX 900F microscope. There were micro-cracks ($< 40 \mu\text{m}$) discovered inside of the long fatigue cycle aged sample, NRCB1-90%60kc, as shown in Figure 5.5. Those micro-cracks could be responsible for the decrease of $nI_{3/1}(\gamma_0 = 70\%)$.

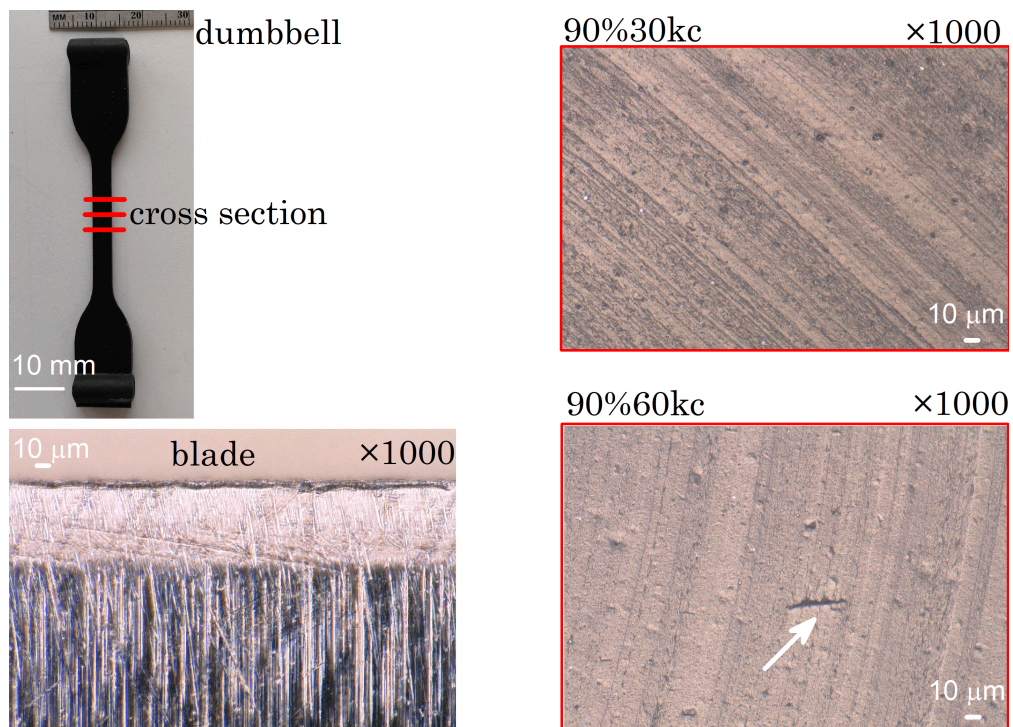


Figure 5.5: The representative cross section images of NRCB1-90%30kc or NRCB1-90%60kc at magnifications of 1000 times on VHX 900F microscope. There were ca.30 micrometer long cracks observed from NRCB1-90%60k samples. The striations perpendicular with respect to the blade were also magnified to 1000 times as reference.

5.2. Aged at larger stretching ratio

The NRCB1 sample was also mechanically aged under larger stretching ratio $\varepsilon_0 = 140\%$ with a fatigue life of $N_f = 40$ kc. For aging studies, the dumbbell specimens were removed from the Fatigue Tester at $20 \text{ kc} = 0.5N_f$ (named as NRCB1-140%20kc), i.e. at half fatigue life same as NRCB1-90%60kc. In the following, NRCB1-140%20kc are compared with NRCB1-90%60kc to check the influence of the stretching ratio.

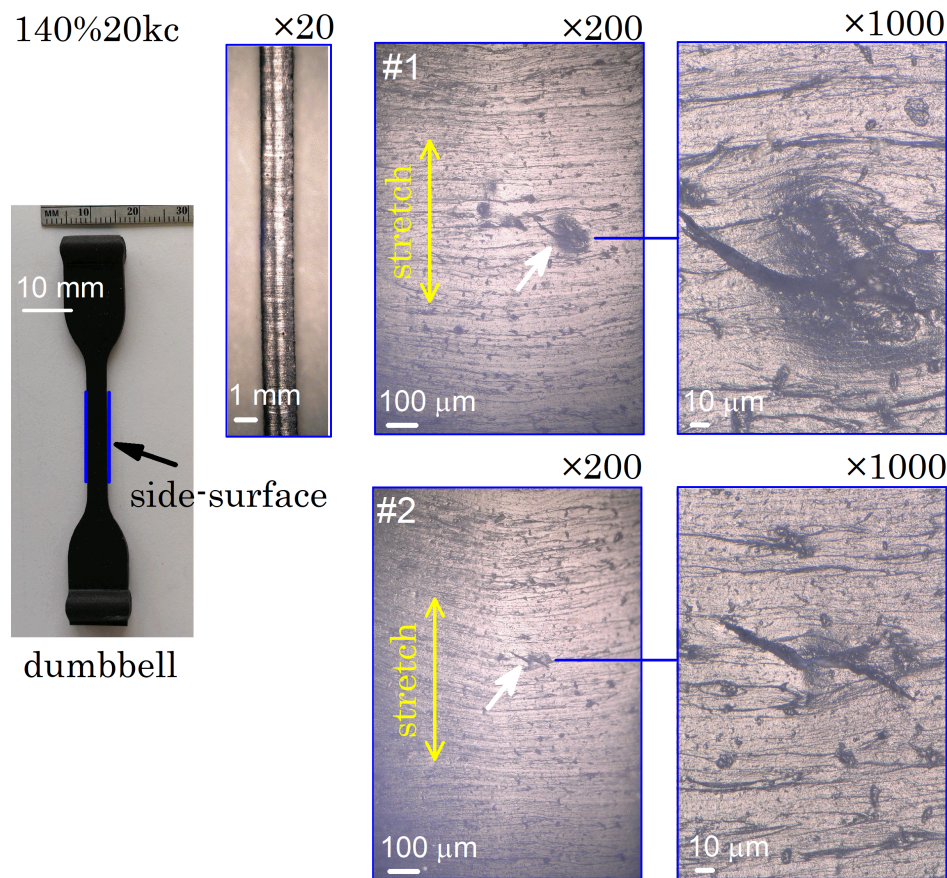


Figure 5.6: The fatigued samples in dumbbell shape and the selective images with microcracks on the side surface in the middle working area of NRCB1-140%20kc at magnifications of 20, 200 and 1000 times under VHX 900F microscope.

Visually, there were no cracks on the surface of the specimens until they were submitted to microscope at large magnification as shown in Figure 5.6. At low magnification of the microscope below 200, there were still no easily recognized cracks on the side surface with the interference of many leftover striations from the dumbbell cutting die. At a magnification of 1000, there were some ca. $100 \mu\text{m}$ long cracks found. In addition, the cracks were

perpendicular towards the stretching direction during fatigue test as indicated by the yellow double arrows in the pictures.

In general, the total life of rubber parts subjected to fatigue consists of two stages: the crack initiation and crack propagation [179]. The morphology of the cracks at initiation and during propagation have been examined in literature with scanning electron microscopy (SEM), offline [185, 186] and in-situ [129, 187], or with X-ray micro-computed tomography (XmCT) [188–190] in literatures.

Huneau and coworkers [191, 192] proposed the crack initiation and propagation mechanism of CB filled NR by using statistics with 1260 pieces of SEM micrographs from fatigued samples. The size of the open cavities (cracks) as well as the size of solid particles on the crack edge were measured from the micrographs systemically. The 43 phr CB N550 (in present work, N339 was used) filled NR vulcanizates were fatigued at different strain levels, $\varepsilon_0 = 60\%/100\%/200\%$, and interrupted before failure at $0.2/0.4/0.6N_f$, respectively. Then the fatigued samples were stretched to $\varepsilon_0 = 10\%$ to open the cracks and the cylindrical surfaces were observed thoroughly by rotating the specimen for every 90° . It was found that mostly the cracks were initiated on the big solid inclusions in the rubber matrix, e.g. the CB agglomerates in size of $5\text{--}40\ \mu\text{m}$, the large zinc oxide (ZnO) particles in diameter of ca. $5\text{--}10\ \mu\text{m}$ and other oxides from impurities. The chemical origin of those inclusions were identified by the energy dispersive spectrometer of X-rays (EDSX) facilitated in the SEM microscope. For the fatigue driven at low strain level ($\varepsilon_0 = 60\%$ and 100%), no inclusions dominate the number of cracks. Instead, at high strain level ($\varepsilon_0 = 200\%$), the CB agglomerates dominate the number of cracks. Accordingly, the fatigue mechanism initiated from CB agglomerates was proposed [192] with three stages:

- stage 1: debonding at the pole of CB agglomerate sphere, following the stretch direction of the fatigue test
- stage 2: open from the sides perpendicular with respect to the stretch direction
- stage 3: the open cavitation grow at the surface and in the volume, still can be considered as the early stages of crack propagation

The typical micrographs of the cracks with CB agglomerates at the three stages are displayed in Figure 5.7 with the corresponding schematic illustration.

Stage 1 and 2 are associated with the initiation of the crack. There were no broken CB

agglomerates were observed on the cracks but only the debonding between the agglomerates and the matrix. This indicates that the filler-filler cohesion in the spherical agglomerates is stronger than the adhesion of agglomerate-rubber matrix. During the mixing of NR compounds, the CB in pellets were broken into small fractions and some could be eroded into spherical shape. Such CB spheres on the crack edges were even collected by Huneau et al. [192] to check the brittleness. Such CB sphere could be easily broken by glass slides with few occluded rubber in it. Without a layer of adsorbed rubber chains on the surface of such CB agglomerates, it is reasonable to claim that it is a debonding mechanism between the CB and rubber matrix other than a cavitation in the matrix for the crack initiation.

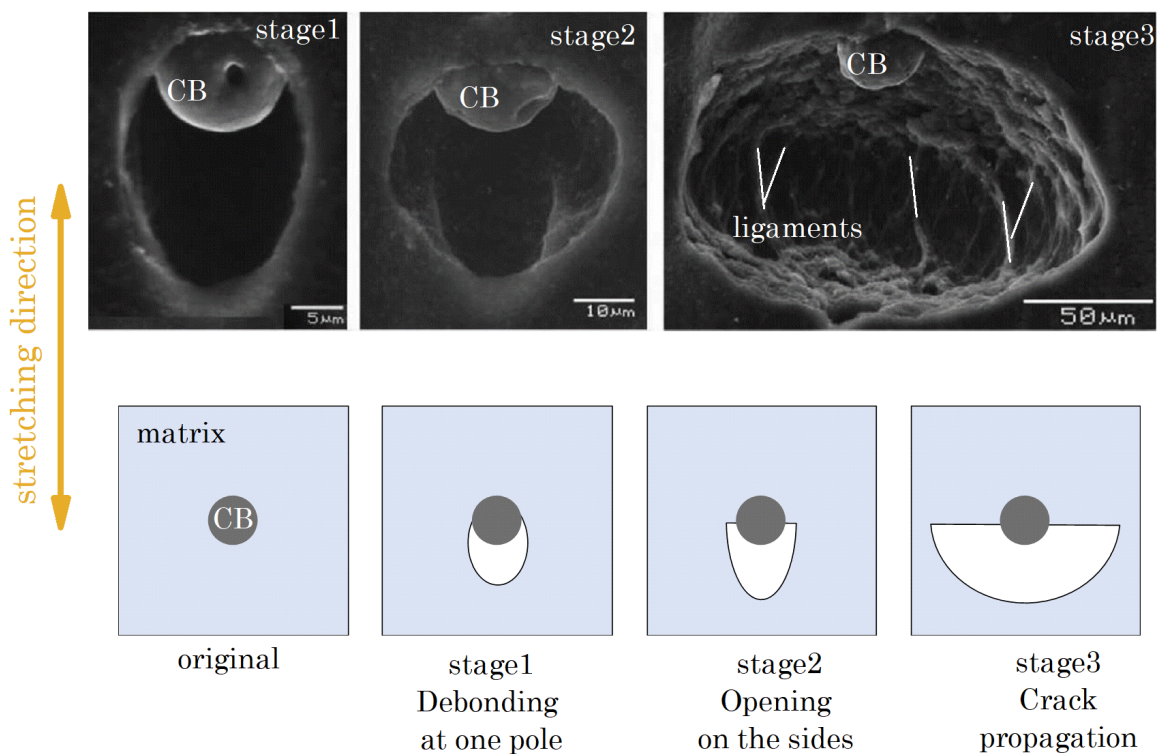


Figure 5.7: Representative SEM micrographs of the CB agglomerates initiated cracks and the schematic illustration of the crack initiation mechanism at three stages according to Huneau et al. Figures are adapted from [191] with Copyright © 2015 by Taylor & Francis Group. Reprinted by permission.

The length of cracks was compared with the sized of the inclusions (see Figure 8 in reference [192]). Interestingly, when there were big CB agglomerates on the crack, the length of the crack was much larger than the CB agglomerates. When there were only inclusions like ZnO or other oxides on the crack, the crack length was almost the size of the oxides. This implies the cracks that originated from CB agglomerates lead to a propagation while

the oxides only open a cavity without propagation, unless coalesce with neighboring cracks. However, there were also cavities without any oxides at the edge, which the inclusions may fall out from the cavity during the fatigue test or the handling of the specimen. In addition, the average size of the CB agglomerates on the cracks determines the life to failure, N_f (see Figure 13 in reference [192]). The samples with shorter N_f were frequently accompanied with larger CB agglomerate sizes on the cavities.

Above discussion unveiled the reason for the crack initiation. One of the remaining question is what is the mechanism of the crack propagation as the stage 3 in Figure 5.7. Furthermore, in Figure 5.7 one can observe some ligaments on the tip of the cracks as indicated by the white lines. Similar ligament strings were also observed from other studies [129, 185, 187].

A convincing explanation for the propagation mechanism was proposed by Le Cam et al. [129], using an in-situ SEM observation on the cracks tips during propagation. The cylindrical dumbbell sample were firstly fatigued to generate cracks on the surface. Then the specimen were fixed on the frame and elongated at slightly higher stretching ratio as the previous fatigue. The opened crack captivity were submitted for SEM. During SEM observation, the crack tip vicinity were in-situ "micro-cut" by focusing high energy electron beam on the interested area. In this way, the underlying cavities or flaws of the crack vicinity were revealed progressively. The in-situ micrographs are shown in Figure 5.8.

The micro-cracks were concentrated in the tip of the whole crack, pointing to the direction perpendicular to the stretch axis. Those micro-cracks were embedded in a smooth area in elliptical shape, laying beside the stretched ligaments. The broken ligaments shrank at the two ends of this area. In the relief part of the smooth elliptical area, there were spherical particle aggregates in diameter of hundred nanometer to $5 \mu\text{m}$. According to EDSX analysis of the elements, the particle was mostly ZnO. After micro-cutting of this smooth area in the crack tip, the artificial micro-crack generated from the electron beam slowly expanded and stopped at adjacent ligaments. During the progressive expansion of the micro-cut cracks, the underlying cavities were revealed. Interestingly, most of the underlying cavities contained oxides. Afterwards, the neighboring micro-cracks coalesced as bigger cracks during this propagation. However, the applied electron energy were maintained in low level that could not break the ligaments. Therefore, the revealing and coalescence of the cavities are driven by the decohesion between the oxides and rubber matrix. The low cohesion interaction between those oxides with rubber matrix can be considered as the activated micro-voids in the bulk sample. The density of those voids (numbers of voids per volume) linearly decreases the fatigue life of rubber as proven via NMR imaging with a resolution down to sub-millimeter [193]. Therefore,

the crack propagation during fatigue is a process to open the oxides-containing cavities, which underlies the tip of the crack.

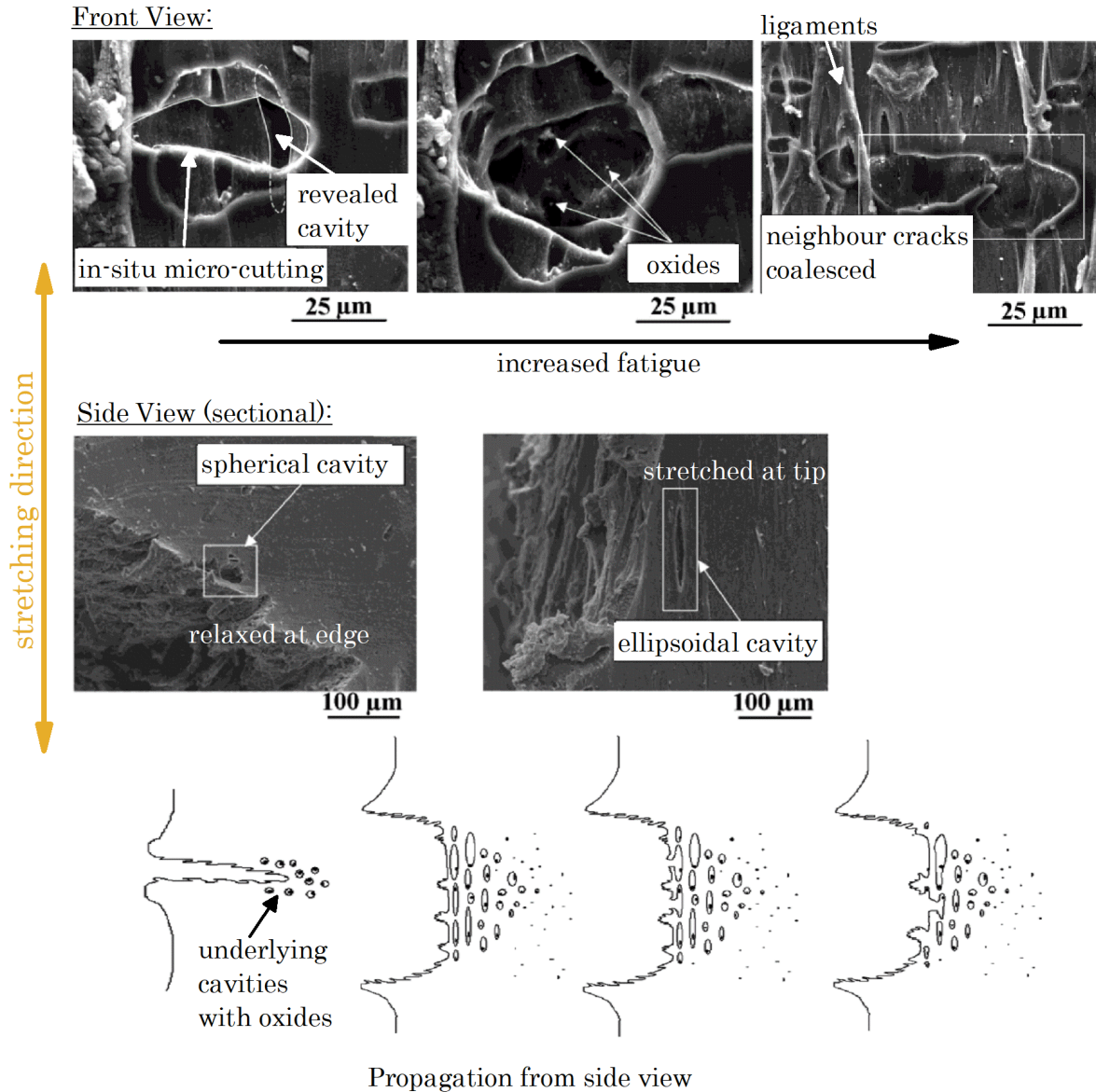


Figure 5.8: The representative SEM micrographs and schematic illustration of the crack propagation (stage 3 of Figure 5.7) from side view at of a crack tip according to Le Cam et al. Adapted from [129] with Copyright © 2004, American Chemical Society. Reprinted by permission.

The fatigued sample at large stretch ratio, NRCB1-140%20kc, was cut out from the working area to observe the internal section under light microscope as shown in Figure 5.9. Cracks with length ca. 100 μm were found inside of NRCB1-140%20kc. There are also in ellipsoidal (string,

see #1) or spherical shapes (see #2). Comparing Figure 5.9 with Figure 5.5, one can find that the cracks' size of NRCB1-140%20kc is distinctively bigger than that of NRCB1-90%60kc, although both of them are aged at the same fatigue life, $0.5N_f$ (at $\varepsilon_0 = 90\%$, $0.5N_f = 60$ kc; at $\varepsilon_0 = 140\%$, $0.5N_f = 20$ kc). It suggests that, at the same fatigue life, a larger stretch ratio ε_0 during fatigue induces bigger size of the cracks in the rubber composites. This finding is consistent with the results from the statistical studies via SEM in literatures [192, 194] (at $0.6N_f$, the population of cracks of the fatigued rubber increased 6 times from $\varepsilon_0 = 100\%$ to $\varepsilon_0 = 200\%$). Based on XmCT technique, it was also found that under larger stretching ratio during fatigue, both the population density and the maximum size of the cracks increased [190].

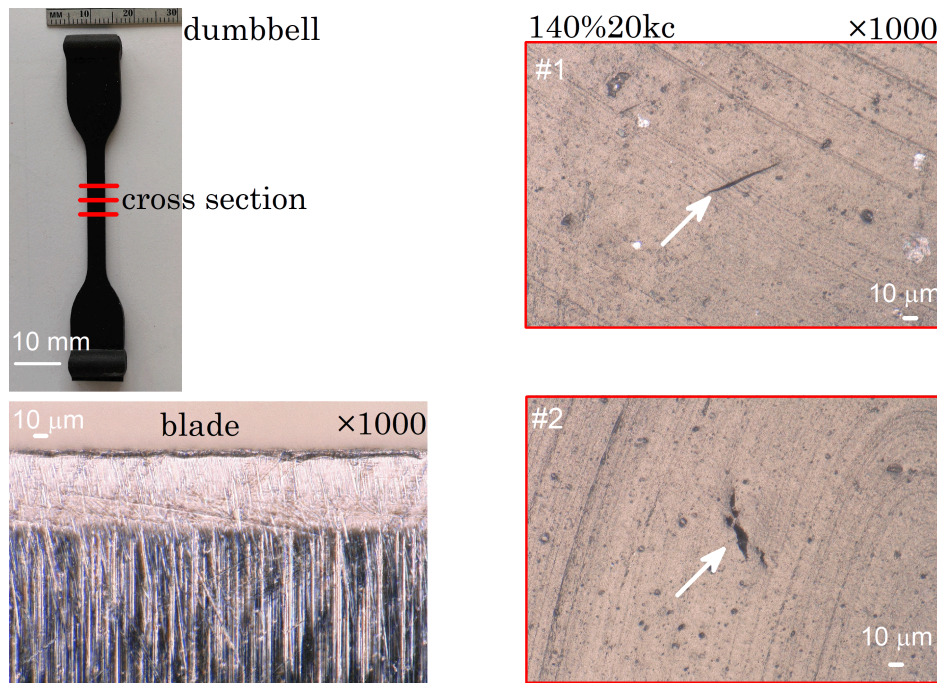


Figure 5.9: The selective cross-sectional images with micro-cracks in the middle working area of NRCB1-140%20kc at magnifications of 1000 times under VHX 900F microscope.

In summary for the fatigue process in CB filled NR, the big CB agglomerates spheres (average diameter of 9–17 μm [192]) with less occluded rubber are responsible for the initiation of the cracks by debonding from the rubber matrix. During the crack propagation, the pre-existing active voids, such as the oxides with low adhesion interaction and internal cohesion force, will open the cavities progressively at the tip of the crack under stretch [129]. Following this, the ligaments besides the cavities will only be broken mechano-chemically at large enough stretch energy, leading to the coalescence of neighboring cavities. At the same fatigue life, a larger stretch ratio produces more cracks with bigger size.

With regards to the rheological response of NRCB1-140%20kc, its linear and FT-rheological parameters are compared with the original sample and NRCB1-90%60kc as shown in Figure 5.10.

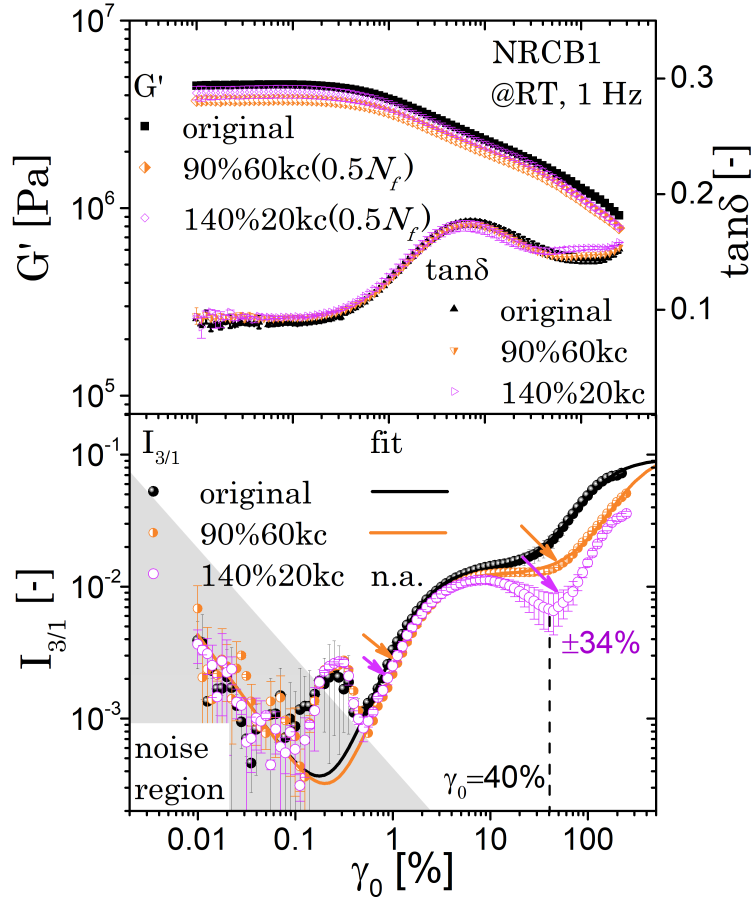


Figure 5.10: The strain dependence of the linear and FT-rheological parameters of NRCB1 before and after mechanical aging at same fatigue life but different stretching ratio. The large error bars of the $I_{3/1}$ at strain amplitudes around $\gamma_0 = 45\%$ of NRCB1-140%20kc indicated the low repeatability properties between the specimens. Data were acquired from oscillatory torsion on ARES-G2 at $\omega_1/2\pi = 1$ Hz and room temperature.

Similar to NRCB1-90%60kc, the linear rheological parameters of NRCB1-140%20kc, G' and $\tan\delta$, only changed slightly. The nonlinearity of the filler network in NRCB1-140%20kc, $I_{3/1}(\gamma_0 = 2.5\%)$, decreased slightly to a similar amplitude as NRCB1-90%60kc. This implies that for the same batch of NR composites, the amount of reversible rubber chains retracted from CB filler surface are similar. As suggest in reference [192], the debonded CB agglomerates from the rubber matrix (see the CB aggregates on the edge of micro-cracks in Figure 5.7) were very brittle thus few rubber chains adhered on them. While there are also CB aggregates consist of occluded rubber with a layer of the rubber chains absorbed on the filler surface.

This forms gel-like agglomerates [7, 35], which should not be brittle. During the fatigue of NRCB1, it is possible that mainly the brittle CB agglomerates have been debonded instead of the gel-like ones. Consequently, there was only a minor change of the filler-matrix interaction, compared to the starting material. This could explain why the rheological nonlinearity of the filler network in NRCB1 only decreased slightly after mechanical aging.

However, compared to NRCB1-90%60kc, the $I_{3/1}$ of NRCB1-140%20kc dropped more drastically from the original sample at a large strain amplitude around $\gamma_0 = 40\%$, as indicated by the dashed line in Figure 5.10. This strain amplitude fell in between the two characteristic strain amplitudes, the $\gamma_{cF} = 2.5\%$ of the filler network and the $\gamma_{cP} = 70\%$ of the polymer network. The $I_{3/1}$ of NRCB1-140%20kc even decreased after $\gamma_{cF} = 2.5\%$, without a limiting plateau of $I_{3/1}(\gamma_0)$ as commonly observed as before. As a consequence, the Equation 4.5 of $I_{3/1}(\gamma_0)$ is not applicable for NRCB1-140%20kc. This $I_{3/1}(\gamma_0)$ behavior could be related to the strong disconnection between the filler network and the polymer network at the cracks (in size of $100 \mu\text{m}$ or even bigger). Those open cavities results in a macroscopic non-continuous body. Under deformation, the movement of the network at the cavity point does not follow the same amplitude as the rubber networks. Thus it presents a "disconnection" between the region of the filler network induced $I_{3/1}$ (near γ_{cF}) and that of the polymer network induced (near γ_{cP}).

Moreover, in the disconnection region around $\gamma_0 = 40\%$, the $I_{3/1}$ of NRCB1-140%20kc strongly fluctuated with a standard deviation of $\pm 34\%$, as labeled in Figure 5.10. The deviation is much stronger than that of NRCB1-90%60kc in the same region ($\pm 3\%$). According to the statistics of the cracks size in Figure 8 of reference [192], at the same fatigue life, the size of the resulting cracks scatters more severely for the larger stretch ratio aged samples (ε_0 from 60% to 200%). Results from XmCT [190] (Figure 9) also reveals that the rubber composite fatigued at larger stretch ratio contains a broader distribution of the volumetric densities of the cavities with bigger size. Compared to NRCB1-90%60kc, the cracks in NRCB1-140%20kc may also have a broader distribution with bigger size. During the rheological characterization on the ARES-G2, the working zone of the rectangular specimens between the torsion clamps was very small ($3 \times 1.5 \times 1 \text{ cm}^3$, see Chapter 2). The size and density of the cracks in each specimen of NRCB1-140%20kc could have a large variation, resulting in the strong fluctuation of $I_{3/1}$ at $\gamma_0 = 40\%$.

To further prove the influence of those cracks on $I_{3/1}$, non-reinforcing fillers as artificial cracks can be intentionally blended into the NRCB1. The size and shape of the filler should be similar as the cracks in NRCB1-140%20kc. The candidates includes the montmorillonite clay or

other silicate flakes [195,196] with a diameter of $100\ \mu\text{m}$. Without organic chemical treatment of the surface of those inorganic fillers, the filler-polymer incorporation is neglectable in comparison with the reinforcing filler such as the CB in this work. In this way, the pre-existing "disconnection" zone at the artificial cracks may lead to the similar behavior of $I_{3/1}$ at large strain amplitude.

With respect to the structures of the rubber network in molecular level, the DQ-NMR results of the mechanically aged samples are compared to the original NRCB1 in Figure 5.11. Similar to NRCB1-90%60kc, the DQ buildup curve of NRCB1-140%20kc was also close to the original NRCB1. The crosslink density and network defects, in terms of D_{res} and I_{def} , did not change after fatigue at both conditions. This suggests that, even fatigued at the large stretch ratio of $\varepsilon_0 = 140\%$, the chemical structures of the rubber network in NRCB1 still do not change drastically. However, NRCB1-140%20kc does consist of $100\ \mu\text{m}$ cracks. In other words, the overall mechano-chemical breakage of the NR chains during the crack propagation is still trivial in comparison with the whole chemically crosslinked matrix. This is not the case for the pure chemical scission of NR chains under hot-air aging as found in Chapter 4. After hot-air aging at 120°C for 3 days, the mesh size distribution of NRCB1 increases from $\sigma_D = 32.7$ to $90.4\ \text{Hz}$ and the amount of network defects is doubled.

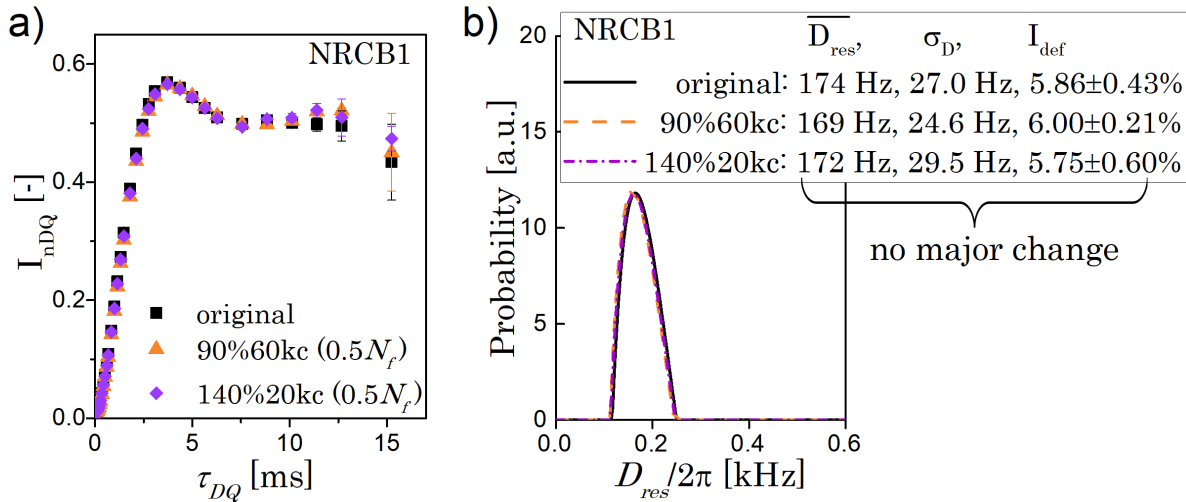


Figure 5.11: a) The normalized DQ buildup curves and b) the distribution of D_{res} of original NRCB1 and two mechanically aged counterparts at $0.5N_f$ and two stretching levels, NRCB1-90%60kc and NRCB1-140%20kc. There were no major change could be detected between the fatigued samples. The DQ-NMR raw data were acquired from mq20 NMR analyzer at 60°C .

In summary, although at the same fatigue life of NRCB1 ($0.5N_f$), there are more resulting

cracks with bigger size in the samples fatigued at a larger stretching ratio of $\varepsilon_0 = 140\%$ in comparison with that at $\varepsilon_0 = 90\%$. According to DQ-NMR, there are no obvious structural changes of the crosslinked rubber matrix at molecular level for both fatigued samples. This indicates that during the crack initiation and propagation, the mechano-chemical breaking of the rubber chains are trivial for the whole crosslinked network. The linear rheological properties of the two mechanically aged samples are similar. However, compared to NRCB1-90%60kc, NRCB1-140%20kc exhibits a stronger decline of $I_{3/1}$ at large strain amplitude with a disconnection zone between γ_{cF} and γ_{cP} .

5.3. Structural changes at the nano- and the micrometer scales

To understand the structural changes of NR during aging, the ^1H DQ-NMR technique was employed to characterize the averaged molecular level structures (at the nanometer scale) of the rubber network in a bulk sample. With the aid of microscopy, the surface or internal section of NR samples was observed at as low as micrometer scale. Based on DQ-NMR, the residual dipolar coupling constant, D_{res} , is directly proportional to the crosslink density. After regularization algorithm of the DQ buildup curve, a distribution curve of D_{res} can be deduced to describe the mean value of crosslink density as well as the broadness of the mesh grids. The tail intensity from the defects, I_{def} , can describe the percentage of network defects such as the broken chain ends, sols, etc. To investigate the potential micro-cracks under a light microscope, the surface of the substrate should be smooth with a good color contrast between the cracks and the matrix. A rough surface is commonly given via the marked patterns of the vulcanization mold or the leftover striations from the cutting blade. In addition, if the internal section is of interest, one has to destructively cut through the specimen at an arbitrary point. However, with proper preparation of the specimen, the micro-cracks in mechanical aged samples in this work has been characterized qualitatively. Correspondingly, the linear and FT-Rheological responses are acquired using specimens with millimeter size.

As has been reported for the mechanical aging of NRCB1 as above, the long term cyclic stretch on the materials before failure mainly produces cracks in the micrometer range other than the alternation of the chemical structures of the rubber matrix in nanometer range. Therefore, we claim that the micro-cracks are mainly responsible for the change of the rheological properties after fatigue. In contrast, during the static aging of NRCB1 in hot-air as shown in Chapter 4, the crosslink density or network defects or both of the rubber matrix changes through thermal-oxidation. Yet there was no micro-crack discovered in the hot-air aged samples as shown in Figure 5.12 below.

Therefore, one can summarize the structural changes of this NR composite under the two aging processes (hot-air and mechanical) as illustrated in Figure 5.12, based on the observation through DQ-NMR and light microscope. In the original composites, the rubber chains (the blue curly lines) are crosslinked by the sulfidic bridges (the red dots) with assistant of zinc oxides as activator (the yellow ellipsoids) and oxides from other additives. The matrix is reinforced by blending in CB fillers (the averaged diameter of CB grade N339 is 103

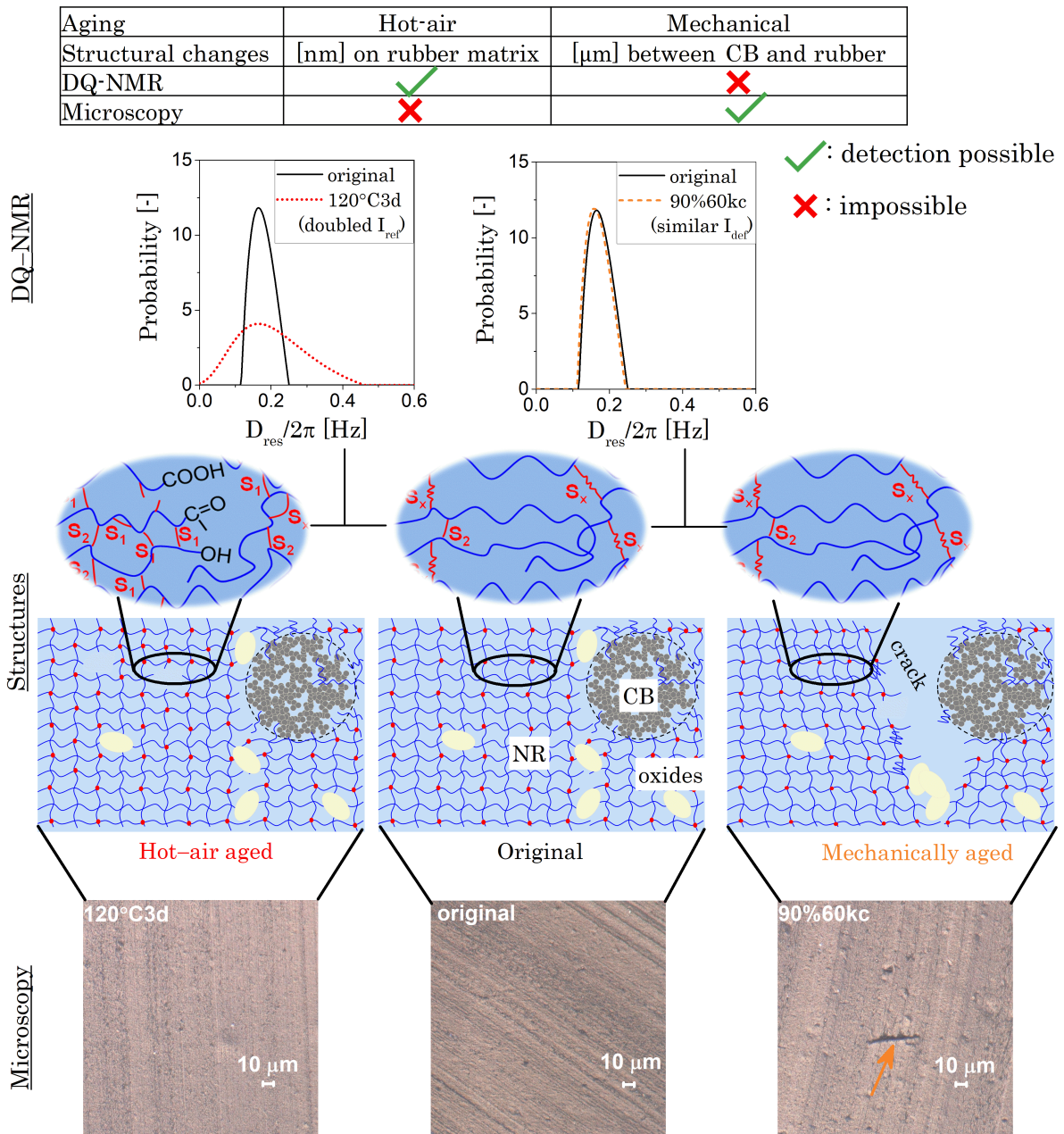


Figure 5.12: Schematic illustration of the network changes of NRCB1 composites in two types of aging process and the feedback from DQ-NMR and microscopy. The curly lines in blue are the rubber chains, which are chemically crosslinked by sulfidic bonds depicted as the red dots. The DQ-NMR only detect the structural changes of rubber chains at nanometer scale. One should notice that the DQ-NMR results are the averaged characters of all the rubber networks in the whole measured sample, but not just one spot of the black ellipse in the figure. Through the light microscope, only the cracks larger than micrometer size can be recognized under the microscope, which is just a small area of the fatigued sample.

nm in rubber matrix [35]), where some CB aggregates entangled with each other forming agglomerates with a diameter of 5-30 μm [192]. Under static hot-air aging, e.g. at 120 $^{\circ}\text{C}$ for 3 days, some polysulfidic links transform into mono-sulfidic bonds thus dense meshes. Meanwhile, there is thermal-oxidation induced chain scission. Eventually, the resulting rubber matrix is a polymer network with broadly distributed mesh size and high amount of defects. Those changes can be successfully detected by ^1H DQ-NMR in terms of D_{res} and I_{def} , as marked by a tick "✓" in Figure 5.12. However, the nanometer scale differences between the original and the hot-air aged can not be observed via light microscope, marked by a cross "×" in the figure. Under mechanical fatigue by cyclic stretching, micro-cracks initiates near a big CB agglomerate, which has less absorbed rubber chains on it. The crack propagate perpendicularly towards the stretching direction and break mainly along the area with oxides in the matrix. The cracks with length of more than 10 μm can be revealed via light microscope. However, there are no changes in the DQ-NMR results, since the mechano-chemical breakage of the rubber chains along the crack propagation is trivial in comparison with the whole crosslinks in the rubber matrix.

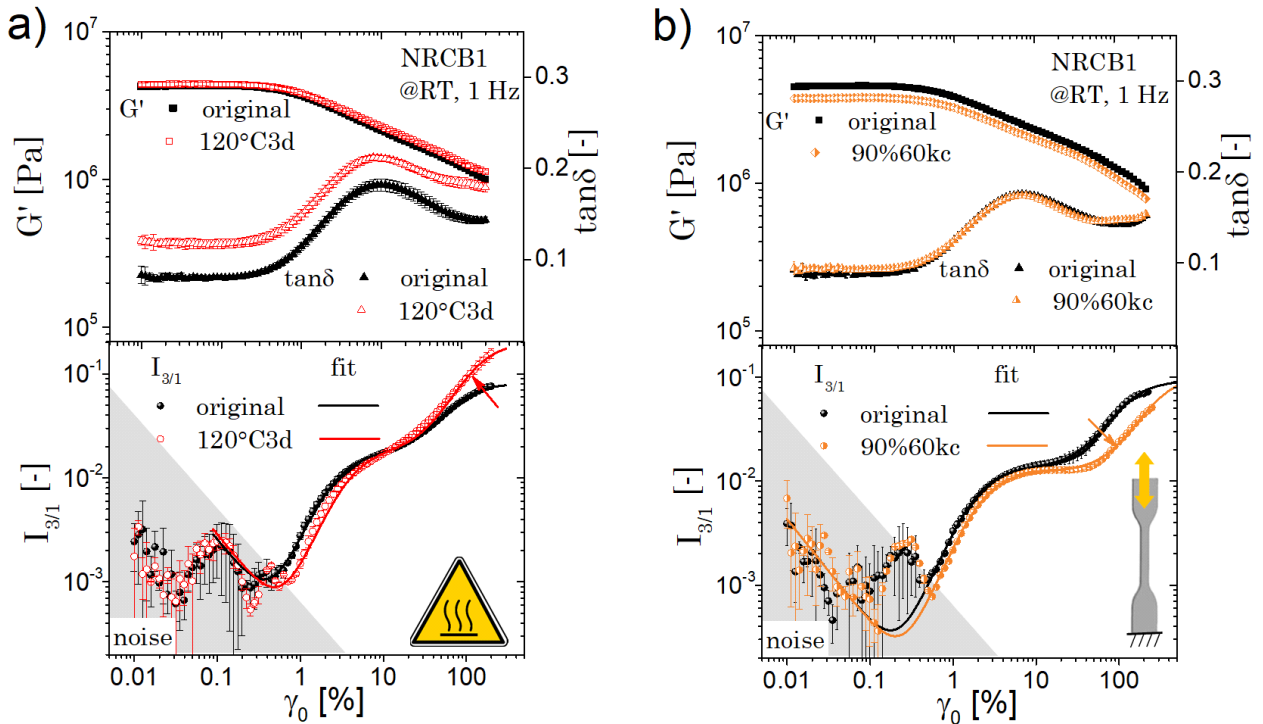


Figure 5.13: The response of linear and FT-rheological properties of NRCB1 to different aging processes: a) hot-air aging and b) mechanical aging. Notice, the original batch for hot-air aging and mechanical fatigue experiments were prepared separately and the properties are only compared with their original bathes, respectively.

With respect to the rheological response from the specimens at the millimeter size, the results of NRCB1 are shown in Figure 5.13 for the hot-air aged and the mechanical aged, respectively. After hot-air aging at 120 °C for 3 days (120C3d), only $\tan\delta$ in linear rheological parameters of NRCB1 shows a distinctive change (the $\tan\delta_0$ increased by 47%). The rheological nonlinearity of the material increases at large strain amplitude in the FT-Rheological term, $I_{3/1}$ (the $I_{3/1}$ at $\gamma_0 = 70\%$ increased by 37%) for the inhomogeneous rubber network with more defects. After fatigue at $\varepsilon_0 = 90\%$ for 60 kc (90%60kc), only minor changes of G' and $\tan\delta$ have been detected (less than 15%). The $I_{3/1}$ declines distinctively at large strain amplitude (the $I_{3/1}$ at $\gamma_0 = 70\%$ increased by 47%) for the fatigued sample with micro-cracks.

Table 5.1: Summary of the response from four methodologies (DQ-NMR, light microscopy, linear rheology and FT-rheology) to the two aging process of NRCB1. The up arrow and down arrow indicate the increase and the decrease of the parameters after aging, respectively, compared to the value of the original. The relative sensitive changes ($> 30\%$) and the detectable changes with a light microscope are highlighted in blue.

NRCB1	Hot-air aged 120 °C 3 days	Mechanically aged $\varepsilon_0 = 90\%$ 60 kc (0.5 N_f)
<i>DQ-NMR:</i>		
$\overline{D_{res}}$	↑4%	↓0.6%
σ_D	↑177%	↓9%
I_{def}	↑131%	↑2%
<i>Microscopy:</i>		
micro-cracks on surface	no	no
micro-cracks inside	no	yes
<i>Linear rheology:</i>		
G'_0	↑0.5%	↓16%
$\tan\delta_0$	↑36%	↑7%
<i>FT-rheology:</i>		
$I_{3/1}(\gamma_0 = 2.5\%)$	↓22%	↓21%
$I_{3/1}(\gamma_0 = 70\%)$	↑36%	↓47%
n_P	↑186%	↑27%
${}^3Q_{0P}$	↓8%	↓78%

The response to the two types of aging effect from the four characterization methods, DQ-NMR, light microscopy, linear rheology and FT-rheology, are summarized in Table 5.1. The relative changes higher than 30% and the effective response (detectable micro-cracks in light microscope) are highlighted in blue color. The limiting nonlinearity and the intrinsic nonlinearity of the polymer network, n_{cP} and ${}^3Q_{0P}$, have also been listed here.

Based on the definition of the intrinsic nonlinearity from FT-rheology (Equation 1.22) and the fitting function of $I_{3/1}(\gamma_0)$ (Equation 4.5), one can describe the intrinsic nonlinearity of the polymer networks as

$$\begin{aligned}
 {}^3Q_{0P} &\equiv \lim_{\gamma_0 \rightarrow 0} \frac{I_{3/1}(\gamma_0)}{\gamma_0^2} \\
 &= \lim_{\gamma_0 \rightarrow 0} \frac{n_P \frac{(\gamma_0/\gamma_{cP})^2}{(1+\gamma_0/\gamma_{cP})^2}}{\gamma_0^2} \\
 &= \frac{n_P \frac{(\gamma_0/\gamma_{cP})^2}{(1+0)^2}}{\gamma_0^2} \\
 &= \frac{n_P}{\gamma_{cP}^2}
 \end{aligned} \tag{5.1}$$

Thus ${}^3Q_{0P}$ can be calculated from n_{cP} and the critical strain of polymer network, γ_{cP} from the fitting of $I_{3/1}(\gamma_0)$ by Equation 4.5. The parameter n_{cP} was almost tripled (increased 186%) after the 120C3d hot-air aging, which was the highest changes. The ${}^3Q_{0P}$ of the 90%60kc fatigued NRCB1 declined more than 3 times (decreased 78%) than the original sample, stronger than other other parameters during mechanical aging.

Considering the summary in Table 5.1, the selection of detecting tools for two types of aging of NR could be explained as following. For NR undergoing chemical aging such as in hot-air, the structural changes occur on the rubber matrix at nanometer scale. The changes can be unveiled through ${}^1\text{H}$ DQ-NMR. For NR undergoing mechanical aging at early stage before failure, the structural changes occur in the composites near to the pre-existing flaws such as big filler agglomerates. Light microscope can be employed to reveal the changes until the cracks grow up to micrometer size from the flaws. However, this is a qualitative manner with arbitrary selection of the sample surface. Compared to the linear rheological response, the FT-rheological parameter at large strain amplitude could be taken as reference to detect the structural changes at nano-/micro-meter scales. Moreover, $I_{3/1}$ at large strain amplitude exhibits higher sensitivity, particularly, for the early stage mechanically aged NR composites.

6. Conclusion and Outlook

Due to its excellent elasticity and durability, natural rubber (NR) is an irreplaceable material in industry. The global consumption of NR is 13.9 million tonnes per year [2], which is the sum quantity of all other types of synthetic rubbers. In their service life, NR products are typically aged by thermal-oxidation or fatigued by long-term large deformation. Hence the aging mechanism of NR and the development of corresponding characterization methods are of great interest to improve the long time performance of the products. As typical viscoelastic materials, rubbers are commonly studied using dynamic mechanical analysis. Conventionally, the dynamic mechanical properties of NR are evaluated through linear rheological parameters such as the elastic modulus, G' , and the mechanical loss factor, $\tan\delta$. However, this analysis is only adequate in the linear viscoelastic regime (LVE) at small strain amplitude, where the stress response is still linear for the excited sinusoidal strain. In the nonlinear viscoelastic regime (NVE) at large strain amplitude, the stress waveform is distorted, i.e. nonlinear. The G' and $\tan\delta$ are acquired from a linear quantification of the nonlinear waveform, missing substantial information veiled in it. So the question then arises as to what would be the quantity and physical meaning of the nonlinear portion of the waveform in NVE as well as its response to the aging effect? To answer this question, the rheological nonlinearity of NR before and after aging were quantitatively examined by using a recently developed method, the Fourier-transform rheology (FT-rheology) [57, 59] in this work. In FT-rheology, the stress signal in NVE is Fourier transformed into the frequency domain and the relative intensity of the 3rd harmonic in the spectra, $I_{3/1}$, can be used as the direct quantity of the rheological nonlinearity. The FT-rheology technique has been examined successfully on polymer melts [61], colloids [60], plastics below the glass transition temperature [184] and rubbers in unvulcanized state [9, 10, 63]. To the best of our knowledge, it is the first time that this technique was used on vulcanized rubber.

The investigated samples are crosslinked NR that have been vulcanized in presence of sulfur and accelerators, filled with or without carbon black (CB). FT-rheology of the NR vulcanizates was implemented with an oscillatory torsion fixture on a strain controlled rheometer for the

strain sweep test at room temperature (RT) and an excitation frequency of $\omega_1/2\pi = 1$ Hz. The 1.5 mm thick rectangular samples were fixed sturdily on the torsion clamps so that the materials could be strain-swept from LVE to NVE regime, up to a oscillatory strain amplitude of $\gamma_0 = 200\%$. The behaviors of G' , $\tan\delta$ and $I_{3/1}$ as a function of γ_0 were acquired for the unaged (original) and differently aged NR vulcanizates. Using linear rheology, it is known that the introduction of filler networks into the matrix leads to a strain softening of the G' at small strain amplitude [48], known as the Payne effect [49]. Thus, the averaged value of the linear rheological parameters in LVE, G'_0 and $\tan\delta_0$, are selected as the representative of linear rheological properties. With respect to FT-rheology of NR vulcanizates, $I_{3/1}(\gamma_0)$ firstly pass a region where the noise dominates with a slope of -1 in the double logarithmic plot. Afterwards, the $I_{3/1}(\gamma_0)$ increase quadratically, until reaching a plateau after a critical strain amplitude. Such phenomena are consistent with other materials in literature from both experimental [9, 61] and simulation results [60]. The CB filled sample possesses an extra quadratic growth region of $I_{3/1}(\gamma_0)$ at a smaller critical strain amplitude. Accordingly, an empirical model was proposed as

$$I_{3/1}(\gamma_0) = n_F \frac{(\gamma_0/\gamma_{cF})^2}{1 + (\gamma_0/\gamma_{cF})^2} + n_P \frac{(\gamma_0/\gamma_{cP})^2}{1 + (\gamma_0/\gamma_{cP})^2} \quad (6.1)$$

for the growth of $I_{3/1}$ at the critical strain amplitudes for the filler network and polymer network, γ_{cF} and γ_{cP} , with the limiting nonlinearity, n_{cF} and n_{cP} , respectively [197]. The model is in well agreement with the experimental data, providing the $\gamma_{cF} = 2.5\%$ and the $\gamma_{cP} = 70\%$. The $I_{3/1}$ at the critical strain amplitudes, $I_{3/1}(\gamma_0 = 2.5\%)$ and $I_{3/1}(\gamma_0 = 70\%)$, can represent the rheological nonlinearity of the filler and polymer networks. Those two parameters were also used for the NR aging analysis.

To reveal the molecular level network structures of the NR vulcanizates, nuclear magnetic resonance (NMR) in time domain, such as ^1H double quantum NMR (DQ-NMR) [109], can be applied to gain the information about the polymer chain dynamics at a nanometer scale. The polymer chains in NR vulcanizate do not fluctuate isotropically like the dissolved molecules in dilute solutions due to the topological constrains from the crosslinks. At long time, the anisotropic fluctuation of polymer segments between the fix crosslinks leads to a residual local orderliness, which can be reflected by the residual dipolar coupling constants from DQ-NMR, D_{res} . For a crosslinked network well above the glass transition temperature, the D_{res} is independent of the temperature and proportional to the crosslink density (number of crosslinks per volume) thus can be directly used to quantify the mesh size of NR network. The DQ-NMR of NR vulcanizates were conducted using a low-field NMR analyzer with a

Baum-Pines NMR pulse sequence [132] at 60 °C, which is higher than $100\text{ K} + T_g$ of NR. Based on an established procedure from literature [134], the distribution of crosslink density was obtained in term of D_{res} . The portion of the defects in the network, such as dangling ends, sols and broken segments after aging, was quantified by the intensity of the defects, I_{def} . Compared to the rather complex high-field NMR spectrometers, the low-field NMR analyzer in a bench-top size is more efficient to conduct the DQ-NMR experiments, providing sufficient information about the network structures. Additionally, the DQ-NMR approach is more environmentally friendly in comparison to traditional characterization methods for the crosslink density, e.g. the swelling equilibrium test of crosslinked rubber in solvents such as toluene.

With the additional aid of a light reflection microscope, the surface or the internal section of the samples were checked for generated cracks larger than micrometer size, particularly, in some mechanically aged samples.

Vulcanization kinetics of NR:

Depending on the vulcanization chemicals in sulfur-accelerator-NR system, the types of sulfidic links and their compositions in NR vulcanizates are different. It is of essential importance to clarify them since the chemical nature of the crosslinks determines the resistance of the vulcanizates against aging. According to the efficiency of the sulfur usage to generate crosslinks, the vulcanization systems can be categorized into three types with the sulfur to accelerator ratio from high to low: the conventional vulcanization (CV), the semi-efficient vulcanization (SEV) and the efficient vulcanization (EV). Five NR samples with those vulcanization systems at high, medium or low concentrations of the chemicals were prepared for this study, namely CVhigh, CVlow, SEVmed, EVhigh and EVlow.

The vulcanization kinetics of rubber have been studied in a variety of approaches, e.g. using rheology to check the macroscopic elasticity development as a function of the curing time, $G'(t_{curing})$, or conducting NMR relaxometry experiments to investigate the molecular level dynamics in term of the transversal relaxation time during curing, $T_2(t_{curing})$. However, it is not possible to directly correlate G' with T_2 as the results are acquired from separated experiments. In this work, the rheological experiment and the NMR relaxometry of NR were conducted in parallel on a unique combination of a 25 MHz lab-made NMR with a rheometer, RheoNMR [123], at 140 °C. For rheological characterization, the samples were sheared on grooved ceramic parallel-plates at a frequency of 1 Hz and $\gamma_0 = 0.5\%$ in the LVE regime of NR. The in-situ NMR transversal relaxation experiments were conducted with a NMR pulse sequence of magic sandwich echo, followed by a train of 180° pulses along -x and +x axis

with phase cycling (MSE-xx4) [127]. This allows a direct correlation between the macroscopic elasticity from rheology and the molecular dynamics from NMR.

During vulcanization of NR, the initial intensity of NMR magnetization was stable while the relaxation curves distinctively shifted to short relaxation time. There are mainly two types of polymer segments in NR. One is the mobile segments far away from the crosslinks with a long relaxation time, $T_{2M} = \text{ca. } 5 \text{ ms}$, and the other is the rigid segments close to the crosslinks, T_{2R} . The relaxation curves were analyzed through the combination of a compressed exponential function, $\exp[-(\frac{t}{T_{2R}})^\beta]$, on the rigid segments with the compression factor $\beta = 1.6$ and a single exponential term on the mobile counterparts. The main evolution occurred on the rigid segments, $T_{2R}(t_{curing})$, which the trend was similar to $G'(t_{curing})$. However, due to the interdependence of T_{2R} with other NMR parameters during fitting, it is not suitable to describe the chain dynamic of the whole sample singly by the T_{2R} . Therefore, it may be misleading to correlate only the T_{2R} with G' .

To derive a single representative parameter from the NMR, an averaged chain dynamic value was calculated via the inverse Laplace transformation (ILT). The relaxation curves were firstly transformed into the distribution of D_{res} , which is related to the relaxation rate $1/T_2$, via ILT with a Gaussian-type kernel. Then the number averaged value from the distribution, $D_{res,n}$, was used to correlate with G' .

The macroscopic elasticity, G' , of the bulk sample is proportional to the crosslink density ν since $G' \propto \nu RT$ with R the universal gas constant and T the temperature. The number-averaged residual dipolar coupling constant, $D_{res,n}$, is the representative parameter for local (nanometer scale) rigidity of the rubber chain segments. The chain segments bonded by long polysulfidic links ($-S_x-$) should be more mobile than those bonded by short mono-/disulfidic bridges ($-S_{1,2}-$). In EV samples, the evolution of $D_{res,n}$ as a function of G' is linear, indicating only one type of crosslinks generated in EV. However, $D_{res,n}(G')$ of CV samples is developed nonlinearly and accelerated at the end of the vulcanization period. During the middle period, the $D_{res,n}$ of EV samples were higher than their CV counterparts at the same G' . This implies that at the same crosslink density, the polymer segments in EV are more rigid. This is attributed to the $-S_{1,2}-$ bridges in EV, while the segments of CV in this period are crosslinked by $-S_x-$. At the end period of CV vulcanization, the acceleration of $D_{res,n}(G')$ suggests that the enhancement of local chain rigidity is stronger than the production of new crosslinks. This is because the polysulfidic bonds in CV samples transform into mono-/disulfidic bonds. The different build-up kinetics of sulfidic crosslinks between EV and CV samples are summarized in Figure 6.1. The $D_{res,n}(G')$ correlation curve of SEVmed fluctuates in between that of

EVhigh and CVhigh. This suggests that both mono-, di- and polysulfidic links are produced along the vulcanization course of SEVmed. Consequently, the varying crosslink types for NR with different vulcanization systems are deduced with this unique setup on an unperceived level and the interpretation agrees with the findings in literature [24].

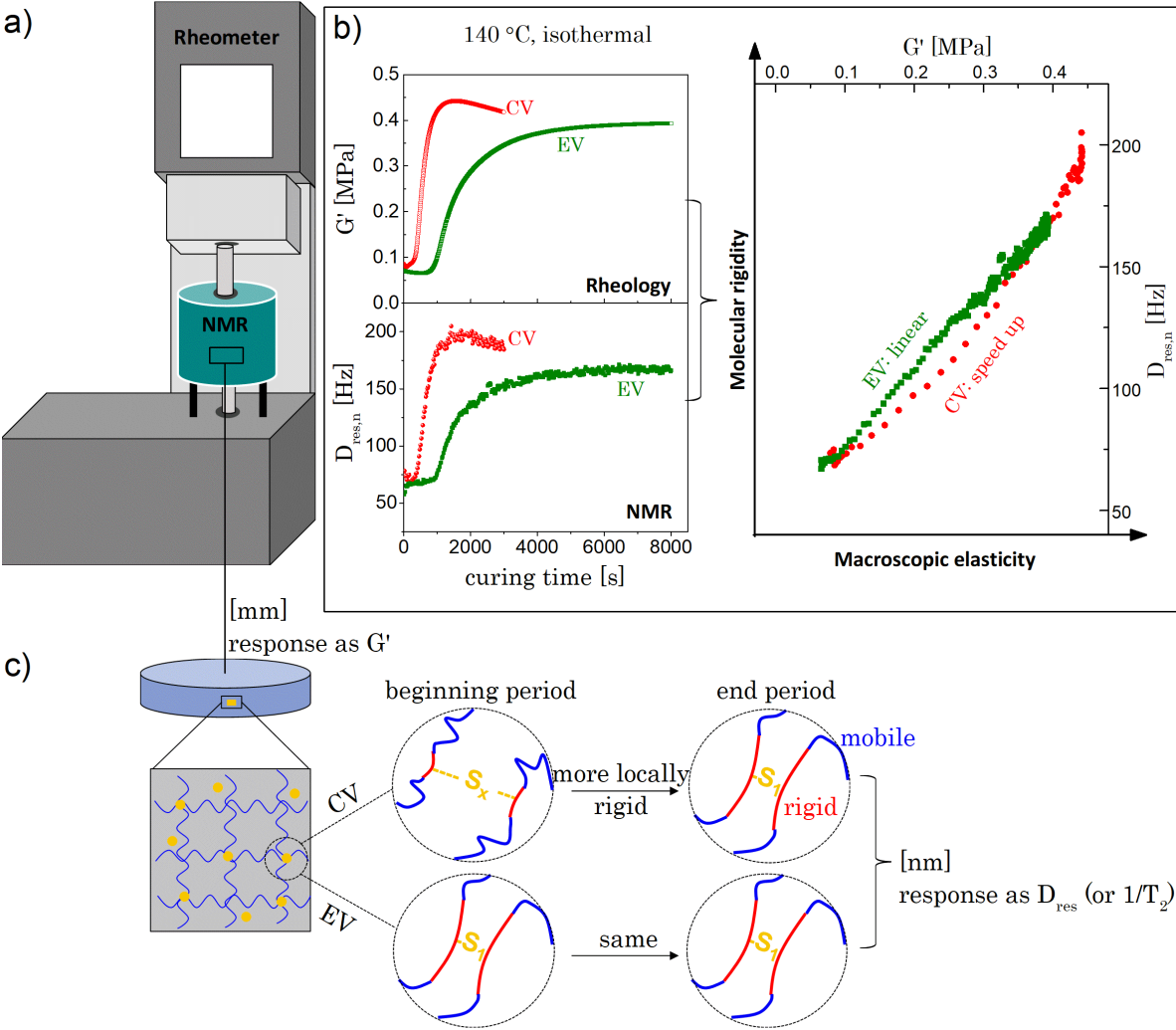


Figure 6.1: With a) the worldwide unique hyphenation of rheology and NMR, one can correlate the local molecular rigidity $D_{res,n}$ to the macroscopic elasticity G' of NRs during vulcanization. In efficient vulcanization system (EV), the $D_{res,n}(G')$ is linear. While in conventional vulcanization system (CV), the $D_{res,n}(G')$ speeds up at the end period. This is originated from c) the different build-up kinetics of sulfidic links in the two systems.

Hot-air aging of NR:

The vulcanized NR sheets were aged in a heating oven in air atmosphere (hot-air aging) at 70 °C or 120 °C for different duration. Both the original and the hot-air treated samples were submitted to rheology and DQ-NMR characterization to gain knowledge about the macroscopic and molecular changes.

During the hot-air aging at 70 °C aged for 28 days of the unfilled sample, NR1, the network became denser without generating more network defects. At this relatively low temperature aerobic aging, the polysulfidic links in the starting materials mainly transform into more crosslinks in the form of mono-/disulfidic bonds [28, 164]. This increased crosslink density is responsible to the monotonic increase of the elasticity, G'_0 , and the decrease of the loss factor, $\tan\delta_0$. Those aged materials exhibit a lower rheological nonlinearity of the polymer network, $I_{3/1}(\gamma_0 = 70\%)$. For the hot-air aging of NR1 at 120 °C, the aging trend in the early stage was similar as the 70 °C aging but then inverted after 0.5 days. At 120 °C for 3 days, the network became inhomogeneous with a doubled amount of network defects. This originates from the chain scission reactions via thermal-oxidation on the unsaturated diene rubber chains [28]. In response, $\tan\delta_0$ increases with a high rheological nonlinearity. The retention ability of NR towards hot-air aging was also compared for the samples with different vulcanization systems. The crosslink density as well as the rheological properties of the CV samples change most drastically since the polysulfidic links in CV are not stable [24]. The EV samples with mono-/disulfides linked networks show the best resistance to the aerobic aging, followed by the SEVmed sample.

With respect to the 50 phr CB (grade N339) filled NR sample with normal dosage of anti-oxidant, NRCB1, the evolution of the rheological properties under progressive aerobic aging at 120 °C was delayed by 0.5 days with respect to NR1. This is attributed to the filler CB, which can attract the free radicals thus slow down the thermal-oxidation of the rubber chains. The rheological nonlinearity of the filler involved network, $I_{3/1}(\gamma_0 = 2.5\%)$, always decreased after hot-air aging. One possible explanation is that the polymer chains desorb from the filler surface after heat treatment, reducing the nonlinearity of the filler network.

Doubling the amount of anti-oxidant in NRCB1 will take affect after 1 days for hot-air aging at 120 °C, according to the evolution of $I_{3/1}(\gamma_0 = 70\%)$. Within the compared samples, the FT-rheological parameter $I_{3/1}(\gamma_0 = 70\%)$ shows a highest relative sensitivity towards hot-air aging effect (maximum change by 90%) than the linear rheological parameters, the G'_0 (maximum change by 18%) and the $\tan\delta_0$ (maximum change by 63%).

Mechanical aging of NR:

The mechanical aging was examined only on the 50 phr CB reinforced NR sample, NRCB1, which is more relevant. The dumbbell specimens were mechanically aged/fatigued under cyclic stretching at $\varepsilon_0 = 90\%$ / 140% for kilo cycles (kc) before the cycle number of failure, N_f , i.e. without visually observable cracks on the surface or a drastic drop of the modulus. NRCB1 were either fatigued at the same stretch ratio of $\varepsilon_0 = 90\%$ but different life (at $30\text{kc} = 0.25N_f$ and at $60\text{kc} = 0.5N_f$) or at the same life but a larger stretch ratio of $\varepsilon_0 = 140\%$ (at $20\text{kc} = 0.5N_f$). The fatigued samples were named as NRCB1-90%30kc, NRCB1-90%60kc and NRCB1-140%20kc, correspondingly.

After aging at $\varepsilon_0 = 90\%$, only minor changes of the linear rheological parameters were observed with a maximum decrease of the storage moduli in LVE regime, G'_0 , by 15%. The number of fatigue cycles has no obvious influence on the linear rheological properties. However, the rheological nonlinearity at large strain amplitude, $I_{3/1}(\gamma_0 = 70\%)$, dropped distinctively as a function of the fatigue cycle, with a maximum change by 50% for the NRCB1-90%60kc. This can be attributed to the micro-cracks ($< 40\mu\text{m}$) inside of the NRCB1-90%60kc as discovered under a microscope.

The NRCB1-140%20kc was the sample fatigued at a large stretch ratio but the same life as NRCB1-90%60kc (both were $0.5N_f$). There were more micro-cracks found in NRCB1-140%20kc in size of $100\mu\text{m}$. As suggested in literature [129, 192], at the initiation stage, the cracks are generated from the debonding between the big CB agglomerates ($> 10\mu\text{m}$) and the rubber matrix. Such CB agglomerates are brittle with few adsorbed rubber chains on the surface. At the crack propagation stage, the active flaw in the rubber matrix with oxides progressively open and then tear up the surrounding rubber ligaments. The linear rheological properties of NRCB1-140%20kc and NRCB1-90%60kc are similar. However, in comparison with NRCB1-90%60kc, the $I_{3/1}$ of NRCB1-140%20kc dropped more drastically at large strain amplitude from the original, with a disconnection of $I_{3/1}(\gamma_0)$ between the region of the filler network and the polymer network.

Based on the DQ-NMR results, there were no distinctive structural changes of the rubber matrix after mechanical aging on a nanometer scale in average since this method measures the averaged local molecular dynamics of the whole sample. It indicates that the mechano-chemical breakage of the polymer chains is neglectable on this volume average of the whole crosslinked rubber matrix. Therefore, the resulting micro-cracks from fatigue are responsible for the changes of rheological properties. To detect the effect of mechanical aging at early stage, $I_{3/1}$ at large strain amplitude exhibits higher sensitivity than the linear rheological

parameters.

In conclusion:

By using the unique combination of a rheometer and a NMR, the macroscopic rheological properties of NRs during vulcanization has been successfully correlated for the first time with their local chain dynamics. The correlation between the local residual dipolar coupling, $D_{res,n}$, and the mechanical property G' are different among the vulcanization systems, due to the varying build-up kinetics of sulfidic crosslinks. In efficient vulcanization system, the correlation curve is linear since only mono-/disulfidic crosslinks are generated along the vulcanization. In conventional vulcanization system, the rubber segments with mono-/disulfidic crosslinks at the end period of vulcanization is more locally rigid ($D_{res,n}$) than the polysulfidic linked segments at the beginning, while the macroscopic elasticity (G') only depends on the total number of the effective crosslinks.

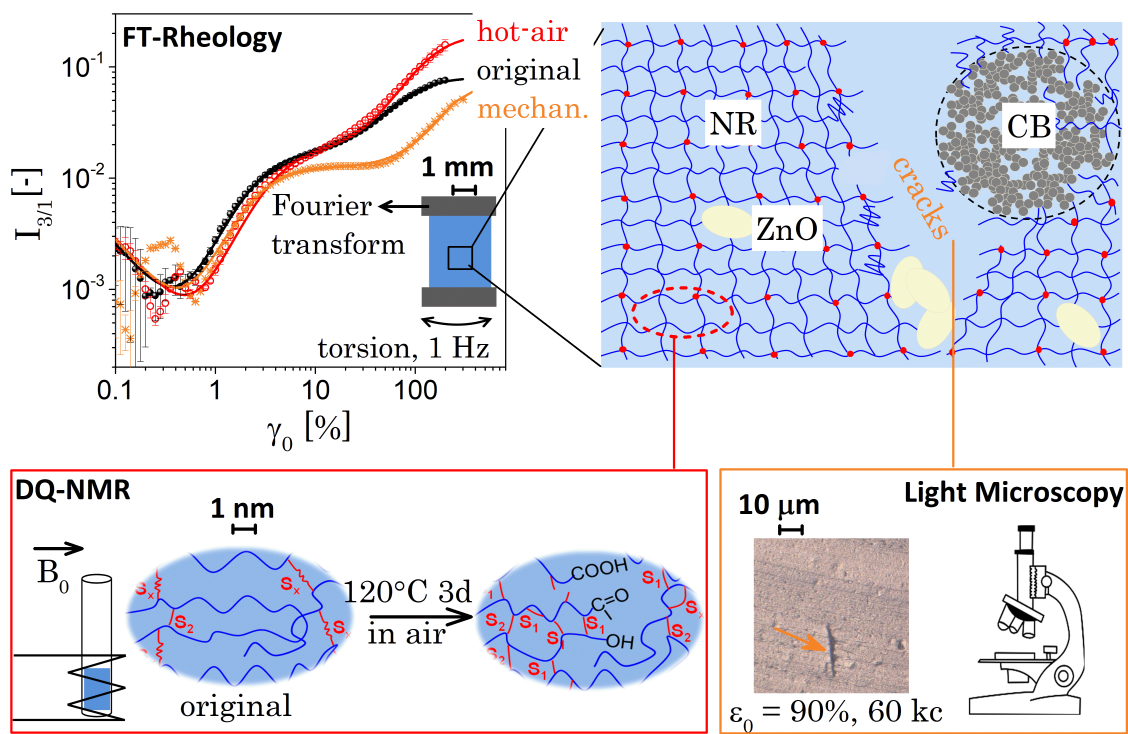


Figure 6.2: Both the hot-air aging and the mechanical aging of NR vulcanizates can be detected via FT-rheology for a sample on the millimeter size. After hot-air aging, the structural change of the NR matrix at nanometer scale can be revealed by using DQ-NMR. While the generated cracks in micrometer size after mechanical aging can be examined under a light microscope.

FT-rheology is a powerful tool to detect both the effect of hot-air aging and mechanical aging

on NR vulcanizates by providing the information of rheological nonlinearity, $I_{3/1}$, which is more sensitive than the parameters from linear rheology. With the aid of the rather simple DQ-NMR and optical microscope, one can deduce the origin of the structural changes in NR or its composites during aging at nanometer scales for the polymer matrix and at micrometer scales for the generated cracks as depicted in Figure 6.2.

Outlook of FT-rheology on the aging of rubber materials:

With the results and conclusions so far, further efforts to do on the FT-rheology of aged rubber materials can be proposed in several aspects as below.

To fully understand the nonlinear rheological response of the crosslinked rubber network, the experimental results from FT-rheology could be verified by simulation through proper constitutive models. For example, the Kelvin-Voigt model in Chapter 1.2.1 can be adapted with a Hookean spring and a non-Newtonian dash-pot to represent the crosslinked rubber network [39]. It is expected that a uniform network with a high crosslink density will response with a low rheological nonlinearity. Instead, for the inhomogeneous rubber network after hot-air aging, extra elements with different parameters for the springs and dash-pots should be generalized.

The $I_{3/1}$ from FT-rheology already exhibits higher sensitivity than the linear rheological parameters to the aging effect. However, the relative level of standard deviation for each method should also be taken into consideration. Statistic studies could be designed with enough number of specimens (e.g. more than ten). The detection reliability of one rheological parameter towards the aging effect of rubber can be defined as its sensitivity over its standard deviation in analogy to the concept of signal to noise ratio. Except the $I_{3/1}$ at the critical strain amplitudes, other parameters from FT-rheology, such as the limiting nonlinearity (n_{cF} , n_{cP}) and the intrinsic nonlinearity 3Q_0 ($=n/\gamma_c^2$), are worth being extracted as well for analysis.

In this work, the micro-cracks are only qualitatively investigated by cutting through the samples randomly and checking the surface. Quantitative manners such as the X-ray micro-computed-tomography (XmCT) [188] can be used to calculate the total volume of the cavities in a nondestructive way of the samples. The total volume could be correlated to the rheological nonlinearity at large strain amplitude, $I_{3/1}(\gamma_0 = 70\%)$, as suggested from the current results. An alternative approach to investigate the influence of the micro-cracks is by blending non-reinforcing fillers into NRCB1. Such fillers can be clay flakes of micrometer size as artificial cracks [195], supposed to be the similar effect as the micro-cracks in the fatigued

samples. In this way, one can deduce the influence of the volume of flaws/cracks on $I_{3/1}$.

The FT-rheology technique has been employed on the aging detection of rubber-based materials. However, some engineering products also contain skeleton components [198,199] such as carbon fibers and steels, where the rubber is bonded to them as shown in Figure 6.3. During usage, mechanical aging commonly occurs between the rigid skeleton and the soft rubber [200–202]. The application of FT-rheological methodology could be expanded to an assembly of the two components, e.g. by sinusoidally deforming the steel cord and Fourier transforming the stress response of the rubber side. In comparison with linear rheology, it is expected that the FT-rheology can characterize the mechanical aging of those products at an earlier stage.

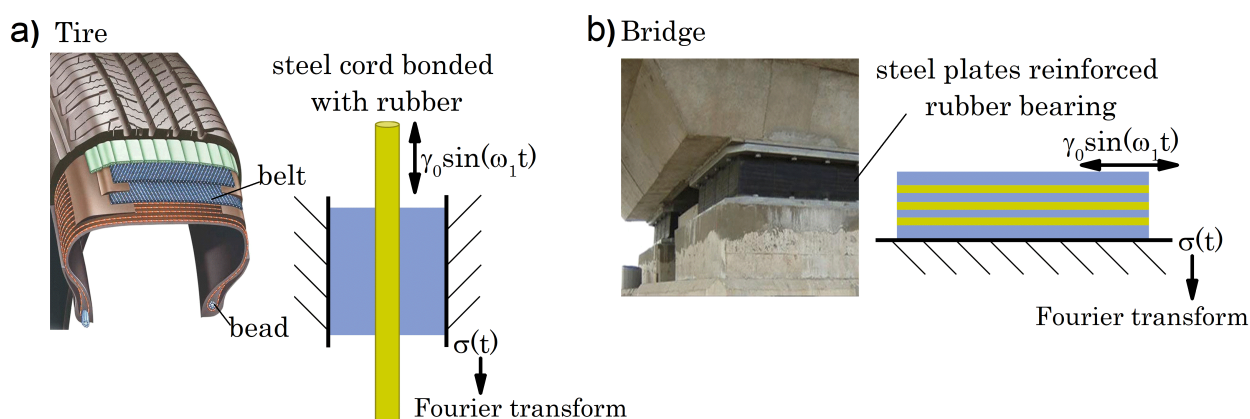


Figure 6.3: Many rubber-containing products consist of not only rubbers but also high modulus materials as the skeleton components, such as a) the belt and bead with steel cords in a tire, and b) the rubber bearing with steel plates under a bridge. Mechanical aging normally occurs at the interface between the steel and the rubber materials, which could be more effectively investigated via the FT-rheology technique. The structure the rubber network at molecular level can be revealed through the DQ-NMR technique. Before the DQ-NMR measurement, the rubber should be splitted from the metal skeleton, e.g. with a sharp blade, to make sure that there is no interference from the electronic conductive materials.

Bibliography

- [1] P. E. Hurley. History of natural rubber. *Journal of Macromolecular Science-Chemistry*, 15(7):1279–1287, 1981.
- [2] Resources from International Rubber Study Group (IRSG). *Rubber Statistical Bulletin*. 2018.
- [3] C. Goodyear. *Gum-elastic and its Varieties: With a Detailed Account of its Applications and Uses, and of the Discovery of Vulcanization*, volume 2. Published for the author, 1853.
- [4] K. Nagdi. *Rubber as An Engineering Material: Guideline for Users*. Hanser Publishers, Munich, 1993.
- [5] ASTM D7050-04. *Standard Practice for Rubber from Natural Sources–Sampling and Sorting Bales Based on Predicted Processing Properties*. ASTM International, West Conshohocken, PA, United States, 2019.
- [6] ASTM D3194-17. *Standard Practice for Rubber from Natural Sources–Plasticity Retention Index (PRI)*. ASTM International, West Conshohocken, PA, United States, 2017.
- [7] J. L. Leblanc. *Filled Polymers: Science and Industrial Applications*. CRC Press, Boca Raton, FL, United States, 2009.
- [8] G. Kraus. Reinforcement of elastomers by carbon black. In *Fortschritte der Hochpolymeren-Forschung*, pages 155–237. Springer, 1971.
- [9] L. Schwab, N. Hojdis, J. Lacayo-Penida, and M. Wilhelm. Fourier-transform rheology of unvulcanized, carbon black filled styrene butadiene rubber. *Macromolecular Materials and Engineering*, 301(4):457–468, 2016.
- [10] S. Nie, J. Lacayo-Pineda, and M. Wilhelm. Fourier-transform rheology of unvulcanized styrene butadiene rubber filled with increasingly silanized silica. *Soft Materials*, 17(3):269–282, 2019.
- [11] C. G. Moore, L. Mullins, and P. McL. Swift. Structural characterization of vulcanizates. part I. crosslinking efficiency of sulfur in unaccelerated natural rubber–sulfur systems. *Journal of*

Applied Polymer Science, 5(15):293–298, 1961.

- [12] C. G. Moore and B. R. Trego. Structural characterization of vulcanizates. part IV. use of triphenylphosphine and sodium di-n-butyl phosphite to determine the structures of sulfur linkages in natural rubber, cis-1, 4-polyisoprene, and ethylene-propylene rubber vulcanizate networks. *Journal of Applied Polymer Science*, 8(5):1957–1983, 1964.
- [13] C. G. Moore and A. A. Watson. Structural characterization of vulcanizates. part III. the cis-1,4-polyisoprene tetramethylthiuram disulfide-zinc oxide system. *Journal of Applied Polymer Science*, 8(2):581–602, 1964.
- [14] C. G. Moore and B. R. Trego. Structural characterization of vulcanizates. part II. use of triphenylphosphine to determine the structures of sulfur linkages in unaccelerated natural rubber-sulfur vulcanizate networks. *Journal of Applied Polymer Science*, 5(15):299–302, 1961.
- [15] G. M. Bristow and M. Porter. Structural characterization of vulcanizates. part V. determination of degree of chemical crosslinking of natural rubber gum vulcanizate networks. *Journal of Applied Polymer Science*, 11(11):2215–2226, 1967.
- [16] C. G. Moore and M. Porter. Structural characterization of vulcanizates. part VI. the 2-mercaptobenzothiazole-accelerated natural rubber-sulfur system. *Journal of Applied Polymer Science*, 11(11):2227–2253, 1967.
- [17] M. Porter. Structural characterization of vulcanizates. part VII. the n-cyclohexyl benzothiazole-2-sulfenamide-accelerated natural rubber-sulfur system. *Journal of Applied Polymer Science*, 11(11):2255–2269, 1967.
- [18] M. Porter, T. D. Skinner, and M. A. Wheelans. Structural characterization of vulcanizates. part VIII. the n-cyclohexylbenzothiazole-2-sulfenamide-accelerated sulfur vulcanization of natural rubber at 140–180 °C. and of synthetic cis-1, 4-polyisoprene at 140 °C. *Journal of Applied Polymer Science*, 11(11):2271–2283, 1967.
- [19] D. J. Elliott and C. G. Moore. Structural characterization of vulcanizates. part IX. comparison of the vulcanization of natural rubber and cis-trans-isomerized natural rubber with sulfenamide-accelerated sulfur and dicumyl peroxide vulcanization systems. *Journal of Applied Polymer Science*, 11(11):2285–2293, 1967.
- [20] D. S. Campbell. Structural characterization of vulcanizates. part X. thiol-disulfide interchange for cleaving disulfide crosslinks in natural rubber vulcanizates. *Journal of Applied Polymer Science*, 13(6):1201–1214, 1969.

-
- [21] D. S. Campbell. Structural characterization of vulcanizates. part XI. network-bound accelerator residues. *Journal of Applied Polymer Science*, 14(6):1409–1419, 1970.
- [22] D. S. Campbell. Structural characterization of vulcanizates. part XII. efficient vulcanization using a sulfenamide–thiuram disulfide accelerator system. *Journal of Applied Polymer Science*, 15(11):2661–2666, 1971.
- [23] B. Saville and A. A. Watson. Structural characterization of sulfur-vulcanized rubber networks. *Rubber chemistry and technology*, 40(1):100–148, 1967.
- [24] R. P. Quirk. Overview of curing and crosslinking of elastomers. *Prog. Rubber. Plast. Technol.*, 4:31, 1988.
- [25] M. Akiba and A. S. Hashim. Vulcanization and crosslinking in elastomers. *Progress in Polymer Science*, 22(3):475–521, 1997.
- [26] J. Y. Buzaré, G. Silly, J. Emery, G. Boccaccio, and E. Rouault. Aging effects on vulcanized natural rubber studied by high resolution solid state ^{13}C -NMR. *European Polymer Journal*, 37(1):85–91, 2001.
- [27] ASTM D572-04. *Standard Test Method for Rubber–Deterioration by Heat and Oxygen*. ASTM International, West Conshohocken, PA, United States, 2015.
- [28] N. M. Mathew and S. K. De. Thermo-oxidative aging and its effect on the network structure and fracture mode of natural rubber vulcanizates. *Polymer*, 24(8):1042–1054, 1983.
- [29] G. Previati and M. Kaliske. Crack propagation in pneumatic tires: Continuum mechanics and fracture mechanics approaches. *International Journal of Fatigue*, 37:69–78, 2012.
- [30] P. Behroozinia, R. Mirzaeifar, and S. Taheri. A review of fatigue and fracture mechanics with a focus on rubber-based materials. *Proceedings of the Institution of Mechanical Engineers, Part L: Journal of Materials: Design and Applications*, 233(5):1005–1019, 2019.
- [31] B. Näser. *Zur numerischen Bruchmechanik dissipativer Materialien: Theorie und Anwendung der Methode der materiellen Kräfte*. PhD thesis, Institute for Structural Analysis, Technical University of Dresden, 2009.
- [32] ASTM D430-06. *Standard Test Method for Rubber Deterioration – Dynamic Fatigue*. ASTM International, West Conshohocken, PA, United States, 2018.
- [33] ASTM D4482-11. *Standard Test Method for Rubber Property – Extension Cycling Fatigue*. ASTM International, West Conshohocken, PA, United States, 2017.

- [34] W. V. Mars and A. Fatemi. Factors that affect the fatigue life of rubber: a literature survey. *Rubber Chemistry and Technology*, 77(3):391–412, 2004.
- [35] J.-B. Donnet, R. C. Bansal, and M.-J. Wang. *Carbon black: science and technology, second edition*. Marcel Dekker Inc, New York, United States, 1993.
- [36] G. J. Lake and P. B. Lindley. The mechanical fatigue limit for rubber. *Journal of Applied Polymer Science*, 9(4):1233–1251, 1965.
- [37] H. Chun and A. N. Gent. Strength of sulfur-linked elastomers. *Rubber chemistry and technology*, 69(4):577–590, 1996.
- [38] J. M. Dealy and K. F. Wissbrun. *Melt rheology and its role in plastics processing: theory and applications*. Kluwer Academic Publishers, Dordrecht, Boston, London, 1999.
- [39] J. D. Ferry. *Viscoelastic properties of polymers*. John Wiley & Sons Inc., New York, Chichester, Brisbane, Toronto, 1980.
- [40] H. Watanabe. Viscoelasticity and dynamics of entangled polymers. *Progress in Polymer Science*, 24(9):1253–1403, 1999.
- [41] D. Roylance. Engineering viscoelasticity. *Department of Materials Science and Engineering—Massachusetts Institute of Technology, Cambridge, MA, United States*, 2139:1–37, 2001.
- [42] P.-G. de Gennes. Reptation of a polymer chain in the presence of fixed obstacles. *The Journal of Chemical Physics*, 55(2):572–579, 1971.
- [43] M. Doi and S. F. Edwards. Dynamics of concentrated polymer systems. part 1.—brownian motion in the equilibrium state. *Journal of the Chemical Society, Faraday Transactions 2: Molecular and Chemical Physics*, 74:1789–1801, 1978.
- [44] M. Doi and S. F. Edwards. Dynamics of concentrated polymer systems. part 2.—molecular motion under flow. *Journal of the Chemical Society, Faraday Transactions 2: Molecular and Chemical Physics*, 74:1802–1817, 1978.
- [45] M. Doi and S. F. Edwards. Dynamics of concentrated polymer systems. part 3.—the constitutive equation. *Journal of the Chemical Society, Faraday Transactions 2: Molecular and Chemical Physics*, 74:1818–1832, 1978.
- [46] M. Doi and S. F. Edwards. *The theory of polymer dynamics*, volume 73. Oxford University Press, 1988.

-
- [47] M. L. Williams, R. F. Landel, and J. D. Ferry. The temperature dependence of relaxation mechanisms in amorphous polymers and other glass-forming liquids. *Journal of the American Chemical Society*, 77(14):3701–3707, 1955.
- [48] J. L. Leblanc. Rubber–filler interactions and rheological properties in filled compounds. *Progress in Polymer Science*, 27(4):627–687, 2002.
- [49] A. R. Payne. The dynamic properties of carbon black-loaded natural rubber vulcanizates. part I. *Journal of Applied Polymer Science*, 6(19):57–63, 1962.
- [50] K. S. Cho, K. Hyun, K. H. Ahn, and S. J. Lee. A geometrical interpretation of large amplitude oscillatory shear response. *Journal of Rheology*, 49(3):747–758, 2005.
- [51] K. Hyun, S. H. Kim, K. H. Ahn, and S. J. Lee. Large amplitude oscillatory shear as a way to classify the complex fluids. *Journal of Non-Newtonian Fluid Mechanics*, 107(1-3):51–65, 2002.
- [52] R. H. Ewoldt, A. E. Hosoi, and G. H. McKinley. New measures for characterizing nonlinear viscoelasticity in large amplitude oscillatory shear. *Journal of Rheology*, 52(6):1427–1458, 2008.
- [53] M. Abramowitz and I. A. Stegun. *Handbook of mathematical functions with formulas, graphs, and mathematical tables*, volume 55. US Government printing office, 1948.
- [54] R. N. Bracewell and R. N. Bracewell. *The Fourier transform and its applications*. McGraw-Hill, New York, 1986.
- [55] M. Wilhelm, D. Maring, and H. W. Spiess. Fourier-transform rheology. *Rheologica Acta*, 37(4):399–405, 1998.
- [56] S. Onogi, T. Masuda, and T. Matsumoto. Non-linear behavior of viscoelastic materials. i. disperse systems of polystyrene solution and carbon black. *Transactions of the Society of Rheology*, 14(2):275–294, 1970.
- [57] K. Hyun, M. Wilhelm, C. O. Klein, K. S. Cho, J. G. Nam, K. H. Ahn, S. J. Lee, R. H. Ewoldt, and G. H. McKinley. A review of nonlinear oscillatory shear tests: Analysis and application of large amplitude oscillatory shear (LAOS). *Progress in Polymer Science*, 36(12):1697–1753, 2011.
- [58] M. Wilhelm, P. Reinheimer, and M. Ortseifer. High sensitivity fourier-transform rheology. *Rheologica Acta*, 38(4):349–356, 1999.
- [59] M. Wilhelm. Fourier-transform rheology. *Macromolecular Materials and Engineering*, 287(2):83–

105, 2002.

- [60] D. Merger, M. Abbasi, J. Merger, A. J. Giacomin, C. Saengow, and M. Wilhelm. Simple scalar model and analysis for large amplitude oscillatory shear. *Applied Rheology*, 26(5):12–26, 2016.
- [61] M. A. Cziep, M. Abbasi, M. Heck, L. Arens, and M. Wilhelm. Effect of molecular weight, polydispersity, and monomer of linear homopolymer melts on the intrinsic mechanical nonlinearity in MAOS. *Macromolecules*, 49(9):3566–3579, 2016.
- [62] D. Ahirwal, H. Palza, G. Schlatter, and M. Wilhelm. New way to characterize the percolation threshold of polyethylene and carbon nanotube polymer composites using Fourier transform rheology. *Korea-Australia Rheology Journal*, 26(3):319–326, 2014.
- [63] J. L. Leblanc and G. Nijman. Engineering performance and material viscoelastic analyses along a compounding line for silica-based compounds, part 2: Nonlinear viscoelastic analysis. *Journal of applied polymer science*, 112(3):1128–1141, 2009.
- [64] J. L. Leblanc, M. Putman, and E. Pianhanuruk. A thorough study on the relationships between dispersion quality and viscoelastic properties in carbon black filled SBR compounds. *Journal of Applied Polymer Science*, 121(2):1096–1117, 2011.
- [65] J. L. Leblanc. Effect of temperature on dynamic rheological properties of uncured rubber materials in both the linear and the nonlinear viscoelastic domains. *Journal of Applied Polymer Science*, 126(2):408–422, 2012.
- [66] K. Hyun and M. Wilhelm. Establishing a new mechanical nonlinear coefficient Q from FT-rheology: First investigation of entangled linear and comb polymer model systems. *Macromolecules*, 42(1):411–422, 2008.
- [67] E. M. Purcell, H. C. Torrey, and R. V. Pound. Resonance absorption by nuclear magnetic moments in a solid. *Physical Review*, 69(1-2):37, 1946.
- [68] F. Bloch, W. W. Hansen, and M. E. Packard. Resonance absorption by nuclear magnetic moments in a solid. *Physical Review*, 69:12, 1946.
- [69] F. Bloch. Nuclear induction. *Physical Review*, 70(7-8):460–474, 1946.
- [70] M. Wilhelm. *NMR-spectrometry of polymers, Lecture notes*. Institute of Chemical Technology and Polymer Chemistry, Karlsruhe Institute of Technology, private copy, 2009.
- [71] C. P. Slichter. *Principles of Magnetic Resonance*, volume 1. Springer Science & Business

- Media, 2013.
- [72] K. Schmidt-Rohr and H. W. Spiess. *Multidimensional solid-state NMR and polymers*. Academic Press, 2012.
- [73] F. A. Bovey, L. Jelinski, and P. A. Mirau. *Nuclear Magnetic Resonance Spectroscopy, 2nd Edition*. Academic Press, 1988.
- [74] B. Blümich. *Essential NMR for Scientists and Engineers, 2nd Edition*. Springer, 2019.
- [75] R. Kimmich and E. Anoardo. Field-cycling nmr relaxometry. *Progress in Nuclear Magnetic Resonance Spectroscopy*, 44(3-4):257–320, 2004.
- [76] D. Besghini, M. Mauri, and R. Simonutti. Time domain NMR in polymer science: from the laboratory to the industry. *Applied Sciences*, 9(9):1801, 2019.
- [77] V. J. McBrierty and D. C. Douglass. Recent advances in the NMR of solid polymers. *Journal of Polymer Science: Macromolecular Reviews*, 16(1):295–366, 1981.
- [78] F. Fujara, D. Kruk, and A. F. Privalov. Solid state field-cycling NMR relaxometry: Instrumental improvements and new applications. *Progress in Nuclear Magnetic Resonance Spectroscopy*, 82:39–69, 2014.
- [79] N. Bloembergen, E. M. Purcell, and R. V. Pound. Relaxation effects in nuclear magnetic resonance absorption. *Physical Review*, 73(7):679, 1948.
- [80] E. L. Hahn. Spin echoes. *Physical review*, 80(4):580, 1950.
- [81] H. Y. Carr and E. M. Purcell. Effects of diffusion on free precession in nuclear magnetic resonance experiments. *Physical Review*, 94(3):630, 1954.
- [82] S. Meiboom and D. Gill. Modified spin-echo method for measuring nuclear relaxation times. *Review of Scientific Instruments*, 29(8):688–691, 1958.
- [83] T. Gullion, D. B. Baker, and M. S. Conradi. New, compensated carr-purcell sequences. *Journal of Magnetic Resonance*, 89(3):479–484, 1990.
- [84] J. P. Cohen-Addad. NMR and fractal properties of polymeric liquids and gels. *Progress in nuclear magnetic resonance spectroscopy*, 25(1-3):1–316, 1993.
- [85] J. P. Cohen-Addad, M. Domard, and J. Herz. NMR observation of the swelling process of polydimethylsiloxane networks. average orientational order of monomeric units. *The Journal*

of *Chemical Physics*, 76(5):2744–2753, 1982.

- [86] J. P. Cohen-Addad and A. Guillermo. Effects of polymer chain disentanglement on NMR properties. I. proton magnetic relaxation in polyisobutylene. *Journal of Polymer Science: Polymer Physics Edition*, 22(6):931–955, 1984.
- [87] J. W. ten Brinke, V. M. Litvinov, J. Wijnhoven, and J. W. Noordermeer. Interactions of silica with natural rubber under the influence of coupling agents, studied by ^{13}C NMR and T_2 relaxation analysis. *Macromolecules*, 35(27):10026–10037, 2002.
- [88] V. M. Litvinov and P. Steeman. EPDM–carbon black interactions and the reinforcement mechanisms, as studied by low-resolution ^1H NMR. *Macromolecules*, 32(25):8476–8490, 1999.
- [89] V. M. Litvinov, R. A. Orza, M. Klüppel, M. Van Duin, and P. Magusin. Rubber–filler interactions and network structure in relation to stress–strain behavior of vulcanized, carbon black filled EPDM. *Macromolecules*, 44(12):4887–4900, 2011.
- [90] U. Heuert, M. Knörger, H. Menge, G. Scheler, and H. Schneider. New aspects of transversal proton NMR relaxation in natural rubber vulcanizates. *Polymer Bulletin*, 37(4):489–496, 1996.
- [91] V. M. Litvinov and A. A. Dias. Analysis of network structure of UV-cured acrylates by ^1H NMR relaxation, ^{13}C NMR spectroscopy, and dynamic mechanical experiments. *Macromolecules*, 34(12):4051–4060, 2001.
- [92] U. Hoffmann, W. Gronski, G. Simon, and A. Wutzler. Determination of crosslink densities of carbon black filled natural rubber sulfur vulcanizates by ^{13}C NMR MAS spectroscopy and ^1H NMR transversal relaxation. *Die Angewandte makromolekulare Chemie*, 202(1):283–293, 1992.
- [93] V. M. Litvinov, W. Barendswaard, and M. Van Duin. The density of chemical crosslinks and chain entanglements in unfilled EPDM vulcanizates as studied with low resolution, solid state proton NMR. *Rubber Chemistry and Technology*, 71(1):105–118, 1998.
- [94] G. Simon, K. Baumann, and W. Gronski. M_c determination and molecular dynamics in crosslinked 1,4-cis-polybutadiene: a comparison of transversal proton and deuterium NMR relaxation. *Macromolecules*, 25(14):3624–3628, 1992.
- [95] IIC Dr. Kuhn GmbH & Co. KG. *NMR Elastomer or Polymer Analyzer*, accessed 11.01.2020. <http://www.iic-nmr.com/>.
- [96] P. Zhang, F. Zhao, Y. Yuan, X. Shi, and S. Zhao. Network evolution based on general-purpose

- diene rubbers/sulfur/TBBS system during vulcanization (I). *Polymer*, 51(1):257–263, 2010.
- [97] Y. Zou, Y. Sun, Y. Zhang, J. He, Z. Tang, L. Zhu, Y. Luo, and F. Liu. Antioxidative behavior of a novel samarium complex in styrene-butadiene rubber/silica composites. *Polymer Degradation and Stability*, 133:201–210, 2016.
- [98] S. R. Smith and J. L. Koenig. Observation of crosslink density dispersion in sulfur donor-vulcanized polybutadiene using NMR imaging. *Macromolecules*, 24(12):3496–3504, 1991.
- [99] W. Kuhn, P. Barth, S. Hafner, G. Simon, and H. Schneider. Material properties imaging of cross-linked polymers by NMR. *Macromolecules*, 27(20):5773–5779, 1994.
- [100] G. B. McKenna, K. M. Flynn, and Y. Chen. Swelling in crosslinked natural rubber: experimental evidence of the crosslink density dependence of χ . *Polymer*, 31(10):1937–1945, 1990.
- [101] W. Kuhn, E. Peterli, and H. Majer. Freezing point depression of gels produced by high polymer network. *Journal of Polymer Science*, 16(82):539–548, 1955.
- [102] D. Honiball, M. G. Huson, and W. J. McGill. A nucleation theory for the anomalous freezing point depression of solvents in swollen rubber gels. *Journal of Polymer Science Part B: Polymer Physics*, 26(12):2413–2431, 1988.
- [103] L. R. G. Treloar. *The physics of rubber elasticity*. Oxford University Press, USA, 1975.
- [104] M. Mooney. A theory of large elastic deformation. *Journal of Applied Physics*, 11(9):582–592, 1940.
- [105] R. S. Rivlin. Large elastic deformations of isotropic materials IV. further developments of the general theory. *Philosophical Transactions of the Royal Society of London. Series A, Mathematical and Physical Sciences*, 241(835):379–397, 1948.
- [106] W. Gronski, H. Hasenhindl, B. Freund, and S. Wolff. High resolution solid state ^{13}C NMR studies of the crosslink structure in accelerated sulfur vulcanized natural rubber. *Kautschuk und Gummi, Kunststoffe*, 44(2):119–123, 1991.
- [107] P. J. Flory and J. Rehner Jr. Statistical mechanics of cross-linked polymer networks I. rubberlike elasticity. *The Journal of Chemical Physics*, 11(11):512–520, 1943.
- [108] K. Saalwächter. Artifacts in transverse proton NMR relaxation studies of elastomers. *Macromolecules*, 38(4):1508–1512, 2005.

- [109] K. Saalwächter. Proton multiple-quantum NMR for the study of chain dynamics and structural constraints in polymeric soft materials. *Progress in Nuclear Magnetic Resonance Spectroscopy*, 51(1):1–35, 2007.
- [110] R. Graf, A. Heuer, and H. W. Spiess. Chain-order effects in polymer melts probed by ^1H double-quantum NMR spectroscopy. *Physical Review Letters*, 80(26):5738, 1998.
- [111] R. Graf, D. E. Demco, S. Hafner, and H. W. Spiess. Selective residual dipolar couplings in cross-linked elastomers by ^1H double-quantum NMR spectroscopy. *Solid State Nuclear Magnetic Resonance*, 12(2-3):139–152, 1998.
- [112] K. Saalwächter and A. Heuer. Chain dynamics in elastomers as investigated by proton multiple-quantum NMR. *Macromolecules*, 39(9):3291–3303, 2006.
- [113] J.-U. Sommer, W. Chassé, J. L. Valentín, and K. Saalwächter. Effect of excluded volume on segmental orientation correlations in polymer chains. *Physical Review E*, 78(5):051803, 2008.
- [114] W. Kuhn. Über die Gestalt fadenförmiger Moleküle in Lösungen. *Kolloid-Zeitschrift*, 68(1):2–15, 1934.
- [115] P. J. Flory. *Statistical mechanics of chain molecules*. Interscience Publishers, New York, 1969.
- [116] K. Saalwächter, B. Herrero, and M. A. López-Manchado. Chain order and cross-link density of elastomers as investigated by proton multiple-quantum NMR. *Macromolecules*, 38(23):9650–9660, 2005.
- [117] J. E. Mark. Random-coil configurations of cis-1,4-polybutadiene and cis-1,4-polyisoprene: Theoretical interpretation. *Journal of the American Chemical Society*, 88(19):4354–4359, 1966.
- [118] M. Doxastakis, V. G. Mavrantzas, and D. N. Theodorou. Atomistic monte carlo simulation of cis-1,4-polyisoprene melts I: Single temperature end-bridging monte carlo simulations. *The Journal of Chemical Physics*, 115(24):11339–11351, 2001.
- [119] K. Saalwächter, P. Ziegler, O. Spyckerelle, B. Haidar, A. Vidal, and J.-U. Sommer. ^1H multiple-quantum nuclear magnetic resonance investigations of molecular order distributions in polydimethylsiloxane networks: Evidence for a linear mixing law in bimodal systems. *The Journal of Chemical Physics*, 119(6):3468–3482, 2003.
- [120] B. Gabrielle, E. Gomez, and J.-P. Korb. Probing rubber cross-linking generation of industrial polymer networks at nanometer scale. *The Journal of Physical Chemistry B*, 120(24):5581–5589, 2016.

-
- [121] A. Mujtaba, M. Keller, S. Ilisch, H.-J. Radusch, T. Thurn-Albrecht, K. Saalwächter, and M. Beiner. Mechanical properties and cross-link density of styrene-butadiene model composites containing fillers with bimodal particle size distribution. *Macromolecules*, 45(16):6504–6515, 2012.
- [122] A. Vieyres, R. Pérez-Aparicio, P. Albouy, O. Sanseau, K. Saalwächter, D. R. Long, and P. Sotta. Sulfur-cured natural rubber elastomer networks: correlating cross-link density, chain orientation, and mechanical response by combined techniques. *Macromolecules*, 46(3):889–899, 2013.
- [123] K.-F. Ratzsch, C. Friedrich, and M. Wilhelm. Low-field rheo-NMR: A novel combination of NMR relaxometry with high end shear rheology. *Journal of Rheology*, 61(5):905–917, 2017.
- [124] K. Halbach. Design of permanent multipole magnets with oriented rare earth cobalt material. *Nuclear Instruments and Methods*, 169(1):1–10, 1980.
- [125] V. Röntzsch, M. B. Özen, K.-F. Ratzsch, E. Stellamanns, M. Sprung, G. Guthausen, and M. Wilhelm. Polymer crystallization studied by hyphenated rheology techniques: Rheo-NMR, Rheo-SAXS, and Rheo-Microscopy. *Macromolecular Materials and Engineering*, 304(2):1800586, 2019.
- [126] N. W. Radebe, K.-F. Ratzsch, C. O. Klein, and M. Wilhelm. Use of combined Rheo-NMR to investigate the relationship between the molecular and mechanical properties of early cement paste hydration. In *Rheology and Processing of Construction Materials*, pages 256–265. Springer, 2019.
- [127] A. Maus, C. Hertlein, and K. Saalwächter. A robust proton NMR method to investigate hard/soft ratios, crystallinity, and component mobility in polymers. *Macromolecular Chemistry and Physics*, 207(13):1150–1158, 2006.
- [128] J. S. Dick. *Basic Rubber Testing: Selecting Methods for a Testing Programme*. West Conshohocken, PA, United States, 2003.
- [129] J.-B. Le Cam, B. Huneau, E. Verron, and L. Gornet. Mechanism of fatigue crack growth in carbon black filled natural rubber. *Macromolecules*, 37(13):5011–5017, 2004.
- [130] D. Merger and M. Wilhelm. Intrinsic nonlinearity from LAOS experiments on various strain- and stress-controlled rheometers: a quantitative comparison. *Rheologica Acta*, 53(8):621–634, 2014.
- [131] J. L. Valentín, P. Posadas, A. Fernández-Torres, M. A. Malmierca, L. González, W. Chassé,

- and K. Saalwächter. Inhomogeneities and chain dynamics in diene rubbers vulcanized with different cure systems. *Macromolecules*, 43(9):4210–4222, 2010.
- [132] J. Baum and A. Pines. NMR studies of clustering in solids. *Journal of the American Chemical Society*, 108(24):7447–7454, 1986.
- [133] D. R. Burfield and K. L. Lim. Differential scanning calorimetry analysis of natural rubber and related polyisoprenes. measurement of the glass transition temperature. *Macromolecules*, 16(7):1170–1175, 1983.
- [134] W. Chassé, J. L. Valentín, G. D. Genesky, C. Cohen, and K. Saalwächter. Precise dipolar coupling constant distribution analysis in proton multiple-quantum NMR of elastomers. *The Journal of Chemical Physics*, 134(4):044907 1–10, 2011.
- [135] L. Bateman. *Chemistry and Physics of Rubber-like Substances: Studies of the Natural Rubber Producers' Research Association*. Wiley, London, Maclaren, New York, 1963.
- [136] J. Höpfner. *A new method of seawater desalination via acrylic acid based hydrogels: synthesis, characterization and experimental*, PhD thesis. PhD thesis, Karlsruhe Institute of Technology, 2013.
- [137] C. E. Morriss, .R Freedman, C. Straley, M. Johnston, H. J. Vinegar, and P. N. Tutunjian. Hydrocarbon saturation and viscosity estimation from NMR logging in the belridge diatomite. In *SPWLA 35th Annual Logging Symposium*. Society of Petrophysicists and Well-Log Analysts, 1994.
- [138] D. V. Widder. What is the Laplace transform? *The American Mathematical Monthly*, 52(8):419–425, 1945.
- [139] P. T. Callaghan, S. Godefroy, and B. N. Ryland. Use of the second dimension in PGSE NMR studies of porous media. *Magnetic Resonance Imaging*, 21(3-4):243–248, 2003.
- [140] P. T. Callaghan, S. Godefroy, and B. N. Ryland. Diffusion–relaxation correlation in simple pore structures. *Journal of Magnetic Resonance*, 162(2):320–327, 2003.
- [141] J. Höpfner, G. Guthausen, K. Saalwächter, and M. Wilhelm. Network structure and inhomogeneities of model and commercial polyelectrolyte hydrogels as investigated by low-field proton NMR techniques. *Macromolecules*, 47(13):4251–4265, 2014.
- [142] F. Cavalli, C. Pfeifer, L. Arens, L. Barner, and M. Wilhelm. Analysis of the local mobility of RAFT mediated poly(acrylic acid) networks via low field ^1H NMR techniques for investigation

- of the network topology. *Macromolecular Chemistry and Physics*, 221:1900387, 1–14, 2019.
- [143] J. R. Klauder and P. W. Anderson. Spectral diffusion decay in spin resonance experiments. *Physical Review*, 125(3):912–932, 1962.
- [144] P. W. Anderson and P. R. Weiss. Exchange narrowing in paramagnetic resonance. *Reviews of Modern Physics*, 25(1):269–276, 1953.
- [145] L. Jakisch, M. Garaleh, M. Schäfer, A. Mordvinkin, K. Saalwächter, and F. Böhme. Synthesis and structural NMR characterization of novel PPG/PCL conetworks based upon heterocomplementary coupling reactions. *Macromolecular Chemistry and Physics*, 219(3):1700327 1–9, 2018.
- [146] C. Morriss, D. Rossini, C. Straley, P. Tutunjian, and H. Vinegar. Core analysis by low-field NMR. *The Log Analyst*, 38(43–56), 1997.
- [147] A. R. Payne and R. E. Whittaker. Low strain dynamic properties of filled rubbers. *Rubber Chemistry and Technology*, 44(2):440–478, 1971.
- [148] G. Kraus. Mechanical losses in carbon-black-filled rubbers. In *Journal of Applied Polymer Science: Applied Polymer Symposium*, volume 39, pages 75–92, 1984.
- [149] P.G. Maier and D. Göritz. Molecular interpretation of the payne effect. *Kautschuk Gummi Kunststoffe*, 49(1):18–21, 1996.
- [150] G. Heinrich, M. Klüppel, and T. A. Vilgis. Reinforcement of elastomers. *Current Opinion in Solid State and Materials Science*, 6(3):195–203, 2002.
- [151] C. Wrana. *Introduction to Polymer Physics*. LANXESS AG, Leverkusen, Germany, 2009.
- [152] J. Berriot, H. Montes, F. Lequeux, D. Long, and P. Sotta. Evidence for the shift of the glass transition near the particles in silica-filled elastomers. *Macromolecules*, 35(26):9756–9762, 2002.
- [153] K. W. Stockelhuber, A. S. Svistkov, A. G. Pelevin, and G. Heinrich. Impact of filler surface modification on large scale mechanics of styrene butadiene/silica rubber composites. *Macromolecules*, 44(11):4366–4381, 2011.
- [154] Z. Tang, J. Huang, X. Wu, B. Guo, L. Zhang, and F. Liu. Interface engineering toward promoting silanization by ionic liquid for high-performance rubber/silica composites. *Industrial & Engineering Chemistry Research*, 54(43):10747–10756, 2015.

- [155] L. Schwab. *Fourier transform Rheology of complex, filled rubber materials, PhD thesis*. PhD thesis, Karlsruhe Institute of Technology, 2016.
- [156] S. M. Nagaraja, A. Mujtaba, and M. Beiner. Quantification of different contributions to dissipation in elastomer nanoparticle composites. *Polymer*, 111:48–52, 2017.
- [157] A. Kato, Y. Ikeda, Y. Kasahara, J. Shimanuki, T. Suda, T. Hasegawa, H. Sawabe, and S. Kohjiya. Optical transparency and silica network structure in cross-linked natural rubber as revealed by spectroscopic and three-dimensional transmission electron microscopy techniques. *Journal of the Optical Society of America B*, 25(10):1602–1615, 2008.
- [158] G. J. Schneider, S. A. Fink, R. Rachel, and D. Goritz. Three-dimensional structure of precipitated silica as determined by electron tomography. *Kautschuk und Gummi Kunststoffe*, 58(9):461–463, 2005.
- [159] J. Ramier, L. Chazeau, C. Gauthier, L. Guy, and M.-N. Bouchereau. Grafting of silica during the processing of silica-filled SBR: Comparison between length and content of the silane. *Journal of Polymer Science Part B: Polymer Physics*, 44(1):143–152, 2006.
- [160] J. Hager, R. Hentschke, N. W. Hojdis, and H. A. Karimi-Varzaneh. Computer simulation of particle–particle interaction in a model polymer nanocomposite. *Macromolecules*, 48(24):9039–9049, 2015.
- [161] V. Röntzsch, J. Klein, and M. Wilhelm. Synthesis and purification of crosslinked polystyrene beads. *unpublished results, Karlsruhe Institute of Technology*, 2019.
- [162] A. Mordvinkin and K. Saalwächter. Microscopic observation of the segmental orientation autocorrelation function for entangled and constrained polymer chains. *The Journal of Chemical Physics*, 146(9):094902, 2017.
- [163] J. Weese. A reliable and fast method for the solution of Fredholm integral equations of the first kind based on Tikhonov regularization. *Computer Physics Communications*, 69(1):99–111, 1992.
- [164] R. Fan, Y. Zhang, C. Huang, Y. Zhang, Y. Fan, and K. Sun. Effect of crosslink structures on dynamic mechanical properties of natural rubber vulcanizates under different aging conditions. *Journal of Applied Polymer Science*, 81(3):710–718, 2001.
- [165] E. J. Blackman and E. B. McCall. Relationships between the structures of natural rubber vulcanizates and their thermal and oxidative aging. *Rubber Chemistry and Technology*, 43(3):651–663, 1970.

-
- [166] Y. S. R. Yahya, A. R. Azura, and Z. Ahmad. Effect of curing systems on thermal degradation behaviour of natural rubber (SMR CV 60). *Journal of Physical Science*, 22(2):1–14, 2011.
- [167] C. R. Parks and O. Lorenz. Effect of network structure on aging of natural rubber vulcanizates. *Industrial & Engineering Chemistry Product Research and Development*, 2(4):279–284, 1963.
- [168] W. Zheng, L. Liu, X. Zhao, J. He, A. Wang, T. W. Chan, and S. Wu. Effects of lanthanum complex on the thermo-oxidative aging of natural rubber. *Polymer Degradation and Stability*, 120:377–383, 2015.
- [169] M. Narathichat, K. Sahakaro, and C. Nakason. Assessment degradation of natural rubber by moving die processability test and ftir spectroscopy. *Journal of Applied Polymer Science*, 115(3):1702–1709, 2010.
- [170] J. Zhi, Q. Wang, M. Zhang, Z. Zhou, A. Liu, and Y. Jia. Coupled analysis on hyper-viscoelastic mechanical behavior and macromolecular network alteration of rubber during thermo-oxidative aging process. *Polymer*, 171:15–24, 2019.
- [171] Y. Zhang, J. R. Choi, and S. J. Park. Enhancing the heat and load transfer efficiency by optimizing the interface of hexagonal boron nitride/elastomer nanocomposites for thermal management applications. *Polymer*, 143:1–9, 2018.
- [172] G. Kraus and J. Dugone. Adsorption of elastomers on carbon black. *Industrial & Engineering Chemistry*, 47(9):1809–1816, 1955.
- [173] G. Kraus and J. Dugone. Adsorption of elastomers on carbon black. *Rubber Chemistry and Technology*, 29(1):148–165, 1956.
- [174] H. H. Le, S. Ilisch, and H.-J. Radusch. Characterization of the effect of the filler dispersion on the stress relaxation behavior of carbon black filled rubber composites. *Polymer*, 50(10):2294–2303, 2009.
- [175] Z. Cibulková, P. Šimon, P. Lehocký, and J. Balko. Antioxidant activity of p-phenylenediamines studied by DSC. *Polymer Degradation and Stability*, 87(3):479–486, 2005.
- [176] G.-Y. Li and J. L. Koenig. Ftir imaging of oxidation of polyisoprene 2. the role of N-phenyl-N'-dimethyl-butyl-p-phenylenediamine antioxidant. *Polymer Degradation and Stability*, 81(3):377–385, 2003.
- [177] P. Rapta, A. Vargová, J. Polovková, A. Gatial, L. Omelka, P. Majzlík, and M. Breza. A variety of oxidation products of antioxidants based on N,N'-substituted p-phenylenediamines.

- Polymer Degradation and Stability*, 94(9):1457–1466, 2009.
- [178] W. V. Mars and A. Fatemi. A literature survey on fatigue analysis approaches for rubber. *International Journal of Fatigue*, 24(9):949–961, 2002.
- [179] W. V. Mars and A. Fatemi. Factors that affect the fatigue life of rubber: a literature survey. *Rubber Chemistry and Technology*, 77(3):391–412, 2004.
- [180] A. N. Gent, P. B. Lindley, and A. G. Thomas. Cut growth and fatigue of rubbers. I. the relationship between cut growth and fatigue. *Journal of Applied Polymer Science*, 8(1):455–466, 1964.
- [181] G. J. Lake and P. B. Lindley. Cut growth and fatigue of rubbers. II. experiments on a non-crystallizing rubber. *Journal of Applied Polymer Science*, 8(2):707–721, 1964.
- [182] L. Mullins. Softening of rubber by deformation. *Rubber Chemistry and Technology*, 42(1):339–362, 1969.
- [183] J. Diani, B. Fayolle, and P. Gilormini. A review on the Mullins effect. *European Polymer Journal*, 45(3):601–612, 2009.
- [184] V. Hirschberg, L. Schwab, M. Cziep, M. Wilhelm, and D. Rodrigue. Influence of molecular properties on the mechanical fatigue of polystyrene (PS) analyzed via Wöhler curves and Fourier transform rheology. *Polymer*, 138:1–7, 2018.
- [185] A. N. Gent and C. T. R. Pulford. Micromechanics of fracture in elastomers. *Journal of Materials Science*, 19(11):3612–3619, 1984.
- [186] S. V. Hainsworth. An environmental scanning electron microscopy investigation of fatigue crack initiation and propagation in elastomers. *Polymer Testing*, 26(1):60–70, 2007.
- [187] S. Beurrot, B. Huneau, and E. Verron. In situ SEM study of fatigue crack growth mechanism in carbon black-filled natural rubber. *Journal of Applied Polymer Science*, 117(3):1260–1269, 2010.
- [188] K. L. G. Jago. X-ray computed microtomography of rubber. *Rubber Chemistry and Technology*, 85(3):387–407, 2012.
- [189] Y. Marco, V. Le Saux, S. Calloch, and P. Charrier. X-ray computed μ -tomography: a tool for the characterization of fatigue defect population in a polychloroprene rubber. *Procedia Engineering*, 2(1):2131–2140, 2010.

-
- [190] V. Le Saux, Y. Marco, S. Calloch, and P. Charrier. Evaluation of the fatigue defect population in an elastomer using X-ray computed micro-tomography. *Polymer Engineering & Science*, 51(7):1253–1263, 2011.
- [191] B. Huneau, I. Masquelier, Y. Marco, V. Le Saux, S. Noizet, C. Schiel, and P. Charrier. Initiation mechanisms of fatigue cracks in carbon black filled natural rubber. *Constitutive Models for Rubber IX*, 89(1):395–401, 2015.
- [192] B. Huneau, I. Masquelier, Y. Marco, V. Le Saux, S. Noizet, C. Schiel, and P. Charrier. Fatigue crack initiation in a carbon black-filled natural rubber. *Rubber Chemistry and Technology*, 89(1):126–141, 2016.
- [193] P. Adriaensens, A. Pollaris, D. Vanderzande, J. Gelan, J. L. White, and M. Kelchtermans. Relationships between microvoid heterogeneity and physical properties in cross-linked elastomers: An NMR imaging study. *Macromolecules*, 33(19):7116–7121, 2000.
- [194] Y. Marco, B. Huneau, I. Masquelier, V. Le Saux, and P. Charrier. Prediction of fatigue properties of natural rubber based on the descriptions of the cracks population and of the dissipated energy. *Polymer Testing*, 59:67–74, 2017.
- [195] E. Manias, A. Touny, L. Wu, K. Strawhecker, B. Lu, and T. C. Chung. Polypropylene/montmorillonite nanocomposites: review of the synthetic routes and materials properties. *Chemistry of Materials*, 13(10):3516–3523, 2001.
- [196] P. Bala, B. K. Samantaray, S. K. Srivastava, and G. B. Nando. Organomodified montmorillonite as filler in natural and synthetic rubber. *Journal of Applied Polymer Science*, 92(6):3583–3592, 2004.
- [197] S. Nie, J. Lacayo-Pineda, N. Willenbacher, and M. Wilhelm. Aging of natural rubber studied via Fourier-transform rheology and double quantum NMR to correlate local chain dynamics with macroscopic mechanical response. *Polymer*, 181:121804, 2019.
- [198] W. J. van Ooij. Mechanism and theories of rubber adhesion to steel tire cords: an overview. *Rubber Chemistry and Technology*, 57(3):421–456, 1984.
- [199] D. H. Turkington, A. J. Carr, N. Cooke, and P. J. Moss. Seismic design of bridges on lead-rubber bearings. *Journal of Structural Engineering*, 115(12):3000–3016, 1989.
- [200] B. L. Lee, D. S. Liu, M. Chawla, and P. C. Ulrich. Fatigue of cord-rubber composites. *Rubber Chemistry and Technology*, 67(5):761–774, 1994.

- [201] S. Rao, I. M. Daniel, and D. McFarlane. Fatigue and fracture behavior of a steel cord/rubber composite. *Journal of Thermoplastic Composite Materials*, 14(3):213–224, 2001.
- [202] Y. Itoh and H. S. Gu. Prediction of aging characteristics in natural rubber bearings used in bridges. *Journal of Bridge Engineering*, 14(2):122–128, 2009.

Appendix

A. Photographs and Mechanical Drawing

A.1. Photographs of the sample preparation apparatus and the RheoNMR setup

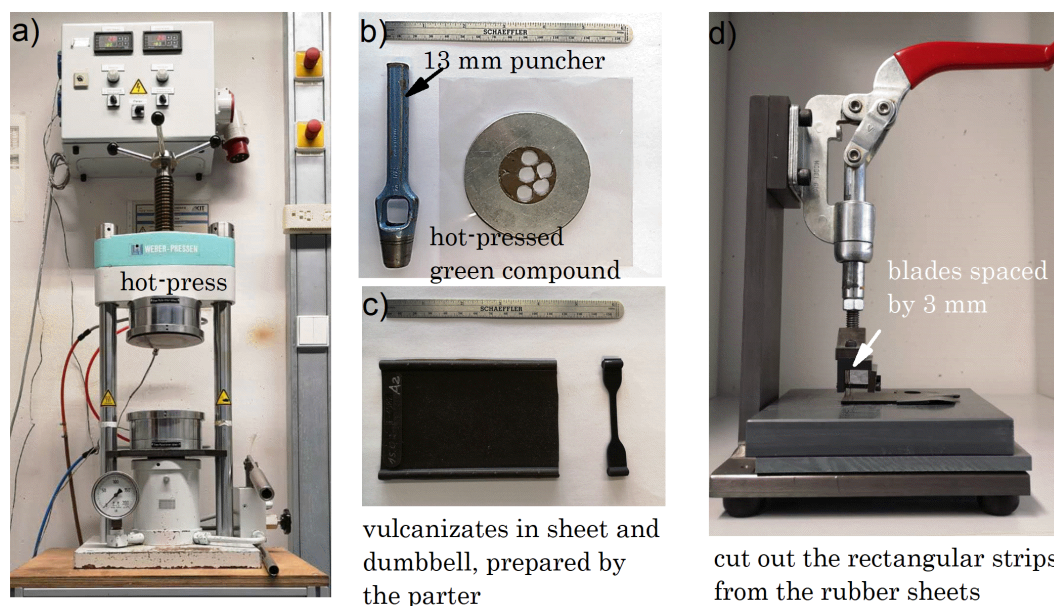


Figure A.1: Photographs of a) the hot-press, b) the hot-pressed NR compound for vulcanization studies, c) the vulcanized NR for aging studies and d) the cutter used to cut out strips for rectangle torsion in rheology.



Figure A.2: A photograph of the RheoNMR employed for NR vulcanization studies.

A.2. Mechanical drawing of the grooved ceramic plates

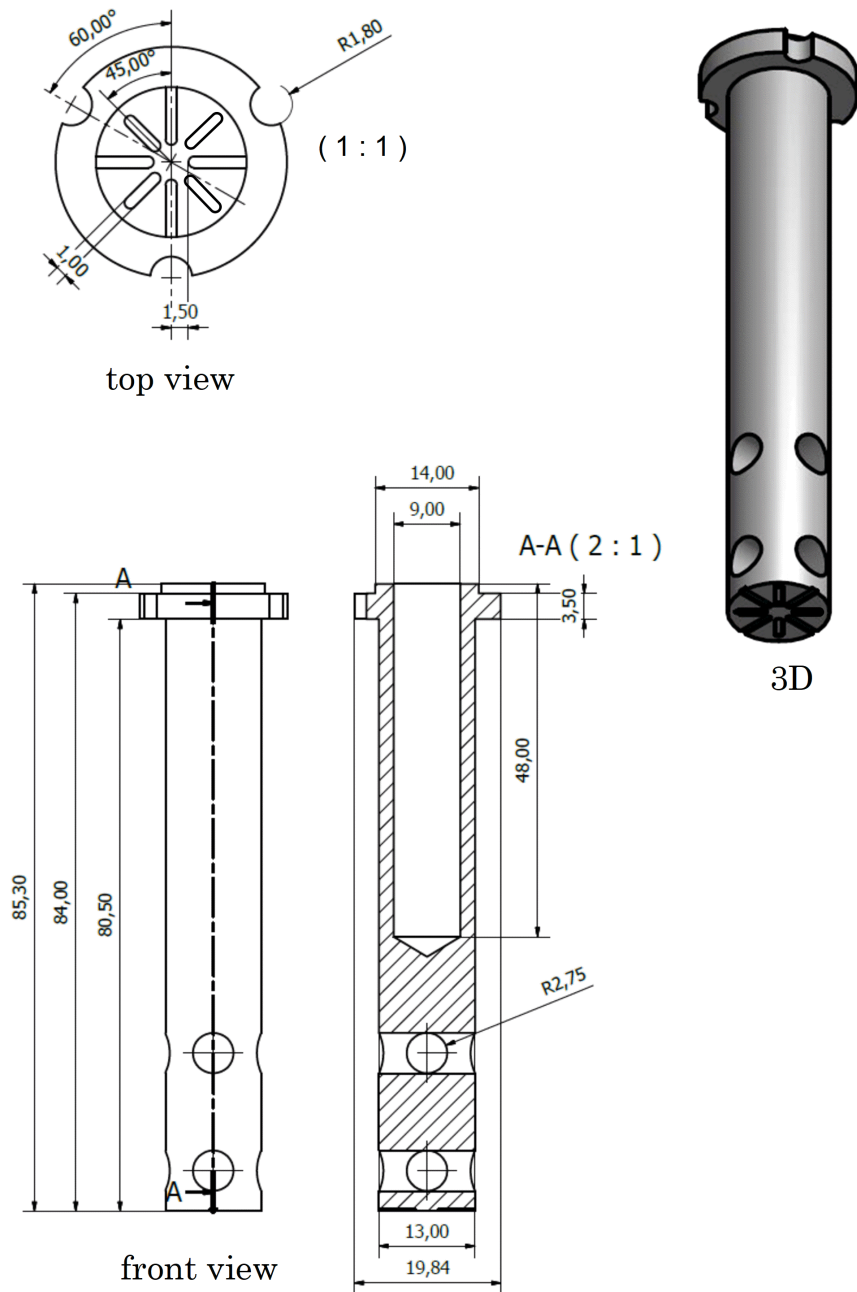


Figure A.3: Mechanical drawing of the grooved ceramic plates, unit in mm.

B. Supplementary Data

B.1. Supplementary rheological data

B.1.1. Strain sweep of NRCB1 with different data density

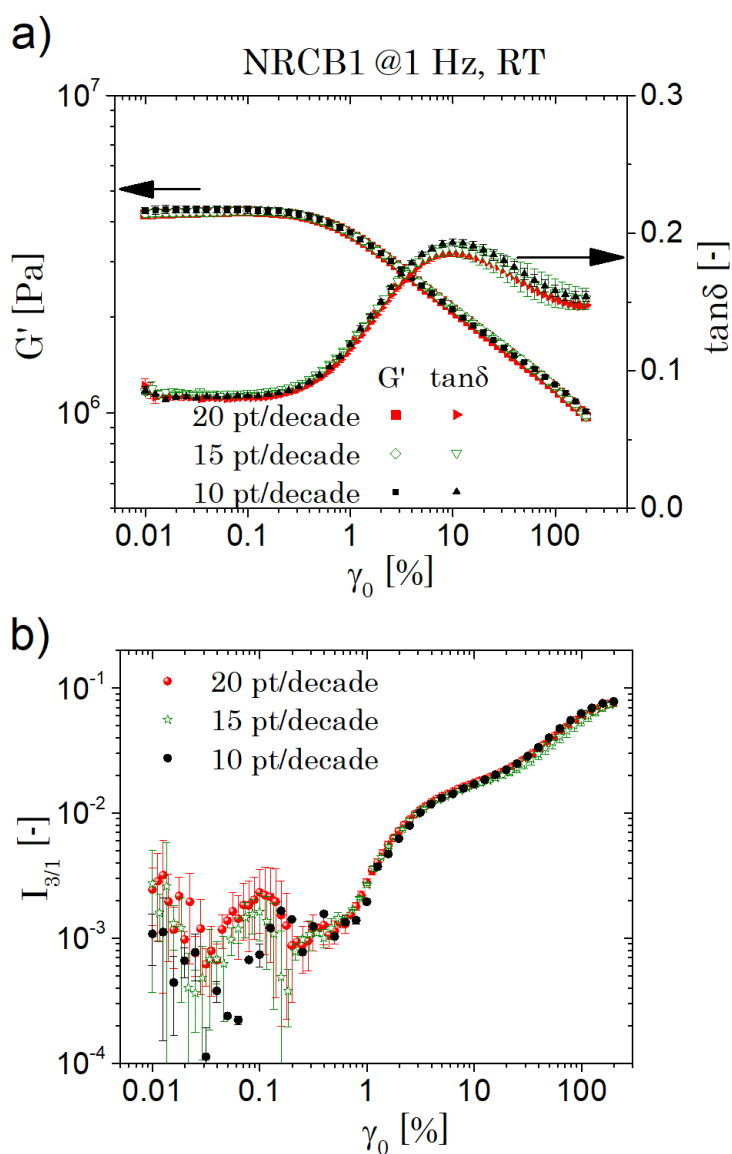


Figure B.1: To examine the influence of the strain amplitude density on the strain sweep results, the NRCB1 were strain-swept on ARES-G2 oscillatory torsion at $\omega_1/2\pi = 1$ Hz and room temperature, with 10/15/20 points per decade. At least three specimens were used for reproducibility. The a) linear rheological data and b) the $I_{3/1}$ from FT-rheology were almost identical, indicating that the data density have no influence on the strain sweep results.

B.1.2. Temperature ramp of NR vulcanizates

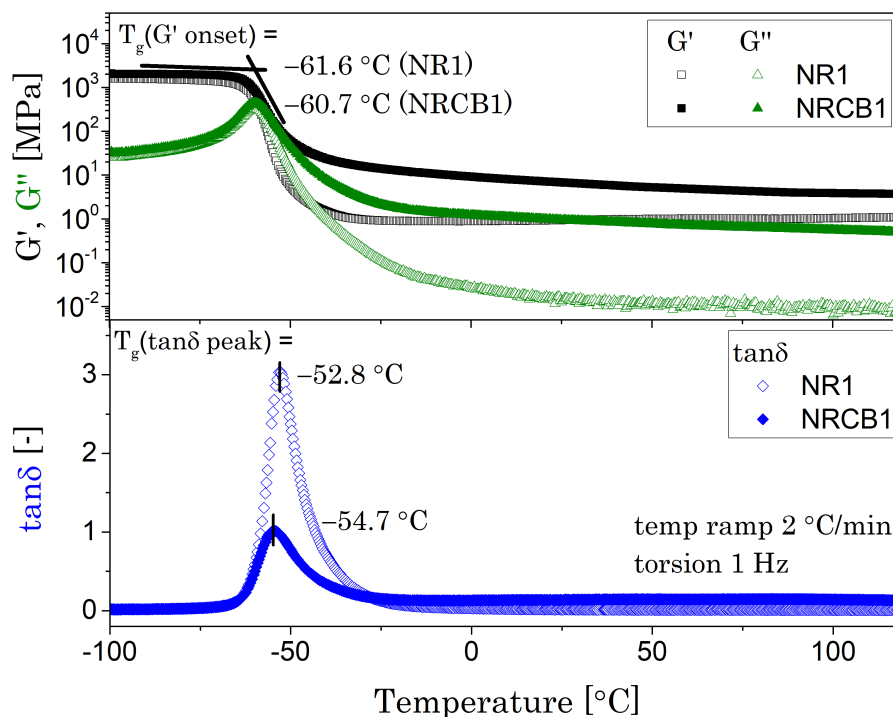


Figure B.2: Temperature ramp of NR vulcanizates on oscillatory torsion fixture of ARES-G2 from -100 – 120 °C at 2 °C/min and an oscillatory frequency of $\omega/2\pi = 1$ Hz. The corresponding glass transition temperatures, T_g , were extrapolated and labeled in the figure. To achieve good data quality with the limitation torque of ARES-G2 (0.2 N·m), the specimens were swept at the auto-adjustment mode for the strain amplitude and the torque. For NR1, testing parameters were set as $\gamma_0 = 0.005$ – 3% , torque = 0.5 – 20×10^{-3} N·m. For NRCB1, testing parameters were set as $\gamma_0 = 0.001$ – 1% , torque = 3 – 20×10^{-3} N·m. All conditions were still in the LVE regime of the materials.

B.2. RheoNMR data of all tested NRs

The development of the shear moduli G^* , the transversal relaxation rate of rigid chain segments $1/T_{2R}$, the normalized distribution of the residual dipolar coupling constants $P_i(D_{resi})$ and the number averaged values D_{resn} during isothermal vulcanization on RheoNMR are displayed as following. The vulcanization experiments on RheoNMR were carried out at 140 °C ($\gamma_0 = 0.5\%$ and 1Hz for rheology, 8 scans with MSE-xx4 pulses for the transversal relaxation of NMR). The samples are five NRs with different vulcanization systems in Chapter 3.

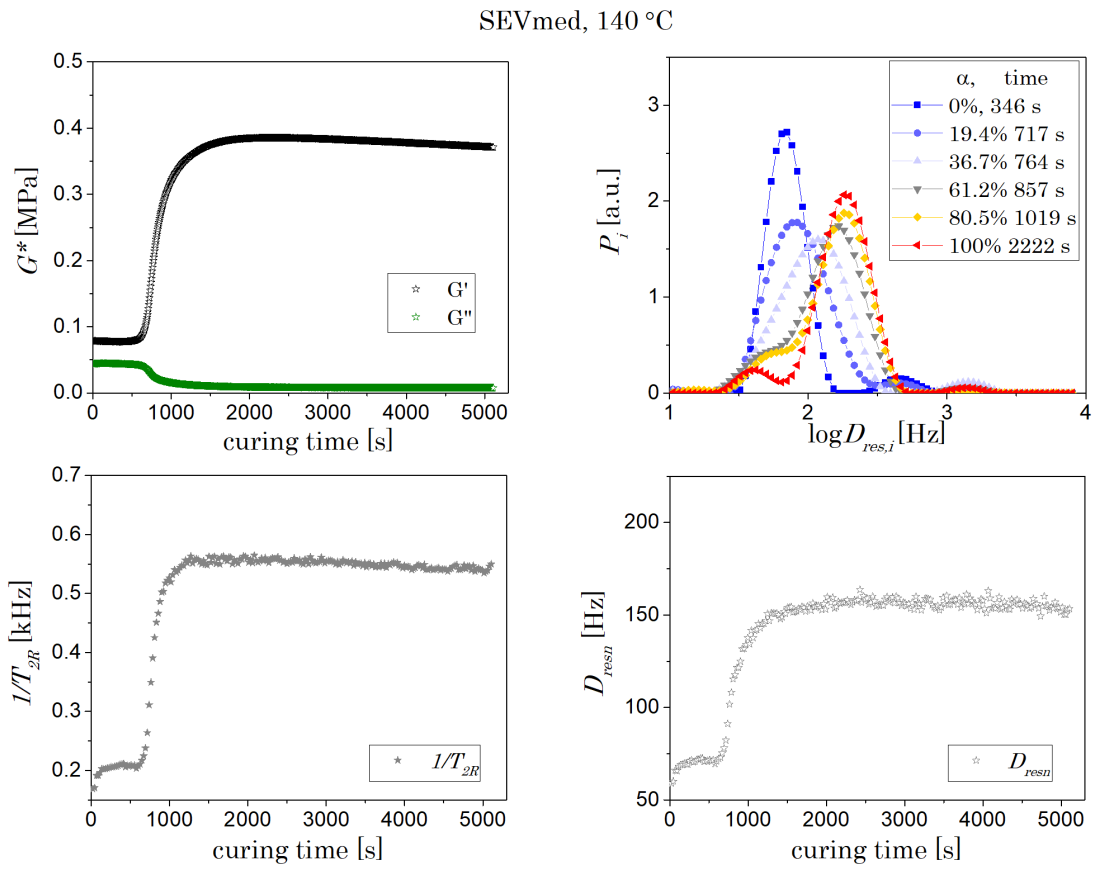


Figure B.3: RheoNMR data of SEVmed (NR1).

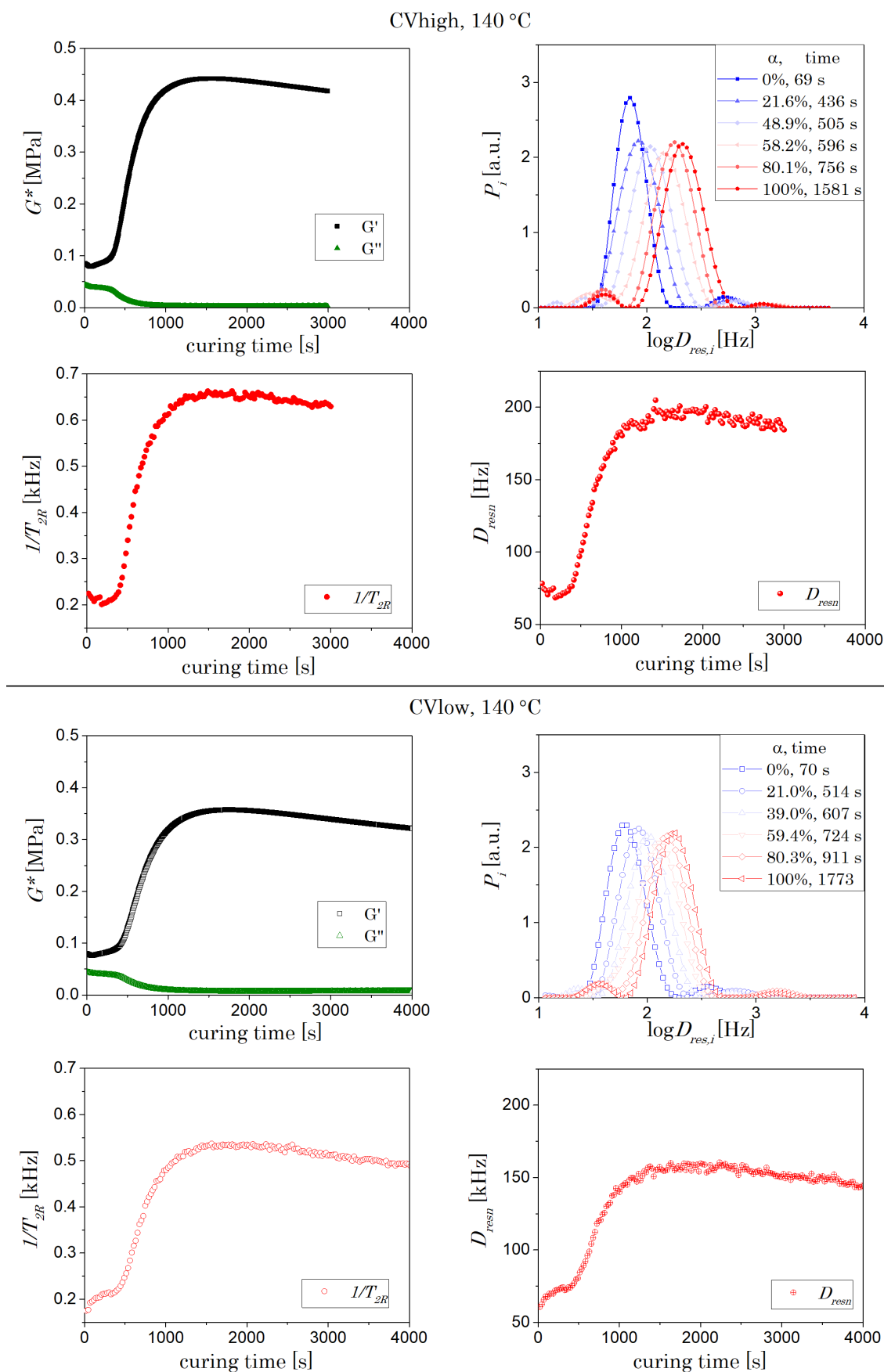


Figure B.4: RheoNMR data of CVhigh and CVlow.

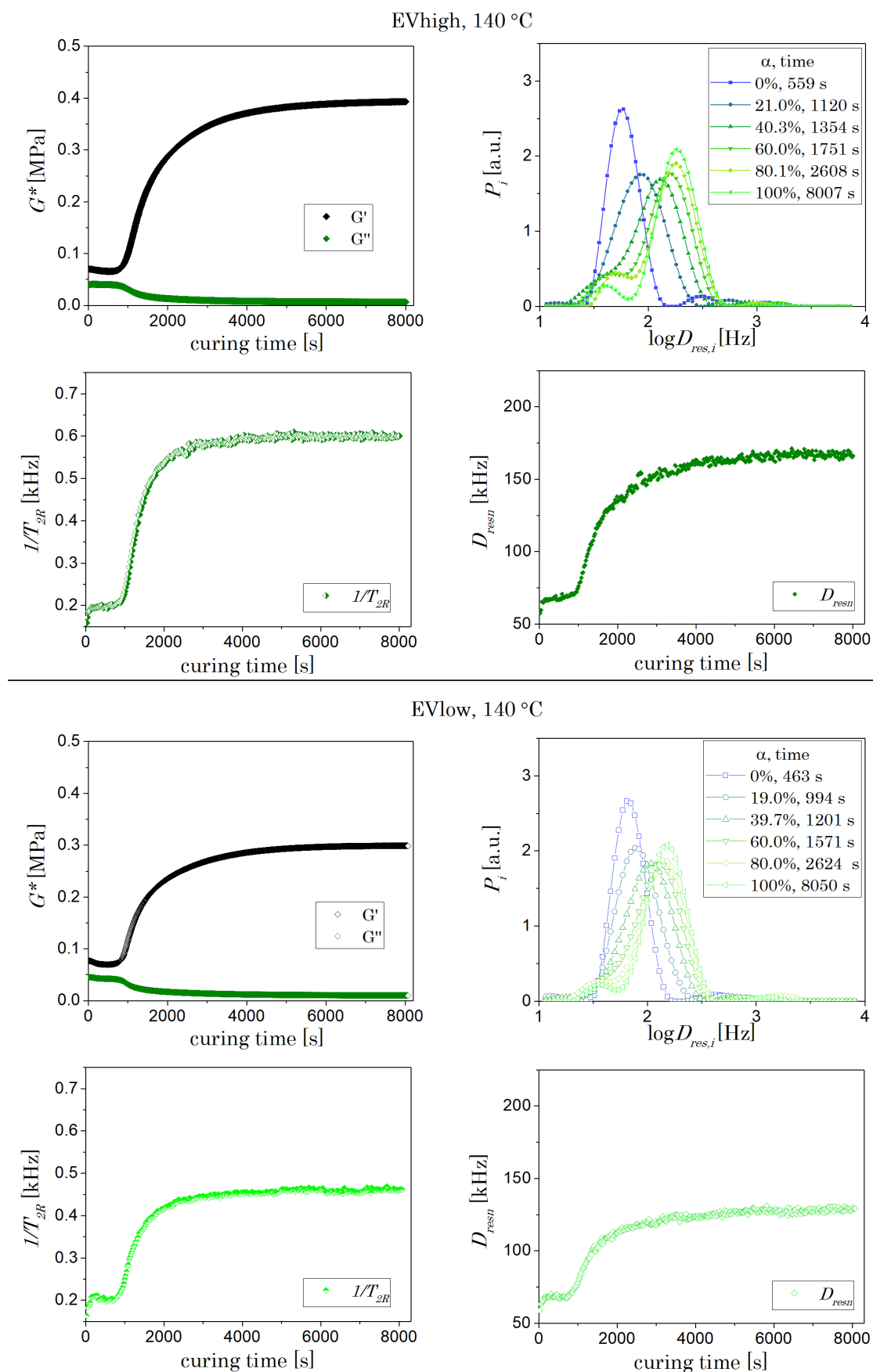


Figure B.5: RheoNMR data of EVhigh and EVlow.

Curriculum Vitae

Name: Shouliang Nie
Born: 1987 from Shandong, China
Address(work): KIT, ITCP-Polymeric Materials
Engesserstr. 18
76131 Karlsruhe
E-Mail: shouliang.nie@kit.edu
shouliang.nie@hotmail.com



EDUCATION

- 03/2016 – Karlsruhe Institute of Technology (KIT), Germany
Promotion, Chemical Engineering
Thesis: Investigation of crosslinked rubber aging by Fourier-transform rheology and time-domain NMR
Advisor: Prof. Dr. Manfred Wilhelm (KIT)
Advisor: Prof. Dr. Norbert Willenbacher (KIT)
Partner advisor: Prof. Dr. Jorge Lacayo-Pineda (Continental Reifen Deutschland)
- 09/2013 – 09/2015 University of Waterloo, Canada
Master of Applied Science, Chemical Engineering
Thesis: Rheological properties of tailor-made metallocene and Ziegler-Natta based controlled rheology polypropylenes
Advisor: Prof. Dr. Costas Tzoganakis
- 09/2005 – 07/2009 Qingdao University of Science and Technology, China
Bachelor of Engineering, Polymer Engineering
Thesis: Finite element simulation of the tire bead unseating resistance
Advisor: Asso. Prof. Dr. Wei Wang

WORK EXPERIENCE

- 09/2015 – 01/2016 Research Assistant
University of Waterloo, Canada
- 06/2011 – 07/2013 Lab Specialist
LANXESS Chemicals - Rubber Research Center Qingdao, China
- 07/2009 – 05/2011 Material Technician
Yokohama Tire Hangzhou, China

PUBLICATIONS

1. S. Nie, J. Lacayo-Pineda, N. Willenbacher and M. Wilhelm*, Aging of natural rubber studied via Fourier-transform rheology and double quantum NMR to correlate local chain dynamics with macroscopic mechanical response, *Polymer*, 181, **2019**: 121804.
2. S. Nie, J. Lacayo-Pineda, M. Wilhelm*, Fourier-transform rheology of unvulcanized styrene butadiene rubber filled with increasingly silanized silica, *Soft Materials*, 17, **2019**: 269–282.
3. S. Nie, L. Schwab, V. Hirschberg, M. Cziep, J. Lacayo-Pineda and M. Wilhelm*; Fourier transform (FT)-rheology on rubber materials; book chapter, *Anwenderseminar TA-Instruments, Würzburg: Charakterisierung von Hochleistungswerkstoffen und Elastomeren mit thermischen und mechanischen Prüfverfahren*, **2019**; ISBN 978-3-940184-13-9.
4. S. Nie and C. Tzoganakis*, Tailor-made controlled rheology polypropylenes from metallocene and Ziegler-Natta resins, *Polymer Engineering & Science*, 59, **2019**: 1114–1121.
5. W. Wang* and S. Nie, Simulation and analysis of tire unseating test on radial tire (in Chinese), *China Elastomerics*, 1, **2013**: 33–36.

CONFERENCES

- KHK2021 S. Nie, K.-F. Ratzsch, J. Lacayo-Pineda and M. Wilhelm, Rubber crosslinking on unique combination of Rheo-NMR: correlate the chain dynamics to the macroscopic rheological properties, *14th Fall Rubber Colloquium (KHK)*, oral presentation, **submitted**, Hannover, Germany.
- AERC2019 S. Nie, J. Lacayo-Pineda and M. Wilhelm, Investigation of crosslinked rubber aging by Fourier-transform rheology and double quantum NMR, *Annual European Rheology Conference*, oral presentation, **2019**, Portoroz, Slovenia.
- KHK2018 S. Nie, K.-F. Ratzsch, V. Röntzsch, J. Lacayo-Pineda and M. Wilhelm, Investigation on rubber crosslinking via Rheo-NMR: microscopic chain dynamic and macroscopic rheological response, *13th Fall Rubber Colloquium (KHK)*, poster, **2018**, Hannover, Germany; ISBN 9783981407631.
- DKG-Nord2017 S. Nie, J. Lacayo-Pineda and M. Wilhelm, Investigation of crosslinked rubber aging by Fourier-transform rheology, *DKG Nord*, oral presentation, **2017**, Hannover, Germany.
- KHK2016 L. Schwab, S. Nie, J. Lacayo-Pineda and M. Wilhelm, Fourier-transform rheology of unvulcanized, carbon black filled SBR, *12th Fall Rubber Colloquium (KHK)*, poster, **2016**, Hannover, Germany.

Acknowledgements

Without the support from my supervisors, partners, colleagues, friends and family in many perspectives, this thesis can not be fulfilled. On this occasion, I would like to express my gratitude to

my supervisor **Prof. Dr. Manfred Wilhelm** for providing me the opportunity to work in his group on this interesting topic. For his guidance, encouragement and inspiring ideas during our conversations. Additionally, for supporting me to attend conferences and training seminars, which has greatly broadened my view.

my supervisor **Prof. Dr. Nobert Willenbacher** for his kind guidance of my study in KIT, his review and inputs on this topic from time to time with the solid knowledge of rheology.

my advisor **Prof. Dr. Jorge Lacayo-Pineda** from Continental Tire for providing this interesting topic with his deep insights in rubber technology and lots of effort to coordinate this project.

Continental Reifen Deutschland GmbH for the financial support and samples preparation with the assistant and helpful discussion from **Dr. Anna-Lena Dreier**, **Dr. Christoph Vatterott** and **Dr. Frank Fleck**.

Dr. Lukas Schwab for warmly introducing me to this group at the very beginning and showing me the rubber testing facilities; **Dr. Christopher "Kiki" Klein** for teaching me the rheological measurements and the Labview software for FT-rheology; **Dr. Mahdi Abbasi** and **Dr. Valerian Hirschberg** for helpful comments on the rheological methods and results.

Dr. Karl-Friedrich Ratzsch for the RheoNMR setup, together with **Mr. Jonas Keller** and **Dr. Volker Röntzsch** for teaching me the NMR theory, instrumentation and the help they kindly offered to improve the NMR experiments; **Prof. Dr. Kay Saalwächter**, **Dr. Victor Litvinov** and **Prof. Dr. Bernhard Blümich** for their valuable suggestions on my NMR measurements and results.

Mr. Florian Rothenhäusler and **Mr. Jochen Klein** for their hard work and assistant to run FT-rheology on the model polystyrene melts-fillers system.

Ms. Nonkululeko Radebe, **Mr. Jonas Keller**, **Mr. Lorenz Faust** and **Dr. Valerian Hirschberg** for their time to correct this thesis; **Mr. Carlo Botha**, **Dr. Micheal Pollard** and **Dr. Ciprian Iacob** for the tiring effort they made to proofread the relevant publications.

Mrs. Sabine Weiland for the clear and concise organization of the documents about my work, traveling and so on.

Mr. Daniel Zimmermann for the super efficient IT support always.

Workshop of ITCP for their patience and carefulness on the required mechanical construction.

colleagues in the group of Prof. Wilhelm for the pleasure time in the office and lab, memorable moments during excursion, trips, BBQ, parties, Christmas movies, workshops for Doktorwagen, etc.

my friends in Germany for their accompanying to let me enjoy the life in Germany.

my girlfriend and **my family** for their encouragement and unconditional love.

Epilogue

Raised up in the rural day by day, the teacher's boy took books on the way,
from harsh winter to blooming May, from a spoiled homebody to breakaway.

What is rubber? Here comes bachelor. What is tire? Here comes engineer.

What is research? Graduate studies to search.

Hack into the snowy north, rheology is really worth.

What is nonlinear on earth? Karlsruhe master tells the course.

Paired birds been separating, fly to Europe for reuniting.

Self cooking for mom missing, leaving the elderly for grandson's visiting.

Future is under over-mulling, both sides are hard for balancing.

Wish the time is prolonging, with patience we are chasing.

—Shouliang Nie, April 2020, Karlsruhe.

一席布衣身，出入书门第。学堂多寒暑，少小奔波里。
初识高分子，学士文之立。徒业材料术，橡胶与炭黑。
增年实验工，研而为之趣。雪国取经路，流变诚为艺。
劳燕多纷飞，欧罗巴相聚。物者非线性，卡鲁师长技。
慈母遥遥念，异域陌陌炊。花翁垂垂老，游子迟迟归。
探前路漫漫，难全长依依。但愿人长久，来者之可追。

—二零二零年 四月 聂守亮 于 德国·卡尔斯鲁厄